Measurement of the Proton Structure Function xF_3 in High Q^2 DIS Events Using ZEUS Data

by

Amaya López-Durán Viani

Measurement of the Proton Structure Function xF_3
in High Q^2 DIS Events Using ZEUS Data

D i s s e r t a t i o n

zur Erlangung des des akademischen Grades
d o c t o r r e r u m n a t u r a l i u m
(Dr. rer. nat.)
im Fach Physik
eingerichtet an der

Mathematisch-Naturwissenschaftlichen Fakultät I
der Humboldt-Universität zu Berlin
von

Licenciada Amaya López-Durán Viani
22. Dezember 1973, Madrid, Spanien

Präsident der Humboldt-Universität zu Berlin
Prof. Dr. Jürgen Mlynek

Dekan der Mathematisch-Naturwissenschaftlichen Fakultät I
Prof. Dr. Bernhard Ronacher

Gutachter/innen:
1. Prof. Dr. Thomas Lohse
2. Prof. Dr. Paul Söding
3. Prof. Dr. Ulrich Katz

Tag der mündlichen Prüfung: 2. November 2001

Abstract

In neutral current $e^{\pm}p$ deep inelastic scattering events the exchanged electroweak boson between the lepton and the proton is the photon γ or the Z-boson. The exchange of the massless γ masks at low Q^2 values the exchange of the massive Z. Therefore weak interactions only become observable for values of Q^2 bigger than the Z-mass.

Weak interactions violate parity, the Z boson couples differently to electrons and positrons. When the double differential cross section is written in terms of the structure functions of the proton, the parity violation terms are absorbed in the structure function $xF_3(x, Q^2)$. In the high Q^2 region the cross sections for electrons and positrons deviate from each other, being higher for the electrons. This difference can be exploited to extract $xF_3(x, Q^2)$.

$xF_3(x, Q^2)$ not only provides a test of weak interactions due to the Z-boson exchange, it also gives a handle on the valence quarks density functions inside the proton.

A first measurement of the structure function $xF_3(x, Q^2)$ of the proton in neutral current $e^{\pm}p$ events has become possible with the delivery of a statistical relevant sample of $e^{-}p$ data by HERA during the years 1998 to 1999. Using ZEUS data the extraction has been done in a kinematic region outside the coverage from other collider experiments. This is the first test of weak interactions in neutral current events with the ZEUS detector.

Zusammenfassung

In tiefinelastischen $e^{\pm}p$-Streuereignissen mit neutralem Stromaustausch ist das schwache Austauschboson zwischen dem Lepton und dem Proton das Photon γ oder das Z-Boson. Der Austausch des masselosen γ verdeckt bei niedrigen Werten von Q^2 den Austausch des massiven Z. Deswegen werden die Effekte der schwache Wechselwirkung nur bei Q^2 größer als die Z-Masse beobachtbar.

Die schwache Wechselwirkung verletzt Parität, das Z-Boson koppelt verschieden an Elektronen und Positronen. Wenn der doppel-differenzielle Wirkungsquerschnitt als Funktion der Strukturfunktionen des Protons geschrieben wird, werden die paritätsverletzenden Terme in der Strukturfunktion $xF_3(x, Q^2)$ absorbiert. In der Region mit hohem Q^2 unterscheiden sich die Wirkungsquerschnitte für Elektronen und Positronen, er ist größer für Elektronen. Diese Differenz kann genutzt werden, um $xF_3(x, Q^2)$ zu extrahieren.

$xF_3(x, Q^2)$ bietet nicht nur einen Test der schwachen Wechselwirkung durch den Z-Bosonaustausch, sondern ermöglicht außerdem einen Zugriff auf die Bestimmung der Impulsdichtefunktionen der Valenzquarks innerhalb des Protons.

Eine erste Messung der Strukturfunktion $xF_3(x, Q^2)$ des Protons in $e^{\pm}p$-Ereignissen mit neutralem Stromaustausch ist durch die Lieferung eines statistisch relevanten Satzes von $e^{-}p$-Daten bei HERA während der Jahre 1998 bis 1999 möglich geworden. Unter Verwendung von ZEUS-Daten wurde die Extraktion in einem kinematischen Bereich außerhalb der Reichweite von anderen Beschleunigerexperimenten durchgeführt. Dies ist der erste Test der schwachen Wechselwirkung in Ereignissen mit neutralem Stromaustausch mit dem ZEUS-Detektor.

Contents

1 Introduction **1**

2 Theory **5**

2.1 Standard Model 5

2.1.1 Matter 5

2.1.2 Forces 5

2.1.3 Higgs mechanism 6

2.2 Cross section for Deep Inelastic Scattering 6

2.3 Parton Model 8

2.4 Extended Parton Model 10

2.4.1 Perturbative QCD 11

2.4.2 The factorization theorem of QCD 13

2.4.3 DGLAP equations 14

2.4.4 The hadronic final state 15

2.5 Electroweak Theory 15

2.6 Phenomenology of $xF_3(x, Q^2)$ 17

2.7 Structure Functions of the Proton in the Standard Model 19

2.8 Sum Rule for $xF_3(x, Q^2)$ 20

2.9 $xF_3(x, Q^2)$ in Neutrino Experiments 24

2.10 QED NLO Corrections 24

3 HERA **27**

4 ZEUS **31**

4.1 The Central Tracking Detector 33

4.1.1 CTD acceptance region 35

4.2 The Uranium Calorimeter 35

4.3 The Presampler . . . 36
4.4 Hadron Electron Separator . . . 37
4.5 The Luminosity Monitor . . . 38
4.6 The ZEUS Trigger and Data Acquisition System . . . 38

5 Cross Section Analysis and Extraction of $xF_3(x, Q^2)$ 41

5.1 Cross Section Extraction . . . 41
5.2 Unfolding Procedures . . . 42
5.3 Bin Center Correction . . . 43
5.4 Extraction of $xF_3(x, Q^2)$ . . . 44

6 Monte Carlo simulation 47

6.1 Introduction . . . 47
6.2 Simulation of DIS Events . . . 47
6.2.1 Radiative corrections included in the Monte Carlo simulation . . . 48
6.2.2 Generation of diffractive events . . . 49
6.2.3 Estimation of the diffractive sample . . . 49
6.3 Photoproduction Events . . . 50
6.4 Detector Simulation . . . 50
6.5 Failures of the Simulation . . . 50
6.5.1 Theoretical Features . . . 51
6.5.2 Experimental Features . . . 51
6.6 Monte Carlo Reweighting . . . 51

7 Reconstruction of Event Kinematics 53

7.1 Observables in DIS . . . 53
7.2 Electron Method . . . 54
7.3 Jacquet-Blondel Method . . . 54
7.4 Double Angle Method . . . 55
7.5 Comparison of the Different Methods for the Calculation of the Kinematic Variables 58
7.6 Kinematic Peak Events . . . 59

8 Data Sample **63**

8.1 Reconstruction of Event Variables . . . 63

8.1.1 Trigger reconstruction . . . 65

8.1.2 Vertex reconstruction . . . 66

8.1.3 Calorimeter cluster reconstruction . . . 66

8.1.4 Identification of the scattered lepton . . . 69

8.1.5 Scattered lepton energy . . . 69

8.1.6 Scattered lepton position . . . 70

8.1.7 Hadronic reconstruction . . . 71

8.2 Improvement of the Measurement . . . 74

8.2.1 Calorimeter alignment . . . 74

8.2.2 Electron vertex . . . 76

8.2.3 Vertex reweighting . . . 77

8.2.4 Corrections to the scattered lepton energy . . . 77

8.3 Backgrounds . . . 85

8.3.1 Photoproduction background . . . 85

8.3.2 Beam induced background . . . 86

8.3.3 Cosmic and halo muons . . . 86

8.3.4 QED-Compton events . . . 87

8.4 Event Properties and Summary of Cuts . . . 87

8.4.1 On-line event selection . . . 87

8.4.2 Off-line event selection . . . 88

9 Systematic Studies **91**

9.1 Monte Carlo Simulation Studies . . . 91

9.1.1 Trigger studies . . . 91

9.1.2 Vertex reweighting . . . 92

9.2 Scattered Lepton Finding Efficiency . . . 93

9.2.1 Efficiency in data and Monte Carlo events . . . 93

9.2.2 Determination of SIRA 5 efficiency for Monte Carlo events . . . 96

9.3 Efficiency of the Track Requirement Cuts . . . 99

9.4 Electromagnetic Energy Studies . . . 101

9.4.1 RCAL studies . . . 101

9.4.2 BCAL studies . . . 101

9.4.3 Conclusion . . . 102
9.5 Other Scattered Lepton Systematic Studies . . . 102
9.5.1 Scattered lepton isolation . . . 102
9.5.2 Electron energy smearing . . . 103
9.6 Hadronic Final State Studies . . . 104
9.6.1 Diffractive sample . . . 104
9.6.2 Hadronic energy scale . . . 105
9.7 Background Studies . . . 106
9.7.1 Estimation of the PHP background . . . 106
9.7.2 PHP background rejection with y_e cut . . . 107
9.7.3 Estimation of the beam-gas background . . . 107
9.8 Luminosity uncertainty . . . 108
9.9 Extraction of the Cross Sections and $xF_3(x, Q^2)$ . . . 108
9.9.1 Statistical error . . . 108
9.9.2 Systematic uncertainty . . . 108
9.9.3 Quality of the bins . . . 109

10 Measurement of Cross Sections **111**
10.1 Measurement of the Single Differential Cross Section $d\sigma/dQ^2$ . . . 111
10.2 Measurement of the Single Differential Cross Section $d\sigma/dx$ . . . 112
10.3 Measurement of the Single Differential Cross Section $d\sigma/dy$ . . . 114
10.4 Measurement of the Double Differential Cross Section $d\sigma/dx\,dQ^2$ . . . 116

11 Results of the Extraction of the Structure Function $xF_3(x, Q^2)$ **119**
11.1 Extraction of the Structure Function $xF_3(x, Q^2)$ . . . 119
11.2 Extraction of $xG_3(x, Q^2)$ . . . 120
11.3 Comparison with other experiments . . . 120
11.4 Sum rule for $xF_3(x, Q^2)$ . . . 121

12 Summary and Outlook **125**

A Adding the $(e^+p)^{920}$ Data for the Extraction of $xF_3(x, Q^2)$ **131**
A.1 Combination of the Data Samples . . . 132
A.2 Reduction of the Statistical Error with Increasing Luminosity. . . . 132

B Plots to the Monte Carlo Energy Smearing Estimation **135**

C Causes of Inefficiency of the Electron-Finder SINISTRA95 **138**

C.1 Wrong Vertex Measurement 138

C.2 Radiative Events 138

C.3 Other Inefficiencies 140

D Comparison Between Different Electron-Finders **141**

E Plots to the Electromagnetic Energy Scale **143**

F Plots to the Efficiency of the Track Requirement Cuts Study **148**

G Different Reconstruction Methods of the Hadronic Variables **153**

H Control Plots for the Data Samples $(e^+p)^{820}$ and $(e^+p)^{920}$ **156**

H.1 Data Sample 1996/1997 156

H.2 Data Sample 1999/2000 156

I Systematic Uncertainties for the Cross Section Measurement **162**

I.1 Systematic Uncertainty for the Single Differential Cross Section $d\sigma/dQ^2$ 162

I.2 Systematic Uncertainty for the Single Differential Cross Section $d\sigma/dx$ 162

I.3 Systematic Uncertainty for the Single Differential Cross Section $d\sigma/dy$ 163

I.4 Systematic Uncertainty for the Double Differential Cross Section $d^2\sigma/dx\,dQ^2$ . . 163

J Data tables **169**

List of Figures **185**

List of Tables **191**

Bibliography **193**

Chapter 1

Introduction

Fundamental particles appear, at present, to be of two distinct types. The first group consists of quarks and leptons. These are spin $\frac{1}{2}$ particles obeying the Fermi-Dirac statistics (fermions). The second group consists of the so-called gauge bosons. These are integer spin particles obeying Bose-Einstein statistics (bosons). The gauge bosons appear to be responsible for mediating the interaction forces between quarks and leptons. Existing results show clear evidence for four types of interactions in nature. These are the strong, electromagnetic, weak and gravitational forces. The theoretical knowledge of these interactions comes from the understanding of the underlying symmetries which appear to exist in nature and in the way in which they appear to be broken. The concept of gauge theories is an effective way to connect the symmetries with the interactions.

Classical field theory gives an adequate description of the properties of the long-range interaction, namely electromagnetism and gravitation. However it fails at the subatomic scale and, in this domain, quantum field theory must be used. Whereas, classically, an interaction at a distance is described in terms of a field or a potential, in quantum field theory forces are mediated by the exchange of particles.

The interaction of leptons and photons can be calculated perturbately in quantum electrodynamics (QED). The strong interaction is mediated, in nature, by eight massless colored vector gluons as described by the quantum chromodynamics (QCD).

Until 1973 experimental data on weak interactions, both from studies of the weak decays of strange and non-strange mesons and baryons and from low energy neutrino interactions, were consistent with there being only charge current interactions. Theoretically, all these observations could be explained within the framework of the Fermi theory of weak interactions, which involves the point-like coupling of four fermions. However, this theory predicted that the total neutrino-electron cross section would grow without bound, as the energy of the neutrino was increased. The introduction of the charged vector boson (W) to mediate the weak interaction (in a way analogous to the photon in QED) solved this problem, but only at the expense of introducing uncontrollable divergences in higher order calculations. The theoretical remedy to this problem postulated in the Standard Model was the introduction of a neutral vector boson (Z), whose contributions canceled the divergences. According to this model the Z particle mediates weak neutral currents and so the total neutral current consists of both γ and Z exchange in a precisely defined mixture.

This mixture is described by the Glashow-Weinberg-Salam model. Strictly speaking it is not a "unified field theory" of the electromagnetic and weak interactions since one introduces two

distinct coupling constants for the $SU(2)$ and $U(1)$ interactions.

Spontaneous symmetry breaking gives the solution to the problem that faced the physicist trying to write down a suitable theory of weak interactions in the 1950s and 1960s. It allows the construction of a gauge theory with massive gauge bosons. In addition it preserves the renormalizability of the theory.

The world that surrounds us is made of protons, neutrons and electrons. Only electrons are fundamental particles, protons and neutrons consist of quarks, antiquarks and gluons. Due to its compositeness the study of the internal structure of the proton has always been of interest. The structure becomes directly apparent if the nucleon is probed to distances less than the nucleon size (≤ 1 fm). Such small distances can only be resolved by scattering experiments in which the particles themselves act as the probes.

In HERA the proton is probed by the collision of two high energy beams of which the first is electrons or positrons and the second is protons. The probability of a collision to happen between the lepton and the proton is reflected by the cross section which is a decreasing function of the transfered momentum squared between the lepton and the proton.

This cross section can be expressed as a combination of the structure functions of the proton. A measurement of them will give information of the internal structure of the proton.

This work concentrates on the measurement of the structure function $xF_3(x, Q^2)$ of the proton that contains the parity violation terms of the weak interactions.

Parity violation has already been tested in neutral and charged current events in other than the HERA experiments. In 1984 the BCDMS collaboration published the first measurement of parity violation in neutral current events using polarized muon beams on a fixed target, spanning the kinematical region $40 < Q^2 < 180$ GeV^2 .

The structure function $xF_3^{CC}(x, Q^2)$ of the proton has been measured, with high statistics, in charged current events in neutrino–nucleon deep inelastic scattering experiments, CCFR and NuTev, where the exchanged weak bosons are the $W^{\pm}$-bosons. The kinematical region covered by these experiments is $0.01 < x < 0.65$ and $Q^2 < 200$ GeV^2.

The analysis described here uses charged lepton scattering data. It shows the parity violation effects caused by the exchange of the Z boson in $e^{\pm}p$ scattering. $xF_3(x, Q^2)$ is extracted from the difference of the cross sections for e^+p and e^-p data at high Q^2. In this analysis another kinematic range as in the neutrino experiments is accessible $0.01 < x < 1.0$ and $Q^2 > 3000$ GeV^2.

This work is structured as follows:

- Chapter 2 gives a short theoretical introduction to the Standard Model and the calculation of the cross section of the $e^{\pm}p$ process in this theoretical framework.

- In chapters 3 and 4 the HERA ring and the ZEUS detector are explained. These are merely an overview and only the components of the ZEUS detector used in the analysis are described in detail.

- Chapter 5 contains a description of the measurement of the cross section and the extraction of the structure function $xF_3(x, Q^2)$ of the proton.

- Monte Carlo simulations are an indispensable tool for the measurement of the cross section. The different programs to simulate signal events, background events and the detector are explained in chapter 6.

- The way to reconstruct the kinematical variables with the measured quantities is explained in chapter 7. Different methods are considered as well as a comparison of their resolution.

- The extraction of the structure function $xF_3(x, Q^2)$ involves the analysis of three different data samples $(e^+p)^{820}$, $(e^-p)^{920}$ and $(e^+p)^{920}$, where 820 and 920 stands for the proton energy. These data samples have been taken during the periods 1996/97, 1998/99 and 1999/2000 respectively. For simplicity only the analysis of the $(e^-p)^{920}$ sample will be shown in chapter 8. The final results for the two other data samples can be found in the appendices.

- The systematic studies done to test the stability of the measurement and its precision are shown, again only for the $(e^-p)^{920}$ data sample, in chapter 9.

- Chapter 10 contains the results of the measurement of the cross sections with statistical errors and systematic uncertainties for all the data samples analyzed.

- In chapter 11 one can find the extraction of the structure function $xF_3(x, Q^2)$ and a phenomenological interpretation.

- Finally the summary and outlook can be found in chapter 12.

Chapter 2

Theory

Over the centuries one of the interests of the human-kind has been the search of the basic constituents of matter and their interactions. Nowadays all the knowledge acquired in this field is compiled into a model that is able to account for, with extreme accuracy, most of the experimental results. Such a model is known as the Standard Model (SM) ([Gla61, Sal, Wei67]). Nevertheless it should be understood that the SM is not a model of everything. Neither the fundamental parameters, masses and couplings, nor the symmetry pattern can be derived. These elements are merely built into the model by hand. In addition the SM is not able to describe gravitation.

2.1 Standard Model

The SM postulates that matter is composed of leptons and quarks. These interact through forces created by fields and mediated by bosons. In this model particles acquire mass through the Higgs mechanism.

2.1.1 Matter

Leptons and quarks are the basic constituents of matter. They are $\frac{1}{2}$-spin particles grouped in three families each one with identical structure. Each family contains left- and right-handed leptons and quarks. The matter fermions carry isospin. The left-handed fermions form isospin doublets, while the right-handed are isospin singlets [SSZ00]:

$$\begin{bmatrix}\nu_e\\ e^-\end{bmatrix}_L \quad \nu_{eR} \quad e^-_R \qquad \begin{bmatrix}\nu_\mu\\ \mu^-\end{bmatrix}_L \quad \nu_{\mu R} \quad \mu^-_R \qquad \begin{bmatrix}\nu_\tau\\ \tau^-\end{bmatrix}_L \quad \nu_{\tau R} \quad \tau^-_R$$

$$\begin{bmatrix}u\\ d\end{bmatrix}_L \quad u_R \quad d_R \qquad \begin{bmatrix}c\\ s\end{bmatrix}_L \quad c_R \quad s_R \qquad \begin{bmatrix}t\\ b\end{bmatrix}_L \quad t_R \quad b_R$$

2.1.2 Forces

There are three forces in the SM: electromagnetic, weak and strong. These are mediated by spin-1 fields, that describe the photon γ, the gluons g, and the Z and $W^\pm$ bosons.

Interactions between force fields and matter as well as self interactions are described either by Abelian or by non-Abelian local gauge theories. The SM of electroweak and strong interactions is based on the group:

$$G_{SM} = SU(3)_C \otimes SU(2)_W \otimes U(1)_Y,$$

$SU(3)_C$ corresponds to the non-Abelian gluonic gauge fields that couple to the color charges as described by the Quantum Chromo Dynamics (QCD). $SU(2)_W$ is the non-Abelian electroweak-isospin group to which three W gauge fields are associated. $U(1)_Y$ is the Abelian hypercharge group. The electromagnetic and the weak forces are unified in the SM and described by the Glashow-Salam-Weinberg theory. In this theory the B field of the $U(1)_Y$ group and the $I_3 = 0$ component of the W triplet field from the $SU(2)_W$ group mix to form the photonic field A and the electroweak field Z. The relation between the electric charge, the hypercharge and the isospin is given by $Q = (\frac{Y}{2} + I_3)$.

$SU(3)_C$	*color*	G^a_μ	gluon color octet $a = 1, \ldots, 8$
$SU(2)_W$	*isospin*	W^i_μ	isotriplet $i = 1, 2, 3$
$U(1)_Y$	*hypercharge*	B_μ	

2.1.3 Higgs mechanism

In this sector the scalar fields interact with one-other in such a way that the ground state acquires a non-zero field strength, breaking electroweak symmetry spontaneously. The interaction energies of electroweak gauge bosons, leptons and quarks with this field manifest themselves as non-zero masses of these particles.

2.2 Cross section for Deep Inelastic Scattering

In this section the cross section of the lepton-proton deep inelastic scattering process $e^{\pm}p \rightarrow e^{pm}X$ with within the framework of the SM is presented. From all the possible channels the one of interest for this analysis is the Neutral Current (NC) channel. NC events are characterized by the presence of the initial lepton in the final state.

The reaction under study is $ep \rightarrow eX$ (Fig. 2.1). In such a process the interchanged particle between the lepton and the proton can either be a photon γ or a Z-boson. In a first approximation only single γ exchange will be considered. This approximation is valid provided the momentum transfered by the boson is much smaller than the mass of the Z boson ($M_Z = 91.187$ GeV [dg00]).

The cross section, in terms of the scattering amplitude can be written as:

$$d\sigma_n = \underbrace{\frac{1}{|v|2M2E}}_{IS} \underbrace{\frac{d^3k'}{(2\pi)^3 2k'_0}}_{PS_{e'}} \underbrace{\prod_{i=1}^{n} \frac{d^3p_i}{(2\pi)^3 2p_{i0}}}_{PS_{hadrons}} \times \underbrace{\frac{1}{4}}_{spin} \sum_{\sigma,s,s'} |\mathcal{M}_n|^2 \underbrace{(2\pi)^4 \delta^4(p + k - k' - p_n)}_{momentum\ conservation},$$

were IS refers to *initial state*, $PS_{e'}$ is the phase space of the scattered electron and $PS_{hadrons}$ the phase space of the hadrons in the final state. It is desirable to express the cross section in terms of variables that are invariant under Lorentz transformations, e.g., the transfered momentum

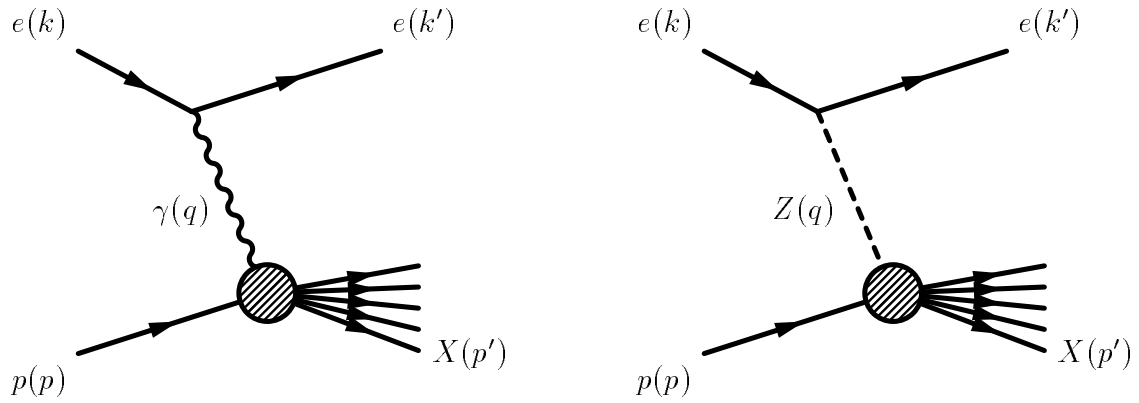

Figure 2.1: Schematic representation of a deep inelastic scattering event with a photon (left) and a Z (right) interchange.

squared of the photon $Q^2 = -q^2 = -(k-k')^2 \geq 0$. For one photon exchange the scattering amplitude has the form:

$$\mathcal{M}_n = e^2 \underbrace{[Q_e \bar{u}(k',s')\gamma^\mu u(k,s)]}_{leptonic\ part} \left(\frac{1}{q^2}\right) \underbrace{[\langle n|J_\mu(0)|p,\sigma\rangle]}_{hadronic\ part},$$

where Q_e denotes the charge relative to the positron's charge, $Q_e = -1$ for electron, and $Q_e = +1$ for positron. This is an inclusive measurement, therefore the integration runs over all the hadronic final states, obtaining a very simple expression in terms of two tensors:

$$\frac{d^2\sigma}{d\Omega\, dE'} = \frac{\alpha^2}{q^4}\left(\frac{E'}{E}\right) \underbrace{l^{\mu\nu}}_{leptonic} \underbrace{W_{\mu\nu}}_{hadronic}, \tag{2.1}$$

$l^{\mu\nu}$ corresponds to the leptonic part calculated using Feynamn rules; for QED $l_{\mu\nu}$ may be written:

$$\begin{aligned} l_{\mu\nu} &= \frac{1}{2}\bar{u}(k',s')\gamma^\mu Q_e \bar{u}(k,s)\gamma^\mu Q_e u(k',s') \\ &= 2Q_e^2\left(k_\mu k'_\nu + k'_\mu k_\nu + \frac{Q^2}{2} g_{\mu\nu}\right), \end{aligned}$$

$W_{\mu\nu}$ corresponds to the unknown hadronic part. It can be most generally parameterized using a combination of tensors:

$$\begin{aligned} W_{\mu\nu} &= -W_1\, g_{\mu\nu} + \frac{W_2}{M^2}\, p_\mu\, p_\nu - i\frac{W_3}{M^2}\, \varepsilon_{\mu\nu\lambda\rho} p_\lambda\, q_\rho + \\ &\quad \frac{W_4}{M^2}\, q_\mu\, q_\nu + \frac{W_5}{M^2}(p_\mu\, q_\nu + p_\nu\, q_\mu) + i\frac{W_6}{M^2}(p_\mu\, q_\nu - p_\nu\, q_\mu). \end{aligned}$$

Since the leptonic tensor is symmetric, it is sufficient for the hadronic tensor to contain only symmetric terms since the antisymmetric ones drop out. This means that one can neglect W_3 and W_6. The number of independent terms reduces further when applying the current conservation constraint. Current conservation implies $q^\mu W_{\mu\nu} = 0$.

This leads to:

$$W_5 = -\frac{p\cdot q}{q^2}\, W_2,$$

and

$$W_4 = \left(\frac{p\cdot q}{q^2}\right)^2 W_2 + \frac{M^2}{q^2} W_1,$$

so that the hadronic tensor can be written as:

$$\begin{aligned} W_{\mu\nu} &= -\left(g_{\mu\nu} - \frac{q_\mu q_\nu}{q^2}\right) W_1 + \left(p_\mu - q_\mu \frac{p\cdot q}{q^2}\right)\left(p_\nu - q_\nu \frac{p\cdot q}{q^2}\right)\frac{W_2}{M^2} \\ &= -g_{\mu\nu} W_1 + p_\mu p_\nu \frac{W_2}{M^2} + \cdots \end{aligned} \tag{2.2}$$

Substituting this into the cross section, Eq. (2.1) one obtains:

$$\frac{d^2\sigma}{dq^2\, d\nu} = \frac{4\pi\alpha^2}{q^4}\frac{E'}{E}\left[W_2(\nu, q^2)\cos^2\left(\frac{\Theta}{2}\right) + 2W_1(\nu, q^2)\sin^2\left(\frac{\Theta}{2}\right)\right],$$

where $\nu = (p\cdot q)/M$, is another Lorentz invariant. The cross section is now given in terms of two structure functions W_1 and W_2. In principle these functions depend on the variables ν and q^2. The SLAC-MIT collaboration has measured these functions obtaining the results shown in Fig. 2.2 for the lower values of Q^2.

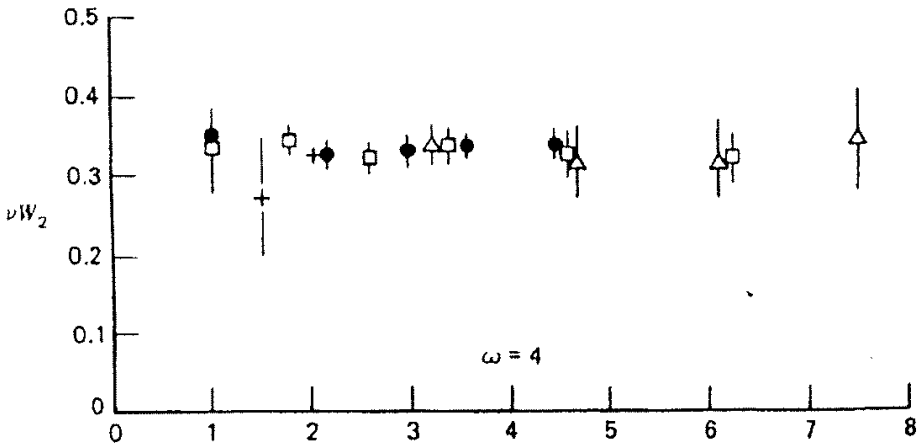

Figure 2.2: The plot shows the scaling behavior of the structure function $F_2 = \nu W_2$ for different Q^2 values at $\frac{1}{w} = x = 0.25$ as a function of ν from a SLAC measurement. Plot taken from [FK72].

It can be seen that for the measured region in $x = \frac{Q^2}{2M\nu}$ and Q^2 the structure functions only depend on the variable x.

$$\begin{aligned} MW_1(q^2, \nu) &\rightarrow F_1(x) \\ \nu W_2(q^2, \nu) &\rightarrow F_2(x). \end{aligned}$$

This behavior is called Bjorken scaling, and the x-variable, Bjorken x.

2.3 Parton Model

Bjorken scaling implies that the photon scatters off a point-like constituent from the proton. Otherwise the structure functions would depend on the ratio Q/Q_0 where $1/Q_0$ would be the typical length scale characterizing the size of the constituents.

The parton model postulates a proton with point-like spin-$\frac{1}{2}$ partons. In the scattering process the parton carries a longitudinal momentum ξp where ξ is the fraction of the proton momentum. The transverse momentum of the parton is negligible.

It can be shown that this variable ξ is the Bjorken x_{Bj} in which the structure functions scale.

$$p' = \xi p + q \xrightarrow{()^2} p'^2 = \xi^2 p^2 + 2M\nu\xi + q^2.$$

Considering the high energy limit i.e. low masses:

$$(\xi p)^2 = (p')^2 = m_q^2 \equiv 0 \rightarrow q^2 + 2M\nu\xi \sim 0,$$

one obtains

$$\xi = \frac{-q^2}{2M\nu} \equiv x.$$

The hadronic tensor in Eq. (2.2), can be calculated in this model knowing that the electron is scattered by particles with spin 1/2, and that these particles carry a momentum ξp as depicted in Fig. 2.3.

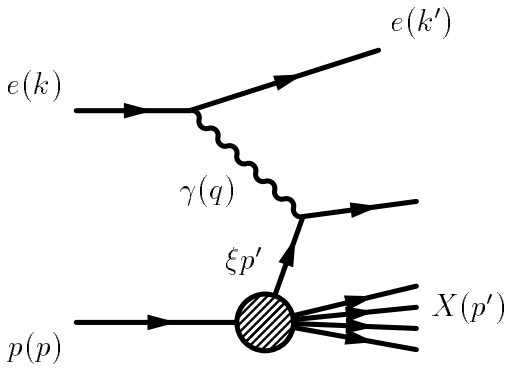

Figure 2.3: Schematic representation of the quark parton model. The incoming lepton is scattered off by a parton from the proton.

The contribution to the hadronic tensor from a single parton reads:

$$K_{\mu\nu}(\xi) = \frac{Q_p^2}{4M\xi} \sum_{spins} [\bar{u}(\xi p)\gamma_\mu u(p')][\bar{u}(p')\gamma_\nu u(\xi p)] \frac{\delta(p_0' - \xi p_0 - q_0)}{2p_0'},$$

were Q_p^2 is the parton charge relative to the positron. The total hadronic tensor is given by integrating this over all possible momentum fractions ξ. Considering the number of partons with momentum ξp to be proportional to some unknown function $f(\xi)$, for only one sort of partons the total hadronic current is given by:

$$W_{\mu\nu} = \int_0^1 f(\xi)\, K_{\mu\nu}(\xi)\, d\xi.$$

Taking all this into account and performing this integral, the first terms of the hadronic tensor can be written as:

$$W_{\mu\nu} = -g_{\mu\nu} \left(\frac{Q_p^2 f(x)}{2M} \right) + p_\mu p_\nu \left(\frac{Q_p^2 x f(x)}{\nu M^2} \right) + \ldots \tag{2.3}$$

Comparing Eq. (2.2) with Eq. (2.3) one can write:

$$MW_1 \rightarrow F_1(x) = \frac{1}{2}Q_p^2 f(x) \tag{2.4}$$

$$\nu W_2 \rightarrow F_2(x) = Q_p^2 x f(x), \tag{2.5}$$

F_1 and F_2 are related by the Callan-Gross relation [CGCG69]:

$$2xF_1(x) = F_2(x). \tag{2.6}$$

This relation reflects the fact that spin-$\frac{1}{2}$ partons cannot absorb longitudinally polarized vector bosons and thus provides an experimental test for the spin-$\frac{1}{2}$ nature of the partons [HM84].

Until now the naïve parton model has been described . It gives the picture of a static proton made of charged spin-$\frac{1}{2}$ partons that in the framework of QCD can be identified with the quarks. Those partons carry a longitudinal momentum proportional to the total proton momentum ξp and a negligible transverse momentum. The structure functions of the proton, used as a tool to parameterized the cross section, describe the parton densities inside the proton. These functions only depend on the variable x.

2.4 Extended Parton Model

In the past years the kinematic range in which $F_2(x)$ has been measured has been increased enormously. With this improvement in the measurement it has been seen that the scaling behavior shown in Fig. 2.2 is only a good approximation in a very restricted area of the kinematic plane [A$^+$93, D$^+$93]. For the region $x \approx 0.25$ (shown in Fig. 2.2) the structure function F_2 does not depend on Q^2, but for low values of x, $F_2(x)$ is no longer flat for all Q^2 (Fig. 2.4) i.e:

$$F_2(x) \rightarrow F_2(x, Q^2).$$

The naïve parton model, although correct for a restricted kinematic region, is not able to explain the scaling violation.

In addition, the Callan-Gross relation Eq. (2.6) which no longer holds can conveniently be parameterized in terms of a new structure function $F_L(x, Q^2)$:

$$F_L(x, Q^2) = F_2(x, Q^2) - 2xF_1(x, Q^2) \neq 0.$$

Another effect the naïve parton model cannot describe is the fact that the integral over the partons' momentum fraction is smaller than unity [E$^+$73]:

$$\int_0^1 x f(x)\, dx \neq 1.$$

For a proton made out of only charged spin-$\frac{1}{2}$ partons, the integration should be unity due to momentum conservation.

The naïve parton model as outlined in the previous section does not describe the experimental data. The reason could lie in the assumptions made, i.e. the parton has negligible transverse momentum and, the proton is made out of charged spin-$\frac{1}{2}$ partons with $m_p = 0$ only.

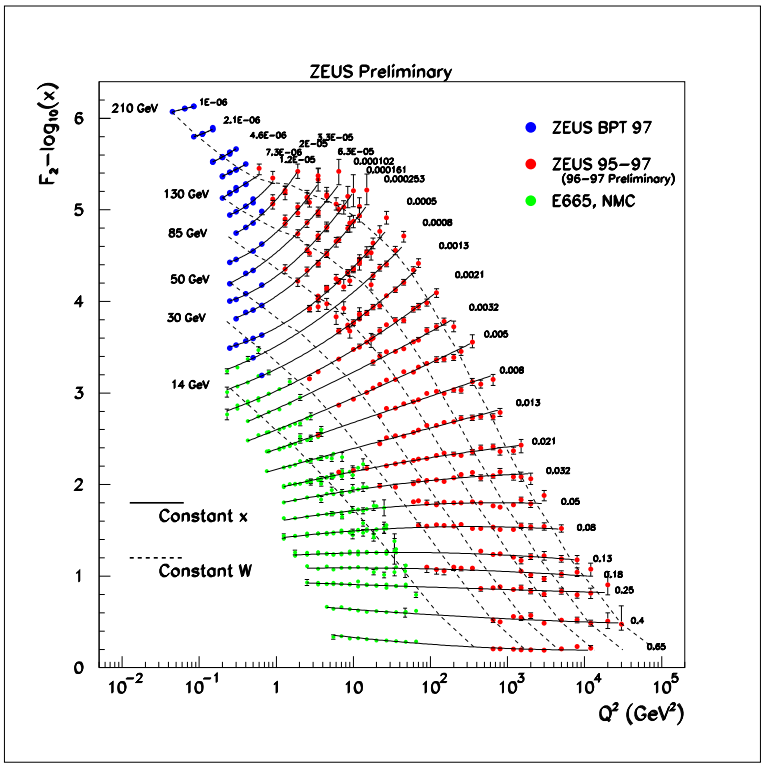

Figure 2.4: $F_2(x, Q^2)$ as a function of Q^2 for different x bins. The scaling violation behavior can be observed. Plot taken from [Yos01].

If quarks are not sole constituents, other must be considered. These must be neutral particles since the charge of the proton is already accounted for. From the violation of the Callan-Gross relation is clear that the other constituents of the proton cannot have spin $\frac{1}{2}$ so neutral spin-$\frac{1}{2}$ particles are not allowed. QCD provides the solution, namely gluons with spin 1, which can be taken as the missing constituent. Making this assumption the static model no longer holds and a new dynamic model has to be considered. A model in which the quarks inside the proton are constantly radiating and absorbing gluons. This produces a cloud of gluons and quark-antiquark pairs that surround the bare quarks. High Q^2 regimes, where the photon is able to probe the internal structure of the proton more deeper, reveal a logarithmic dependence of the structure functions on Q^2. This dependence on Q^2 is predicted by QCD. A schematic representation of the higher order processes in the strong coupling constant α_s is shown in Fig. 2.5. Since those processes are of higher order in α_s all other processes of this order must also be taken into account. One example is shown on the right hand side of Fig. 2.5.

Direct evidence for the existence of gluons was provided in 1979 at DESY via the observation of three-jet events in e^+e^- annihilation [B$^+$79].

2.4.1 Perturbative QCD

When calculating higher order corrections for the cross section, one often encounters logarithmically divergent terms. This problem is solved by a calculation technique called renormalization in which the divergences are absorbed order by order into a redefinition of the electron charge, mass and wave function. Perturbative QCD (pQCD) is only well defined for the regions in which the coupling constant remains small.

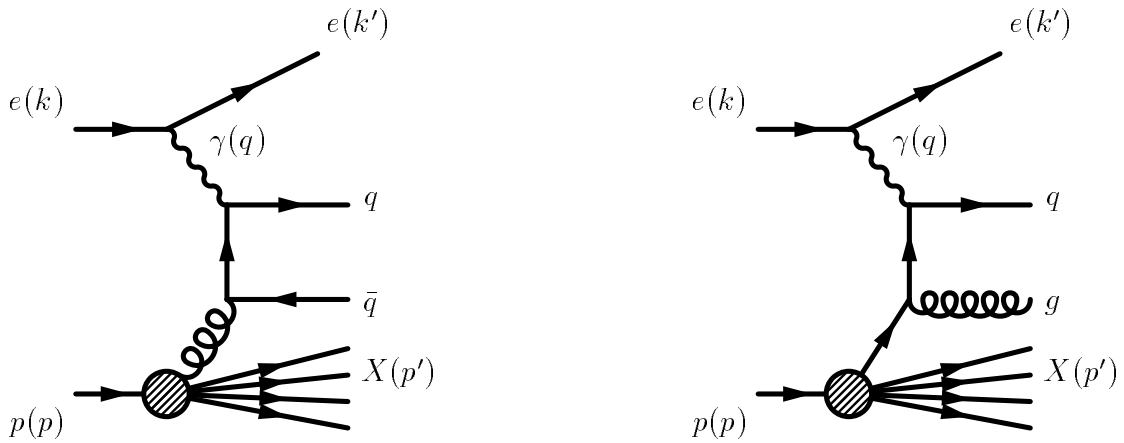

Figure 2.5: Schematic representation of processes that contribute in order α_s. (left) The boson-gluon fusion process: the exchanged photon and the gluon from the proton produce a quark-antiquark pair. (right) The QCD-Compton process: a quark from the proton radiates a gluon before interacting with the photon.

A potential problem in pQCD is that the strong coupling constant α_s is, first highly scale dependent, and second not always small in the accessible experimental range. The scale dependence of α_s is given by [dg00]:

$$\alpha_s(\mu^2) = \frac{12\pi}{(11n - 2n_f)\ln(\mu^2/\Lambda^2)},$$

where $n = 3$ is the number of colors, $n_f = n_f(\mu^2)$ is the number of active quark flavors (at HERA, $n_f = 3, \ldots, 5$) and $\Lambda \approx 100 \ldots 300$ MeV [dg00] is a parameter of QCD. One can see that if μ^2 gets small, then $\alpha_s(\mu^2)$ will be large.

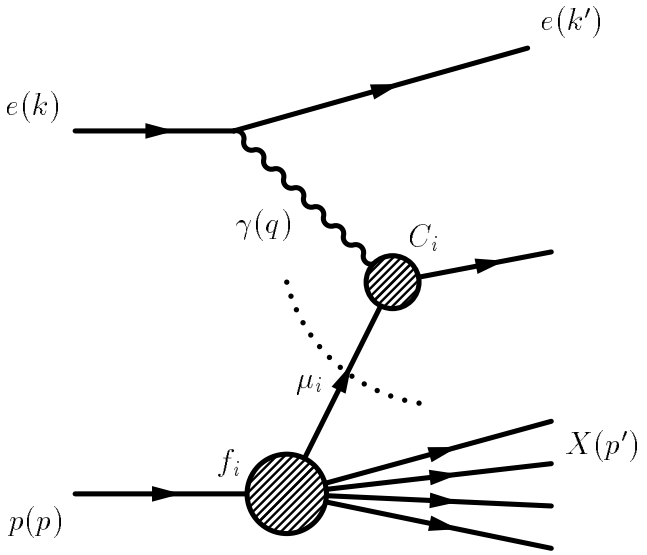

Figure 2.6: Illustration of the QCD factorization theorem for the $ep \to eX$ process. The factorization scale μ_F separates long-range and short-range contributions, which are absorbed into parton densities f_i and coefficient functions C_i respectively.

One can consider two limits: $\alpha_s \to 0$ for $\mu \to \infty$ and $\alpha_s \to \infty$ for $\mu \to \Lambda$. These two limits

have different physical consequences. The first one implies that when $\mu^2 = Q^2$ is high, and hence distances are small, the coupling constant α_s becomes very small. Quarks and gluons inside the proton do not feel each other. This behavior is known as asymptotic freedom. On the other hand, taking the opposite limit, for $\mu^2 = Q^2$ low, which corresponds to long distances, the coupling constant becomes enormous implying that it is impossible to obtain a free quark separate from a bound state. This limit results in confinement of the quarks.

2.4.2 The factorization theorem of QCD

An indication of what "reasonably small" means is given in the factorization theorem of QCD where a new scale μ_F is introduced. This new scale separates the region of soft physics in which perturbative QCD is not applicable and hard scattering physics where it is. These regions are also defined as long and short-distance scales respectively. The second region is the region in which the cross sections are calculated, while the other is the region in which the parton densities are parameterized. Since the parton distributions can not be calculated using pQCD, another method has to be used. The factorization theorem defines the structure functions as:

$$F_2(x, Q^2) = \sum_{i=q,\bar{q},g} \int_x^1 dx' C_i \left(\frac{x}{x'}, \alpha_s(\mu_F^2), \frac{Q^2}{\mu_F^2} \right) f_i(x', \mu_F^2), \tag{2.7}$$

where C_i denotes the coefficient functions responsible for the short-range interaction, and f_i are the parton density functions, parameterizing the short-range terms. The factorization theorem for the $ep \to e'X$ process is illustrated in Fig. 2.6

At leading order in perturbation theory, the C_i are simply the squared parton charges multiplied by a delta function:

$$\begin{aligned} C_q(x) &= Q_q^2 \delta(1-x) \\ C_{\bar{q}}(x) &= Q_{\bar{q}}^2 \delta(1-x) = C_q(x) \\ C_g(x) &= 0. \end{aligned}$$

Substituting this into Eq. (2.7) one obtains the quark parton model $F_2(x)$ defined in Eq. (2.5).

For higher orders there is more freedom in the way the corrections are absorbed either by the C_i coefficients or the parton densities f_i. Different schemes propose different solutions. In the DIS scheme all the corrections are grouped into the parton densities so that the measurable structure function, $F_2(x, Q^2)$, remains simple. In this scheme the structure function $F_2(x, Q^2)$ has the same expression at all orders. The other frequently used scheme, the one usually preferred by theoreticians, is the $\overline{MS}$ (modified minimal subtraction) scheme. In this scheme all structure functions must be evaluated using convolution integrals.

The structure functions are observables, that means that they cannot depend on any factorization scale μ_F. On the other hand the parton densities, since they are not measurable, may depend on an arbitrary factorization scale. As a result, the obtained value of the structure functions is independent of the factorization scheme chosen, and the only difference is the expression for the structure functions in terms of the parton densities.

2.4.3 DGLAP equations

Since parton densities are not observables, they cannot be measured directly. They can be extracted from experimental data at a certain value Q_0^2 and then be evolved to other values of Q^2. There are several parameterizations for these parton densities. The one commonly used in this analysis is the CTEQ5D parameterization [L$^+$95]. The evolution of the parton densities is given by the DGLAP (after Dokshitzer, Gribov, Lipatov, Altarelli and Parisi) equations [GL72], [AP77] and [Dok77].

When increasing the resolution, objects that looked point-like before become now a structure. As said before, quarks can radiate and absorb gluons. A quark with a momentum x' can be resolved now as a quark and a gluon with momenta x and $(x'-x)$ respectively. Other processes like gluon splitting into two quarks or two gluons can also be taken into account. This is an iterative processes that goes into the proton structure as deep as the Q^2 allows.

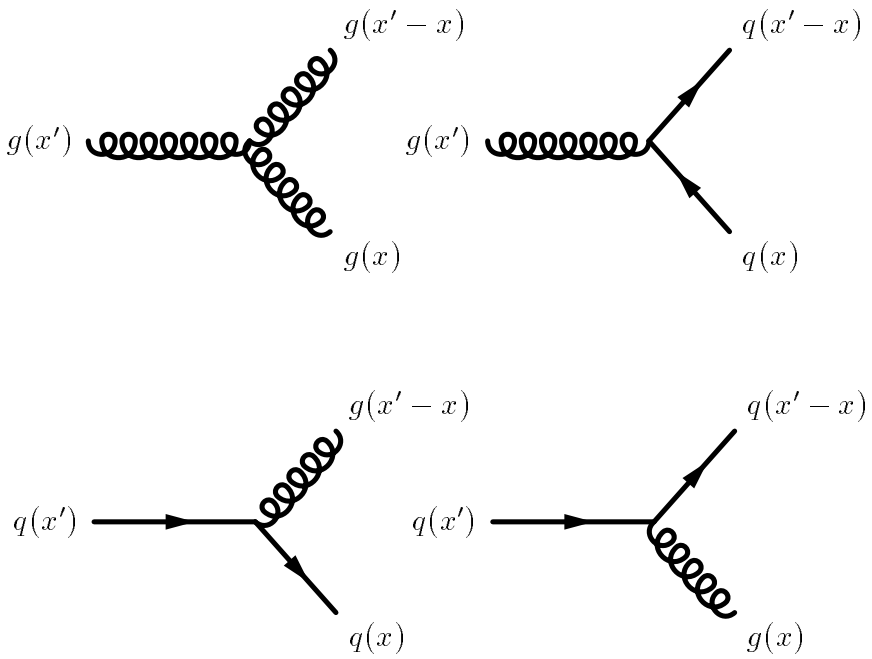

Figure 2.7: (Top) Gluon splitting into two gluons (left) and a quark-antiquark pair (right). (Bottom) Emission (left) and absorption (right) of a gluon by a quark.

The equations describing those processes are:

$$\begin{aligned}
\frac{dg(x,Q^2)}{d\ln Q^2} &= \frac{\alpha_s(Q^2)}{2\pi}\left((P_{gg}\otimes g)(x,Q^2)+\sum_j(P_{gq_j}\otimes q_j)(x,Q^2)\right)\\
\frac{dq_i(x,Q^2)}{d\ln Q^2} &= \frac{\alpha_s(Q^2)}{2\pi}\left((P_{q_ig}\otimes g)(x,Q^2)+\sum_j(P_{q_iq_j}\otimes q_j)(x,Q^2)\right).
\end{aligned}$$

The convolution is defined as:

$$(P\otimes f)(x,Q^2)=\int_x^1\frac{dx'}{x'}f(x',Q^2)P\left(\frac{x}{x'}\right),$$

and $P_{ij}(x/x')$ denotes the splitting functions [AP77] where $g(x,Q^2)$ and $q_i(x,Q^2)$ are the gluon and quark densities. The quantity $\alpha_s(Q^2)P_{ij}(x/x')$ is a measure of the probability that a parton

i with momentum fraction x is radiated from a parton j with momentum $x' \geq x$, when the scale changes by $d \ln Q^2$. The basic diagrams are given in Fig. 2.7. Like the parton densities, the splitting functions also depend on the chosen renormalization scheme.

2.4.4 The hadronic final state

As a consequence of confinement quarks and gluons appear in bound states. In a DIS process, when a parton has such a high momentum that it can escape the proton, a process to restore a colorless final state begins. It consists of the interchange of gluons between the struck quark and the remaining proton. This cascade of gluons split further into quark-antiquark pairs that continue the process. This process, shown in Fig. 2.8, is called hadronization. After this has happened, mesons are built out of the quark-antiquark pairs in a process called fragmentation.

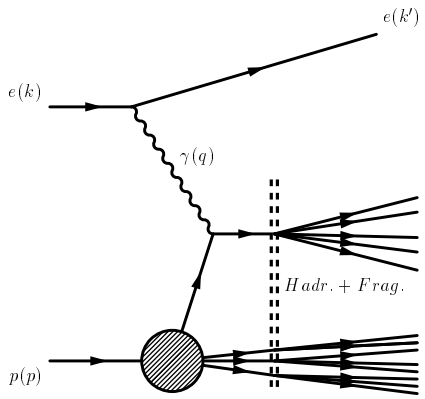

Figure 2.8: Schematic representation of the hadronization and fragmentation that takes place after the scattering process.

The signature observed in LO processes is two jets, one belonging to the proton remnant and the other one associated with the struck quark, that follows the direction of the exchanged boson. In higher orders, diagrams such as the ones shown in Fig. 2.5 lead to a greater number of jets.

Diffractive events

Diffractive events are events in which there is almost no energy filling the gap between the proton remnant and the hadronic system, until now associated to the struck quark. This means that the hadronic system, opposite to the struck quark, has to have reached a color-neutral state long before leaving the proton. This colorless object, emitted by the proton, can be understood as a pair of gluons that balance each other in color.

2.5 Electroweak Theory

Until now only the exchange of a single photon was considered, but when reaching the high Q^2 region ($Q^2 \approx {M_Z}^2$), the probability that the particle exchanged between the electron and the quark is a Z is no longer negligible.

The electroweak boson couples differently to left- and right-handed particles, thus it violates the parity operation

$$P\left(e_L^-\right) = e_R^-.$$

Neglecting small CP-violating effects in the quark sector for CC events, CP is a conserved symmetry in the electroweak theory which means nothing else but that all physical quantities are invariant under the transformation

$$CP\left(e_L^-\right) = e_R^+.$$

If one wants to know a cross section involving a positron only and one knows the cross section for the same process involving electrons one can obtain the first one by applying the charge operation to the second one

$$C\left(\sigma(e^- p)\right) = \sigma(e^+ \bar{p}).$$

In the case of Z and γ exchange the leptonic tensor contains three parts, coming from the photon ($l^{\mu\nu}_{\gamma\gamma}$), the Z-boson ($l^{\mu\nu}_{ZZ}$) and the interference of photon and Z exchange ($l^{\mu\nu}_{Z\gamma}$).

$$\begin{aligned}
l^{\mu\nu}_{ZZ} &= \frac{1}{2}\bar{u}(k',s')\gamma^\mu(v_e - a_e\gamma_5)u(k,s)\bar{u}(k,s)\gamma^\nu(v_e - a_e\gamma_5)u(k',s') \\
&= 2\left[(v_e^2 + a_e^2)[k_\mu k'_\nu + k'_\mu k_\nu + \frac{Q^2}{2}g_{\mu\nu}] - 2a_e v_e i\varepsilon_{\mu\nu\alpha\beta}k^\alpha k'^\beta\right], \qquad (2.8) \\
l^{\mu\nu}_{Z\gamma} &= \frac{1}{2}\bar{u}(k',s')\gamma^\mu(v_e - a_e\gamma_5)u(k,s)\bar{u}(k,s)\gamma^\nu Q_e u(k',s') \\
&= 2Q_e\left[v_e[k_\mu k'_\nu + k'_\mu k_\nu + \frac{Q^2}{2}g_{\mu\nu}] - a_e i\varepsilon_{\mu\nu\alpha\beta}k^\alpha k'^\beta\right], \qquad (2.9) \\
l^{\mu\nu}_{\gamma\gamma} &= \frac{1}{2}\bar{u}(k',s')\gamma^\mu Q_e\bar{u}(k,s)\gamma^\nu Q_e u(k',s') \\
&= 2Q_e^2\left[k_\mu k'_\nu + k'_\mu k_\nu + \frac{Q^2}{2}g_{\mu\nu}\right], \qquad (2.10)
\end{aligned}$$

where the factor $1/2$ comes from spin average.

Each part has a different weight, when calculating the total cross section

$$\frac{d^2\sigma}{d\Omega\, dE'} = \frac{\alpha^2}{q^4}\left(\frac{E'}{E}\right)\left\{l^{\mu\nu}_{\gamma\gamma} + 2\chi_z(Q^2)l^{\mu\nu}_{Z\gamma} + \chi_z^2(Q^2)l^{\mu\nu}_{ZZ}\right\}W_{\mu\nu},$$

with $a_e = -1/2$, $v_e = a_e - 2Q_e \sin\Theta_W$ and χ_z

$$\chi_z(Q^2) = \frac{1}{4\sin^2\Theta_W\cos^2\Theta_W}\,\frac{Q^2}{Q^2 + M_Z^2},$$

is the ratio of the photon and the Z propagator times a constant prefactor containing the weak mixing angle Θ_W.

Since the total leptonic tensor now contains antisymmetric terms the hadronic one cannot be restricted to symmetric terms alone any more, antisymmetric ones have to be added. When proceeding the same way as in the case of pure γ exchange one obtains the structure functions $F_2(x,Q^2)$ and $F_L(x,Q^2)$ as before which are not only CP-invariant but also separately C and

P invariant as in pure QED. Now there is an additional term that accounts for the parity violation of the electroweak interaction. This last function yields a positive contribution to the cross section for $e^- p$ scattering, and a negative one for the $e^+ p$ scattering.

Finally the cross section can be written in terms of the x and Q^2 variables as:

$$\frac{d^2\sigma^\pm}{dx\, dQ^2} = \frac{2\pi\alpha^2(Q^2)}{xQ^4}\left[Y_+ F_2(x,Q^2) \mp Y_- xF_3(x,Q^2) - y^2 F_L(x,Q^2)\right], \tag{2.11}$$

where the kinematic variable is $y = Q^2/(x \cdot s)$ and $Y_\pm = 1 \pm (1-y)^2$.

The flip of the sign comes from the requirement of applying the charge operation to get from electrons to positrons (or vice versa) and the restriction that the CP operation leaves the cross section invariant.

2.6 Phenomenology of $\mathbf{xF_3(x, Q^2)}$

Before giving the complete structure functions of the proton including electroweak interaction some phenomenology of xF_3 is presented. Only LO results will be considered.

The total cross section for the NC DIS can be split into three parts [KR84] which correspond to the three contributions in Eq. (2.8)–(2.10):

$$\begin{aligned}
\sigma^\pm &= \sigma_0\left[\sigma_{\gamma\gamma} + \sigma^\pm_{Z\gamma} + \sigma^\pm_{ZZ}\right], \qquad (2.12)\\
\sigma_0 &= \frac{2\pi\alpha^2}{xQ^4},\\
\sigma_{\gamma\gamma} &= \left[Y_+\left(-Q_e\right) F_2^{em}(x,Q^2)\right],\\
\sigma^\pm_{Z\gamma} &= \chi_z(Q^2)\left[-Y_+(v_e - \lambda a_e)\, G_2(x,Q^2) \pm Y_-(a_e + \lambda v_e)\, xG_3(x,Q^2)\right],\\
\sigma^\pm_{ZZ} &= \chi_z^2(Q^2)\left[Y_+(v_e^2 + a_e^2 + 2a_e v_e \lambda)\, H_2(x,Q^2) \mp Y_-(2a_e v_e - (a_e^2 + v_e^2)\lambda)\, xH_3(x,Q^2)\right],
\end{aligned}$$

where λ is the helicity. Since HERA runs with unpolarized beams, $\lambda = 0$.

The three reduced cross sections $\tilde{\sigma}^+_{\gamma\gamma,Z\gamma,ZZ} = \sigma^+_{\gamma\gamma,Z\gamma,ZZ}/Y_+$ of Eq. (2.12) are shown in Fig. 2.9 for different values of Q^2. It can be seen that for small values of Q^2 the dominant contribution to the cross section comes from the $\gamma\gamma$ term. Only for $Q^2 > 8000$ GeV^2 does the $Z\gamma$ term in the intermediate x region and the ZZ term in the low x region contributes sizable part of the cross section. Since the cross section shown is for positrons the $Z\gamma$ term contributes negatively to the cross section.

The five structure functions defined in Eq. (2.12) can be expressed as functions of the parton distributions:

$$\begin{aligned}
\left(F_2^{em}, G_2, H_2\right)(x,Q^2) &= \sum_f \left(Q_f^2, 2Q_f v_f, a_f^2 + v_f^2\right)\left[xq_f(x,Q^2) + x\bar{q}_f(x,Q^2)\right],\\
\left(xG_3, xH_3\right)(x,Q^2) &= \sum_f \left(2Q_f a_f, 2a_f v_f\right)\left[xq_f(x,Q^2) - x\bar{q}_f(x,Q^2)\right], \qquad (2.13)
\end{aligned}$$

where Q_i is the electric charge relative to the positron and $v_i = T_{3i} - 2Q_i \sin^2\Theta_W$, $a_i = T_{3i}$ are the vector and axial vector couplings of the different quark flavors to the Z-boson defined in terms of the weak isospin T_{3i} and the Weinberg angle Θ_W.

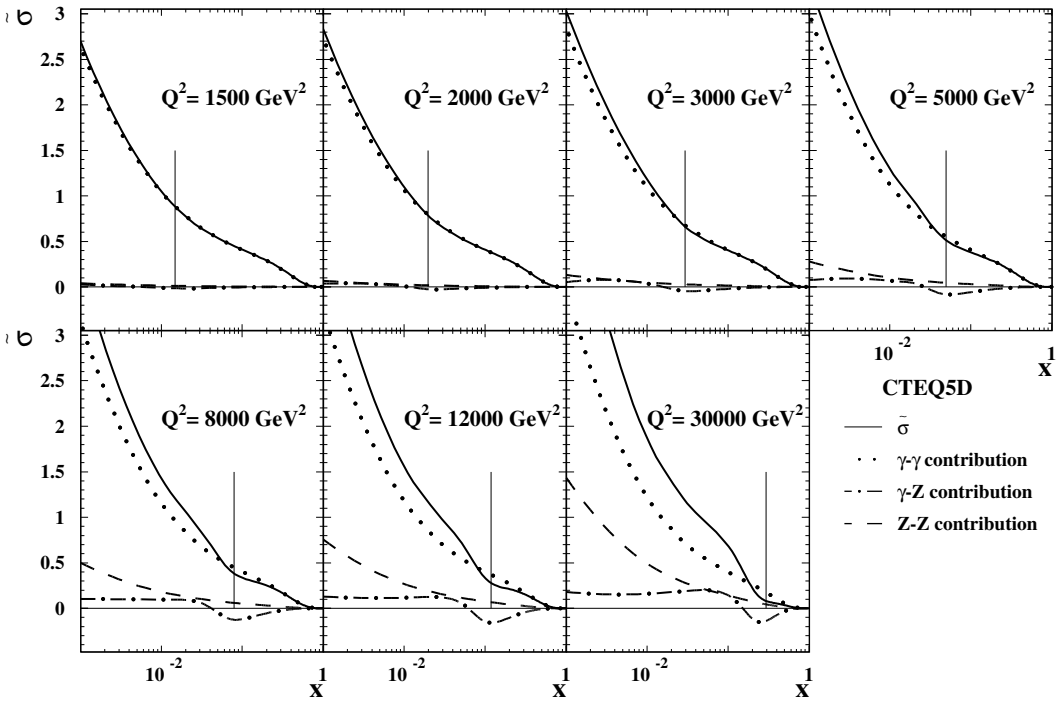

Figure 2.9: The different contributions of the interchange of $\gamma\gamma$, $Z\gamma$ and ZZ to the theoretical reduced cross section for NC e^+p DIS events with $E_p = 920$ GeV are shown for different values of Q^2. The vertical line shows the HERA kinematic limit $y = 1$.

All these structure functions are of the same order of magnitude, as shown in Fig. 2.10. The increase of the functions F_2^{em}, G_2 and H_2 for small x as well as the maximum of xG_3 and xH_3 can be understood from Eq. (2.13) and the parton distributions shown in Fig. 2.11. F_2^{em}, G_2 and H_2 are proportional to the sum of the quark densities and thus primarily sensitive to the sea quarks which grow for small x while xG_3 and xH_3 are proportional to the valence quarks which peak at $x \approx 0.1$.

The structure functions $F_2(x, Q^2)$ and $xF_3(x, Q^2)$ in Eq. (2.11) are a combination of the structure functions F_2^{em}, G_2, H_2 and xG_3, xH_3 respectively :

$$\begin{aligned} F_2(x,Q^2) &= (-Q_e)\, F_2^{em} - v_e\, \chi_z(Q^2)\, G_2(x,Q^2) + (a_e^2 + v_e^2)\, \chi_z^2(Q^2)\; H_2(x,Q^2) \\ xF_3(x,Q^2) &= -a_e\, \chi_z(Q^2)\; xG_3(x,Q^2) + 2a_e v_e\, \chi_z^2(Q^2)\; xH_3(x,Q^2). \end{aligned}$$

The coefficients $-a_e\chi_z(Q^2)$, $-v_e\chi_z(Q^2)$, $(a_e^2+v_e^2)\chi_z^2(Q^2)$ and $2a_ev_e\chi_z^2(Q^2)$ are shown in Fig. 2.12. Since $-Q_e = 1$ one can see from the size of the factors that for $F_2(x, Q^2)$ the main contribution comes from F_2^{em} followed by G_2 and finally H_2. The contribution to xF_3 of xG_3 and xH_3 is shown in Fig. 2.13. For all Q^2 values the contribution of $xH_3(x, Q^2)$ is negligible, so one can safely make the approximation that $xF_3(x, Q^2) = -a_e\chi_z(Q^2)xG_3(x, Q^2)$. Please note that the relative size of the different coefficients is mainly determined by the coupling constants. The $\chi_z(Q^2)$ factor with values between 0.22 and 1.16 for $Q^2 = 1500$ GeV^2 and $Q^2 = 30000$ GeV^2 respectively is not the reason for neglecting xH_3.

The structure function $xG_3(x, Q^2)$ is shown for different values of Q^2 in Fig. 2.14. One can see that the structure function is almost independent of the Q^2 value.

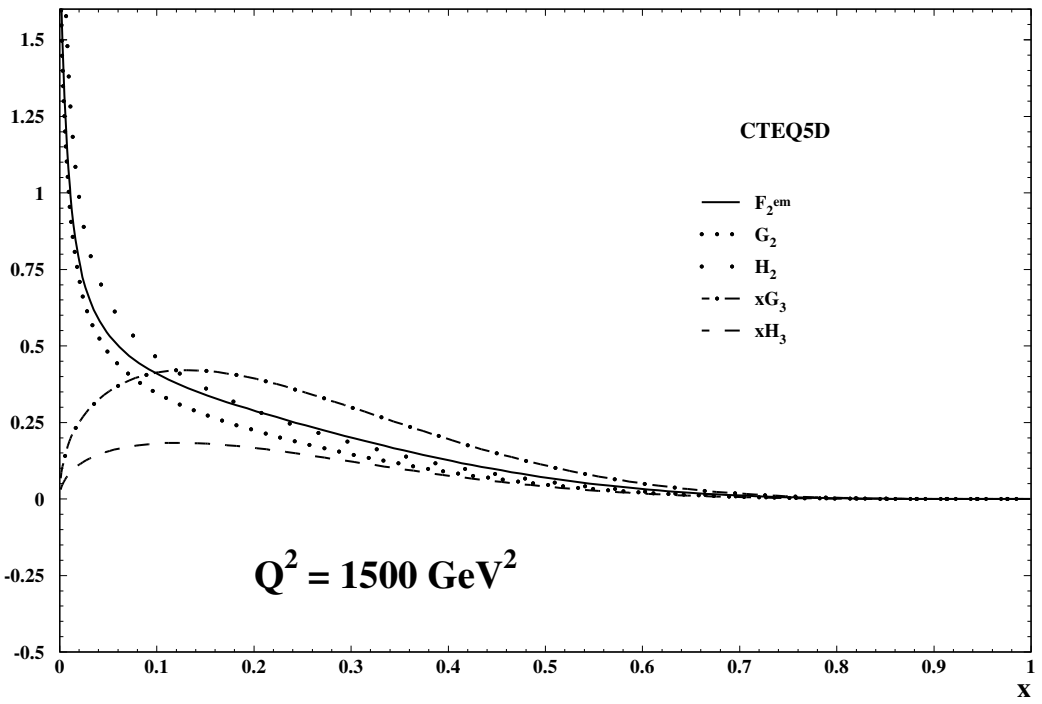

Figure 2.10: Structure functions of the proton F_2^{em}, H_2, G_2, G_3 and H_3 for $Q^2 = 1500$ GeV^2 .

2.7 Structure Functions of the Proton in the Standard Model

The cross section for the $ep \to e'X$ process has been calculated in terms of the structure functions $F_2(x,Q^2)$, $F_L(x,Q^2)$ and $xF_3(x,Q^2)$ (Eq. (2.11)). In the DIS scheme, described above, the structure functions in NLO can be written in terms of the parton densities as follows:

$$\begin{aligned}
F_2(x,Q^2) &= \sum_f A_f(Q^2)\left[xq_f(x,Q^2) + x\bar{q}_f(x,Q^2)\right], \\
xF_3(x,Q^2) &= \sum_f B_f(Q^2)\left[xq_f(x,Q^2) - x\bar{q}_f(x,Q^2)\right. \\
&- \left. 2\frac{2\alpha_s(Q^2)}{3\pi}x\int_x^1 \frac{dz}{z}\left(1+\frac{x}{z}\right)\left(q_f(z,Q^2) - \bar{q}_f(z,Q^2)\right)\right], , \\
F_L(x,Q^2) &= \sum_f A_f(Q^2)\frac{2\alpha_s(Q^2)}{\pi}x\int_x^1 \frac{dz}{z}\left[\frac{2}{3}\frac{x}{z}(q_f(z,Q^2) + \bar{q}_f(z,Q^2)\right), \\
&+ \left.\frac{x}{z}\left(1-\frac{x}{z}\right)g(z,Q^2)\right], \qquad (2.14)
\end{aligned}$$

where $\alpha_s(Q^2)$ is the QCD coupling constant and the coefficients $A_f(Q^2)$ and $B_f(Q^2)$ are defined as:

$$\begin{aligned}
A_f(Q^2) &= \frac{1}{2}\left[(V_f^L(Q^2))^2 + (V_f^R(Q^2))^2 + (A_f^L(Q^2))^2 + (A_f^R(Q^2))^2\right], \\
B_f(Q^2) &= V_f^L(Q^2)A_f^L(Q^2) - V_f^R(Q^2)A_f^R(Q^2),
\end{aligned}$$

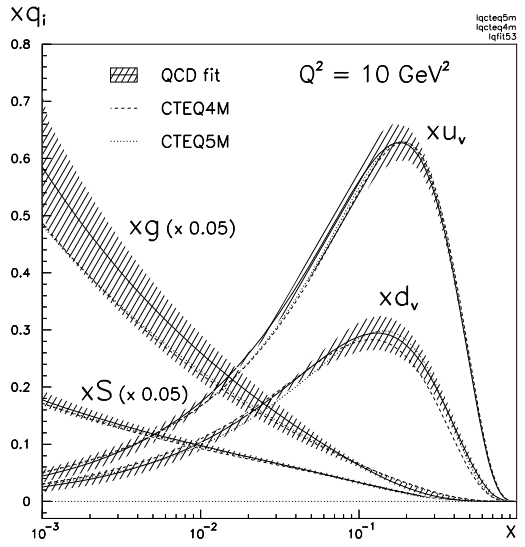

Figure 2.11: Partons distribution inside the proton for $Q^2 = 10$ GeV^2. Plot taken from [Bot00].

and the couplings are defined as:

$$\begin{aligned} V^{L,R}(Q^2) = &\quad Q_f &- (v_e \pm a_e) v_f \chi_z(Q^2), \\ A^{L,R}(Q^2) = &\qquad\quad &- (v_e \pm a_e) a_f \chi_z(Q^2), \end{aligned}$$

Q_i, a_i and v_i are already defined in the previous sections.

As can be seen in Eq. (2.14) the structure function $F_2(x, Q^2)$ depends on the parton densities of the sea and valence quarks. The structure function $F_L(x, Q^2)$, which is zero at LO, depends on the parton densities of the sea and valence quarks, as well as on the gluon density inside the proton. The parity violating structure function $xF_3(x, Q^2)$ is a function only of the difference of the quark and antiquark density and thus a function of the parton densities of the valence quarks. $xF_3(x, Q^2)$ gives a direct handle on these distributions which is impossible in *ep* scattering with the measurement of the functions $F_2(x, Q^2)$ and $F_L(x, Q^2)$ alone.

2.8 Sum Rule for $\mathbf{xF_3(x, Q^2)}$

In order to extract some physical implications from $xF_3(x, Q^2)$ it is useful to integrate this function over x.

$$\begin{aligned} I(Q^2) &= \int_0^1 \frac{dx}{x} xF_3(x, Q^2) \\ &= -a_e \chi_z(Q^2) \int_0^1 \frac{dx}{x} xG_3(x, Q^2) + 2a_e v_e \chi_z^2(Q^2) \int_0^1 \frac{dx}{x} xH_3(x, Q^2) \\ &= -a_e \chi_z(Q^2) J_0 + 2a_e v_e \chi_z^2(Q^2) K_0. \end{aligned} \tag{2.15}$$

The integrals J_0 and K_0 are independent of Q^2 since the number of valence quarks integrated over x inside the proton does no depend on Q^2.

The expressions for the integrals over the two components of $xF_3(x, Q^2)$ are:

$$J_0 = \int_0^1 \sum_f 2a_f Q_f \left[q_f(x, Q^2) - \bar{q}_f(x, Q^2) \right] = \sum_f 2a_f Q_f N_f^{valence},$$

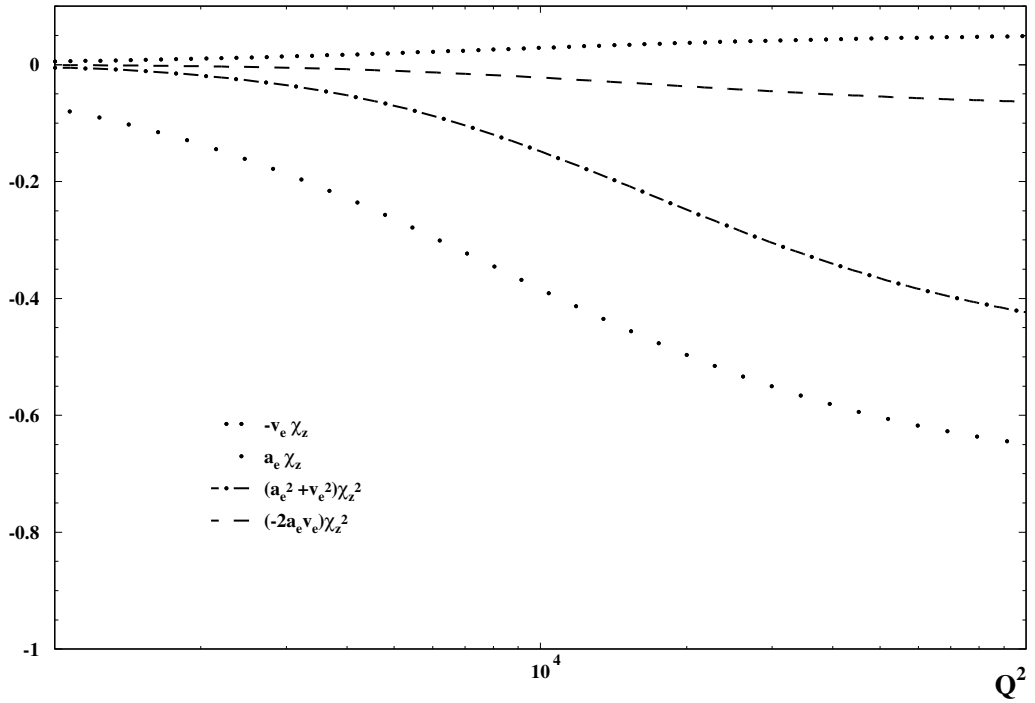

Figure 2.12: Electroweak couplings multiplied by the Z propagator $\chi_z(Q^2)$ ($-a_e\chi_z(Q^2)$, $-v_e\chi_z(Q^2)$, $(a_e^2+v_e^2)\chi_z^2(Q^2)$ and $2a_ev_e\chi_z^2(Q^2)$) for e^+p data as a function of Q^2.

$$K_0 \;=\; \int_0^1 \sum_f 2a_f v_f \left[q_f(x,Q^2) - \bar{q}_f(x,Q^2)\right] = \sum_f 2a_f v_f N_f^{valence},$$

where $N_f^{valence}$ is the number of valence quarks inside the proton. Using the fact that all valence quarks inside the proton are either u or d quarks the integrals can be written as:

$$\begin{aligned} J_0 &= \frac{2}{3}N_u + \frac{1}{3}N_d, \\ K_0 &= \left(\frac{1}{2} - \frac{4}{3}s_W^2\right)N_u + \left(\frac{1}{2} - \frac{2}{3}s_W^2\right)N_d, \end{aligned} \tag{2.16}$$

where the abbreviation $s_W = \sin\Theta_W$ has been used and the superscript *valence* has been droped.

Substituting Eq. (2.16) into Eq. (2.15) one obtains the expression the integral $I(Q^2)$ as a function of the number of valence quarks inside the proton:

$$\begin{aligned} I(Q^2) \;=\; -a_e\chi_z(Q^2) \;\Bigg\{ & \left[\frac{2}{3} + \frac{(1-4s_W^2)(3-8s_W^2)}{6}\chi_z(Q^2)\right] N_u^{valence} \\ + & \left[\frac{1}{3} + \frac{(1-4s_W^2)(3-4s_W^2)}{6}\chi_z(Q^2)\right] N_d^{valence} \Bigg\}, \end{aligned}$$

where again the abbreviations $s_W = \sin\Theta_W$ and $c_W = \cos\Theta_W$ have been used.

As seen in Fig. 2.13 the contribution of $xH_3(x,Q^2)$ to $xF_3(x,Q^2)$ can be safely neglected due to the small prefactor of $\chi_z(Q^2)$:

$$I(Q^2) \approx -a_e\chi_z(Q^2)J_0. \tag{2.17}$$

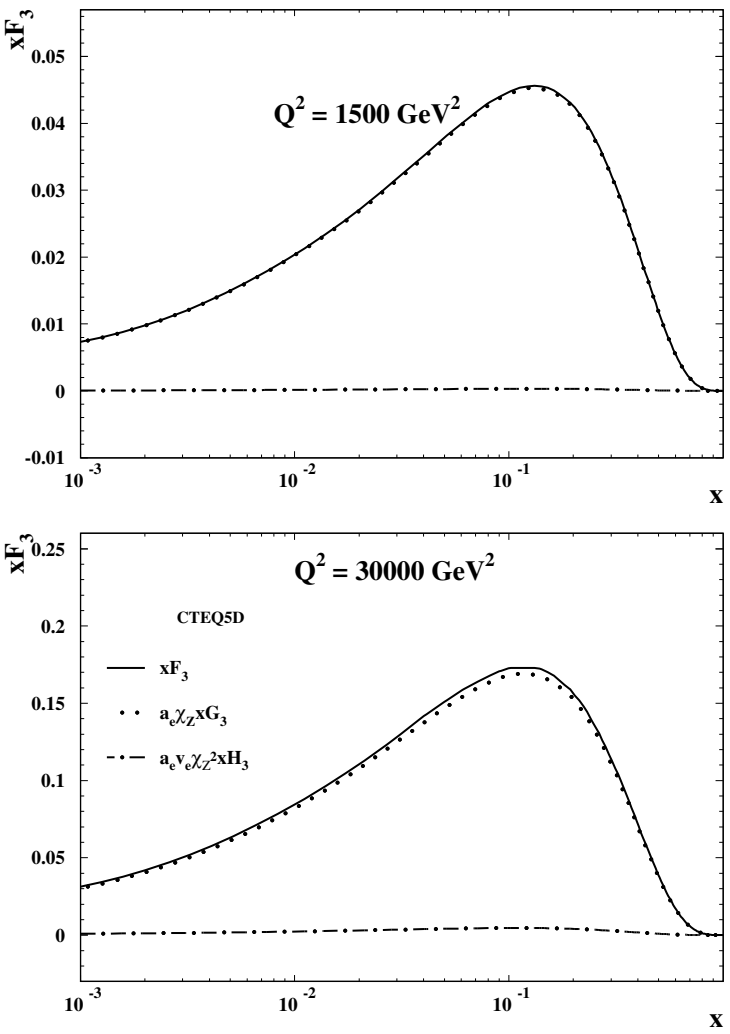

Figure 2.13: Contribution of $xG_3(x, Q^2)$ and $xH_3(x, Q^2)$ to the structure function of the proton $xF_3(x, Q^2)$ for $Q^2 = 1500$ GeV^2 (top) and $Q^2 = 30000$ GeV^2 (bottom). The contribution from $xH_3(x, Q^2)$ is negligible for all Q^2 values.

All the Q^2 dependence of the integral is contained in the χ_z term. Considering only the integral J_0 one can write its expression as a function of the number of valence quarks:

$$J_0 = \int_0^1 \frac{dx}{x}\, xG_3 = \frac{2}{3}\, N_u + \frac{1}{3}\, N_d = \frac{5}{3}. \tag{2.18}$$

Finally, combining Eq. (2.18) and Eq. (2.17) one obtains:

$$\int_0^1 \frac{dx}{x}\, xF_3(x, Q^2) \approx -a_e \chi_z(Q^2) \frac{5}{3}.$$

Through this approximate sum rule $xF_3(x, Q^2)$ is connected to the number of valence quarks in the proton. Due to the different prefactors of $\chi_z(Q^2)$ in the two terms coming from the u- and the d-quark, one can in principle use the measured values of $I(Q^2)$ for different values of Q^2 to extract N_u and N_d separately. Because of the rather small Q^2 dependence of the terms inside the square brackets, this requires a very precise determination of $xF_3(x, Q^2)$.

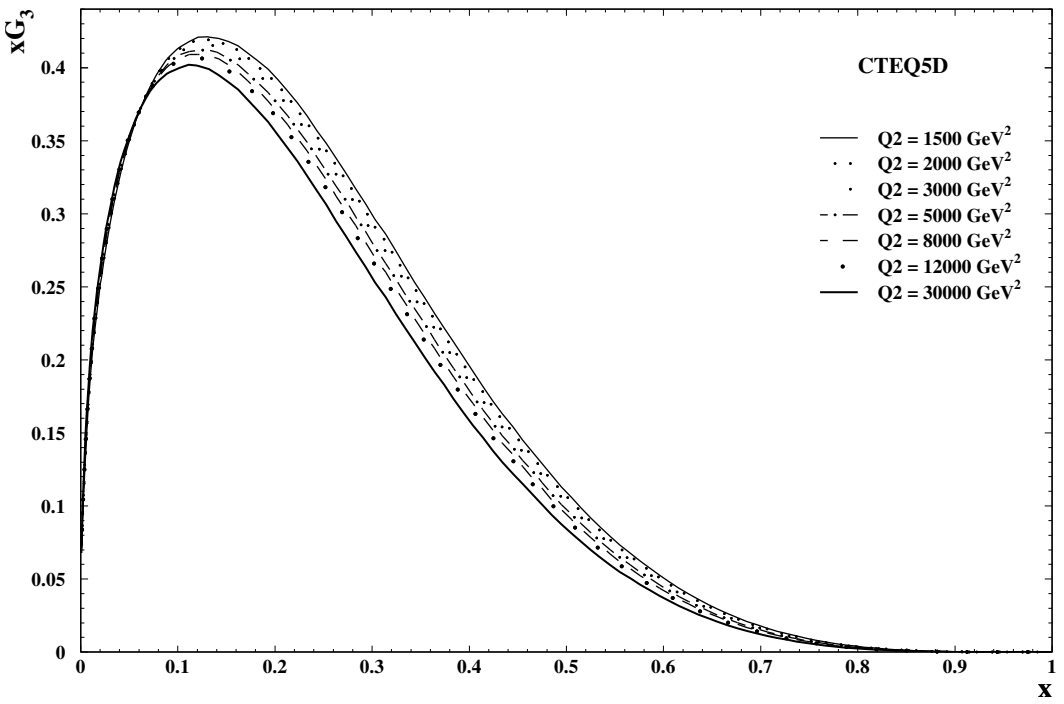

Figure 2.14: Structure function of the proton $xG_3(x, Q^2)$ for different Q^2 values. The function is almost independent of Q^2.

The problem with this method is that the integration cannot be extended experimentally over the whole x range ($0 \leq x \leq 1$) due to the constraint $Q^2 = s \cdot x \cdot y$. The minimum x value (obtained from the condition $y = 1$) depends on Q^2 in the form $x_{min} = Q^2/s$. This introduces an implicit Q^2 dependence in the integral. The result of the integral is in this case:

$$\begin{aligned} J(Q^2) &= \int_{x_{min}(Q^2)}^{1} \frac{dx}{x}\, xG_3 \\ &= \int_{x_{min}(Q^2)}^{1} dx \left\{ \frac{2}{3}\left[q_u(x,Q^2) - \bar{q}_u(x,Q^2)\right] + \frac{1}{3}\left[q_d(x,Q^2) - \bar{q}_d(x,Q^2)\right] \right\}. \end{aligned}$$

Since the integrand (s. Fig. 2.14) is almost independent of Q^2, one can use any available Q^2 bin to perform the integral. Because the lowest Q^2 bin gives the biggest x range this bin is a good choice. From Fig. 2.14 one sees that the contribution of xG_3 to the integral for $x > 0.65$ is negligible, so the integral can be cut off at this value without having a big effect The truncated integral calculated with the CTEQ5D parameterization for $Q^2 = 1500$ GeV^2 and therefore $x_{min} = 0.017$ gives the value:

$$J(Q^2) = \int_{0.017}^{0.65} \frac{dx}{x}\, xG_3 = 1.16, \tag{2.19}$$

where the parton density functions and $xG_3(x, Q^2)$ have been evaluated at NLO. The integral performed for the same x range $[0.017, 0.65]$ but for $Q^2 = 60$ GeV^2 has the value $J(Q^2) = 1.18$, which is a clear identification that the integral is almost independent of Q^2. The value of the integral obtained using the MRST parameterization [M$^+$98] at $Q^2 = 1500$ GeV^2 for $x \in [0.017, 0.65]$ is $J(Q^2) = 1.19$, and $J(Q^2) = 1.18$ for the GRV parameterization [GRV95].

2.9 $\mathbf{xF_3(x, Q^2)}$ in Neutrino Experiments

In neutrino nucleon scattering experiments νN the exchange bosons between the neutrino and the nucleon N are the weak bosons $W\pm$. In this case the structure function xF_3^{CC} can be written as a combination of the parton densities [Sel97]:

$$\begin{aligned} xF_3^{\nu N} &= xu_V + xd_V + 2xq_s - 2xq_c, \\ xF_3^{\bar{\nu} N} &= xu_V + xd_V - 2xq_s + 2xq_c, \end{aligned}$$

where $u_V \equiv q_u - \bar{q}_u$ and $d_V \equiv q_d - \bar{q}_d$ are the valence quarks densities. The asymmetry of the s–c doublet results in $xF_3^{\nu N} \neq xF_3^{\bar{\nu} N}$. The structure function measured by the CCFR experiment is the average of the neutrino and the anti-neutrino structure function [Sel97]:

$$\begin{aligned} xF_3^{CC} &= \frac{xF_3^{\nu N} + xF_3^{\bar{\nu} N}}{2} \\ &= xu_V + xd_V. \end{aligned} \tag{2.20}$$

This function xF_3^{CC} depends very weakly on Q^2. Because xG_3^{NC} has the same property one can compare the results of NC and CC experiments covering different regions in Q^2. From Eq. (2.13) and Eq. (2.20) one can obtain:

$$\frac{xG_3}{xF_3^{CC}} = \frac{2}{3}\left(\frac{1 + \frac{1}{2}\frac{d_V}{u_V}}{1 + \frac{d_V}{u_V}}\right). \tag{2.21}$$

The value of this fraction can be calculated knowing the densities of the valence quarks. Supposing that $d_V/u_V = 1/2$, one obtains a value of 0.55 for Eq. (2.21). If one uses the CTEQ5D parameterization to calculate the parton densities the obtained values are 0.54 at $x = 0.017$ and 0.61 at $x = 0.65$. The value 0.55 used to correct the neutrino data is the one taken at $x = 0.1$ where the valence quarks' distributions peak.

2.10 QED NLO Corrections

Until now only the QCD NLO corrections to the hadronic vertex have been taken into account. The next step is the consideration of the QED NLO corrections which are of special importance for the leptonic vertex [BS87].

The corrections to the vertex are shown in Fig. 2.15. The most relevant contribution come from the emission of a photon from the incoming our outgoing lepton. Considering only this type of emission the net effect can be written as:

$$\frac{d^2\sigma}{dx_{app}\, dQ^2_{app}} = \frac{d^2\sigma^{Born}}{dx\, dQ^2}(1 + \delta_r), \tag{2.22}$$

where δ_r indicates the radiative correction. x_{app} and Q^2_{app} are the so-called "apparent kinematic variables" as obtained when ignoring photon emission. The major correction to the Born cross section are due to Initial State Radiation (ISR), Final State Radiation (FSR), and QED Compton events. The latest can occur either through ISR or FSR diagrams.

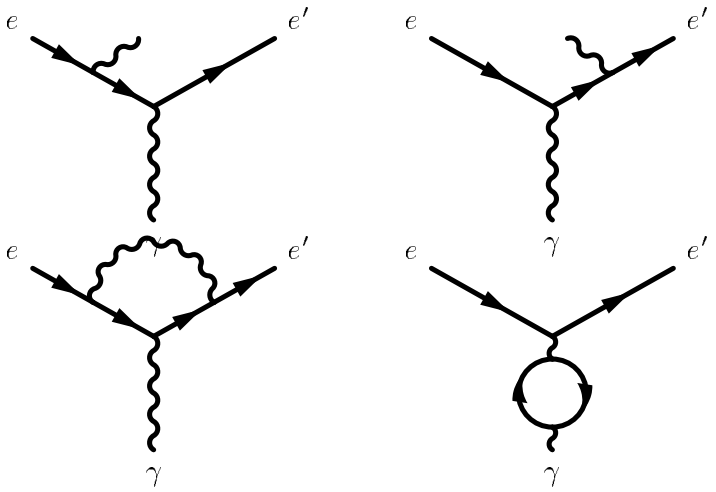

Figure 2.15: Lowest order of QED corrections to the Born level cross section. Photon emission (top) and virtual photon and fermion loop (bottom) corrections.

Neither in theory, nor in experiment is a clear way to distinguish between ISR, FSR and Compton events. The classification is then done according to peaks in probability for the lepton to emit a photon. In the ISR case the probability is higher for photons being emitted collinear to the incoming lepton. In the FSR case, the probability is higher for the photon emitted collinear to the scattered lepton. Compton events are quasi-elastic events in which the lepton gains a large invariant mass and emits a photon which balances its transverse energy.

The inclusion of NLO QED corrections changes the value of α by 10%. This change is due to vacuum polarization.

Chapter 3

HERA

The "Hadron-Elektron-Ring-Anlage" (HERA), the only lepton-proton collider in the world, is located at the DESY laboratory in Hamburg, Germany.

The proposal for the first *ep*-facility in Europe was approved in April 1984. The first *ep* collisions were obtained in October 1991, and the ZEUS experiment took first physics data in spring 1992. Since then the integrated luminosity of HERA has continuously increased. In the year 2000, an upgrade to increase the luminosity has been done. The running will continue, at least, until 2005.

The center of mass energy of the HERA collider is, compared with fixed target experiments, one order of magnitude higher. This opens a new kinematic region for measurements. In the overlapping region comparisons between HERA and fixed target experiments can be done.

The HERA collider consists of two storage rings, one for the leptons, one for the hadrons. The HERA tunnel, located 15-20 m under ground, is made out of four 90 arcs and 360 m long straight sections in between. The total length of the tunnel is 6.5 Km.

The injection of the protons in the ring starts with the acceleration of H^- in the 50 MeV linear accelerator (LINAC). Before injection into the DESY III storage ring, the electrons are stripped off the H^- ions, obtaining protons. These are filled into DESY III in 11 bunches with a bunch spacing identical to HERA, 96 ns, and accelerated to 7.5 GeV. The bunches are then transfered to the PETRA storage ring until 70 bunches are accumulated. In PETRA the bunches are accelerated up to an energy of 40 GeV. The procedure is repeated until HERA is filled with 210 proton bunches. Once in the HERA ring, the protons are accelerated to their final energy 920 GeV (820 GeV until the end of 1997). The proton life time is of order of several days.

The lepton acceleration follows the same procedure as the protons. It starts with two LINACs that accelerate the leptons to a final energy of 450 MeV. The lepton intensity accumulator is then filled with a single bunch of electrons of about 60 mA. This bunch is then transfered to DESY II where it is accelerated to 7 GeV. Afterwards it is injected into PETRA II storage ring until 70 bunches are accumulated. The injection is such that the bunch spacing is, like in HERA, 96 ns. After accelerating the electrons to 14 GeV, they are finally injected into HERA until 210 bunches are filled. The positron life time after acquiring their final energy, 27.5 GeV, is about 8 hours. In the case of having electrons, the life time is considerably reduced to a couple of hours.

Not all the bunches are filled into the HERA ring. That allows the study of beam related backgrounds and cosmic muon background. The first can be done with unpaired bunches,

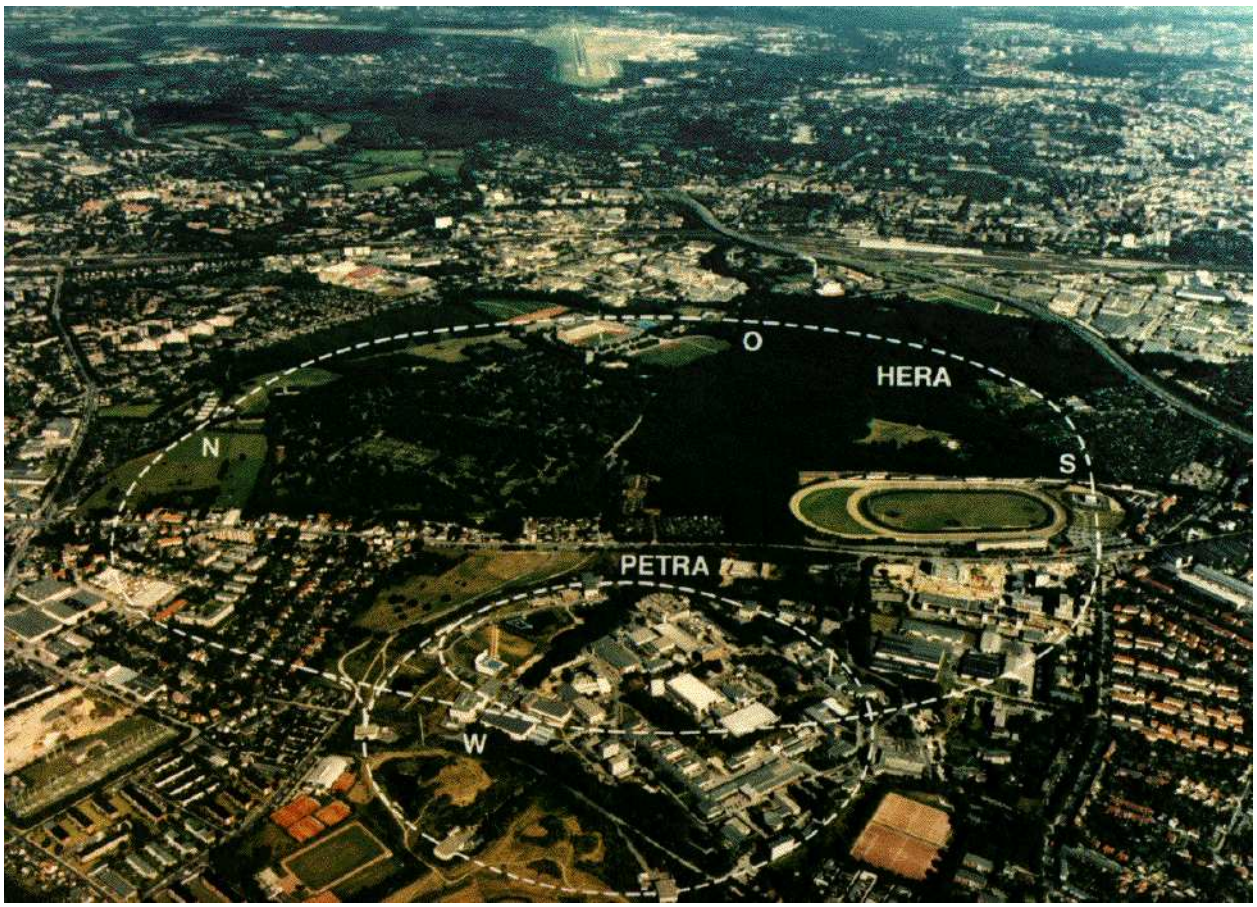

Figure 3.1: Top view of the HERA ring that surrounds the "Volkspark". On the foreground the pre-accelerator PETRA surrounding the DESY site.

pilot-bunches, while the second can be done with empty bunches.

Along the HERA ring four experiments are placed. The collider experiments H1 and ZEUS, in the north and south experimental halls respectively, and the fixed target experiments, HERMES in the east experimental hall, and HERA B in the west experimental hall.

H1 and ZEUS are mainly devoted to the measurement of the structure functions of the proton in DIS events. In both experiments the beams are brought to collision head-on.

The HERMES experiment is designed to study the spin function of the nucleon. The study is done on longitudinal polarized electrons inelastically scattered by a polarized gas jet target such as hydrogen, deuterium or ^{3}He. The polarization of the positron beam is made via spin flip of transversed and longitudinal polarized positrons caused by spin rotators located before and after the east experimental zone.

The HERA B experiment studies CP-violation in the b-$\bar{b}$ system. For this purpose it uses a wire target in the halo of the proton beam for the production of B-mesons.

Between the years 1992 and 2000 several changes to the beams have been performed. These changes can be group in two kinds, (a) increase of the beam energy, and (b) particle exchange in the lepton beam. In the first case the center of mass energy has been raised yielding an increase of the kinematic region. In the second case one can profit from the different physics results only present in $e^- p$ or $e^+ p$ collisions, or the comparison between the two data sets.

In the year 1993 the electron energy was increased from 26.7 GeV to 27.5 GeV, the center of

Figure 3.2: The HERA accelerator complex. On the left the main ring where the ZEUS hall is shown. On the right site the PETRA ring.

mass energy changed from $\sqrt{s} = 296$ GeV to $\sqrt{s} = 300$ GeV. In the year 1994, due to the short lifetime of the electron beam, they were substituted by positrons. The reason for such smaller lifetimes for electron beams, typically of two hours, instead of 8 hours, is probably caused by the capturing of the electron beam by charged dust which originates from ion getter pumps of the HERA electron vacuum system.

In the 1997/1998 winter shutdown the proton energy was raised from 820 GeV to 920 GeV with the consequent change of the center of mass energy to $\sqrt{s} = 310$ GeV. In the same period new ion getter pumps were installed. This solved the electron lifetime problem and HERA agreed to run with electrons again.

Chapter 4

ZEUS

The ZEUS collaboration is formed by 492 physicists[1], and approximate the same number of technicians, coming from 51 institutes from 12 different countries.

The ZEUS detector Fig. 4.1 is a multipurpose detector built for high Q^2 interactions to study the different processes that occur in the lepton proton scattering. The lepton and the proton in the initial state have different energies. This difference results in a boost, in the proton direction, of the center of mass energy. The ZEUS detector is asymmetric to be able to accommodate this special kinematic situation.

Since its complete installation in the south hall of HERA in autumn 1991 the detector has profited of different upgrades. These upgrades are the result of the experience gained by physicist and technicians over the years.

A short overview of the major components of the detector is given below. The essential parts involved in the analysis are described with more detail in the following sections. A complete description of all the components can be found in [Col93]

The ZEUS detector has an onion structure, Fig. 4.2. Starting from the inner part, surrounding the beam pipe, the Central Track Detector (CTD) is a cylindrical drift chamber that measures the momentum and the direction of charged particles as well as their energy losses. In the forward direction, the Forward Tracking Detector (FTD) that consists out of three planar drift chambers FTD1, FTD2 and FTD3 that are intended to improve the track reconstruction at small angles in the forward direction. Filling the gaps between FTD1/FTD2 and FTD2/FTD3, Transition Radiation Detectors (TRD) are located. The FTD and TRD together are referred to as the Forward DETector (FDET). Also belonging to the track system, in the backward direction, the Rear Tracking Detector (RTD) consisting of one planar drift chamber and the Small Angle Rear Tracking Detector (SRTD), a scintillator hodoscope. They improve the track reconstruction for big angles on the backward direction. The tracking detectors measure the momentum of a particle from the curvature of the track. In order to do so the tracking system is located in the field of a super-conducting solenoid magnet, which provides a magnetic field of 1.43 T. This part of ZEUS is called the inner detector.

The inner detector is surrounded by the Uranium-scintillator CALorimeter (UCAL). It measures the energy of both charged and neutral particles[2] and it consists of three parts, the Forward, Barrel and Rear CALorimeters (F/B/RCAL). The PRESampler detector is located in front

[1] state 21.March.01

[2] Except neutrinos.

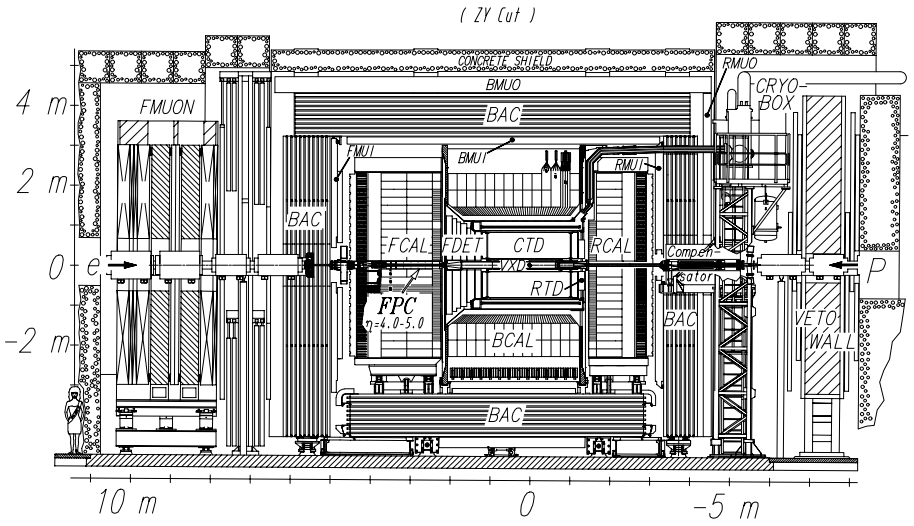

Figure 4.1: Side view of the ZEUS detector along the beam axis

of all calorimeters (F/B/RPRES), it consists of one layer of scintillator tiles. It improves the energy resolution correcting for energy losses caused by showering due to dead material in front of the calorimeter. Inside the calorimeters, 2 cm away from the surface, in the RCAL and the FCAL and consisting of arrays of scintillator pads is the Hadron Electron Separator (R/FHES). It is able to distinguish between electromagnetic and hadronic showers originating from low energy particles (< 5 GeV). The Forward Plug Calorimeter (FPC), has been installed as a continuation of the FCAL towards the beam pipe. It narrows the hole of the beam pipe from 20 x 20 cm to a radius of approximately 2.5 cm. This extends the acceptance of the calorimeter by one unit of pseudo-rapidity (pseudo-rapidity $\eta = -ln(tan(\Theta/2))$). The UCAL is enclosed by the Inner MUon identification chambers (F/B/RMUI) on the inner side of the iron yoke. Surrounding them, the BACking calorimeter (BAC) that also provides the return path for the magnetic filed flux. On the outer side of the yoke, the Outer MUon identification chambers (F/B/RMUO). Both muon chambers, inner and outer, provide a system for identifying muons. On the backward direction, behind the RMUO, a veto wall detector is used to reject beam related background. This set of components, together with the inner detector, is known as the central detector.

Further detectors can be found close to the beam line in both upward and downward (proton) direction. The detectors positioned in the forward direction are useful for detecting the remnant of the dissociated proton, or nucleons scattered at very low angles. Of the first kind is the Proton Remnant Tagger (PRT) that is made of scintillator strip detectors. The Leading Proton Spectrometer (LPS), situated between gaps in HERA beam magnets, measures the longitudinal

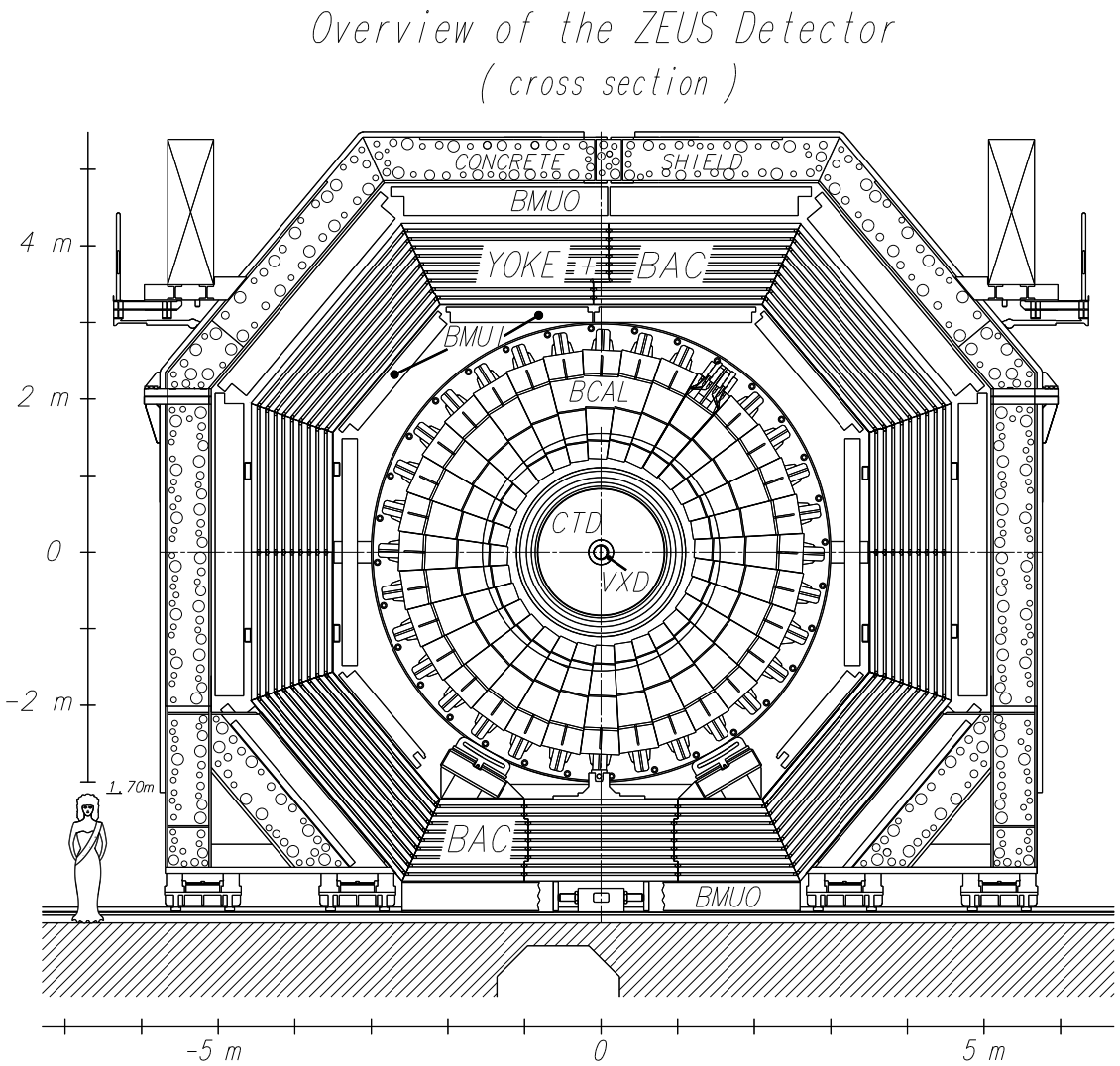

Figure 4.2: Front view of the ZEUS detector perpendicular to the beam axis

and transverse momentum of quasi-elastically scattered protons. Further down the beam the Forward Neutron Calorimeter (FNC) carries out the same job for the neutron than the LPS for the positrons. On the other direction, detectors positioned on the rear direction detect electrons and photons that leave the calorimeter very close to the beam pipe. The Beam Pipe Calorimter (BPC) and the Beam Pipe Tracker (BPT) measure the energy and the position of electrons in the angular region $3.10 < \Theta < 3.12$. Down the beam at 8 m, 35 m and 44 m small taggers (electromagnetic calorimeters) are positioned to measure electrons that emerge even closer to the beam pipe. At 107 m away from the interaction point the LUMI detector measures the luminosity by means of the photons produced in Bethe-Heitler bremsstrahlung processes.

4.1 The Central Tracking Detector

The CTD, Fig. 4.3, is used in the analysis for reconstructing the event vertex and the measurement of the track associated to the scattered lepton, i.e its position reconstructed with the polar coordinates determined by the track. It can also measure the momentum of the particle associated with the track, as well as the energy loss dE/dx used for particle identification.

The CTD has an inner radius of 18.2 cm, an outer radius of 79.4 cm, a length of 205 cm, and it is asymmetrically positioned inside the detector, the z coverage is $-100\text{cm} < z < 105$ cm. It is filled with a gas mixture of argon, CO_2 and ethane. It covers a radial angle of $0.26 < \Theta < 2.86$ and consists of signal and potential wires. This layers are organized in 9 groups, super-layers, of 8 layers each, in between the signal wires, the potential ones.

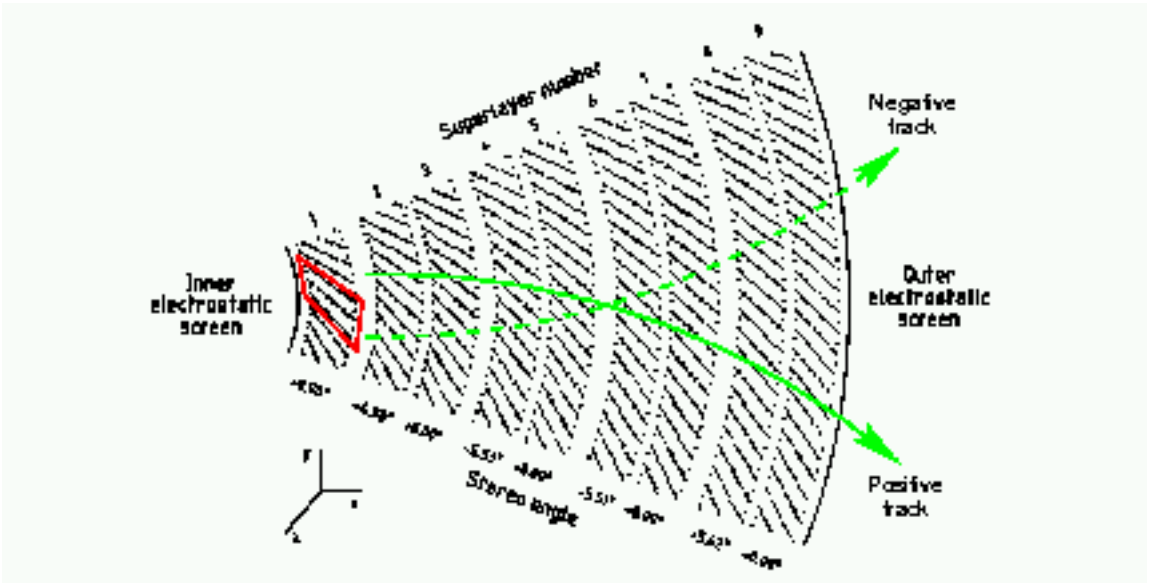

Figure 4.3: Layout of a CTD octant. Two tracks illustrate the path of positive and negative charged particles across the CTD.

The special setup of the wires allows very precise measurements of the x and y coordinates. To measure the z coordinate the odd super-layers, which are axial layers, have the wires parallel to the beam axis; while the even layers, which are stereo layers, are inclined ca. $\pm 5^o$ with respect to the beam axis.

The three inner axial layers incorporate a z-by-timing system. This system allows the reconstruction of the z position by means of the time difference measured on both sides of the wire. Due to the poor resolution of the method of ca. 4 cm, it is only used for trigger purposes.

The transverse momentum of the track is measured using its curvature:

$$p_T[GeV] = 0.2998[GeV] \cdot B[T] \cdot r[m],$$

together with the z position one can extract the total momentum of the track $p = p_T/sin(\Theta)$. The resolution of the measurement depends on the number and precision of hits, and on the contribution from multiple scattering. For long paths the resolution is:

$$\frac{\Delta p_T}{p_T} = 0.58\% \cdot p_T[GeV] + 0.65\% + 0.14/p_T[GeV].$$

The first term accounts for the position resolution of the hits, the second term for the multiple scattering the particle suffers inside the CTD, and the last for the scattering before the particle enters the CTD.

From the reconstructed tracks, z component of the primary interaction vertex can be derived with a typical resolution of 0.4 (0.1) cm along (transverse) to the beam direction. However, the vertex position in transverse direction is better known from the beam profile, to a resolution of 330 μm in x and 90 μm in y.

4.1.1 CTD acceptance region

Figure 4.4 shows the CTD acceptance region for the scattered lepton. This is determined by a maximum and a minimum angle for which the scattered lepton track can be reconstructed using four super-layers. These angles are measured with respect to the event vertex.

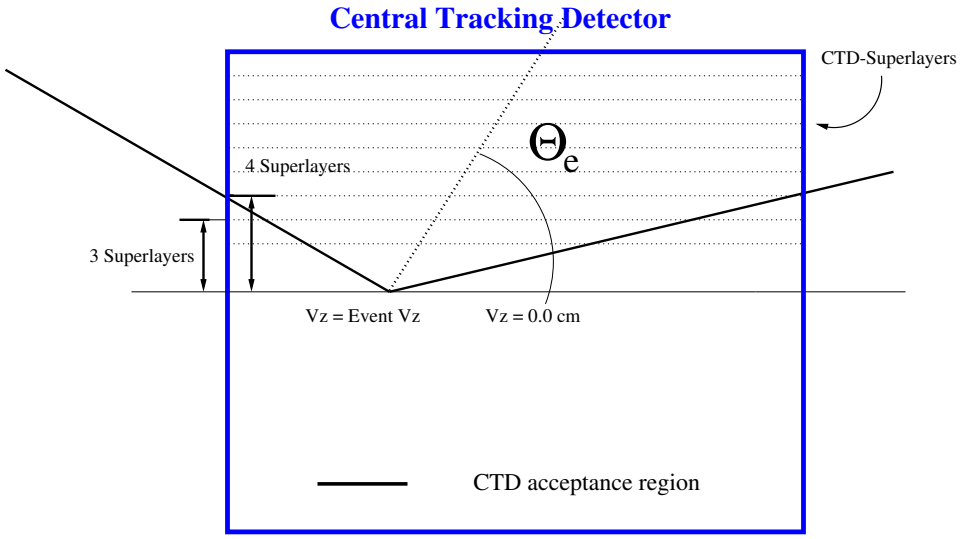

Figure 4.4: CTD Acceptance region.

4.2 The Uranium Calorimeter

The high-resolution uranium calorimeter (UCAL) is the most important component used in the analysis. It is used to identify the scattered electron/positron, to measure its energy and, outside the region in which the CTD can be used, to determine its position. It also plays an important rôle in the reconstruction of the variables from the hadronic final state.

The UCAL is a sampling calorimeter. This means that most of the energy is deposited in a dense absorber and only small samples that reach the active material are used to reconstruct the signal. The ZEUS calorimeter is a sandwich calorimeter. The absorber, depleted uranium and the active material, scintillator, are disposed in alternating layers. The thickness of the layers is chosen so that the response of the calorimeter is the same for electromagnetic and hadronic showers ($e/h = 1$). This optimizes the resolution for hadrons. The relative energy resolution of the calorimeter under test beam conditions is:

$$\frac{\sigma(E)}{E} = \frac{35\%}{\sqrt{E}} \oplus 2\%,$$

for hadrons, and

$$\frac{\sigma(E)}{E} = \frac{18\%}{\sqrt{E}} \oplus 1\%,$$

for electrons with the energy measured in GeV[3].

[3]A detailed study of the energy resolution is shown in Chapter 9

The time resolution of the calorimeter is:

$$\sigma(t) = \frac{1.5}{\sqrt{E}} \oplus 0.5\%,$$

for energy deposits above 3 GeV [Col93]. The timing of the calorimeter can be used to reject beam-related background events.

Mechanically the calorimeter is divided into three main components, FCAL, with an angle coverage of $2.2^0 < \Theta < 39.9^0$, the BCAL covering $36.7^0 < \Theta < 129.2^0$, and finally the RCAL that covers the range $128.1^0 < \Theta < 176.5^0$.

The structure of the three calorimeter components is similar. They are subdivided longitudinally into two parts. The inner part constitutes the ElectroMagnetic Calorimter (EMC) with a depth of about 25 radiation lengths (X_0) or one interaction length (λ) for hadronic interactions. The outer part is called the HAdronic Calorimeter (HAC). It varies in depth from 6 λ in the very forward region to about 3 λ in the rear region. In both FCAL and BCAL the HAC is read out in two sections (HAC1 and HAC2). The planes of division are non-projective for FCAL and RCAL. For FCAL, both EMC and HAC are projective in azimuthal angle (ϕ) but only the EMC is projective in the polar angle Θ. The basic dimension for the cell readout in the transverse direction is 20×20 cm^2 for HAC sections of both FCAL and RCAL. The EMC calorimeter is further segmented into 5×20 cm^2 and 10×20 cm^2 sections for FCAL and RCAL respectively.

The calorimeter is divided into two planar vertical calorimeters, FCAL and RCAL, and a cylindrical barrel calorimeter BCAL. Each of the individual calorimeter is subdivided longitudinally into one EMC and one in the RCAL or two in the B/FCAL hadronic sections. Transversally, the calorimeters are organized in modules consisting of towers which are further subdivided into cells. A schematic representation of an FCAL module can be seen in Fig. 4.5.

In order to avoid neutral particles to escape the BCAL through the module gaps, modules are rotated 2.5^o around the parallel Z-axis.

The information of the calorimeter cells is read out via Photo-Multipliers Tubes (PMTs) on both sides of the cell. The PMTs are coupled to the scintillator via wavelength shifters. The information coming from both PMTs is summed making the energy measurement independent of the impact point.

The uranium natural radioactivity can be used as a powerful tool for calibration, thus it provides a constant perfectly stable reference point [B$^+$90]. Beam test results [A$^+$91] ensure an intercalibration of individual calorimeter sections to about 3% and a stability of calibration to better than 1%.

4.3 The Presampler

The presampler [B$^+$96] is used to correct for energy losses due to dead material in front of the calorimeter. It is situated in front of each calorimeter, but only the Rear PRESampler(RPRES) is used in this analysis. It consists of a 20×20 cm^2 segmented scintillator array read out with wavelength-shifting fibers.

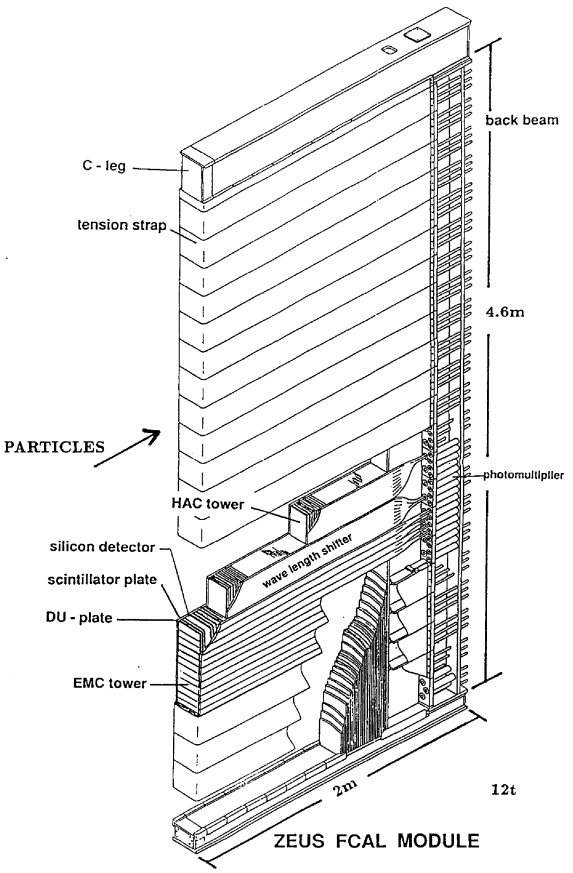

Figure 4.5: ZEUS FCAL module. EMC and HAC sections are shown.

Particles that shower in the material in front of the presampler lead to an increased particle multiplicity which is measured by the presampler. The combined information from the presampler and calorimeter allows an event-by-event measurement of the energy loss in front of the calorimeter.

Beam test studies have proven the feasibility of an electron energy correction accurate to better than 2% in the energy range and for the configuration of inactive material relevant to the ZEUS detector.

4.4 Hadron Electron Separator

The Hadron Electron Separator (HES) [HES] consists of a layer of silicon detectors. The rear HES is located on the RCAL at a depth of 3.3 radiation lengths. Each silicon pad has an area of 28.9×30.5 mm^2, providing a spatial resolution of about 9 mm for a single pad hit. If more than one adjacent pad is hit by a shower, a cluster consisting of at most 3×3 pads around the most energetic pad is considered, which allows reconstruction of the scattered lepton position with the improved resolution of 5 mm.

4.5 The Luminosity Monitor

The measurement of the time-integrated luminosity is essential in any extraction of cross sections. The error of this value is taken into account as an overall normalization error in the measurement.

Knowing the cross section of a process the luminosity can be estimated measuring the rate this process takes place. The process chosen is the Bethe-Heitler process, its cross section is known to 0.5% and it is easy to detect.

The reaction that takes place is $ep \rightarrow ep\gamma$. The LUMInosity monitor (LUMI), Fig. 4.6 constructed to measure this process consists of two detectors. One measures the lepton (LUMI-e) and the other measures the hard bremsstrahlung photons (LUMI-γ). Both detectors consist of a lead-scintillator calorimeter with resolution $\sigma/E = 18.5\%/E(GeV)$ and a position detector. The geometrical acceptance of the LUMI-γ is limited to the detection of electrons with energies $0.2E_{beam} \leq E'_e \leq 0.8E_{beam}$. Only the LUMI-$\gamma$ detector is used in the luminosity calculation [A+92].

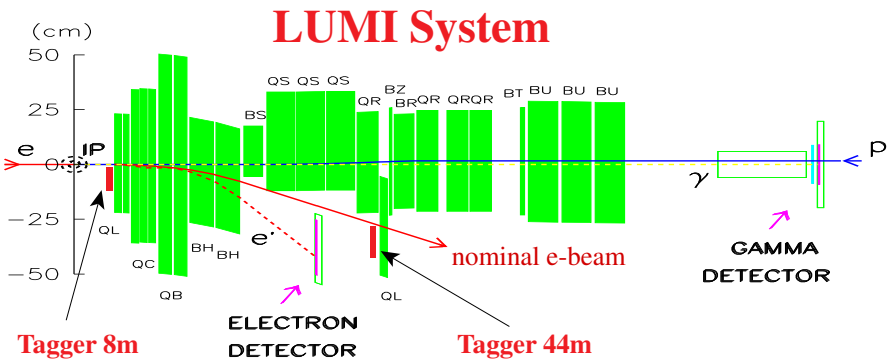

Figure 4.6: Luminosity monitor.

The photons escape the beam pipe through a window at $Z = -92$ m, and are detected at $Z = -107$ m. The electrons, that have lost most of their energy due to bremsstrahlung, are deflected from the nominal beam orbit by the magnetic field from HERA. These electrons abandon the beam pipe earlier than the photons, at $Z = -27$ m, and are detected closer to the interaction point at $Z = -34$ m.

The LUMI-e not only detects the electrons from these processes, but also electrons from photoproduction events. In the later case the electron escapes the detector with a very small angle with respect to the beam pipe. The LUMI-γ can also detect photons from initial state radiation. These photons are radiated by the incoming electrons almost collinear to them.

4.6 The ZEUS Trigger and Data Acquisition System

The HERA bunching spacing time is of 96 ns, equivalent to a rate of ≈ 10 MHz. A great part of the events that take place in the detector are background events with a rate of $\approx 10 - 100$ kHz, while the ep physic events only occur with a rate of a few Hz. The background events are mostly dominated by proton interactions with the residual gas, other minor contributions come from beam halo interactions, electron beam gas and cosmic ray events.

The action of separating the *ep* physic events from the background events is performed by a trigger. The ZEUS trigger [C+96] is a three-level trigger, a schematic diagram of the trigger can be seen in Fig. 4.7. The task of each level is to reduce the input event rate so that it is low enough to be used as input for the next level.

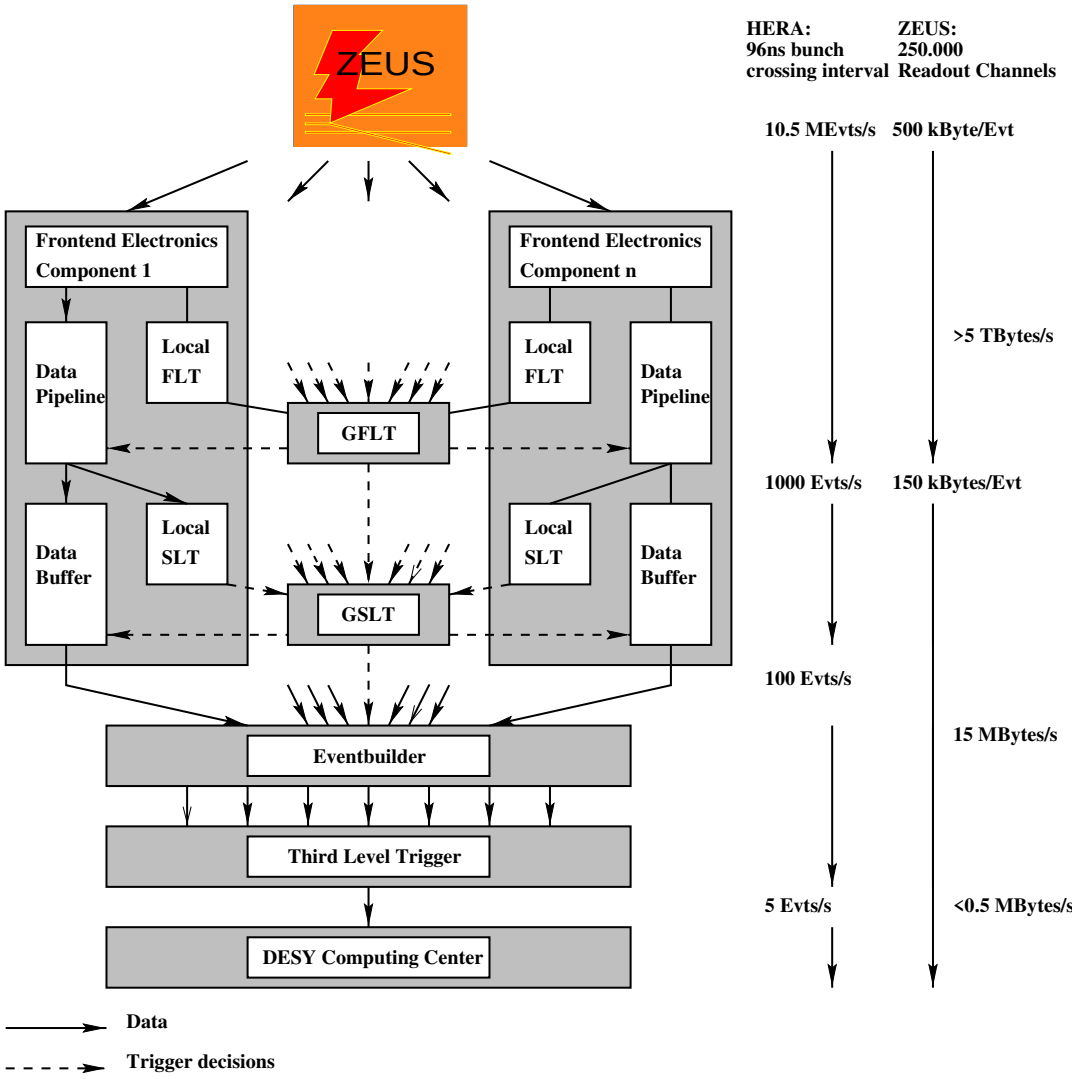

Figure 4.7: Schematic representation of the ZEUS three-level trigger.

The First Level Trigger (FLT) [Smi] is a hardware trigger that reduces the event rate to 1 kHz. It makes its decision predominantly based on CAL energy deposits and CTD hits. Nevertheless each detector has got its own FLT which stores the information in a pipeline and makes the decision within 2 μs. The information coming from each individual FLT is compiled in the Global First Level Trigger (GFLT). In case of a positive decision of the GFLT the pipelines are stopped and the data is read out for further processing in the subsequent levels.

The Second Level Trigger (SLT) [Alp92] is a software trigger. The input rate that arrives from the GFLT is 1 kHz, and the output rate after decision stays below 100 Hz. It is mainly used to reject beam-gas events by means of the energy deposits and timing information from calorimeter that becomes accessible at this stage. As in the FLT case the information coming from the individual SLTs is collected in a Global Second Trigger (GSLT).

The Third Level Trigger (TLT) [B+89] runs on information supplied by the EVent Builder

(EVB). After a positive decision of the GSLT, all components send their information to the EVB which is the first step in the off-line reconstruction of each event. The reconstruction of physics quantities, performed on a Silicon Graphics Farm, such as kinematic variables, global quantities of hadronic final states, electron/positron information, etc, are used to classify the events.

The TLT output rate is of a few Hz. Events selected by the TLT are written to tape, the size of each event is typically $\approx$ 100 KBytes. The information kept for each event is used later for the full off-line reconstruction and data analysis.

Chapter 5

Cross Section Analysis and Extraction of $\mathbf{xF_3(x, Q^2)}$

The main focus of this study is on the extraction of the structure function of the proton $xF_3(x, Q^2)$. As explained in Chapter 2 this structure function arises from the parity violation associated by the Z-boson exchange in the processes $e^- p \to e^- X$ and $e^+ p \to e^+ X$.

The $Z - \gamma$ interference is constructive for $e^- p$ and destructive for $e^+ p$ scattering. This means that $xF_3(x, Q^2)$ contributes positively to the $e^- p$ and negatively to the $e^+ p$ double differential cross sections. Therefore, $xF_3(x, Q^2)$ is extracted by measuring the double differential cross sections for both processes and subtracting them.

In this chapter the extraction of the double differential cross section is explained, as well as the extraction of the structure function of the proton $xF_3(x, Q^2)$.

5.1 Cross Section Extraction

The statistic in an experiment is limited therefore the measurement of the cross section can not be made in a continuous range of x and Q^2 but rather in bins of these variables. The average cross section within a bin can be expressed as:

$$\frac{\Delta^2 \sigma(x, Q^2)}{\Delta x \, \Delta Q^2} = \frac{1}{\Delta x \, \Delta Q^2} \int_{\Delta x} \int_{\Delta Q^2} \frac{d^2 \sigma(x', Q'^2)}{dx' \, dQ'^2} dx' \, dQ'^2.$$

Ideally one would like to make the bins small so that the measurement can be as continuous as possible. The size of the bins is determined by:

- The resolution of the reconstructed variables x and Q^2, as well as systematic migrations in these variables due to particle losses, photon radiation and finite detector resolution and granularity. One requires that the bin widths be of the order of the resolution of the kinematic variables x and Q^2.
- The requirement that the size of the statistical error remain small over the kinematic plane. The cross section drops rapidly, with increasing Q^2, and therefore the size of the bins will increase for higher values of Q^2.

5.2 Unfolding Procedures

Once it is clear that the double differential cross section has to be measured in a bin the cross section is related to the number of events normalized to the total luminosity $\mathcal{L}$:

$$\left.\frac{d^2\sigma}{dx\, dQ^2}\right|_{bin} = \frac{\mathcal{N}|_{bin}}{\mathcal{L}}.$$

The precision and accuracy with which a measurement can be done is always finite due to effects intrinsic to the measurement. The reasons may be (i) detector effects, (ii) physics effects, (iii) event selection efficiency or (iv) background.

(i) Detector effects are the granularity of the calorimeter, loss of efficiency in reconstruction algorithms, energy leakage in cracks, etc.

(ii) The physics effects come usually from radiative events where the photon is not part of the hadronic system, but always considered as if it was. This is the main cause of migrations in the kinematic plane.

(iii) Signal events have to be selected from the whole sample using cuts. Usually one has to find a compromise between rejecting as much background as possible and removing as less signal events as needed. Nevertheless, no selection cut is 100% efficient but there is always an amount of signal lost and a remaining background.

(iv) After applying the analysis cuts there is still some remaining background, that may distort the measurement. And estimation of the background has to be performed in order to obtain a reliable measurement.

Considering the points listed before, it is clear that the number of events counted in a bin is not exactly the number of "true" events that should be measured in this bin in an ideal experiment. The relation between the number of events observed N_{obs}^{Data} in a bin and the true number of events N_{true}^{Data} in this bin is given by:

$$N_{obs}^{Data}(\xi') = \int T^D(\xi', \xi) N_{true}^{Data}(\xi)\, d\xi, \tag{5.1}$$

where ξ are the true variables and ξ' the measured ones. The transition matrix $T^D(\xi', \xi)$ accounts for all effects described above. From Eq. (5.1) the true number of events can be obtained from the measured ones provided one knows the transition matrix. Because of the complexity of the detector and the physic processes involved, the matrix $T^D(\xi', \xi)$ cannot be calculated analytically.

Monte Carlo simulations[1] are able to describe the physic processes and the interaction of the final state particles with the detector, giving a powerful tool to calculate the transition matrix $T^D(\xi', \xi)$.

As for the data, for Monte Carlo events one can write:

$$N_{meas}^{MC}(\xi') = \int T^{MC}(\xi', \xi) N_{gen}^{MC}(\xi) d\xi, \tag{5.2}$$

[1] see next chapter

where N^{MC}_{meas} is the measured number of Monte Carlo events and N^{MC}_{gen} is the generated number of events in a bin. Again $T^{MC}(\xi', \xi)$ is the transition matrix, ξ are the true variables and ξ' the measured ones. In the case of Monte Carlo simulations the transition matrix from Eq. (5.2) can be extracted because both N^{MC}_{obs} and N^{MC}_{gen} are known.

If the Monte Carlo simulation is able to describe the data precisely enough, one can assume:

$$T^{D}(\xi', \xi) = T^{MC}(\xi', \xi).$$

The bins in which the double differential cross section is measured are x and Q^2 bins therefore $\xi \equiv (x, Q^2)$ which leaves an easy to solve discrete problem.

$$N^{MC}_{meas,\,bin\,k} = \sum_{all\ bins\ l} T^{MC}_{k\,l} N^{MC}_{gen,\,bin\,l}, \tag{5.3}$$

$$N^{Data}_{obs,\,bin\,k} = \sum_{all\ bins\ l} T^{Data}_{k\,l} N^{Data}_{true,\,bin\,l}. \tag{5.4}$$

A detailed explanation of the available unfolding procedures can be found in [Qua96]. The one chosen here is the bin-by-bin unfolding because of its simplicity. This method approximates the transfer matrix by a diagonal matrix. This means that it takes into account only the net migrations out of and into a bin, but not the correlations between bins, i.e. the information where migrating events come from and go to. For a diagonal matrix:

$$T_{k\,l} = \delta_{k\,l} T_l,$$

where the elements in the diagonal are given by:

$$T_k = \frac{N^{MC}_{meas}}{N^{MC}_{gen}}.$$

Substituting this expression into Eq. (5.3) and Eq. (5.4) one obtains that the number of true events in data is given by:

$$N^{Data}_{true} = N^{MC}_{gen} \frac{N^{Data}_{obs}}{N^{MC}_{meas}}.$$

The double differential cross section for a given x and Q^2 bin can then be expressed as a function of the number of measured data and Monte Carlo events:

$$\left(\frac{d^2\sigma}{dx\,dQ^2}\right)^{Data}_{true} = \frac{N^{Data}_{obs}}{N^{MC}_{meas}} \left(\frac{d^2\sigma}{dx\,dQ^2}\right)^{MC}_{gen},$$

where $(d^2\sigma/dx\,dQ^2)^{MC}_{gen}$ is the theoretical cross section used for the Monte Carlo generation (see Section 6.2).

5.3 Bin Center Correction

The cross section is usually quoted in a specific point inside the bin so that it can be compared with the theory that, contrary to the measurement, is usually given in a continuous range of x and Q^2.

Nevertheless, it is important to bear in mind that the measurement made is not a genuine measurement of the variable under consideration, in this case the double differential cross section at any particular value of x and Q^2, but the average value of the function over the bin width. According to the mean value theorem:

$$\frac{1}{\Delta\zeta}\int_{\Delta\zeta} f(\zeta)\, d\zeta = f(\xi), \qquad\qquad \xi \in \Delta\zeta,$$

there is a point inside the bin in which the theoretical function is equal to its expectation value inside the bin. The measured value of the double differential cross section should be quoted at these x and Q^2 values. Doing that one obtains a fair comparison between theory and measurement.

5.4 Extraction of $\mathbf{xF_3(x, Q^2)}$

The double differential cross section for NC DIS processes (see Chapter 2) for electron- and positron-proton scattering has the form:

$$\frac{d^2\sigma^{\pm}}{dx\, dQ^2} = \frac{2\pi\alpha^2}{xQ^4}[Y_+F_2(x, Q^2) \mp Y_-xF_3(x, Q^2) - y^2F_L(x, Q^2)].$$

The proton structure function $xF_3(x, Q^2)$ contributes positively to the cross section of e^-p scattering, and negatively to e^+p scattering.

After measuring the double differential cross section for both e^+p and e^-p, $xF_3(x, Q^2)$ can be extracted by subtracting $d^2\sigma^-/dx\, dQ^2$ and $d^2\sigma^+/dx\, dQ^2$, thus eliminating the $F_2(x, Q^2)$ and $F_L(x, Q^2)$ terms that have the same sign in both processes.

The extraction of $xF_3(x, Q^2)$ has become possible with the acquisition of a statistically relevant sample of both e^-p and e^+p data as shown in Table 5.1.

Data Sample	Interaction	Luminosity $\mathcal{L}$	$\mathcal{L}$ Uncertainty	Proton Beam Energy
1996-97	e^+p	29.5 pb$^-$1	1.4%	$E_p = 820$ GeV
1998-99	e^-p	15.8 pb$^-$1	1.9%	$E_p = 920$ GeV
1999-2000	e^+p	56.9 pb$^-$1	2.25%	$E_p = 920$ GeV

Table 5.1: Summary of data samples for the years 1996-200.

In this chapter, only the extraction of $xF_3(x, Q^2)$ from the data samples $(e^+p)^{820}$ and $(e^-p)^{920}$, where 820 and 920 accounts for the proton beam energy, will be discussed. The addition of the $(e^+p)^{920}$ sample is discussed in Appendix A.

After measuring the double differential cross section for both data samples $(e^+p)^{820}$ and $(e^-p)^{920}$ as explained in Section 5.1, $xF_3(x, Q^2)$ can be in principle extracted by subtracting both quantities:

The process in this case requires a more detailed treatment since the data sample for positrons and for electrons have been taken with different proton beam energy: $E_p = 820\, GeV$ for the positrons and $E_p = 920\, GeV$ for the electrons. This means that for the same x and Q^2 value,

the y variable, $y = \frac{Q^2}{x \cdot s}$, gets different values for $\sqrt{s} \approx 300\,GeV$ in the positron case and $\sqrt{s} \approx 320\,GeV$ in the electron case:

$$\begin{aligned}
\frac{d^2\sigma^{-,920}}{dx\,dQ^2} &= \frac{2\pi\alpha^2}{xQ^4}[Y_+^{920}F_2(x,Q^2) + Y_-^{920}xF_3(x,Q^2) - (y^{920})^2F_L(x,Q^2)], \\
- & \\
\frac{d^2\sigma^{+,820}}{dx\,dQ^2} &= \frac{2\pi\alpha^2}{xQ^4}[Y_+^{820}F_2(x,Q^2) - Y_-^{820}xF_3(x,Q^2) - (y^{820})^2F_L(x,Q^2)].
\end{aligned}$$

As a consequence, the $F_L(x,Q^2)$ terms for both double differential cross sections have different factors. When subtracting both cross sections, $F_2(x,Q^2)$ is canceled, but not $F_L(x,Q^2)$. This contribution can be analytically calculated and will be shown in Chapter 10.

The value of $xF_3(x,Q^2)$ obtained from the two different data samples can be written as:

$$xF_3(x,Q^2) = \left(\frac{xQ^4}{2\pi\alpha^2}\right)\left(\frac{Y_-^{920}}{Y_+^{920}} + \frac{Y_-^{820}}{Y_+^{820}}\right)^{-1}\left(\frac{1}{Y_+^{920}}\frac{d^2\sigma^-}{dx\,dQ^2} - \frac{1}{Y_+^{820}}\frac{d^2\sigma^+}{dx\,dQ^2}\right) - \Delta F_L(x,Q^2),$$

where $\Delta F_L(x,Q^2)$ is:

$$\Delta F_L(x,Q^2) = \frac{Y_+^{820}\cdot(y^{920})^2 - Y_+^{920}\cdot(y^{820})^2}{Y_-^{920}\cdot Y_+^{820} + Y_-^{820}\cdot Y_+^{920}} \cdot F_L(x,Q^2).$$

The statistical error on $xF_3(x,Q^2)$ is:

$$\begin{aligned}
\delta^2(xF_3(x,Q^2)) &= \left(\frac{xQ^4}{2\pi\alpha^2}\right)^2\left(\frac{Y_-^{920}}{Y_+^{920}} + \frac{Y_-^{820}}{Y_+^{820}}\right)^{-2} \\
&\quad \left\{\left[\frac{1}{Y_+^{920}}\delta\left(\frac{d^2\sigma^-}{dx\,dQ^2}\right)\right]^2 + \left[\frac{1}{Y_+^{820}}\delta\left(\frac{d^2\sigma^+}{dx\,dQ^2}\right)\right]^2\right\},
\end{aligned}$$

where $\delta\left(\frac{d^2\sigma^\pm}{dx\,dQ^2}\right)$ is the statistical error in the double differential cross section.

Chapter 6

Monte Carlo simulation

6.1 Introduction

For the extraction of physical quantities from the measurements Monte Carlo generators are indispensable prerequisites. The main reasons are, from the experimental point of view, an incomplete coverage of the total solid angle by the detectors, due to the presence of the beam pipe and other non-instrumented gaps and the necessity to apply cuts on the data to filter out events with sensitivity to particular physical processes or quantities. In developing the cuts and determining the necessary acceptance corrections, Monte Carlo generated events, which mimic the data to a high degree, have to be used. The second reason is the presence of strongly interacting particles in the scattering processes. Whereas their interaction can be reliably calculated at small distances in the context of perturbative QCD, the large distance process of hadronization, usually connected to the color confining process, still eludes exact calculations and has to be treated phenomenologically in a Monte Carlo fragmentation procedure.

6.2 Simulation of DIS Events

In the one-boson exchange approximation, the cross section for deep inelastic lepton proton scattering, $ep \to eX$ events where X represents the hadronic final state as depicted in Fig. 6.1,

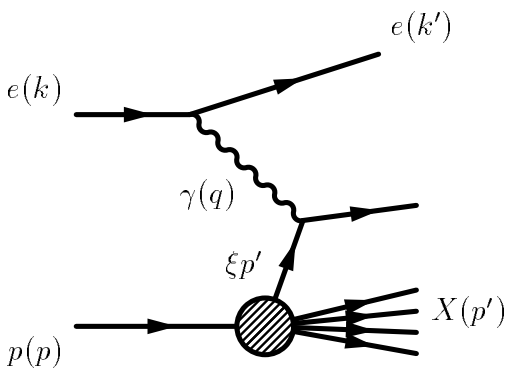

Figure 6.1: Neutral current deep inelastic event.

is described by the three structure functions $F_2(x,Q^2)$, $xF_3(x,Q^2)$ and $F_L(x,Q^2)$ of the proton:

$$\frac{d^2\sigma^{\pm}}{dx\,dQ^2} = \frac{2\pi\alpha^2}{xQ^4}\left[Y_+F_2(x,Q^2) \mp Y_-xF_3(x,Q^2) - y^2F_L(x,Q^2)\right],$$

as explained in Chapter 2.

The simulation should account for the description of the leptonic vertex, the interchange of the gauge boson, γ or Z and the hadronic vertex in LO. Since NLO is required to describe the experimental data QED NLO corrections for the leptonic vertex, as well as QCD NLO corrections for the hadronic vertex should also be implemented.

The simulation is derived from theory expectations and the analytical calculations of the cross sections as done in Chapter 2. Feynman diagrammatic calculations for the lepton vertex are used, as well as the predicted parton densities for the hadronic vertex.

The Monte Carlo event generator used to generate DIS events is DJANGO6 version 2.4 [SS], which is a compilation of different programs. The process $lp \to l'X$ including electroweak corrections of $\mathcal{O}(\alpha)$ is simulated with the help of HERACLES, version 4.5.2 [KSM92]. To simulate QCD effects and allow for generation of events according to QCD cascade models or QCD matrix elements DJANGO6 uses partly modified routines from LEPTO 6.5 [IER97].

6.2.1 Radiative corrections included in the Monte Carlo simulation

The radiative corrections included in the Monte Carlo simulation can be classified in three categories: *i*) pure QCD corrections, *ii*) pure QED and weak corrections and *iii*) combined QCD-QED corrections.

(i) Corrections of $\mathcal{O}(\alpha_s)$. The dominant parts of QCD corrections i.e. the leading logarithms, are absorbed in the parton distribution functions leading to their scale dependence. Non-logarithmic $\mathcal{O}(\alpha_s)$ corrections have to be taken into account explicitly. In the DIS scheme, these corrections show up as non-zero longitudinal structure function $F_L(x,Q^2)$, and a correction to $xF_3(x,Q^2)$. Since the contribution from $xF_3(x,Q^2)$ at HERA energies is less than 5%, it is justified to neglect the $\mathcal{O}(\alpha_s)$ corrections to this function. The longitudinal structure function is taken into account in the calculation of the cross section by HERACLES.

An important consequence of including $\mathcal{O}(\alpha_s)$ corrections is, that they allow more realistic and more detailed description of the hadronic final state: hard gluon emission and boson-gluon fusion give rise to events with two jets in addition to the proton remnant jet.

(ii) Electroweak corrections of $\mathcal{O}(\alpha)$ consist of one-loop virtual corrections and emission of weak photons. In the case of NC scattering, the leptonic radiative cross section can be separated into three parts which are dominated by singularities due to emission of photons collinear with the incoming lepton, emission of photons collinear with the scattered lepton, and emission of hard photons shifting the momentum transfer Q^2 to smaller values; as seen in Chapter 2.

HERACLES includes $\mathcal{O}(\alpha)$ QED corrections due to the photon radiation from both the lepton and the quark as well as a completer one-loop virtual corrections.

(iii) Non-logarithmic corrections of order $\mathcal{O}(\alpha\alpha_s)$ are not included in DJANGO6.

6.2.2 Generation of diffractive events

The program used to simulate this rapidity gap events is RAPGAP version 2.08/00 [Jun95]. The reason for using an independent generator for diffractive events is that it allows to estimate the ratio of non-diffractive to diffractive events performing a fit to the data.

Like in the preceding case the lepton vertex is generated by HERACLES, and ARIADNE and JETSET are used for the hadronization.

The kinematic variables generated for diffractive and non-diffractive events have to be equal. Only then the RAPGAP cross section can be reweighted to the DJANGO6 cross section and subsequently added to the later. The mixture of the two samples is done as following:

$$n(x,Q^2)_{Data} = rg(x,Q^2) \cdot RAPGAP + [1 - rg(x,Q^2)] \cdot DJANGO6,$$

where $rg(x,Q^2)$ is a function of x and Q^2 that parameterizes the fraction of diffractive sample to be added to the non-diffractive sample. This procedure has nothing to do with the study of diffractive events. It is only justified as a method to obtain a good description of the hadronic final states with large rapidity gap and low hadronic mass M_X. It is also needed to obtain the proper acceptance of the hadronic final state.

6.2.3 Estimation of the diffractive sample

Several methods [Wod99] and [Ame99] have been developed to achieve the best description of the diffractive events in data. These methods parameterize the diffractive fraction of Monte Carlo events to be added as a function of x and Q^2. This parameterization is obtained optimizing the description of the η_{max} and M_X distributions in bins of x and Q^2. Unfortunately

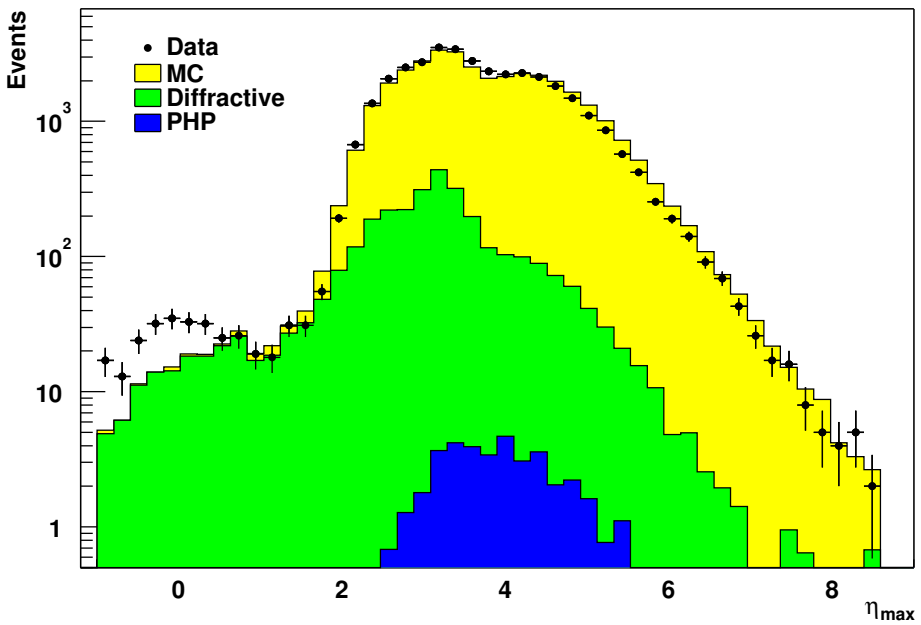

Figure 6.2: η_{max} variable. The diffractive events (middle shaded histogram) are mainly located at the low η_{max} values.

for this analysis the lack of statistics does not allow such a detailed study in bins of x and Q^2.

The diffractive sample is obtained as a constant fraction calculated from the optimization of the η_{max} variable for all x and Q^2 values. The result of the combination of ARIADNE and RAPGAP Monte Carlo events is shown in Fig 6.2.

6.3 Photoproduction Events

The main source for background events are PHotoProduction (PHP) events. By definition PHP events are events in which the scattered electron has a very high angle and cannot be detected in the UCAL. The Q^2 for those events is close to zero, the emitted photon is almost real.

It can happen that one of the particles produced in the final state is misidentified as the scattered lepton. The probability that this happens decreases with increasing Q_f^2, where Q_f^2 is the Q^2 measured with the fake scattered lepton. In the region concerned in our measurement the expected PHP background is negligible [B+99]. The normalization of the PHP background is made with the cross section. The PHP background has been generated using PYTHIA version 5.7 [Sjo94].

6.4 Detector Simulation

To obtain a good simulation detailed information of the detector components has to be supplied. Information such as the geometry of the component as well as its material is used to simulate the interaction of particles with matter, like formation of showers, loss of energy inside the material, etc. The decay of unstable particles is also well simulated in the detector.

Once the physic events are generated, they have to be feeded to the detector simulation. The simulation is performed in three steps carried out by three different programs MOZART [Haa92], ZGANA and ZEPHYR [G+91].

MOZART simulates the interaction of the particles with the detector. It contains extensive information about the materials and geometry of the detector components. It is based on the GEANT [B+] package developed at CERN. The signals left by the particles in the detector components is also simulated using test-beam results from the different components.

The output of MOZART is then given to ZGANA, which simulates the complex three-level trigger used at ZEUS. If the event is accepted by the trigger it is reconstructed by ZEPHYR. From then on data and Monte Carlo events are treated in the same way. After the reconstruction has been done data and Monte Carlo outputs are the same, that simplifies the analysis of the samples.

6.5 Failures of the Simulation

The simulation achieved by the Monte Carlo programs is not perfect. There are several effects that cannot be completely simulated. These can be divided into theoretical and experimental features.

6.5.1 Theoretical Features

As seen in Section 6.2.1 Monte Carlo simulations are not able to account for corrections to all orders. This does not present a problem provided this corrections are small compared to the included LO and NLO order terms.

6.5.2 Experimental Features

The simulation of the detector is known to be incomplete due to lack of information, finite CPU time, or random processes that occur in the real detector and cannot be controlled, some of them are explained below:

- Incomplete calorimeter shower development. In order to reduce CPU time and reproduce the test beam data, two kinds of shower terminators were proposed [Har98]. One of them is an electromagnetic shower terminator, and the other is a neutron shower terminator. These terminators were tuned according to some geometry, changing the geometry would affect the simulation [YS97].

- Sparks and holes. It can happen during data taking that some cells of the UCAL do not supply information. The causes maybe damaged PMT's or electronics. In the BCAL sudden discharges of the static charge between a PMT and its shielding ('sparks') can occur randomly. Neither of these effects are simulated in Monte Carlo programs.

- Dead material, cracks between cells, modules and calorimeters. The information used to simulate dead material maps, cell, module and calorimeter gaps is taken from test beam results. It can happen that the conditions inside the detector are different from beam test condition and therefore the simulation departs from real data.

  As a consequence of the poor simulation of the dead material in front of the calorimeters distributions like the number of cells assigned to the scattered lepton are different in data and Monte Carlo simulations [Qua96]. Another distribution that gets affected is the scattered lepton energy. In general, as shown in Section 8.1.5, the Monte Carlo energy has better resolution than the measured energy with the calorimeter.

In the following chapters some of the incomplete description of the Monte Carlo simulations is tried to be understood and corrected for.

6.6 Monte Carlo Reweighting

Monte Carlo samples are generated for different Q^2 values. To be able to compare data and Monte Carlo events, the Monte Carlo Q^2 distribution has to normalized to the Q^2 data distribution. This is done by reweighting the Monte Carlo events. Figure 6.3 shows the Monte Carlo Q^2 distribution before and after reweighting.

The total Q^2 range is divided into bins. The bin boundaries are determined by each of the Q^2 cuts with which the Monte Carlo distribution has been generated. The weight in each bin is given by the cross section value in this bin divided by the total number of events counted in

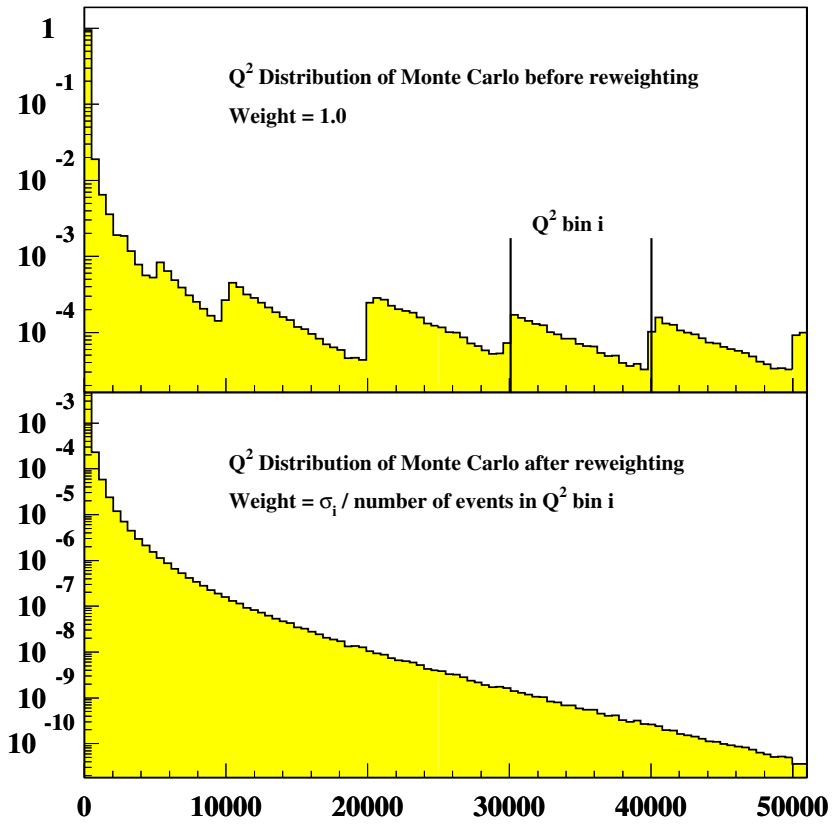

Figure 6.3: Reweighting of the Monte Carlo sample in the Q^2 variable. Plot taken from [Rus00].

this bin. The cross section is given by the difference of the cross sections associated to the Q^2 values that define the bin boundaries.

The weight is given by:

$$w_i = \frac{\sigma_i}{N_{Q^2_{gen,i}}},$$

where $N_{Q^2_{gen,i}}$ is the number of events generated in bin i. This weight is afterwards multiplied by the data luminosity so that both data and Monte Carlo samples are normalized.

Chapter 7

Reconstruction of Event Kinematics

The reconstruction of the Lorentz-invariant kinematic variables, x, Q^2 and y, is made using quantities measured with the ZEUS detector. An accurate measurement of these variables is essential for a proper measurement of the double differential cross section.

Several methods [BEK, Hoe] have been developed to achieve better resolutions depending on the region of the kinematic plane on which the measurement has to be performed. Each method uses different measured quantities.

7.1 Observables in DIS

In a DIS event the incoming lepton with momentum k is scattered by a proton with momentum p. After the scattering the momentum of the lepton is k', the momentum of the jet containing the struck quark and the proton remnant is p'. This is illustrated in Fig. 7.1.

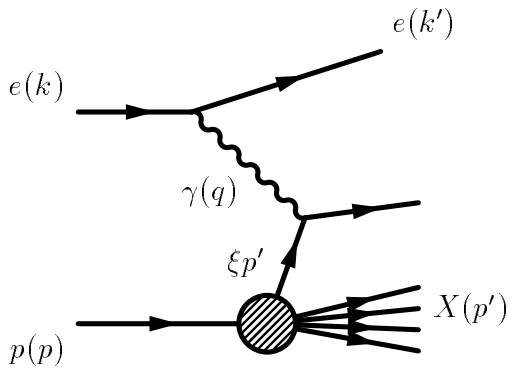

Figure 7.1: Schematic representation of a neutral current DIS event.

Ignoring the particles' rest mass, the four momenta in the ZEUS coordinate system can be written as:

$$\begin{aligned} k &= (E_e, 0, 0, -E_e) \\ k' &= (E'_e, E'_e \sin\Theta \cos\phi, E'_e \sin\Theta \sin\phi, E'_e \cos\Theta) \\ P &= (E_p, 0, 0, E_p) \\ P' &= (E_h, p_{x,h}, p_{y,h}, p_{z,h}), \end{aligned}$$

where E_e and E_p are the initial energies of the incoming lepton and the proton respectively. E'_e, Θ and ϕ are the energy, polar and azimuthal angle of the scattered lepton. E_h, $p_{x,h}$, $p_{y,h}$, $p_{z,h}$ are the energy and momentum of the hadronic final state X, where a summation over all final state objects is assumed. The origin of the coordinate system is the event vertex and beam tilt effects have been neglected.

Special care should be taken when hadronic variables are used for the calculation of kinematic variables. It has to be ensured that any influence from the final state fragmentation, i.e. the rapidity distribution, the number of jets, $\cdots$, be negligible. Furthermore the loss of particles, specially in the forward direction, through the beam pipe should not alter the measurement of the kinematic variables. Hadronic quantities that can be used are the longitudinal momentum $\delta_h = (E - p_z)_h$ and the transverse momentum $p^2_{T,h} = p^2_{x,h} + p^2_{y,h}$

The current jet can be treated as a massless object that carries the energy of the current, E_h, and has an angle γ_h. In the naïve quark parton model, this description would correspond to a struck quark with an energy E_h and an angle γ_h with respect to the proton.

7.2 Electron Method

In this method, the kinematic variables are calculated from the energy and angle of the scattered lepton. So Q^2, x and y can be written as:

$$\begin{aligned} y &= 1 - \frac{E'_e}{2E_e}(1 - \cos\Theta'_e) \\ Q^2 &= 2E_e E'_e(1 + \cos\Theta'_e) \\ x &= E'_e \frac{1 + \cos\Theta'_e}{2y \cdot E_p} = \frac{Q^2}{y \cdot s}. \end{aligned} \tag{7.1}$$

In Fig. 7.2 one can see the contours of constant energy E'_e over the kinematic plane. There is a range of scattered lepton energies $27.0 - 28.0$ GeV that covers a big region on the kinematic plane. A small mismeasurement of the energy E'_e will cause big migrations in this area.

7.3 Jacquet-Blondel Method

The kinematic variables can also be reconstructed using only the hadronic final state [JB79]. This method can be used both for neutral and charged current events, although in neutral current events other methods that yield better resolution are preferred. It can be used provided the $E - p_Z$ and p_T carried by the particles escaping down the beam pipe is negligible. In this case the kinematic variables have the form:

$$\begin{aligned} y_{JB} &= \frac{\sum_h E_h - p_{hz}}{2E_e} = \frac{\delta_h}{2E_e} \\ Q^2_{JB} &= \frac{\left(\sum_h p_{xh}\right)^2 + \left(\sum_h p_{yh}\right)^2}{1 - y_{JB}} = \frac{p^2_{T,h}}{1 - y_{JB}} \\ x_{JB} &= \frac{Q^2_{JB}}{s \cdot y_{JB}}. \end{aligned}$$

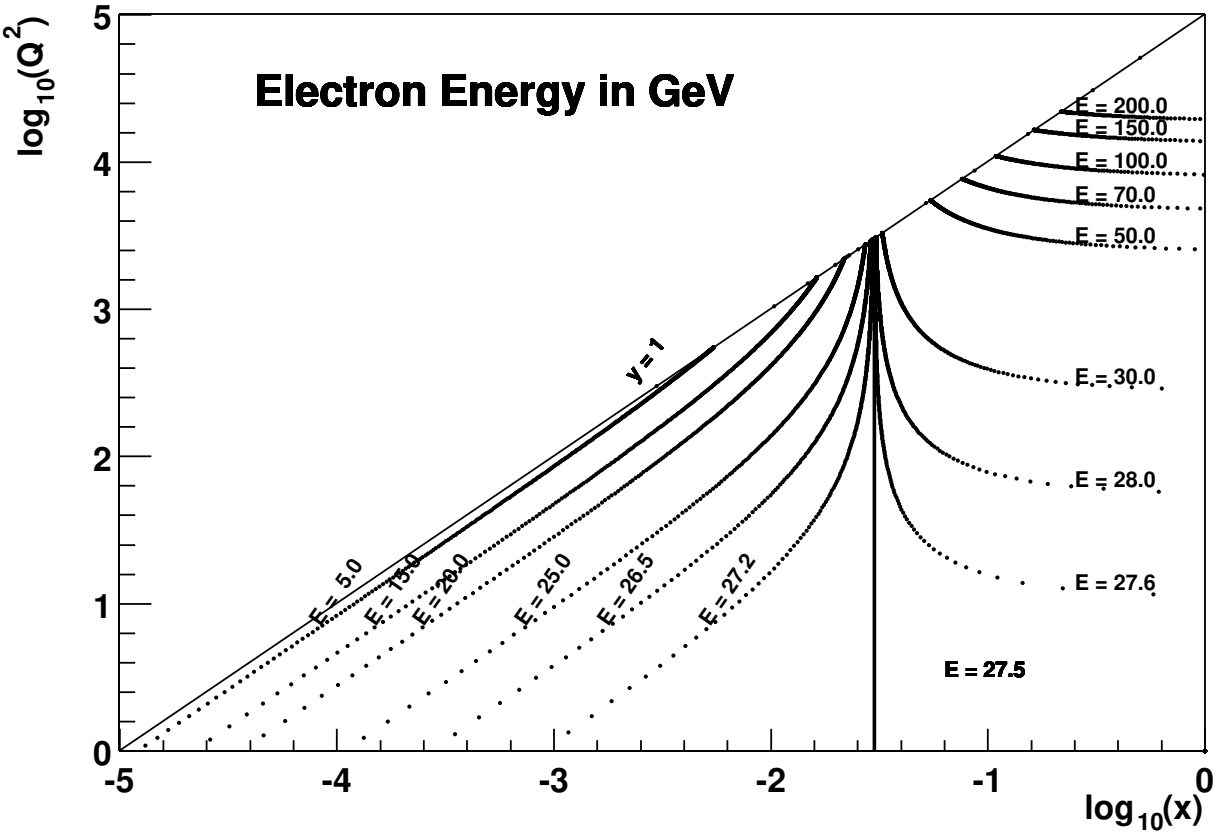

Figure 7.2: Isolines of constant energy for the scattered lepton in the kinematic plane.

In Fig. 7.3 one can see the contours of constant $p_{T,h}$ in the (x, Q^2) plane. They are almost flat in x since $p_{T,h}$ only defines the Q^2 of the event. The δ_h isolines are shown in Fig. 7.4. They are parallel to the y lines. In the region of high y the $p_{T,h}$ and δ_h lines run almost parallel, in this case the resolution of the method deteriorates.

7.4 Double Angle Method

In this method the kinematic variables, x, y and Q^2 are calculated using the angle of the scattered lepton Θ and the angle γ_h of the jet of the struck quark which is treated as massless:

$$p_{jet} = E_{jet}\,(1, \sin\gamma_h \cos\phi_h, \sin\gamma_h \sin\phi_h, \cos\gamma_h)\,.$$

Since most of the proton remnant goes along the beam pipe without being detected, one can make the approximation that only the jet contributes to the detected hadronic system, thus $E_{jet} = E_h$.

This method has the advantage with respect to others that usually the angles are better measured and their measurement is independent of the calorimeter energy scale. For high Q^2 events the scattered lepton is in a region where its angle can be measured from the CTD. The hadronic

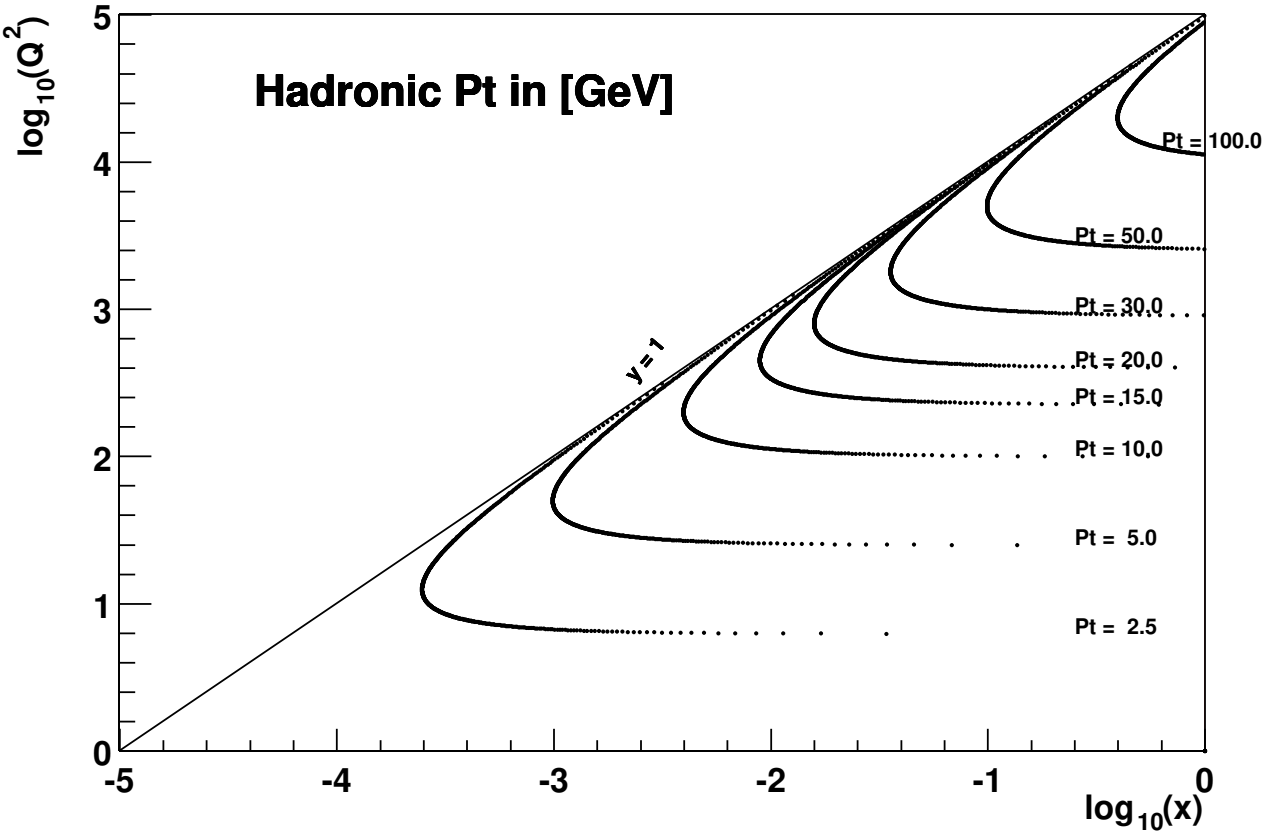

Figure 7.3: Isolines of constant $p_{T,h}$ for the hadronic final state over the kinematic plane.

angle γ_h can be obtained from the transverse and longitudinal momentum of the jet:

$$\cos\gamma_h = \frac{p_{T,h}^2 - \delta_h^2}{p_{T,h}^2 + \delta_h^2}.$$

From the momentum conservation law, the sum of the energy of the incoming lepton E_e and the quark xp has to be the sum of the energies of the scattered lepton E'_e and the hadrons in the final state E_h:

$$xp + E_e = E'_e + E_h.$$

The scattered lepton compensates the transverse momentum of the hadronic jet, therefore:

$$E'_e \sin\Theta = E_h \sin\gamma_h.$$

The longitudinal component of the momentum conservation can be written as:

$$xp - E_e = E'_e \cos\Theta + E_h \cos\gamma_h,$$

combining these expressions to eliminate xp and E_h one can extract the energy of the scattered lepton as a function of the two angles Θ and γ_h:

$$E_{DA} = 2E_e \frac{\sin\gamma_h}{\sin\Theta + \sin\gamma_h - \sin(\Theta + \gamma_h)}.$$

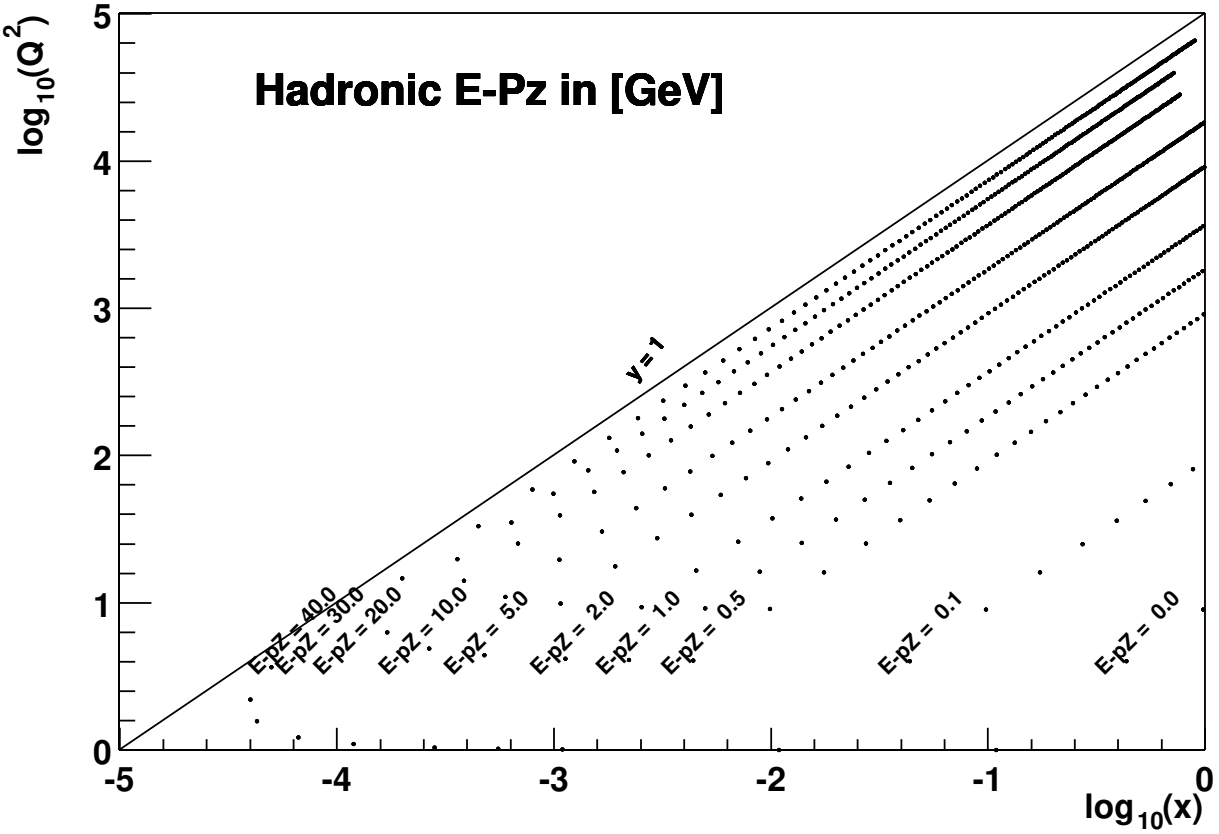

Figure 7.4: Isolines of constant $E - p_Z$ for the hadronic final state over the kinematic plane.

This distribution is shown in Fig. 7.5. From the figure one can see that the Monte Carlo distribution is well simulated and agrees with the data.

This energy can now be substituted in the electron method formulae to obtain the kinematic variables as a function of Θ and γ_h.

$$\begin{aligned} Q^2_{DA} &= 4E_e^2 \frac{\sin\gamma_h(1+\cos\Theta)}{\sin\Theta + \sin\gamma_h - \sin(\Theta+\gamma_h)} \\ y_{DA} &= \frac{\sin\Theta(1-\cos\gamma_h)}{\sin\Theta + \sin\gamma_h - \sin(\Theta+\gamma_h)} \\ x_{DA} &= \frac{E_e}{E_p}\frac{\sin\gamma_h(1+\cos\Theta)}{\sin\Theta(1-\cos\gamma_h)}. \end{aligned}$$

In Fig. 7.6 one sees the scattered lepton angle isolines. They are parallel to the x-axis for x and Q^2 away from the $y = 1$ line. The contours of fixed δ_h are nearly parallel to the contours of fixed γ_h shown in Fig. 7.7 in the high x range. Since γ_h is calculated from $p_{T,h}$ and δ_h, the contours of δ_h and γ_h show that γ_h is most sensitive to the δ_h value. The usage of the γ_h value is one of the most sensitive methods for measuring x for DIS events in the high x region. Near to the $y = 1$ line, low x region, the scattered lepton and hadronic angle isolines become more parallel and the resolution of the double angle method deteriorates.

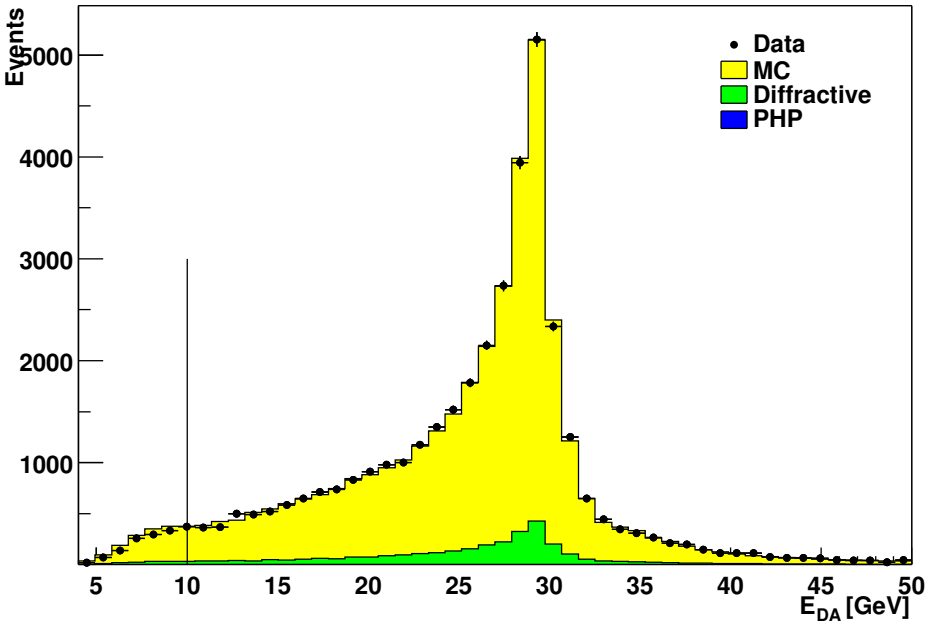

Figure 7.5: Double angle energy for the scattered lepton. The vertical line shows the analysis cut at $E_e = 10$ GeV .

7.5 Comparison of the Different Methods for the Calculation of the Kinematic Variables

Several methods to calculate the kinematic variables x, y and Q^2 have been presented. For the kinematic region in which the extraction of the double differential cross section will be done, $Q^2 > 200$ GeV^2, the best reconstruction method is the double angle method.

The estimation of the scattered lepton angle, done with the CTD in almost all the kinematic region, has a very high resolution. The hadronic angle is also a variable that is independent of the proton remnant and therefore suited for the calculation of the kinematic variables. On the other hand the estimation of the kinematic variables with the energy of the scattered lepton or the hadronic system will strongly depend on corrections[1].

In Fig. 7.8 and Fig. 7.9 one can see the comparison of the kinematic variables calculated with the electron (first row) Jacquet-Blondel, (second row) and double angle (last row) method with respect to the true variables obtained from the Monte Carlo simulation, before and after analysis cuts respectively.

In the electron method case one sees that for low $\log_{10}(y)$ values the measured variables are very spread around the true values. This region corresponds to the high $\log_{10}(x)$ region where one observes the same situation.

The Jacquet-Blondel method gives a very bad resolution of the $\log_{10}(Q^2)$ variable for low values of it.

The double angle method has the best resolution, although not perfect either. Events in the middle $\log_{10}(y)$ and $\log_{10}(x)$ regions tend to migrate to higher and lower values respectively. In the very low $\log_{10}(y)$ and very high $\log_{10}(x)$ region the events migrate in the opposite direction.

[1] See next chapter

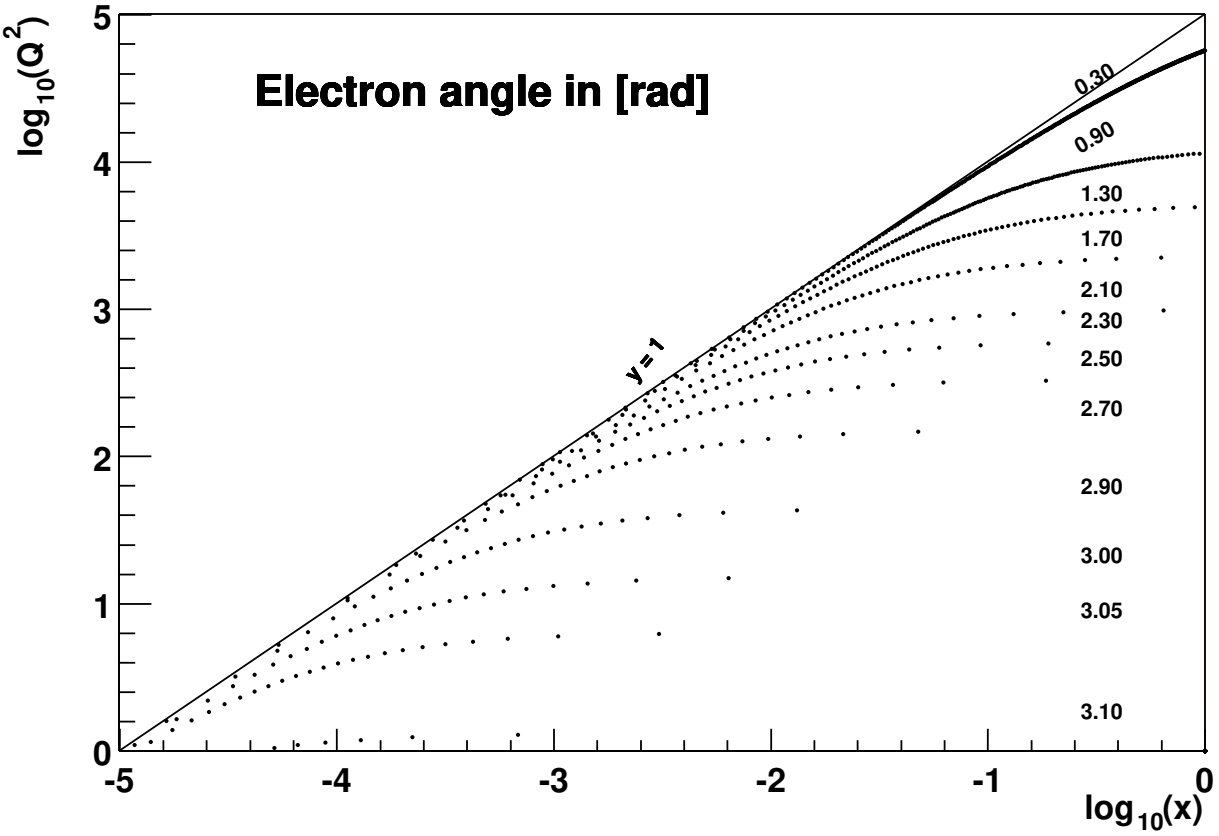

Figure 7.6: Isolines of constant scattered lepton angle Θ over the kinematic plane.

The double angle method is preferred because it is the method that gives the less unbiased result and the best resolution.

7.6 Kinematic Peak Events

Writing the cross section in Eq. (2.11) as $d^2\sigma^{\pm}/dE'_e\,dQ^2$, one can see that it reaches a maximum for $E'_e = E_e = 27.5$ GeV . This corresponds, in the partonic model, to the symmetric process in which the electron and the parton posses the same energy. For this specific process the scattered lepton has the same value of $x = x(E'_e = E_e) = E_e/E_p$ for all possible values of Q^2. This is the value of x at which all isolines in Fig. 7.2 converge.

Events with a higher cross section have a bigger probability to happen than events with lower cross section. Therefore it is expected a big amount of events in which the scattered lepton has an energy close to the energy of the incoming lepton. In Fig. 7.2 one can see a big region in which the energy of the scattered lepton is very close to the energy of the incoming lepton. This region is clearly visible between the isolines with $E'_e = 27.2$ GeV and $E'_e = 27.6$ GeV .

This region is called the Kinematic Peak (KP) region. Events in this region can be selected using specific cuts [C+94]. The advantage of the events in this region is that the have a well defined energy ($E'_e \approx E_e$) which is very useful for corrections to the scattered lepton energy (see [C+94]).

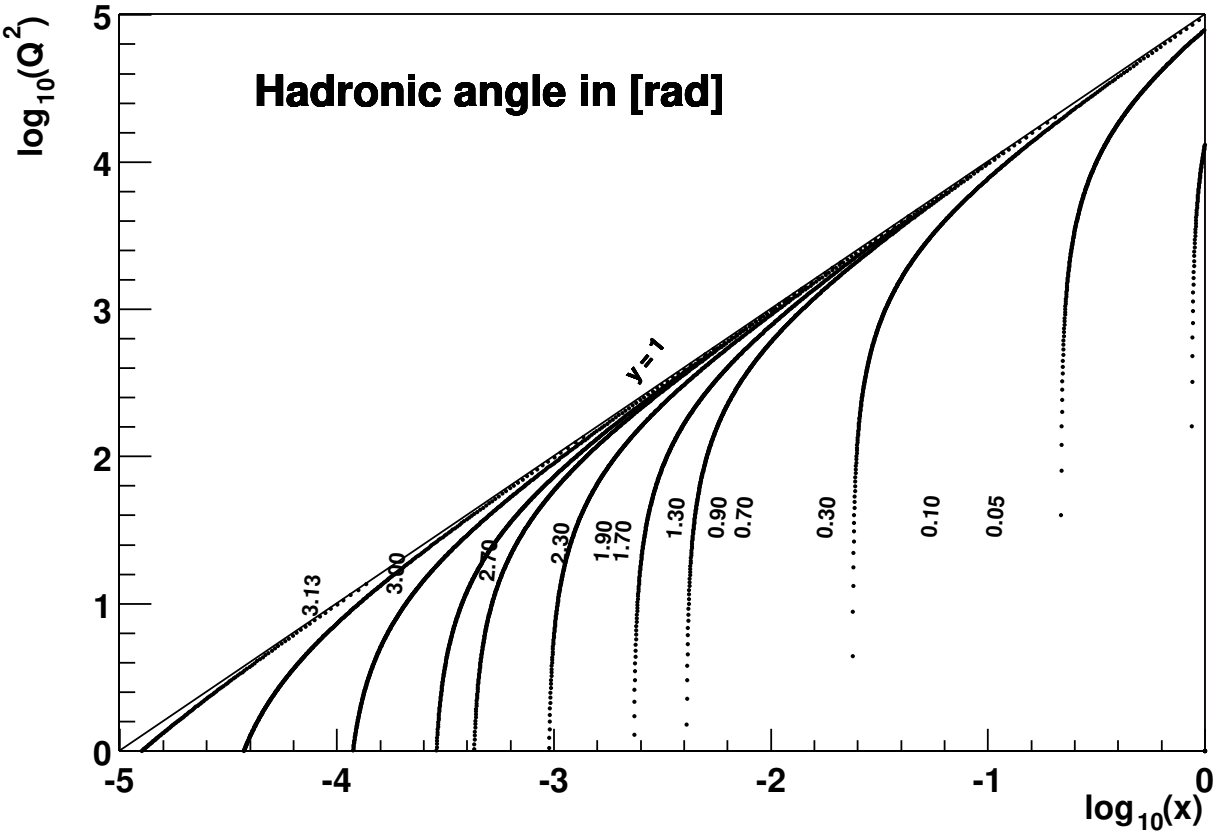

Figure 7.7: Isolines of constant γ_h for the hadronic final state over the kinematic plane.

Unfortunately this region is only reachable for $Q^2 \leq 100$ GeV^2, KP events cannot be used in this analysis for the energy corrections. For this analysis quasi KP events are selected by means of the momentum conservation law:

$$(E - p_Z)^i_{lepton} + (E - p_Z)^i_{proton} = (E - p_Z)^f_{lepton} + (E - p_Z)^f_{hadrons},$$

where i and f stand for initial and final states respectively.

Choosing events in which $(E - p_Z)^f_{hadrons} \leq 1.5$ GeV, low y region, one can predict the energy of the scattered lepton, that in this case will not be the fixed value 27.5 GeV, but will have a dependence in $\cos\Theta$.

$$E'_e = \frac{(E - p_Z)^i_{lepton}}{(E - p_Z)^f_{lepton}} = \frac{2 \cdot E_e}{1 - \cos\Theta}.$$

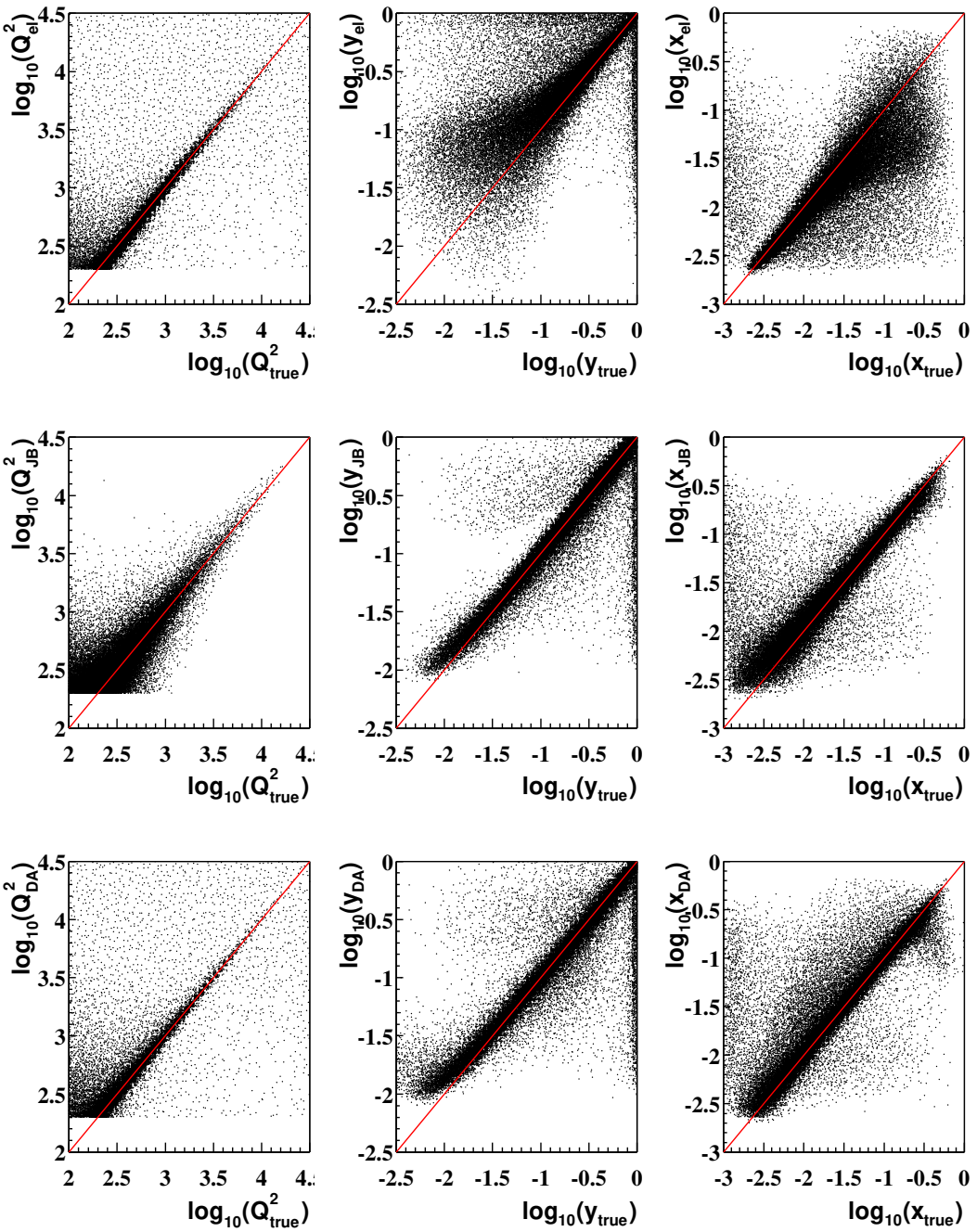

Figure 7.8: Comparison between the true and the measured kinematic variables before analysis cuts for the electron (first row), Jacquet-Blondel (second row) and double angle method (last row).

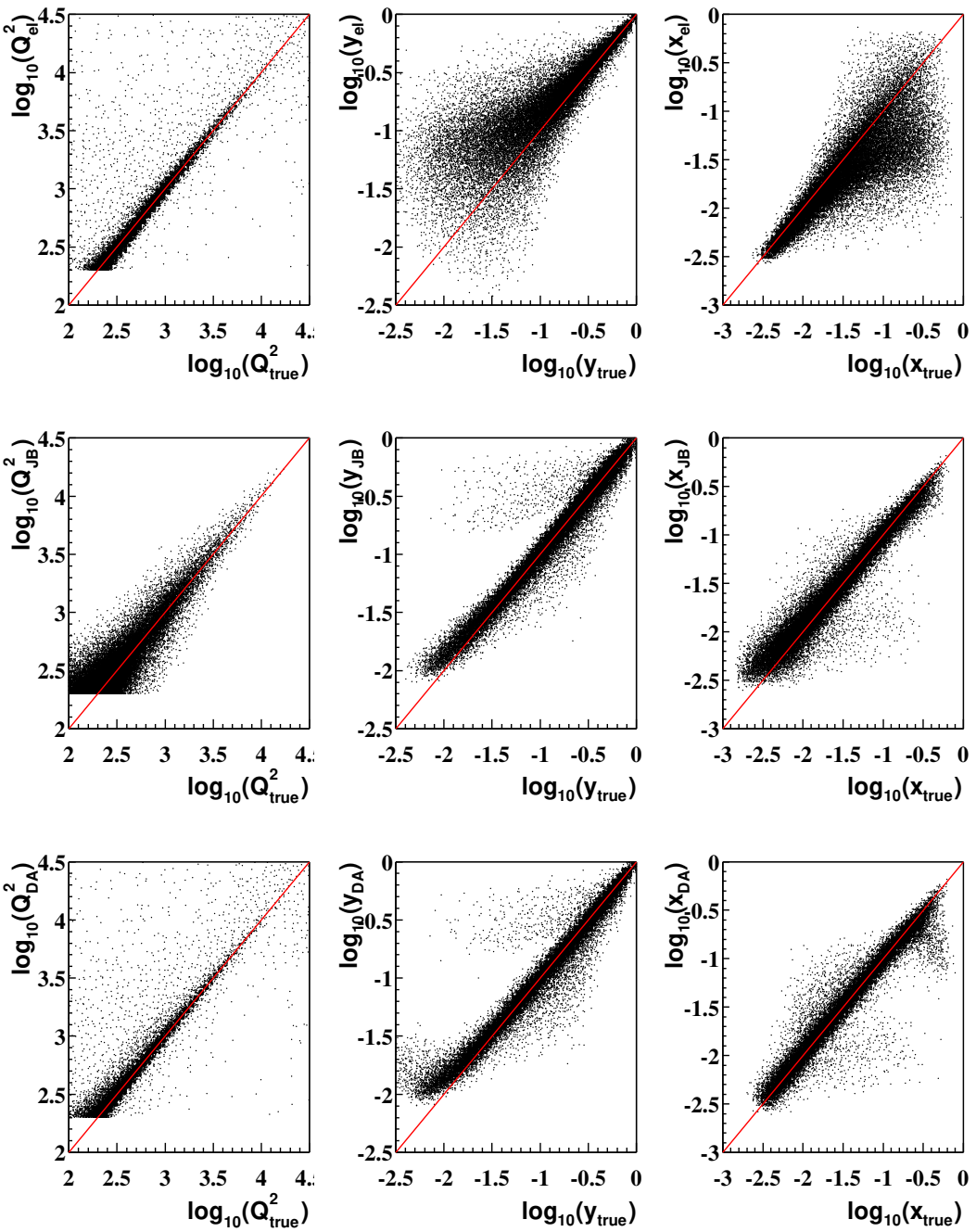

Figure 7.9: Comparison between the true and the measured kinematic variables for the electron (first row), Jacquet-Blondel (second row) and double angle method (last row).

Chapter 8

Data Sample

8.1 Reconstruction of Event Variables

This analysis is based on a data sample of DIS NC events[1] that have a $Q^2 \geq 200$ GeV^2 . The topology of such events is a well defined vertex reconstructed with tracks in the CTD, the scattered lepton[2] observed inside the detector, and a hadronic final state that compensates the p_T of the scattered lepton. All these characteristics can be seen in Fig. 8.1. The energy-

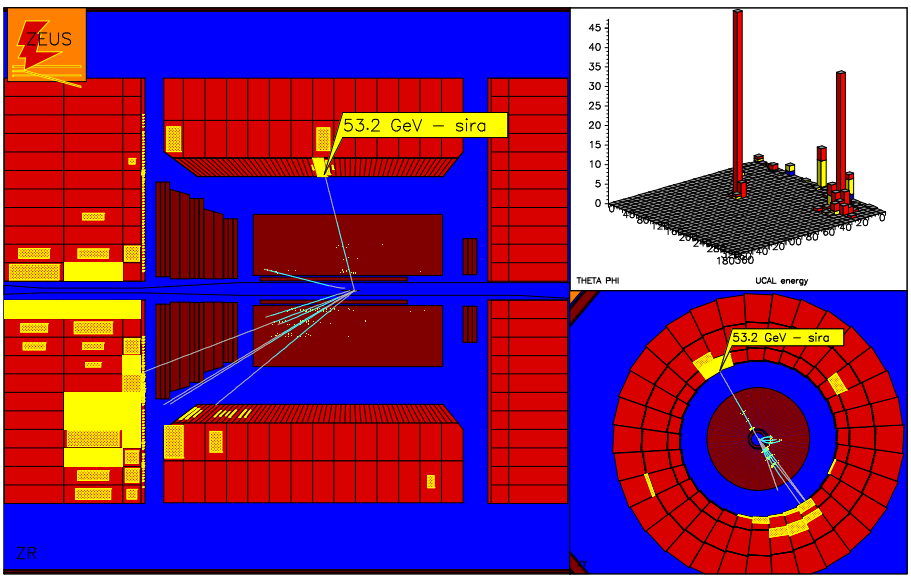

Figure 8.1: Neutral Current event in ZEUS detector.

[1]The analysis has been performed over three different data samples. e^+p for $E_p = 820$ GeV, e^-p and e^+p for $E_p = 920$ GeV. In this chapter and the next one only the e^-p data sample will be shown. The corrections and systematic studies for the data sample $(e^+p)^{820}$ can be found in [Tun01a], [Rus00], [Wod99] and [Def99]. The studies for the $(e^p)^{920}$ can be found in [Mor01] and [Sch01]. In these studies it has been tested that the corrections are applicable to all data samples, and that the systematic studies are consistent along the years. Control plots for the other these samples can be found in Appendix H

[2]To extract $xF_3(x, Q^2)$ one needs a sample of neutral current e^-p events and a sample of e^+p events. In one case one has a positron in the final state and in the other case an electron. To generalize the convention "scattered lepton" has been chosen to refer to the scattered electron or positron in the final state in NC events. Of course charged current events also have a scattered lepton, the neutrino, in the final state, but these events are not considered in this analysis.

momentum conservation law implies that the $E - p_Z$ variable is conserved.

$$(E - p_Z)^i = (E - p_Z)^f,$$

where the initial $(E - p_Z)^i$ is given by the sum of the $E - p_Z$ from the incoming lepton and the one from the incoming proton:

$$\begin{aligned}(E - p_Z)^i &= (E - p_Z)^i_{lepton} + (E - p_Z)^i_{proton} \\ &= (27.5 \cdot 2 + 0.0)\ \text{GeV} \\ &= 55.0\ \text{GeV}\ .\end{aligned}$$

Since both the scattered lepton and the hadronic jet are contained in the detector, the total $E - p_Z$ variable measured in the calorimeter has to be equal to the initial quantity, provided the proton remnant carries negligible $E - p_Z$:

$$55.0\ \text{GeV} = (E - p_Z)^f_{lepton} + (E - p_Z)^f_{jet}.$$

Figure 8.2 shows the total $E - p_Z$ variable for the final state[3]. It can be seen that NC events (lightest histogram, middle grey for diffractive) are mainly found close to the nominal value, 55 GeV. PHP events (darkest histogram)[4], in which the scattered lepton escapes detection taking energy with it, have a much lower value of $E - p_Z$. A way to suppress this background is to place a lower cut on this variable. The selection of NC high Q^2 events is based on the characteristics

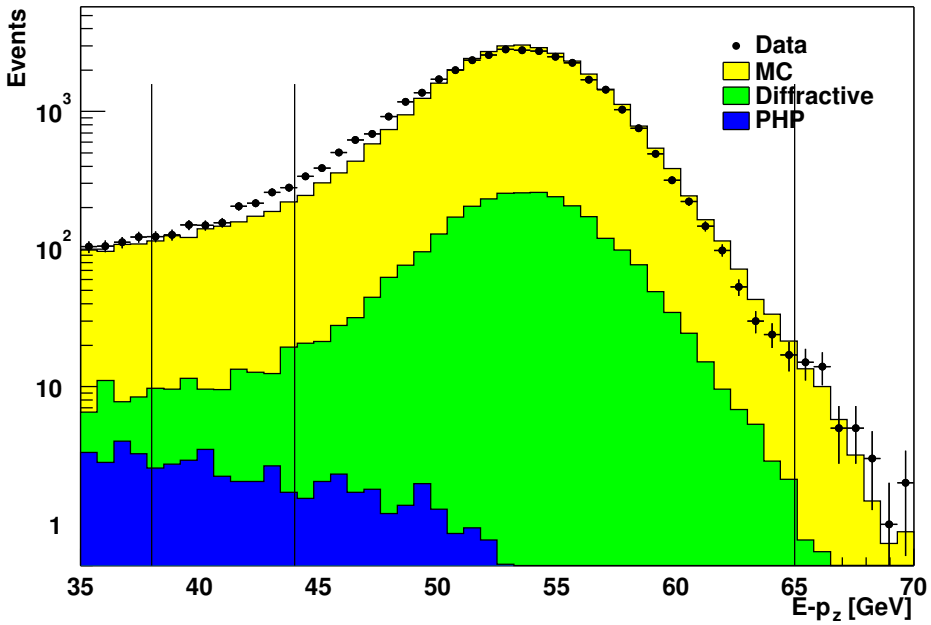

Figure 8.2: Total $E - p_Z$ variable. The vertical lines show the analysis cuts defined in the text.

described above and is made on two steps. First there is an online pre-selection made with the ZEUS three-level trigger. Then, offline cuts are applied in order to obtain a clean sample of events with as less background as possible.

[3]For simplicity the prime for all final state quantities has been removed.
[4]This color code remains for all histograms shown in this an following chapters.

8.1.1 Trigger reconstruction

The three-level trigger is mainly designed to profit from the scattered lepton signal left in the calorimeter. The main trigger chain FLT, SLT and TLT is described below.

First Level trigger

There are different FLTs for the different calorimeter sections, RCAL, BCAL and FCAL.

In terms of the FLT, the RCAL is subdivided in two regions, one corresponding to the first inner ring ($|x| < 60$ cm and $|y| < 60$ cm), and the other excluding this region. Events with an energy in the first inner ring greater than 2 GeV are triggered by the RISOe trigger. Events with an energy greater then 3.5 GeV outside the first inner ring are taken by the REMC trigger.

Scattered leptons in the BCAL are triggered by the BCAL trigger. It requires an EMC energy sum greater than 4.78 GeV and a track in the CTD. The track requirement helps to reduce the halo muons that reach the detector outside the CTD acceptance.

For high Q^2 leptons scattered in the FCAL the hadronic system either has a large transverse momentum, or is scattered at large angles.

Events with the hadronic system having large transverse momentum are selected with the requirement that the calorimeter transverse energy ≥ 20.0 GeV. When the hadronic system is scattered at large angles, the transverse momentum is not as high, but it enters the CTD acceptance. In this case a track in the CTD is required. Events in this region with a transverse energy smaller than 11.6 GeV have to have an FCAL EMC energy ≥ 10 GeV.

Second level trigger

At the second level trigger, the full calorimeter information is available so more detailed trigger selection can be made. Timing cuts are placed to remove upstream interactions of proton with gas in the beam pipe. Proton-gas interactions hit the rear calorimeter before the proton bunch has made it to the interaction point. Cutting events with early RCAL time reduces background.

Cosmic events can also be removed with timing cuts. Cosmic events strike the upper half of the calorimeter before the lower half and are removed with an up-down timing cut. The timing cuts are: RCAL time ≥ -8 ns, FCAL $-$ RCAL time ≤ 8 ns, FCAL time ≤ 8 ns and up-down time ≥ -10 ns.

As said before DIS events conserve the $E - p_Z$ variable. At this stage the $E - p_Z$ variable can be reconstructed from calorimeter information: $E - p_Z = \sum_i E_i(1 - \cos(\Theta_i))$ where i runs over all the energy deposits and Θ_i is the angle of each cluster measured from the vertex.

A cut is done on this calorimeter $E - p_Z$ variable and the energy measured in lumi photon detector E_{lumi_γ}:

$$E - p_Z + 2E_{lumi_\gamma} \geq 29 \text{ GeV} .$$

This cuts reduces the PHP background.

Third level trigger

The event builder collects all the data from the ZEUS components and constructs an event that can be processed by the third level trigger and written to the output stream.

Electron-finding algorithms similar to the off-line ones are run to select only events with a good electron. These electron-finders are SINISTRA95, EMILLE, LOCAL and ELEC5 [ZEU]. The event $E - p_Z$ is calculated using the event vertex z-position from the CTD. Using the event vertex improves the resolution of $E - p_Z$ relative to the SLT value, so a tighter cut is applied to further reduce the low Q^2 background. The cut $E - p_Z + 2E_{lumi_\gamma} \geq 30$ GeV is placed.

The TLT selection of DIS events with high Q^2 is made with the DIS04 trigger. In this trigger a cut on the electron energy $\geq$ 7 GeV and a 30 cm box cut around the beam pipe hole are applied.

Data quality

During and after data taking data quality tests are made. It is checked that all the components of the ZEUS detector are working properly. If this is not the case the events are flagged as not good for physics analysis. All the information is summed up into a subroutine called EVTAKE. For this analysis only events selected with the EVTAKE subroutine are used.

8.1.2 Vertex reconstruction

The interaction point in which the *ep* scattering occurs is the primary vertex, or simply the vertex. Subsequently decays of particles in the final state and interactions can produce secondary vertices. A precise determination of the vertex is needed in order to get a proper measurement of the leptonic and hadronic variables.

The reconstruction of the vertex is performed with the VCTRACK [H$^+$97] package. This package reconstructs tracks from CTD hits and estimates the primary and secondary vertices with them. For this analysis the multi-vertex mode has been used. The z-vertex, Fig. 8.3, distribution has a central peak at $z = -2.3$ cm. The longitudinal size of the proton bunches is bigger than the one from lepton bunches. That means that leptons can collide with protons over an extended longitudinal z region. The spread of the central peak of the z-vertex distribution reflects this fact. At $z = \pm 70$ cm two clear shoulders can be observed, those are vertices of events where leptons collide with protons in satellite bunches.

In Fig. 8.4, the x and y vertices are shown. Since the beam in this direction is more collimated than in the z direction, the x and y vertices are much narrower.

8.1.3 Calorimeter cluster reconstruction

Particles entering the ZEUS calorimeter will shower and deposit their energy in several adjacent detector cells. The rôle of a clustering algorithm is then to merge cells which, in the ideal case, belong to the shower of a single particle. The formed clusters can then be classified. The classification is possible, as shown below, since the shower properties of electromagnetic showers are different from those of hadronic particles.

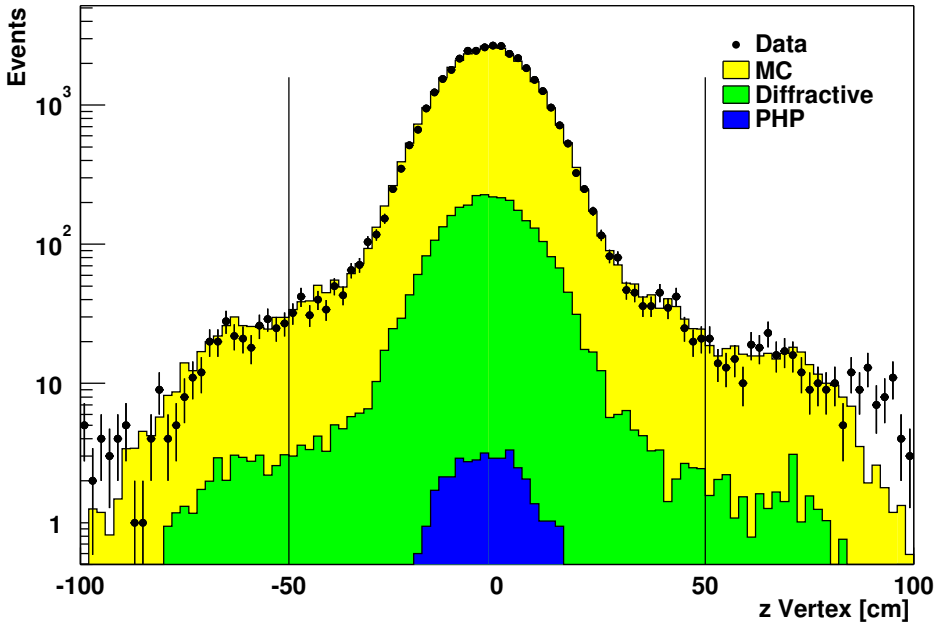

Figure 8.3: z-vertex measured with tracks from the CTD. The vertical lines show the analysis cuts at $|Vtx_z| < 50$cm.

Below a two-stage algorithm for clustering calorimeter cells associated with a particle or a jet is introduced. The first stage is based on local clustering with equivalence relations and leads to cell islands, whereas the second stage is based on global clustering, and is used to create so-called cone islands.

Cell by cell energy corrections

Before the clustering takes place, the calorimeter cells are corrected. First a subroutine is used to remove noisy cells in calorimeter. All cells with an energy below a threshold are removed from the event. This threshold is 60 (140) MeV for EMC (HAC) cells. Cells that are also coincident in all events from a run may be considered as noisy cells and removed from the sample.

Sparks are also removed; the imbalance is the fraction of the total energy measured by one of the two photomultiplier (PMT) that read out each cell. A high imbalance suggests that most of the energy is deposited in the cell was sampled by one PMT, while an imbalance of zero means that both PMTs sampled the same amount of energy. Very high imbalance is a signature of sparks.

After all noisy cells are removed, all the EMC cells in RCAL are rescaled up or down according with a study performed on the 96-97 data sample [Tun01a]. This study was performed with kinematic peak events, Section 7.6. Knowing the energy of the scattered lepton one can rescale the energy of each EMC RCAL cell depending on its response. The average correction is roughly 2.5%. A new study [Mel01] has been performed over the 98-99 data sample obtaining the same results.

The rescaling is performed by the subroutine RCALCORR [ZEU]. This subroutine applies also an overall correction factor of 5% to all EMC BCAL cells [C$^+$98].

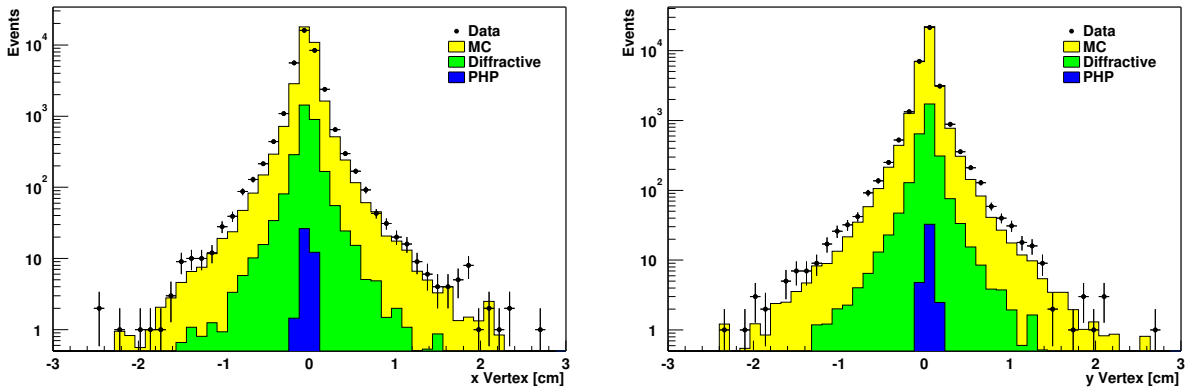

Figure 8.4: x- and y-vertices measured from tracks from the CTD.

The cell island algorithm

The cell island clustering algorithm considers clustering in a local neighborhood only uses an equivalence relation to assign cells to islands. If the cell has sufficient energy, it becomes a

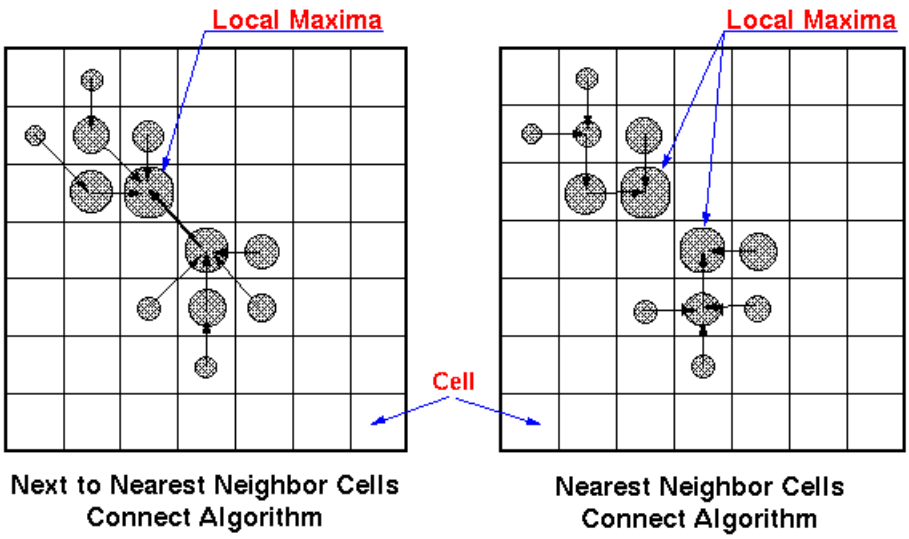

Figure 8.5: Schematic representation of the cell islands algorithm. Plot taken from [Bri98].

candidate to be connected with one of its neighbors. The connections are made to the highest energy neighbor or to the highest energy next to nearest neighbor. This procedure, shown in Fig. 8.5, is repeated for each cell and produces a unique assignment of a cell to an island.

The cone island algorithm

The energy deposit of a single particle can often be split by the local clustering algorithm. Therefore a second pass, the cone island clustering algorithm, has been suggested to collect the cell islands which belong to a shower of a single particle or a jet of particles. The cone island algorithm takes as input the cell islands and performs a clustering in the Θ-ϕ space.

8.1.4 Identification of the scattered lepton

The identification of the scattered lepton is performed by a neural network, SINISTRA95 [SV97a, SV97b, ACS95]. This algorithm uses as input all the energy deposits in calorimeter, analyzes them, and returns as output the probability of each cluster to be the scattered lepton.

The scattered lepton leaves an, usually well isolated, electromagnetic cluster in the calorimeter with a very low hadronic content [ACS95]. Other particles that can leave the same signal in the calorimeter are pions. The difference between pions and the scattered lepton lies in the shower profile of the different particles. The study of the transverse shower profile rules out π^0 particles, while the study of longitudinal shower profiles separates the scattered lepton from $\pi^{\pm}$.

The energy clusters in calorimeter are transformed several times before they can be used to feed the neural network. First the clustering algorithm in cell island mode is used. To overcome the non-projectivity of the calorimeter all islands are then projected into a sphere of radius 1 m around the event vertex. In this way particles falling into a super-crack and leaving energy in different calorimeters will appear as only one and not several particles. To recover the shower profile in depth and width the islands are projected back to their original positions in calorimeter.

The energy distribution of a shower is described in terms of a discrete set of points in phase-space. The number of points vary from shower to shower and therefore this distribution cannot be used yet as input for the neural network. To solve the problem the distribution is expanded in terms of moments of an infinite series expansion done on the Zernike Moments [Zer34].

After all these operations the neural network is able to analyze the information and return a probability. In order to obtain the right answer, the neural network has to be trained. This has been done with a Monte Carlo sample containing 4000 events [SV97a]. After the training the neural network is able to provide us with a probability. According to [SV97a] to obtain a highly pure sample of scattered leptons, a cut on this probability $P_e \geq 0.9$ has to be done.

A secondary program FINDIS95 [ZEU] selects the scattered lepton from the list of candidates returned by SINISTRA95. This program has different options that select the scattered lepton according to different criteria [VS00]. The option used for this analysis is option 5. This option requires a track for the electromagnetic candidate inside the CTD acceptance region[5]. No extra conditions on the track are required. For simplicity SINISTRA95 + FINDIS95 (option 5) is called SIRA 5. The probability for all candidates selected with SIRA 5 is shown in Fig. 8.6. The Monte Carlo simulation is able to describe the data pretty well. The PHP background contamination remains constant over the whole range and is very small compared to the signal.

8.1.5 Scattered lepton energy

The energy of the scattered lepton is measured with the calorimeter. In this analysis this variable is used in the selection of events, two cuts on E_e and $E - p_Z$ depend on it. A disagreement between the data and Monte Carlo distributions will affect the cross section. In Fig. 8.7 the E_e is plotted for data and the Monte Carlo simulation. The distribution shows a kinematic peak behavior, almost all scattered leptons have an energy close to the lepton beam energy $E_e = 27.5$ GeV. The peak in the Monte Carlo distribution is placed at ≈ 27.5 GeV. The peak in the data

[5] See Section 4.1.1 for definition of CTD acceptance region

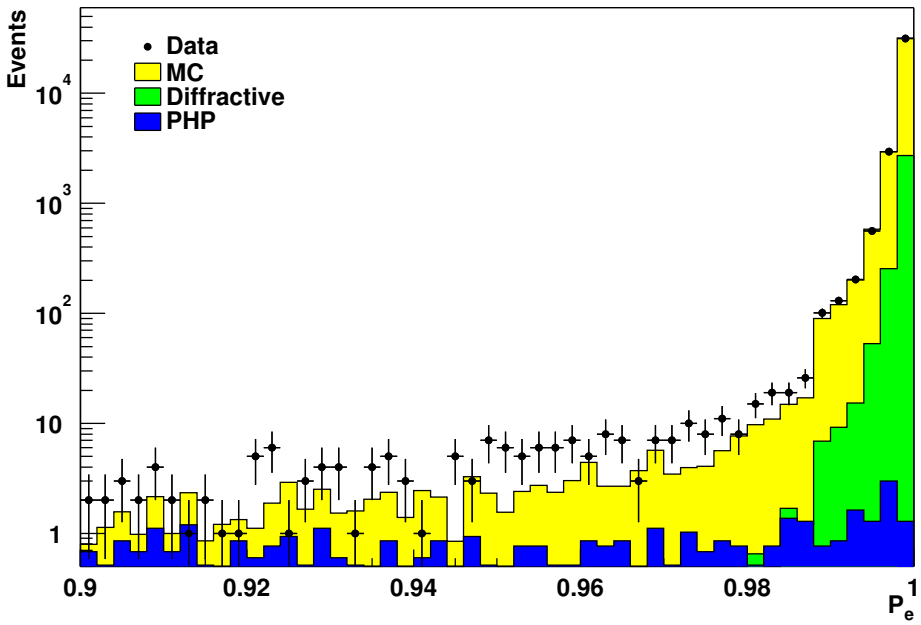

Figure 8.6: SINISTRA95 probability for electromagnetic candidates.

is shifted towards lower values. This may indicate that the scattered lepton loses energy on its way from the interaction point to the calorimeter. This effect, that cause mismatch between data and Monte Carlo events, will be corrected (see Section 8.2.4).

Another feature is that the Monte Carlo distribution is much narrower than the data. The energy resolution is better in Monte Carlo simulation than in the data. Effects like energy loss in cell, module and calorimeter cracks, not completely described in the Monte Carlo program, may be the reason for this difference. These effects will also need to be understood and corrected for (see Section 8.2.4).

8.1.6 Scattered lepton position

The position of the scattered lepton can be determined from calorimeter, track or HES variables. The position of the scattered lepton is used to calculate the kinematic variables. A bad measurement of the position will cause events to migrate from one kinematic region to an other.

The position of the scattered lepton can be given in Cartesian (x, y, z) or polar coordinates (r, Θ, ϕ). In the first case, if the scattered lepton is located either in the FCAL or the RCAL, the z coordinate is fixed, whereas if the scattered lepton is in the BCAL, $R = x^2 + y^2$ is fixed. If the position is measured with the calorimeter, Cartesian coordinates are given. If it is measured with the CTD, polar coordinates are used. To calculate the kinematic variables in the double angle method, see Chapter 7, the Θ angle (Fig. 8.8) of the scattered lepton is used, therefore from now on the position of the scattered lepton will be given in polar coordinates.

In almost all the kinematic region that concerns this analysis the scattered lepton is inside the CTD acceptance region and its position can be determined from its track. Outside the CTD acceptance region the position can be reconstructed either using the calorimeter or the HES.

In principle outside the CTD acceptance region the position of the scattered lepton is better reconstructed with the RHES [Wod99]. Unfortunately the RHES presents regions for data in

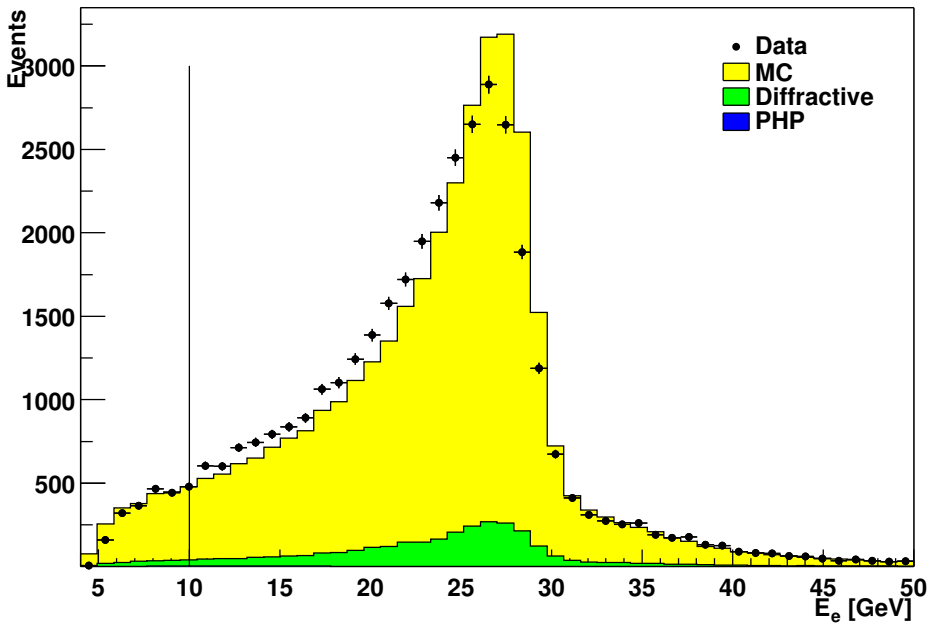

Figure 8.7: Energy of the scattered lepton measured with the calorimeter before corrections. The vertical line shows the analysis cut at $E_e = 10$ GeV .

the xy plane where there is no signal. A not negligible part of the detector has bad channels that are not simulated in the Monte Carlo programs. Using the RHES will produce a disagreement between data and Monte Carlo simulation and can therefore not be done for the determination of the position of the scattered lepton.

Since the RHES is not used to estimate the position of the scattered lepton outside the CTD acceptance region, one needs the calorimeter information. The position is given by ELECPO [Ame97], this algorithm studies the shower profile of the scattered lepton identified by SIRA 5 to properly determine its position. In the electron-finder efficiency study (see Section 9.2) an exhaustive study of the comparison between measured and true angles of the scattered lepton has been made. It can be seen from this study that the track position has better resolution than the calorimeter position. This result is also confirmed in the study [CP97]. The use of the track is therefore favored where possible.

8.1.7 Hadronic reconstruction

Once the scattered lepton is identified, the energy in the cells not associated to the identified scattered lepton in the calorimeter is considered to be hadronic. An advantage with respect to fixed target experiments is that the estimation of the kinematic variables can profit from the measurement of the hadronic variables. The hadronic final state can be described by the variables:

$$\begin{aligned} \delta_h &= \sum_h E_h - p_{z,h} \\ p_{T,h}^2 &= \left(\sum_h p_{x,h}\right)^2 + \left(\sum_h p_{y,h}\right)^2 \end{aligned}$$

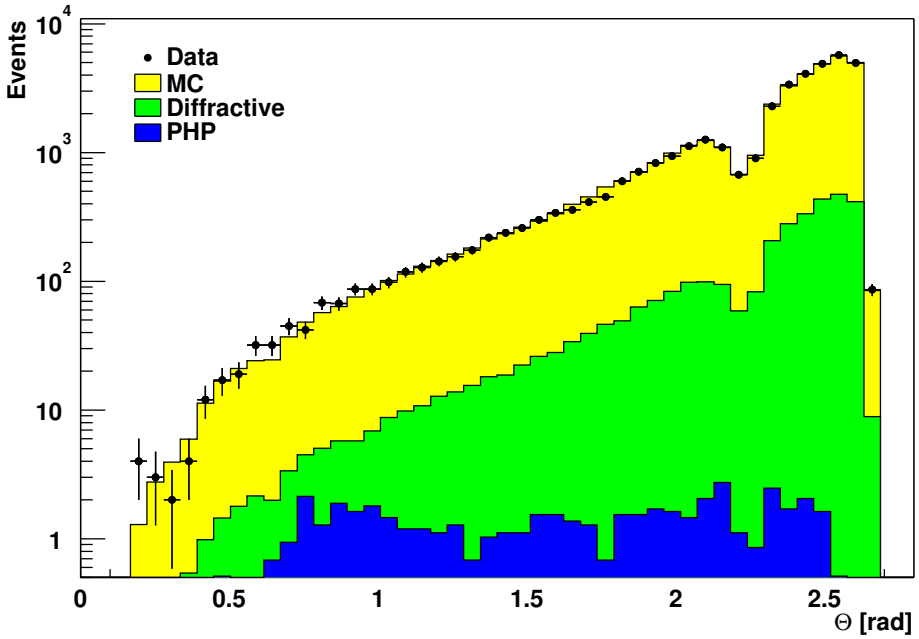

Figure 8.8: Angle of the scattered lepton. In the CTD acceptance region the angle is taken from the track. The calorimeter is used otherwise The PHP background remains constant along the Θ variable. For low Θ values it means that the ratio signal/background decreases.

This variables are selected since they are insensitive to the proton remnant. The $E-p_z$ variable for the proton remnant is negligible, since the remnant has positive values from p_Z and carries almost all its energy in this direction. The variable p_T is in principle also insensitive to the proton remnant since, as said before, the remnant carries all its energy in the z direction.

The variable γ_h being a combination of δ_h and p_T, is also insensitive to the remnant.

In principle one can calculate the hadronic variables from the calorimeter information, but once one gets to compare the data and the Monte Carlo distributions, one sees clear discrepancies. The same happens when comparing the measured variables and the true ones obtained from Monte Carlo simulations. As in the scattered lepton case, the difference in the distributions comes from the not precise description of the Monte Carlo programs of the energy deposits in calorimeter due to dead material or non-uniformities.

The algorithm used in this analysis to properly reconstruct the hadronic final state variables is CORANDCUT [GK97]. This program uses the clustering algorithm in the cone island mode to search for islands that belong to the hadronic jet. Afterwards several corrections are applied so that the measured quantities come closer to the true ones. The effects that are corrected for are listed below:

- Energy loss corrections due to passive material
- Energy corrections in super-cracks
- Correction for energy-overestimation for hadrons at low energy
- Back-splash correction

Particles in a jet have to traverse a considerable amount of inactive material from the interaction point until they finally reach the calorimeter. The mismeasurement of the energy translates into a bad estimation of the hadronic variables, and therefore migrations in the kinematic plane. Jets that have part of their particles falling into a super-crack are also measured with an energy lower than the true one.

The reason for the energy-overestimation for hadrons at low energy is that the probability of hadrons to deposit energy by ionization instead of showering increases as the energy decreases. As the calorimeter response to energy deposition by ionization loss is approximately 60% higher than from showering, the observed overestimation in energy is created.

The energy losses due to inactive material or super-cracks, as well as the energy-overestimation effects are parameterized in data and Monte Carlo simulations, to obtain corrections for them [GK97] and [GK98].

The biggest effect that causes mismatch between the true and the measured values is the overestimation of γ_h or δ_h at the lower end of the y spectrum. This is caused by energy deposits far apart from the jet direction which are erroneously associated with particles from the ep interaction. The responsible mechanisms are: back-splash from the calorimeter, and scattering or showering in the material in front of the calorimeter. To get rid of these effects a cut γ_{max} was developed. All the islands with $E \leq 3$ GeV and an angle bigger than the cut ($\gamma_{island} \geq \gamma_{max}$) were removed. This improves dramatically the agreement between the true and the measured values.

This γ_{max} cut is dependent on γ_h. The parameterization depends on the event characteristics meaning that there is a different parameterization for the $E_p = 820$ GeV and the $E_p = 920$ GeV sample. The general form of the parameterization is:

$$\gamma_{max} = \begin{cases} a + b \cdot \gamma_h & : \quad \gamma_h < g \\ a + b \cdot g + c \cdot (\gamma_h - g) & : \quad \gamma_h > g \end{cases} .$$

For the sample with $E_p = 820$ GeV the value of the constants is: $a = 0.151,\ b = 1.372,\ c = 0.259$ and $g = 1.95$, and for the $E_p = 920$ GeV sample the values are: $a = 0.149,\ b = 1.369,\ c = 0.328$ and $g = 1.90$. Figure 8.9 shows the parameterization for both samples. From the figure one can see that when the jet is manly contained in the FCAL ($\gamma_h < 0.7$) the value of γ_{max} is very close to γ_h. This is the region of low y values where δ_h deviates more from the true value. The γ_{max} cut is linear with γ_h all over the BCAL, and when entering the RCAL region the γ_{max} cut shows an almost flat behavior for all the γ_h values. After all these corrections one can finally obtain the hadronic variables. The hadronic $E - p_Z$ variable is shown in Fig. 8.10. The middle dark area in the Monte Carlo histogram shows the contribution from the diffractive events. The overall agreement between data and Monte Carlo distributions is good, although the Monte Carlo simulation overshoots the data slightly for higher values of this variable. The p_T variable is shown in Fig. 8.11, where again the middle dark histogram corresponds to the contribution from diffractive events. Finally the γ_h variable is plotted in Fig. 8.12. Data and Monte Carlo samples agree very well over the whole range.

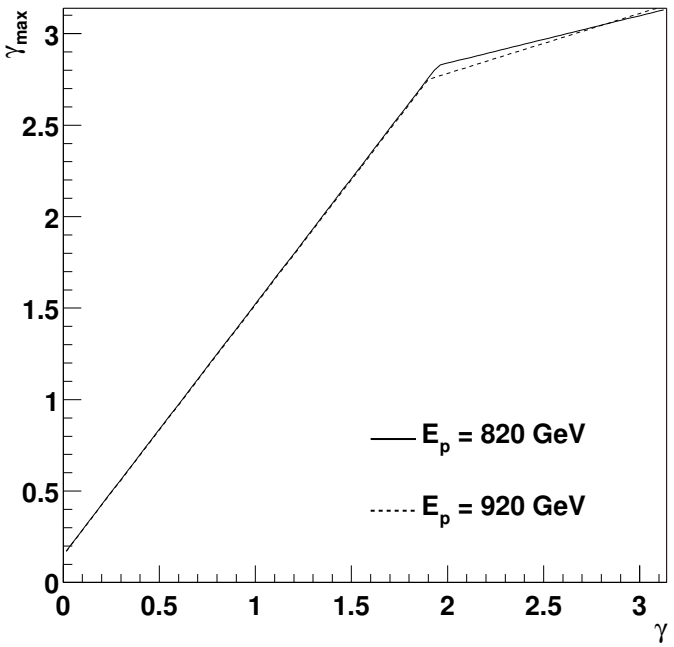

Figure 8.9: γ_{max} cut for CORANDCUT for two different proton energies $E_p = 820$ GeV and $E_p = 920$ GeV .

8.2 Improvement of the Measurement

8.2.1 Calorimeter alignment

To obtain a smooth transition between the determination of the position of the scattered lepton with the track and the calorimeter information, the CTD and the calorimeter have to be aligned. Considering the CTD as the reference system of the ZEUS detector, the calorimeter is aligned when its position relative to the CTD is the same in data and Monte Carlo simulations. Due to statistics, only the BCAL and the RCAL can be aligned. Two different methods have been developed to perform this task, one for the BCAL and another for the RCAL.

BCAL alignment

To align this calorimeter one can take advantage of the behavior of the energy measured with the calorimeter compared to the one predicted by the double angle method (see Section 7.4) for events in which the scattered lepton reaches the calorimeter close to a cell or a module gap.

Due to energy losses in the cell cracks, the distribution E_e/E_{DA} presents a dip for every crack. The measured energy E_e is affected from the energy leakage, while the predicted energy is not. Plotting this distribution as a function of the extrapolated z-position one can determine the position of each cell crack in data and Monte Carlo events.

If the BCAL is aligned along the z-axis, then the position of the dips in data and Monte Carlo simulation should be the same. These positions are calculated by fitting an inverse Gaussian distribution and extracting the mean value as shown in Fig. 8.13. The difference between the positions of the dips lies within 1 mm, therefore the conclusion is that the calorimeter is

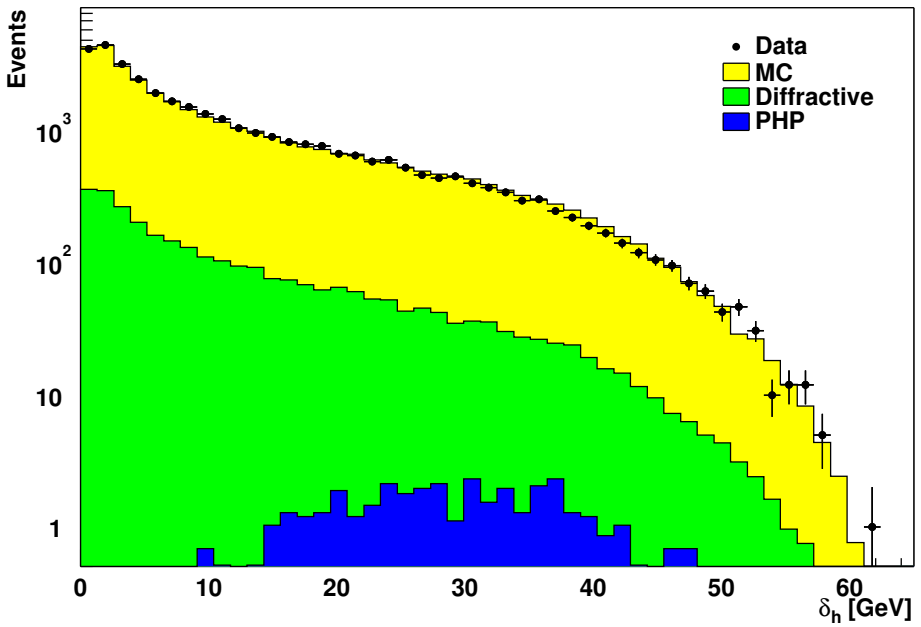

Figure 8.10: $E - p_Z$ variable for the hadronic system measured with CORANDCUT.

not shifted with respect to the CTD along the z-direction. Repeating the same procedure for module cracks, one can search for rotations of the BCAL around the z-axis. One can plot E_e/E_{DA} against the ϕ-angle determined with the track from the scattered lepton. Fitting the peaks in data and Monte Carlo distributions and comparing the obtained values, one can conclude that the BCAL is not rotated around the z-axis either within 0.01 rad.

RCAL alignment

The method used for the BCAL cannot be applied in the RCAL due to its non-projectivity. Therefore a new method has to be used.

The position of the extrapolated track is compared to the position obtained with the RHES. This is preferred since the position of the RHES is more accurate than the one estimated by the calorimeter [Kap]. The RHES and the RCAL are joined together, any shift in the RHES is also taken as a shift in the RCAL. The scattered lepton track measured with the CTD is extrapolated to the RCAL face using a swim-algorithm that takes into account the deflection of the scattered lepton trajectory due to the magnetic field. The distance between the RCAL and the RHES is only 2 cm therefore it is justified to use a straight line to extrapolate the track in this region.

The alignment parameters of each half of the RCAL with respected to the CTD are the following:

- Rotation of the RCAL around the z-axis
- shift in x, y and z

The rotation of the RCAL around the z-axis can be obtained from the slope in the variable $x_{HES} - x_{track}$ when plotted against the y_{HES} variable separately for the left and right halfs of

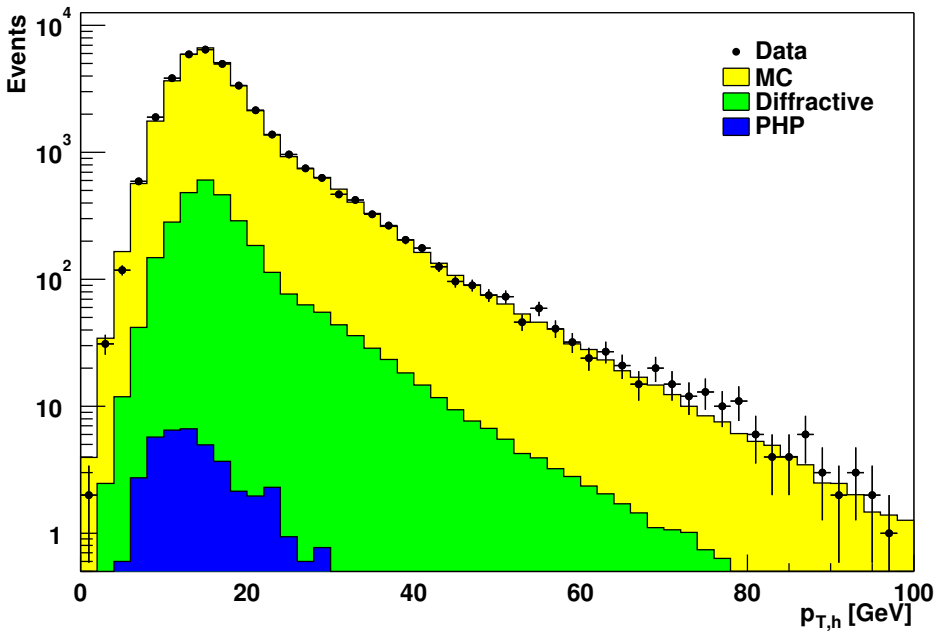

Figure 8.11: p_T variable for the hadronic system measured with CORANDCUT.

the RHES, Fig. 8.14. Fitting the slope one sees that that all values are below $\delta\phi \leq 1$ mrad except for the data in the left half where the slope is $\delta\phi = 2.4$ mrad. The rotations are done with respect to the Monte Carlo distributions, so the left RHES, and therefore the RCAL, half is rotated in data 1.7 mrad around the z axis before studying other shifts. The shift in the x variable can be measured from the offset shown by the variable $x_{HES} - x_{track}$ when plotted against the x_{HES} variable. The left and right half where fitted separately obtaining shifts $\delta x < 0.5$ mm for the Monte Carlo points. For the data one has obtained $\delta x = -1.3$ mm for the left half and $\delta x = -1.1$ mm for the right half.

The shift in the y variable is obtained from the offset of the $y_{HES} - y_{track}$ when plotted as a function of the x_{HES} variable. In this case only the relative shifts of the skis that form the RHES can be seen. No shifts were corrected in this direction.

The shift on the z variable can be obtained from the slope shown by the $y_{HES} - y_{track}$ variable when plotted against the y_{HES} variable. All these shifts are $\delta z < 1.0$ mm except for the data on the left half, in this case the RCAL is shifted $\delta z = 1.8$ mm away from the interaction point.

8.2.2 Electron vertex

One source of inefficiency in the determination of the primary vertex is its misidentification with secondary vertices. This happens in events with a lot of hadronic activity. In 3% of the cases the true vertex lies more than 15 cm apart from the measured vertex. One method to avoid this is to use the electron track, always associated to the primary vertex, as the seed-track to find the vertex. The scattered lepton track has to have a momentum higher than 5 GeV and more than 8 stereo hits to guarantee its quality [Wod99]. Using this method improves the efficiency. The number of events with the measured vertex 15 cm apart from the true one reduces to less than 1%.

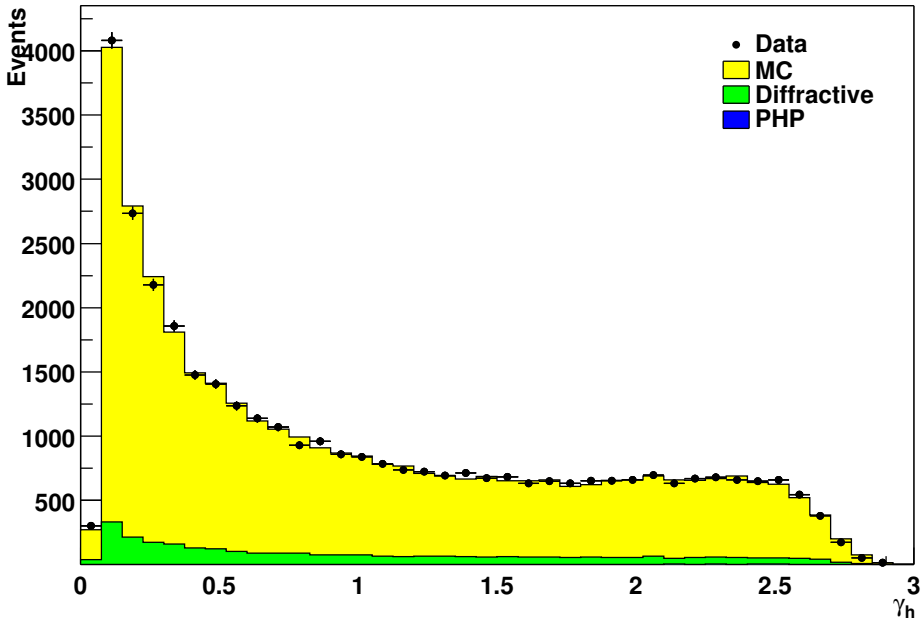

Figure 8.12: γ_h variable for the hadronic system measured with CORANDCUT.

8.2.3 Vertex reweighting

The shape of the z-vertex distribution changes from year to year due to HERA parameter tuning. Every year the distribution in Monte Carlo simulation has to be adjusted so that it describes the data.

The method to determine the correct distribution [QR98] is based on the estimation of an unbiased z vertex distribution in data. The central peak of this distribution is fitted to a Gaussian obtaining a mean value and a spread. The four satellite regions, two on each side of the peak, are subsequently fitted to Gaussian distribution with a fixed spread equal to the one obtained from the central peak fit.

The agreement between data and the Monte Carlo simulation is very good. Nevertheless, any small disagreement will lead to normalization problems in the calculation of the cross section. To avoid it, the Monte Carlo vertex is reweighted to the data [GL00]. This is done bin by bin in bins of 2 cm width. In almost all the cases the obtained weight is one. For the data sample $(e^+p)^{920}$ this reweighting is really needed since the Monte Carlo simulation of the vertex is not made specifically for these years. For the data sample $(e^+p)^{820}$ no reweighting is used.

8.2.4 Corrections to the scattered lepton energy

As seen in Fig. 8.7 the Monte Carlo description does not agree with the data. The reason may be the loss of energy due to inactive material in the scattered lepton's path from the vertex to the calorimeter. If the scattered lepton happens to reach the calorimeter close to a cell, module or calorimeter crack, then the measured energy will be affected by this. Another problem is that one or more cells that belong to the scattered lepton may have a dead PMT. This is not foreseen by Monte Carlo programs and will cause mismatch between data and Monte Carlo simulations. Several techniques [CLS98] have been developed to overcome these problems and they are described below.

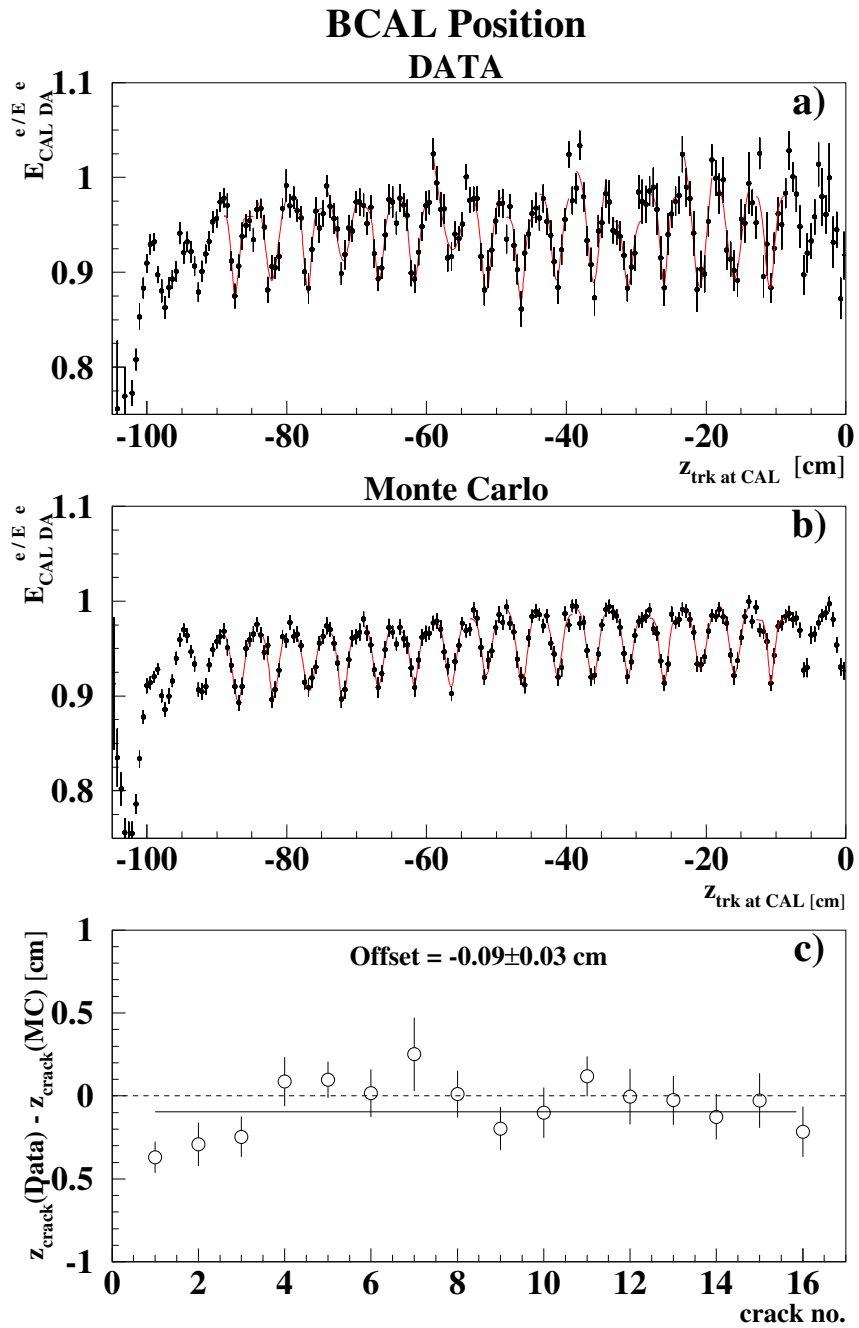

Figure 8.13: E_e/E_{DA} distribution along the z-position. Upper plot data, middle plot Monte Carlo sample. The lower plot shows the difference between the mean values of the inverse Gaussian fits for each dip. Plot taken from [Kap01]

Dead channel corrections

In the BCAL region, an algorithm has been developed to fix dead PMT's from cells associated to the scattered lepton. This algorithm is able to identify dead PMT's and fix them.

There are two approaches. One is to explore the relationship between the imbalance of the concerned cell and the imbalances of its neighboring cells and obtain a correction for the dead PMT from calorimeter information. The other is to directly calculate the imbalance of the concerned cell from CTD information. The energy of the scattered lepton measured with calorimeter is compared with the momentum of the track.

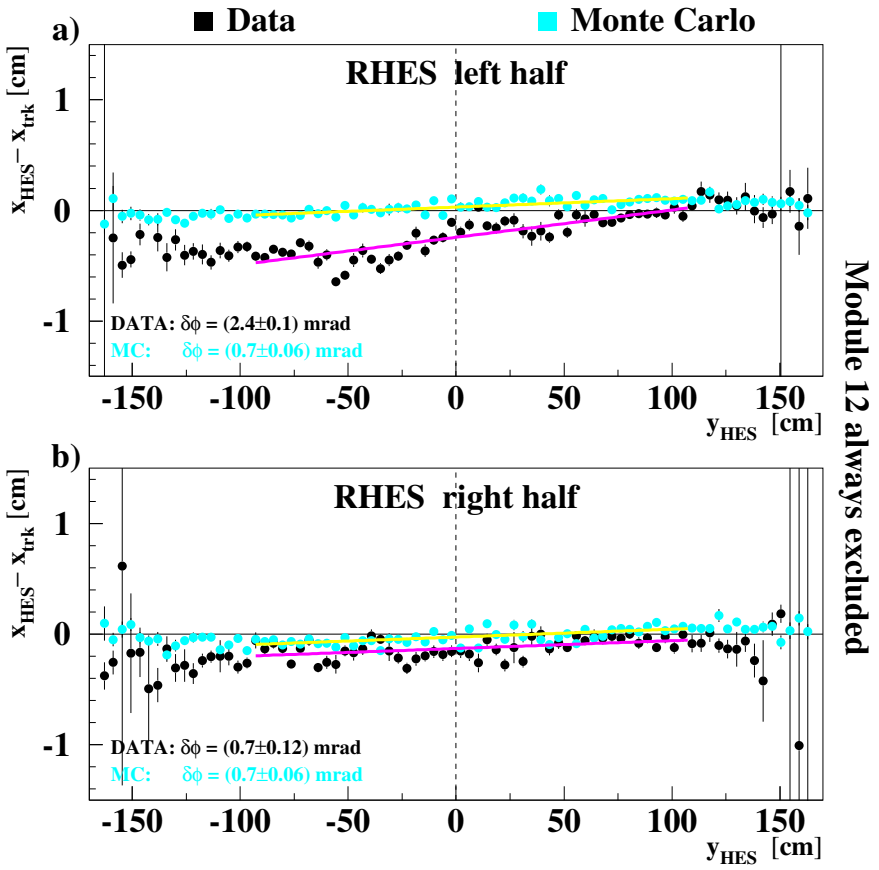

Figure 8.14: $x_{HES} - x_{track}$ plotted against the y_{HES} variable separately for the left and right halfs of the RHES. Plot taken from [Kap01].

It has been shown [CLS98] that the second method yields significantly better result for the most energetic cell in a cluster, but is inferior for other cells. Depending on that, one or the other method is used.

Dead material corrections

The scattered lepton has to travel through inactive material from the interaction point until it reaches the calorimeter. It interacts with this material loosing energy when traversing it. Two different methods, one for the RCAL/FCAL and one for the BCAL have been developed to calculate corrections for this effect. In the first method, the presampler [B+96] is used. In the second the energy is corrected using the momentum of the track [C+98] calculated with the CTD.

For highly energetic electrons/positrons traveling through small amounts of inactive material, as is the case for this analysis, the number of electrons/positrons in the shower is proportional to the energy lost by the incident electron/positron [B+96]. The presampler signals measured in MIPS are proportional to the number of electrons/positrons in the shower. These signals are therefore proportional to the energy lost by the electron/positron in the inactive material.

To use the presampler detector the proportionality constant between energy loss and the number of charged particles is measured. This is done using kinematic peak events [6] for which the

[6] see Section 7.6.

predicted energy is known (see [Tun01a]). The difference between the RCAL energy, after non-uniformity corrections (see next section), and the energy predicted by the KP method is considered to be the energy lost due to inactive material. All the procedure is made in bins of scattered lepton radius on the RCAL face. These bins are chosen so that the inactive material traversed by the scattered lepton remains constant.

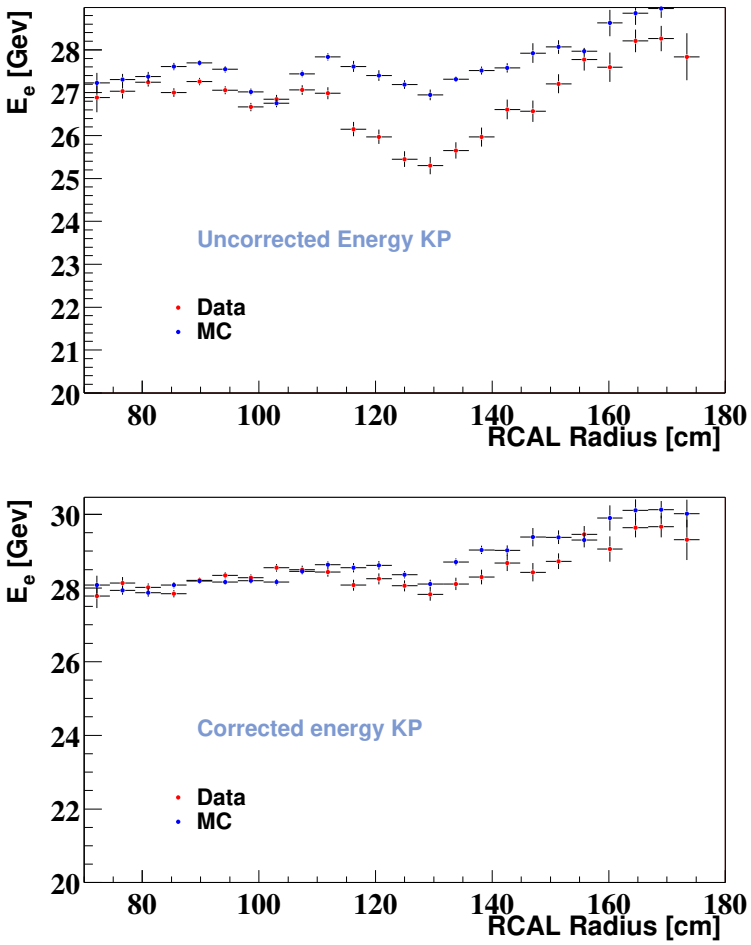

Figure 8.15: Data and Monte Carlo energies before (top) and after (bottom) dead material corrections. The energy of the RCAL scattered leptons is plotted versus the RCAL radius.

In Fig. 8.15, the uncorrected scattered lepton energy for kinematic peak events versus the radius on the RCAL face is plotted for data and the Monte Carlo sample. It can be seen that the data and the Monte Carlo points are in disagreement especially for radius $\geq$ 110 cm. In the lower plot one can see the energy after corrections. Now data and Monte Carlo points agree better within the errors.

The energy of the scattered lepton in the BCAL can be corrected using the momentum of its track. The advantage of this method is that the measurement of the momentum of the track and of the calorimeter energy are independent. Another advantage is that when the momentum of the track is measured, the scattered lepton has not traveled through as much dead material as when it reaches the calorimeter. For the BCAL energy correction the momentum of the track is considered as the "true" energy of the scattered lepton.

The energy loss due to dead material in front of the BCAL is parameterized in terms of the

momentum of the track and its angle [CLS98].

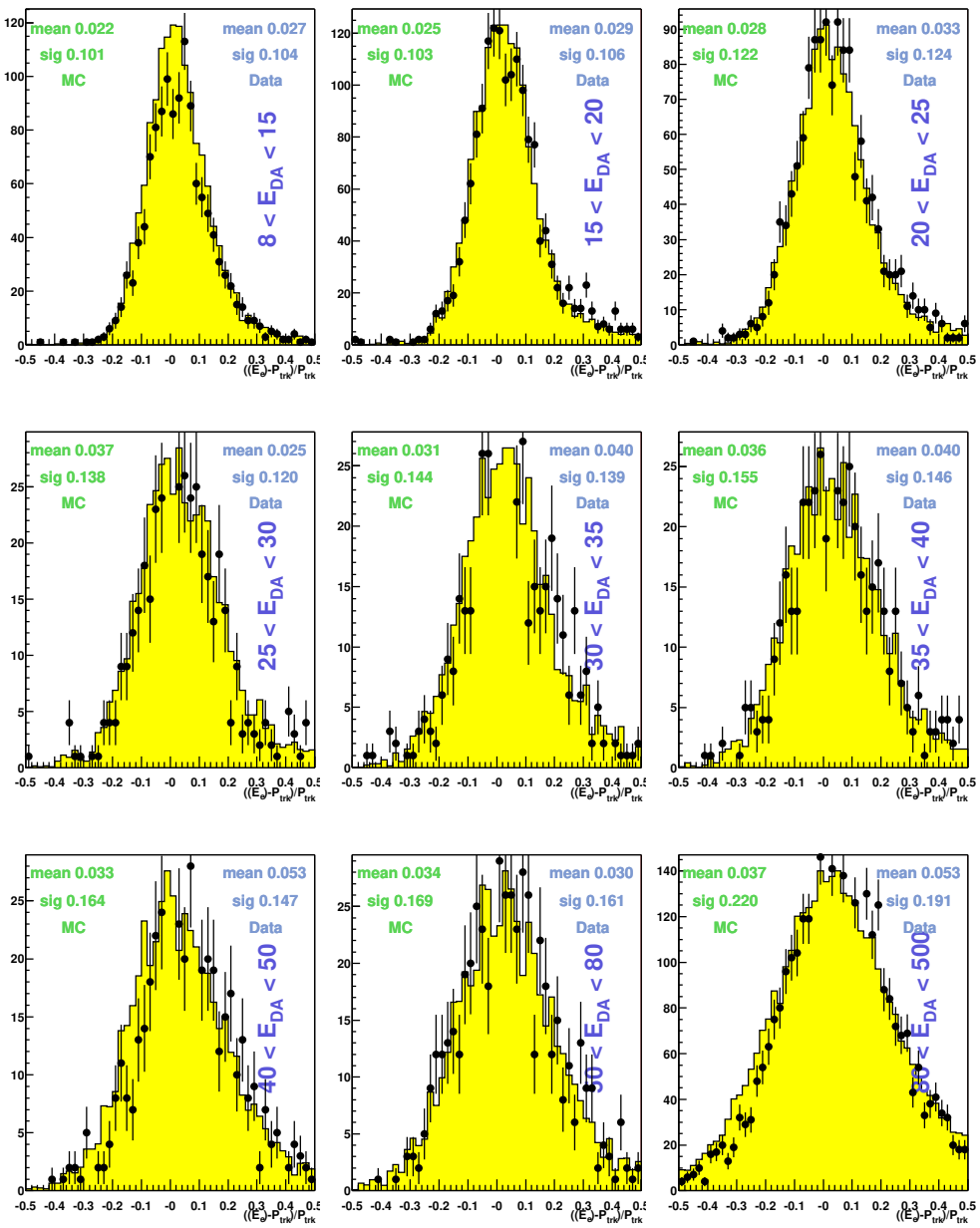

Figure 8.16: Comparison of the corrected energy in the BCAL with the momentum of the track in bins of E_{DA}.

Figure 8.16 shows a comparison of the measured energy and the momentum of the track in bins of the scattered lepton energy calculated with the double angle method. It can be seen that there is good agreement between data and Monte Carlo distributions for all the bins in energy. This shows that the calculated corrections work properly.

The effect of the corrections is to shift the measured energy towards the "true" energy, and to improve the resolution.

Non-uniformity corrections

In the studies of the calorimeter alignment the behavior of the E_e/E_{DA} distribution in the neighborhood of a cell or a module crack has been shown. The dip that appears in the distribution, although very useful to align the calorimeter, is an unwanted feature when trying to obtain the true energy of the scattered lepton. Another problem is also that the Monte Carlo simulation is not able to fully describe the data in this regions. Corrections for non-uniformities in the calorimeters have been calculated for RCAL and BCAL separately. In the FCAL, there is not enough statistics to measure any effect.

As for the alignment, the dips and peaks have been fitted to Gaussian distributions to obtain a parameterization that yields a correction different for data and Monte Carlo samples. This corrections have been calculated as a function of the position of the scattered lepton with respect to the cell or module gap. In the BCAL the position of the scattered lepton is taken from the track [C+98], while in the RCAL the position is taken from calorimeter information [Def99]. Since the track measurement does not suffer itself from non-uniformities in the calorimeter, the corrections in the BCAL are better than the ones in the RCAL. In the upper plot of Fig. 8.17

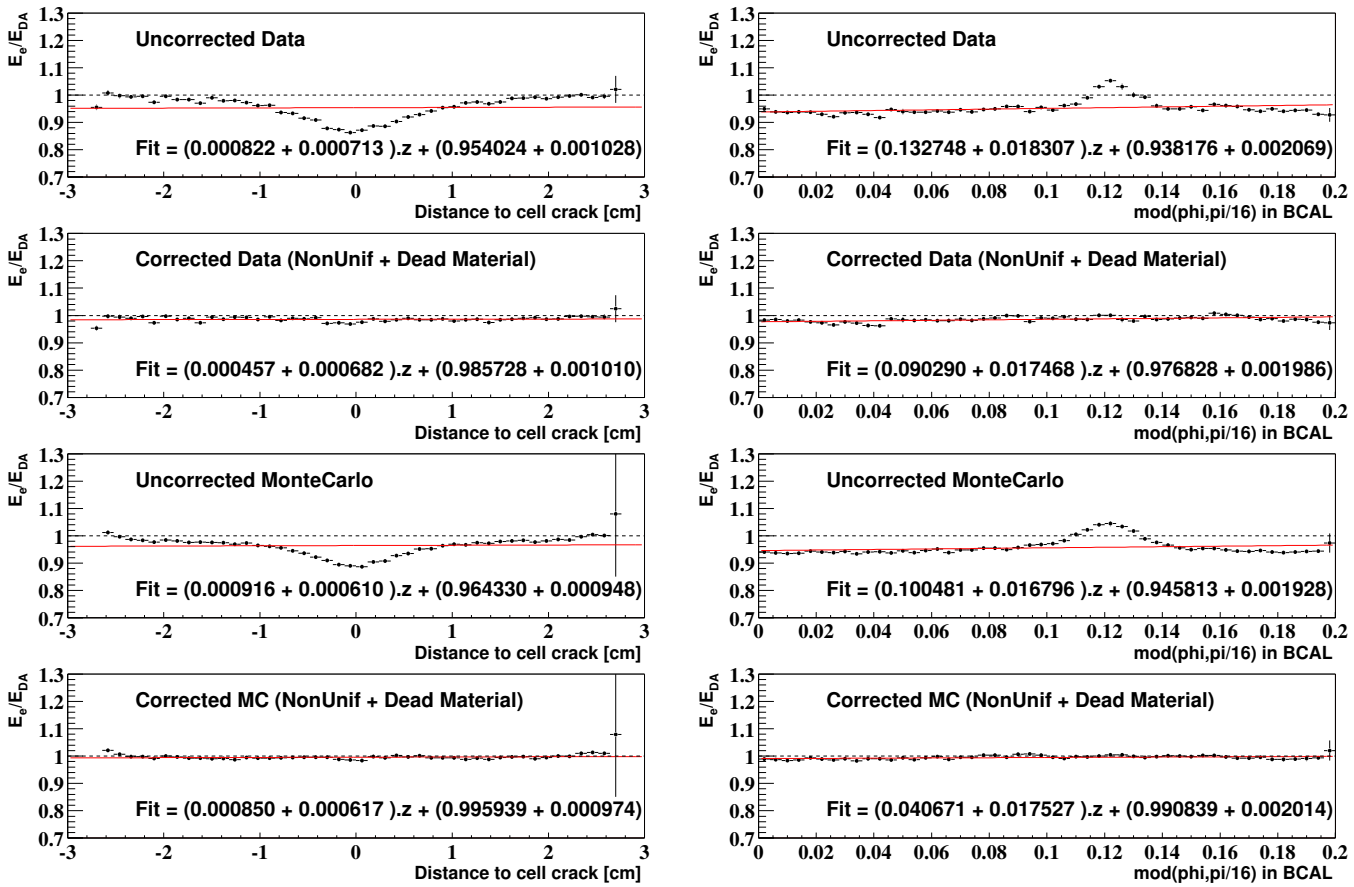

Figure 8.17: Non-uniformity corrections for cell gaps (left) and module gaps (right) in the BCAL. The two upper plots represent the data before and after non-uniformity corrections. The two lower plots are for Monte Carlo simulation. After corrections the energy loss/gain in the gap has disappeared and the Monte Carlo simulation is able to describe the data within 1%.

the distribution E_e/E_{DA} is plotted as a function of the distance to the cell crack (left) and the module crack (right) in the BCAL. In the upper plot the data without corrections is shown.

The dip corresponds to scattered leptons hitting the crack between the cells. The next plot shows the data after non-uniformity and dead material corrections: now the dip is gone and the data lies closer to the nominal value $E_e/E_{DA} = 1.0$ than before. In the lower half of the plot, the same plots for Monte Carlo points are shown. Is should be noticed that data and Monte Carlo points come closer together after the corrections.

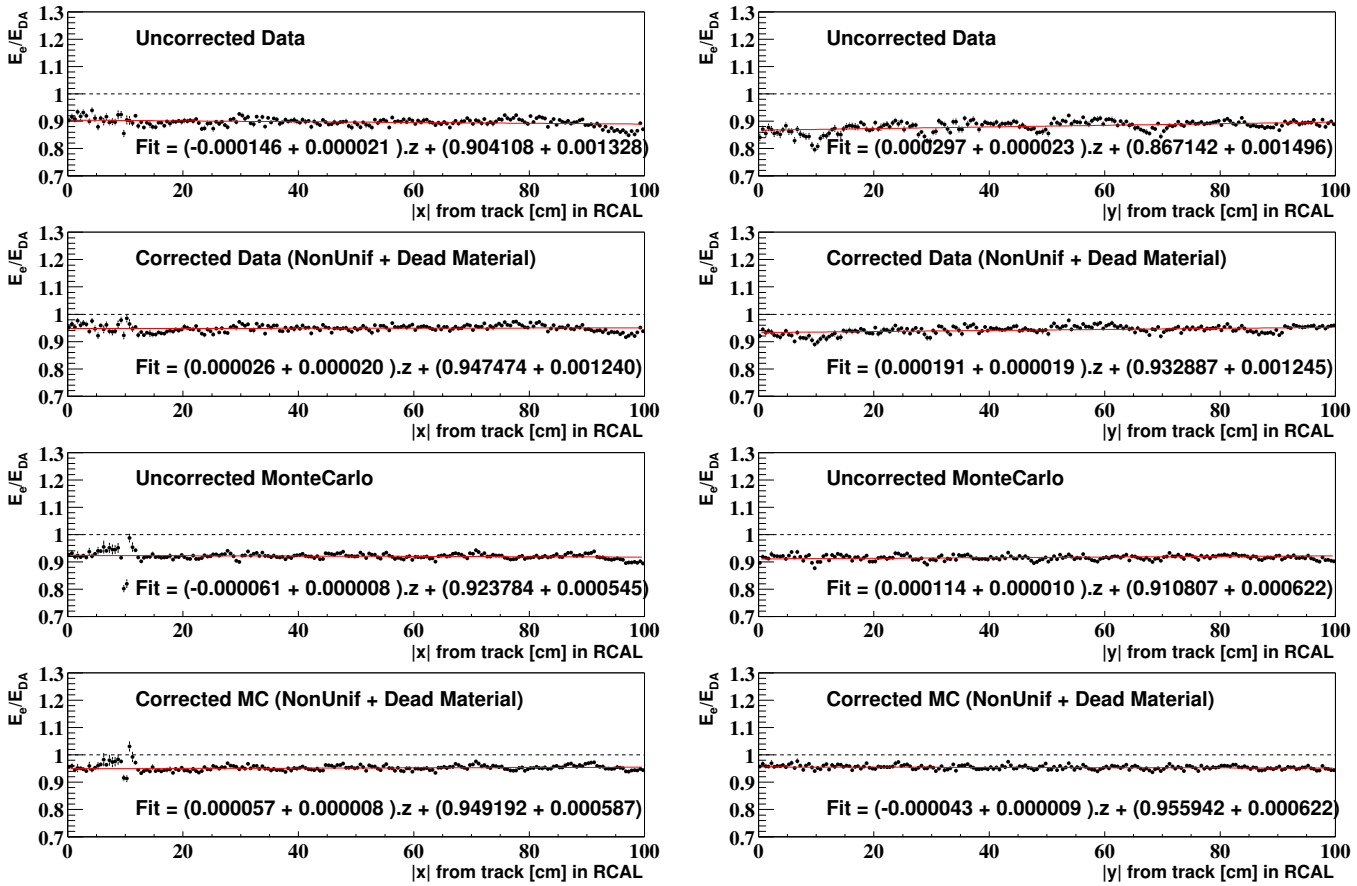

Figure 8.18: Non-uniformity corrections along the $|x|$ (left) and $|y|$ (right) variables measured with the track in the RCAL. The two upper plots present the data before and after non-uniformity corrections. The two lower plots are for Monte Carlo simulation. After corrections the energy loss in the gaps has disappeared and the Monte Carlo simulation is able to describe the data better.

In the left plot of Fig. 8.18 the distribution E_e/E_{DA} versus $|x|$ in the RCAL is plotted. Starting from the top, the first plot presents the uncorrected data. The E_e/E_{DA} value is different from one and towards the beginning and the end of the calorimeter the value of E_e/E_{DA} is ca. 0.8. After non-uniformity and dead material corrections E_e/E_{DA} gets closer to one and the distribution becomes flatter. On the lower half the Monte Carlo distribution is shown. The distribution before corrections is already flatter than the data, and after corrections the value E_e/E_{DA} is also closer to one. After corrections the Monte Carlo simulation is able to describe the data better than before.

On the right side of Fig. 8.18 one can see E_e/E_{DA} versus $|y|$ in the RCAL. Following the same scheme as in the preceding plots, the upper one is uncorrected data. This time the cracks between the modules are easy to recognize. These cracks are gone, as expected, when applying the non-uniformity corrections (second plot). In the Monte Carlo sample (next plot) the

cracks between modules cannot be identified as clearly as in the data. This means that before correction the Monte Carlo points are not able to fully describe the data. After corrections the situation improves leading to a better agreement between data and Monte Carlo samples as seen from the fits.

Monte Carlo energy smearing

After all corrections the measured energy simulated with Monte Carlo generators is able to describe pretty well the data as seen in Fig. 8.19. Nevertheless there are still small differences.

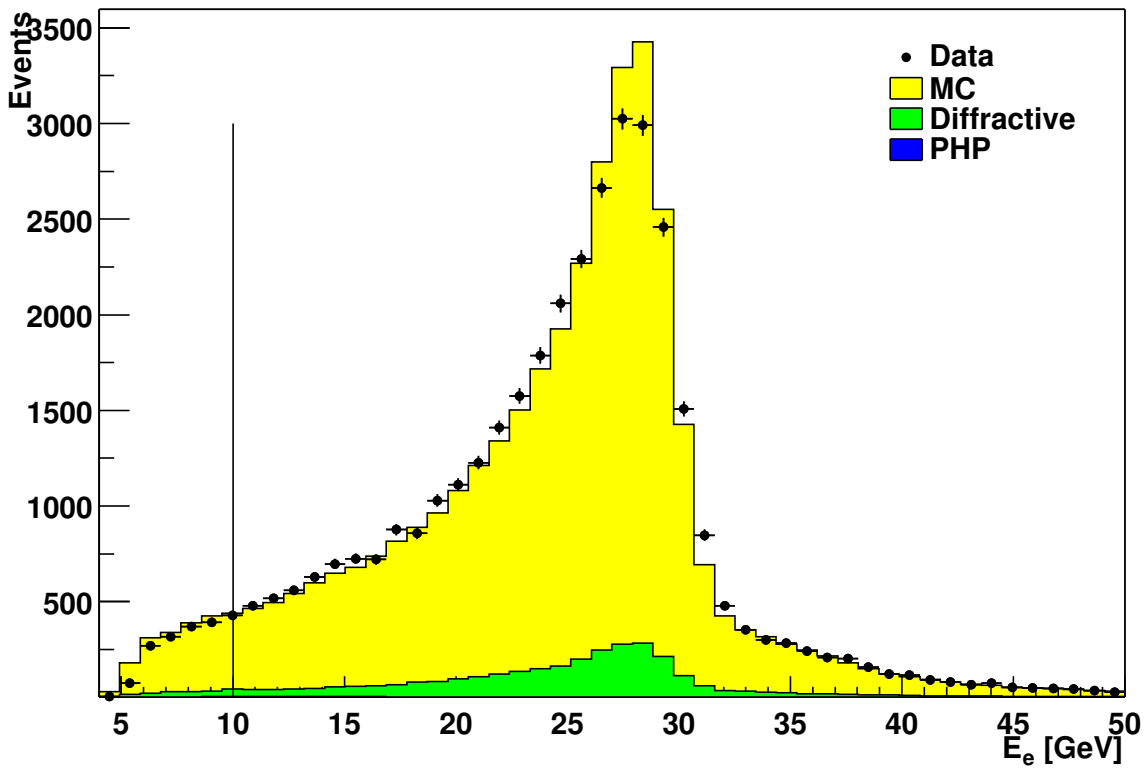

Figure 8.19: Scattered lepton energy after dead material and non-uniformity corrections. The vertical line shows the analysis cut by $E_e = 10$ GeV .

Although the peak of the distributions is for data and Monte Carlo distribution in the same position, the Monte Carlo histogram seems to be narrower than the data. To solve this problem a smearing to the Monte Carlo energy has been applied. This method consists in applying a random constant smearing to the measured energy, after corrections, in Monte Carlo simulation. The formula used for the smearing is:

$$E_e = E_e + N_{rand,gauss} C E_e.$$

Where $N_{rand,gauss}$ is a random number, between zero and one, generated with a Gaussian distribution, and C is a constant number that has to be calculated. To calculate C several bins in E_e have been made. In each bin the distribution E_e/E_{DA} for data and Monte Carlo distributions is fitted to a Gaussian. The plots of these distributions can be found in Appendix B. The sigma from the Gaussian fit for data and Monte Carlo distributions can be seen in Fig. 8.20: it is

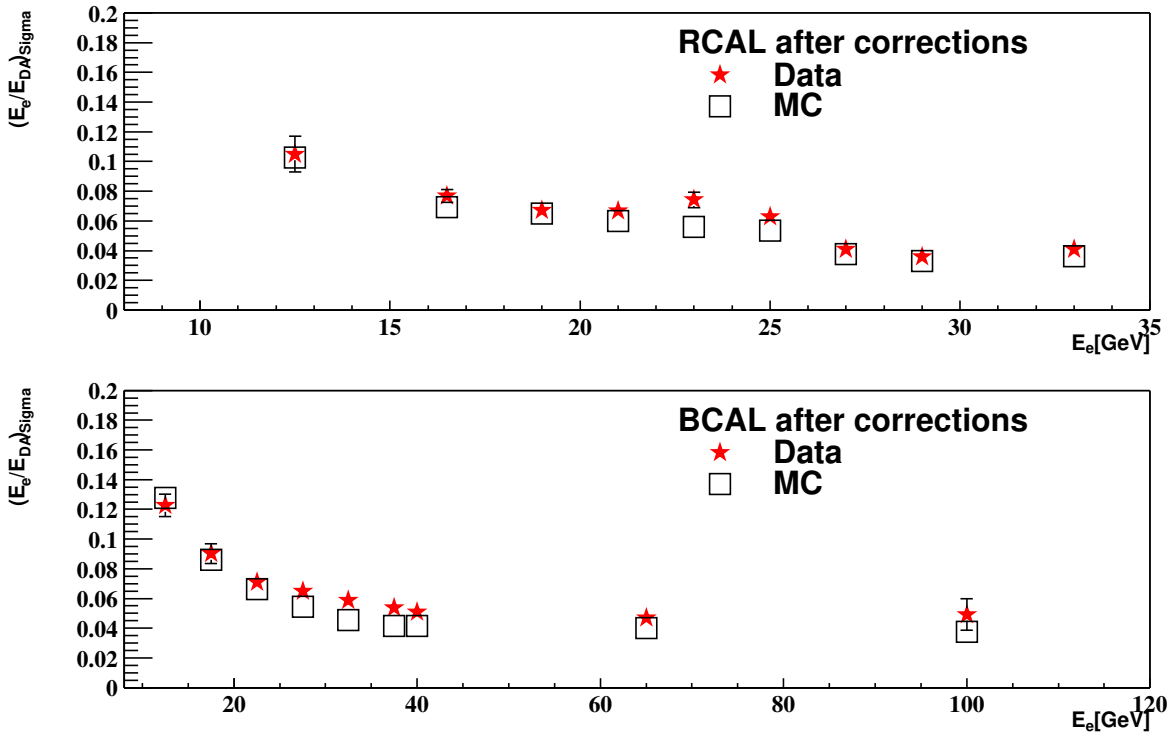

Figure 8.20: Sigma from Gaussian fit of the distribution E_e/E_{DA} (Gaussian distributions can be found in Appendix B). The upper plot shows the results for the RCAL. The lower plot for the BCAL.

bigger for low energies, and decreases with the energy. Except for the first point in the BCAL, the sigma for the data is bigger than for the Monte Carlo simulation.

In the next step the quantity $\sqrt{\sigma^2_{data} - \sigma^2_{MC}}$ is calculated and plotted against E_e. This is then fitted to a constant (Fig. 8.21) that is the value C we need to smear the Monte Carlo energy. In the BCAL (lower plot), the point for the lowest energy is placed at zero since the sigma of the data was greater than for the Monte Carlo distribution. The study has been done independently for the RCAL and the BCAL, obtaining the values $C_{RCAL} = 0.018$ and $C_{BCAL} = 0.03$.

Applying the smearing the Monte Carlo distribution becomes broader, describing the data better as seen in Fig. 8.22 compared to Fig. 8.7.

8.3 Backgrounds

After all selection cuts there is still a small residual sample of background events. The estimation of this background is very important, especially in regions of low statistic where the background events could represent a sizable fraction of the events.

8.3.1 Photoproduction background

Photoproduction events are events with Q^2 close to zero, in which although the scattered lepton escapes the calorimeter undetected, an electromagnetic particle in the hadronic shower fakes it.

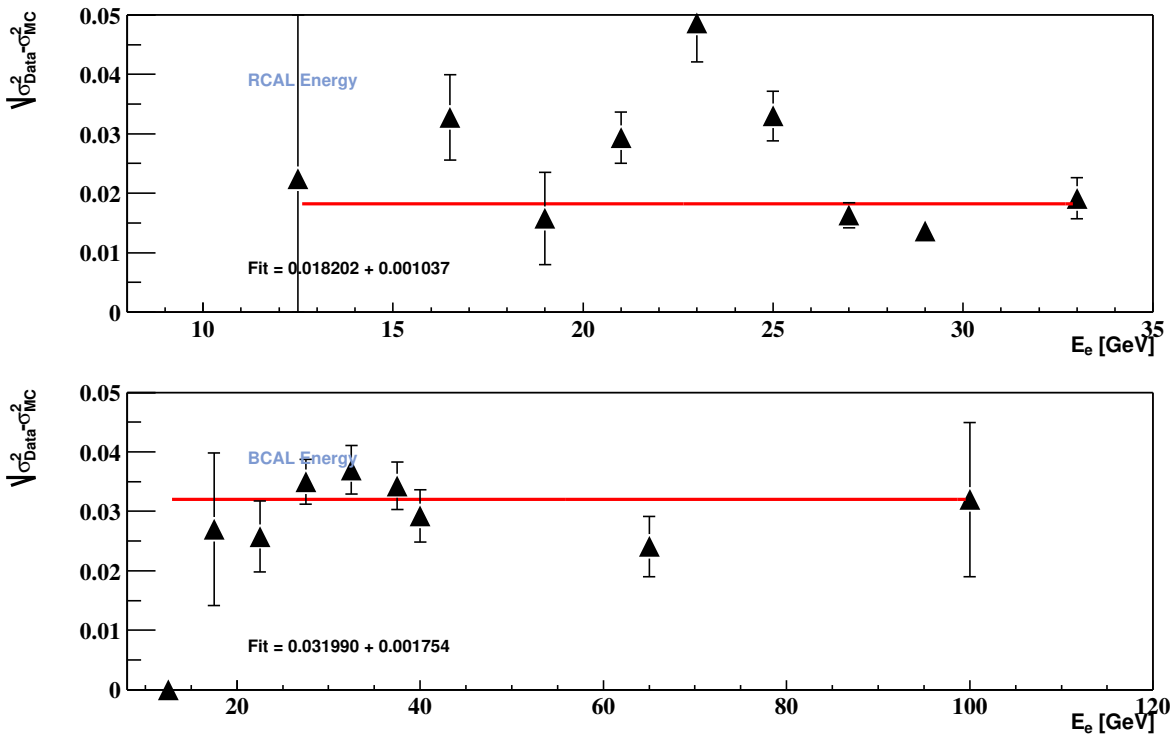

Figure 8.21: Calculation of the smear constant for RCAL and BCAL. See text for details.

The majority of this PHP events can be rejected with the $\delta \geq 38$ GeV cut. Nevertheless some PHP events remain in the sample and have to be subtracted statistically from the sample. The method to estimate the PHP background is using a Monte Carlo simulation.

8.3.2 Beam induced background

The proton and lepton beams can interact with a gas particle in the detector giving rise to a fake DIS event. The interaction can happen outside or inside the detector. Timing cuts, already included in the trigger, can be used against interactions happening outside the detector. To estimate the beam background for interactions happening inside the detector, proton and lepton pilot bunches are used. For this purpose the number of events that pass the final DIS selection and originate from proton or lepton pilot bunches is determined and scaled with the ratio of the currents in the paired and unpaired (pilot) bunches (see Section 9.7.3).

8.3.3 Cosmic and halo muons

Cosmic rays converting to muons in the upper atmosphere can produce fake physics events in the detector. These events are easy to identified since they produce an up-down path in the calorimeter, leaving at most two tracks in the CTD. Cosmic muons are already rejected at trigger level with a time cut. Nevertheless there are a few number of events which shower in an electromagnetic cell giving rise to fake high Q^2 events. To remove those an off-line cut is placed on the ratio of the transverse momentum P_T to the square root of the transverse energy E_T. This cut, $P_T/\sqrt{E_T}$, is used to remove cosmic events by requiring P_T balance for low E_T events (see Fig. 8.23).

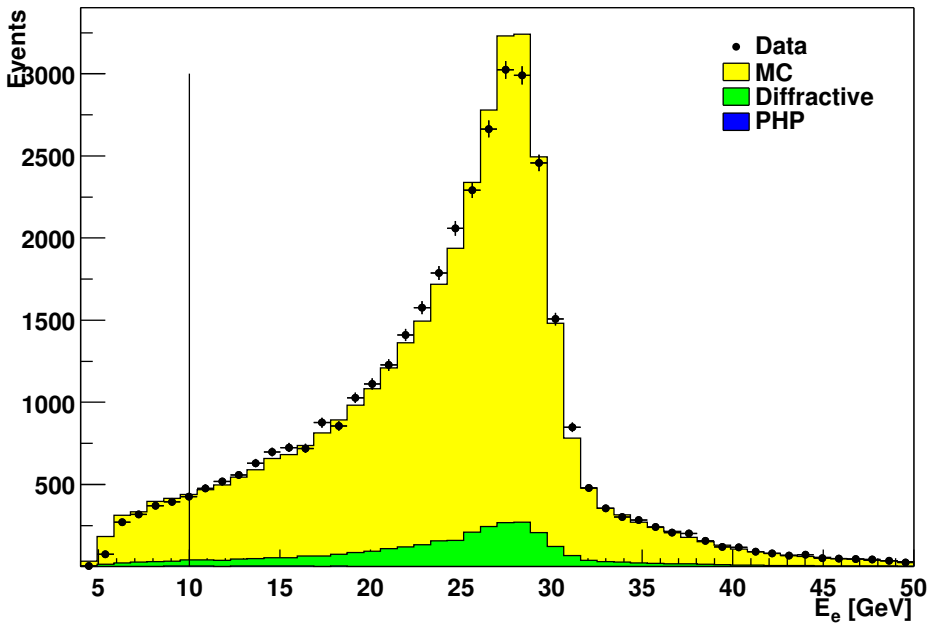

Figure 8.22: Energy of the scattered lepton after dead material and non-uniformity corrections, and smearing. The vertical line shows the analysis cut $E_e = 10$ GeV .

8.3.4 QED-Compton events

QED-Compton events are treated as background because they are not well simulated in Monte Carlo programs and cause large Q^2 migrations. The QED-Compton cross section peaks close to zero Q^2. Generally the scattered lepton and the photon are found at very high angles with respect to the beam direction. If both momenta are used to reconstruct the Q^2, then the value is found to be close to zero. If, on the contrary, only the scattered lepton is used, then a much higher value is obtained. Since these events have usually low Q^2 values, they do not contribute to the structure function $xF_3(x, Q^2)$, but represent a background source if reconstructed at higher Q^2 values.

8.4 Event Properties and Summary of Cuts

8.4.1 On-line event selection

The combination of FLT, SLT and TLT described in Section 8.1.1 is listed below:

- FLT Slots:
  - FLT 28 High Q2 high ET, or
  - FLT 30 RCAL Iso E, or
  - FLT 40 Total EMC, or
  - FLT 41 High ET, or
  - FLT 43 High ET and good track, or

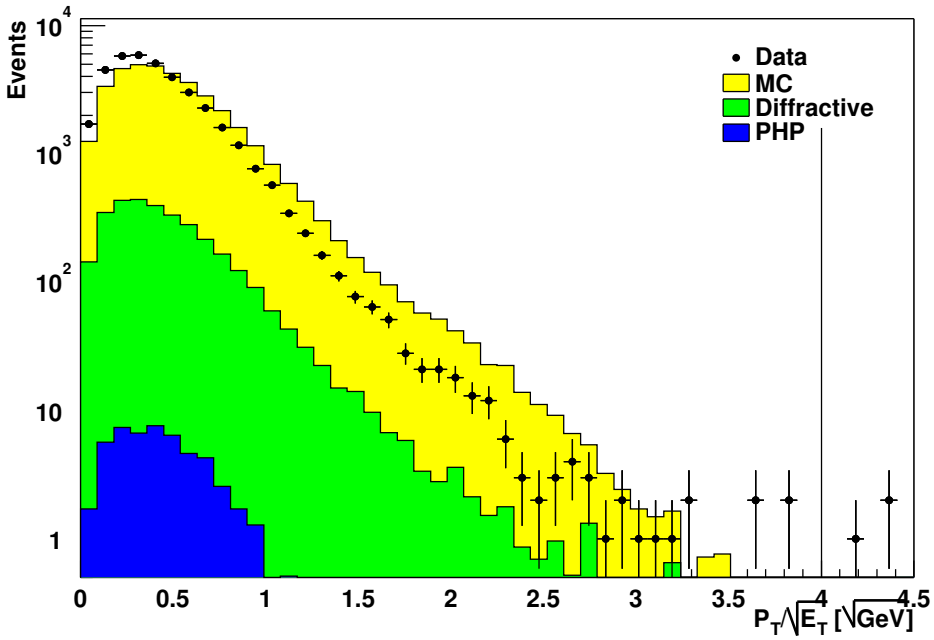

Figure 8.23: $Pt/\sqrt{Et}$ distribution. Events with $Pt/\sqrt{Et} > 4.0$ are most probably cosmic events. In this region, as expected, no Monte Carlo events can be found.

  - FLT 44 REMC or BEMC, or
  - FLT 46 RCAL Iso E

- SLT DIS06
- TLT DIS04

8.4.2 Off-line event selection

Additional off-line cuts are applied to improve the purity of the sample. The cuts are listed below

Vertex Cut

As seen in Section 8.2.3, the simulation of the shoulders of the z-vertex is not perfect. Therefore for this analysis only events that are in the central peak are taken. A cut on the z-vertex is placed: $|Vtx_z| < 50$ cm.

$E - p_Z$ cut

Deep inelastic scattering events conserve the $E-p_z$ variable. To ensure a pure sample of neutral current events and reduce the PHP background, a cut on the $E-p_Z$ variable ($E-p_Z > 38$ GeV) is placed. The contamination of PHP background is bigger for lower angles of the scattered lepton. To reject these events outside the CTD acceptance in the FCAL region the lower cut is raised to $E - p_Z > 44$ GeV . An upper cut $E - p_Z < 65$ GeV is used to reduce beam gas background.

Scattered lepton cuts

Several cuts are applied to the scattered lepton found by SIRA5:

- A probability cut: only electromagnetic candidates with a probability $P_e \geq 0.9$ are taken.

- A corrected energy cut: To select a region in which the efficiency of the electron-finder is high [VS00] a cut on the corrected scattered lepton energy, $E_e > 10$ GeV is applied.

- A y_e cut: Another cut to reduce PHP background is the one performed on y_e. Since PHP background concentrates mainly on the high y region, only events with $y_e < 0.95$ are selected.

- It has been shown [VS00] that for some events the electromagnetic candidate is found inside a jet. To avoid these events an η-ϕ cone of radius $R = 1$ around the candidate is built. If the energy inside the cone not belonging to the candidate is greater than 5 GeV ($E_{in\,cone\,not} > 5$ GeV) then the event is rejected.

- Calorimeter super-cracks cut: due to the poor Monte Carlo simulation of the energy leakage in calorimeter super-cracks, these regions are excluded. Another reason to exclude them is the loss of efficiency [VS00] of the electron-finders in these regions. These regions are defined as:

$$125\,\text{cm} \leq R_e \leq 126\,\text{cm} \begin{cases} -90.0\,\text{cm} > z > -110.0\,\text{cm} & : \text{ RCAL side} \\ 174.0\,\text{cm} < z < 162.5\,\text{cm} & : \text{ FCAL side} \end{cases} .$$

  An extra cut [Mor01] has been applied to the scattered lepton radius on the RCAL face

$$R < 175\,\text{cm}$$

  .

- A chimney cut: the chimney is an empty region in the RCAL situated at $|x| < 12$ cm and $y > 90$ cm that contains all the CTD cabling [Col93]. The Monte Carlo simulation is not able to describe the chimney in the RCAL, therefore this region is also excluded in this analysis.

- Track requirement cuts: In the CTD acceptance region the scattered lepton is required to have a track. This track has also to fulfill some quality criteria in order to reduce PHP background: the distance of the extrapolated track to the calorimeter face and the calorimeter cluster have to be within 10 cm ($DCA < 10cm$), and the momentum of the track has to be greater than 5 GeV ($P_{track} > 5$ GeV).

- PHP rejection cuts outside CTD acceptance region: Outside the CTD acceptance region towards the FCAL the transverse momentum of the scattered lepton has to be greater than 30 GeV, $P_T > 30$ GeV.

Kinematic cuts

The double differential cross sections are measured starting at $Q^2 \geq 185$ GeV^2 . The single differential cross sections $d\sigma/dx$, $d\sigma/dy$ and $d\sigma/dQ^2$ are measured for $Q^2 > 200$ GeV^2 , $d\sigma/dx$ is also measured for $Q^2 > 10000$ GeV^2 . $xF_3(x, Q^2)$ is extracted for $Q^2 \geq 1500$ GeV^2 .

All the control plots shown in this chapter and following have been made with a $Q^2 > 200$ GeV^2 cut.

The cut $y(1 - x)^2 \geq 0.004$ is applied since outside this region the Monte Carlo simulation is not able to describe the radiative cross section properly [KSM92].

Valid *ep* bunch

Only events resulting from a valid *ep* collision are considered in the analysis, thus the luminosity is only calculated for these events. Figure 8.24 shows the bunch structure for a run. The small gaps are reserved for the unpaired lepton and proton bunches, the larger gaps accommodate the empty bunches.

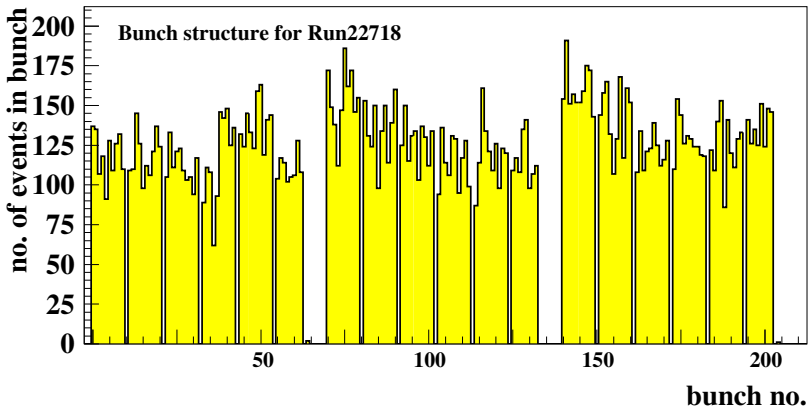

Figure 8.24: Bunch structure of run 22718 for paired bunches. The small gaps are reserved for the unpaired lepton and proton bunches, the larger gaps accommodate the empty bunches. Plot taken from [Rus00].

Chapter 9

Systematic Studies

This chapter is dedicated to the study of those effects, related to the detector, Monte Carlo simulation, background, energy scales, etc, that may distort the measurement. The level of understanding of such effects will be quoted as a systematic uncertainty in the measurement. Along this chapter the procedure to extract these uncertainties will be explained. These studies have been done on the $e^{-}p$ data sample, see footnote 1.

9.1 Monte Carlo Simulation Studies

In this section the trigger efficiency studies and the systematic uncertainty associated to the reweighting of the vertex will be illustrated.

To select NC events, every event has to pass the trigger chain, FLT, SLT and TLT described in Section 8.1.1. The three level trigger is also simulated in Monte Carlo programs so that Monte Carlo events can be selected in the same way as the data.

It has also been mentioned (see Section 8.2.3) that the shape of the event vertex has to be determined each year for the Monte Carlo simulation. The effect on the cross section introduced by changing the shape of the vertex will be studied.

9.1.1 Trigger studies

A difference in the trigger efficiency between data and Monte Carlo samples would directly affect directly the cross section measurement and should be corrected for. The most critical selections in the trigger chain are made in the FLT and thus the studies focus on the efficiency of the FLT slots.

The event sample used to study a given slot has been obtained independently of that slot. The efficiency of the trigger slot is estimated as the percentage of events in the independent sample that pass the trigger requirements. This efficiency is usually studied as a function of relevant off-line quantities [Kap01].

RCAL triggers

For the FLT RCAL triggers, the independent slots are the BEMC and the high E_T FLT slots, with the additional requirement to have a scattered lepton in the RCAL.

The efficiency of the RISOe trigger has been calculated as a function of the measured energy after corrections E_e of the scattered lepton and its radius the RCAL on face R_e (Fig. 9.1). In general, there is good agreement between data and Monte Carlo samples for both distributions.

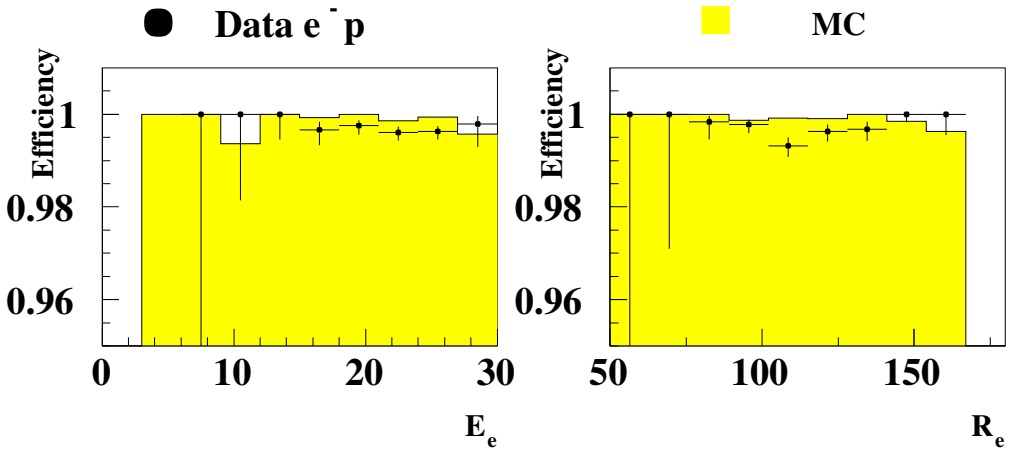

Figure 9.1: Efficiency of the ISOe trigger as a function of the scattered lepton energy E_e and its radius the RCAL face R_e. Plot taken from [Kap01].

The efficiency of the REMC trigger is again calculated as a function of E_e and R_e. For $R_e \leq 160$ cm the data and Monte Carlo efficiencies are a high as 100%. The agreement between data and Monte Carlo results for both variables is good.

BCAL triggers

To check the efficiency of the FLT BCAL triggers, the independent sample was obtained from the high E_T trigger with no other requirements. The efficiency in this case is calculated as a function of the corrected energy E_e and the z-position of the lepton scattered in BCAL (Fig. 9.2). Data and Monte Carlo results agree well within errors and the efficiency is high for all the energies under consideration and even the whole z range in the BCAL.

9.1.2 Vertex reweighting

In the procedure to calculate the unbiased vertex (see Section 8.2.3) the z interval of $[-100, 100]$ cm was divided in three regions in which different cuts were applied. The selection efficiency [GL00] for each of the regions was calculated. Each distribution was afterwards normalized by this efficiency to obtain the final vertex distribution for the entire z-range.

The systematic uncertainty associated to Monte Carlo vertex reweighting has been obtained varying the selection efficiency in the satellite regions. The efficiency of the central peak is fixed by the to overall normalization.

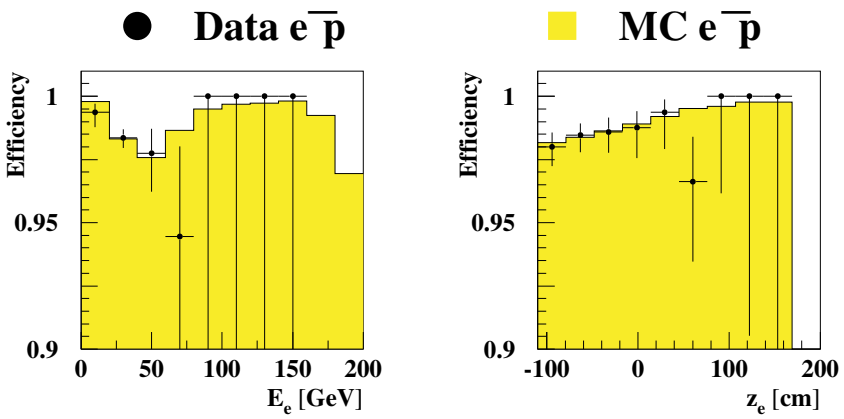

Figure 9.2: Efficiency of the BMC trigger as a function of the scattered lepton energy E_e and its z-position along the BCAL. Plot taken from [Kap01].

Calling region 1 and 2 the satellite regions towards negative and positive values of z $[-100, -50]$ cm and $[50, 100]$ cm respectively, one is left with four different possibilities to vary the normalization. Both regions up, region 1 up and 2 down, region 1 down and 2 up, and both down. Doing this the Gaussian fit changes giving rise to a new set of Monte Carlo weights.

The systematic uncertainty is extracted from the different results obtained with different Monte Carlo weights.

9.2 Scattered Lepton Finding Efficiency

The electron-finder SIRA 5 has been chosen in this analysis to find the scattered lepton inside the calorimeter (see Section 8.1.4). In order to obtain a reliable result in the measurement of the cross section, the performance of the algorithm should be the same in data and Monte Carlo events.

Two studies have been made to investigate the efficiency of the electron-finder. The first compares the data and Monte Carlo results.

As explained in Section 8.1.4, SINISTRA95 has been optimized for a small region of the calorimeter. The second study, done only with Monte Carlo events, shows that the efficiency of SIRA 5 is high for all the calorimeter regions.

9.2.1 Efficiency in data and Monte Carlo events

When trying to study the performance of an electron-finder in data and Monte Carlo events, one should be able to tag the scattered lepton independently of the algorithm.

Having a look at the event shown in Fig. 8.1 one can see that the scattered lepton has left a track in the CTD well isolated from the hadronic jet. This is always the case provided the event has high E_T, in this case both the scattered lepton and the hadronic jet are contained in the CTD and opposite to one and other. The efficiency of the electron-finder for both data and Monte Carlo events can be quoted as the fraction of events for which the isolated track is identified as the scattered lepton.

The sample of high E_T events has to be selected with a trigger combination which is independent of electron-finders. The trigger chain chosen for this study consists of a FLT, SLT and a TLT slot. The FLT slot requires the calorimeter transverse energy to be greater than 11.6 GeV and a track to be found. Since the scattered lepton energy must be balanced in transverse energy with the hadronic system, this transverse energy cut selects all scattered leptons in the tracking acceptance above $11.6/2 = 5.8$ GeV. The second level trigger only requires a loose $E - p_z$ cut. The third level trigger requires a calorimeter transverse energy greater than 25 GeV: the choice of this trigger is made in such a way that it is independent of any electron-finder.

After obtaining the triggered sample two additional cuts are made. First a tighter cut is applied on the $E - p_Z$ variable 44 GeV $\leq E - p_Z \leq$ 65 GeV. It is also required that the electromagnetic energy within the first inner ring around the rear beam pipe ($\approx$ 70 cm) be less than 0.464 GeV, to ensure that the scattered lepton is inside the CTD acceptance.

From the remaining sample only events with high momentum isolated tracks are used for this study. The selection of such events is done in two steps. In the first one, only events with at most one isolated track are selected. In the second one, tight cuts are made to ensure the isolation of the track.

In the first iteration events with at most one isolated track with momentum $P_{trk} \geq 4.0$ GeV are selected. To fulfill the requirement of isolation no other track with $P_{trk} \geq 0.5$ GeV has to be within 90^0 in Θ and ϕ from the isolated track.

Afterwards a tighter isolation cut is applied to the remaining events. No other track with momentum $P_{trk} \geq 0.1$ GeV can be found within 30^0 in Θ and ϕ from the selected track.

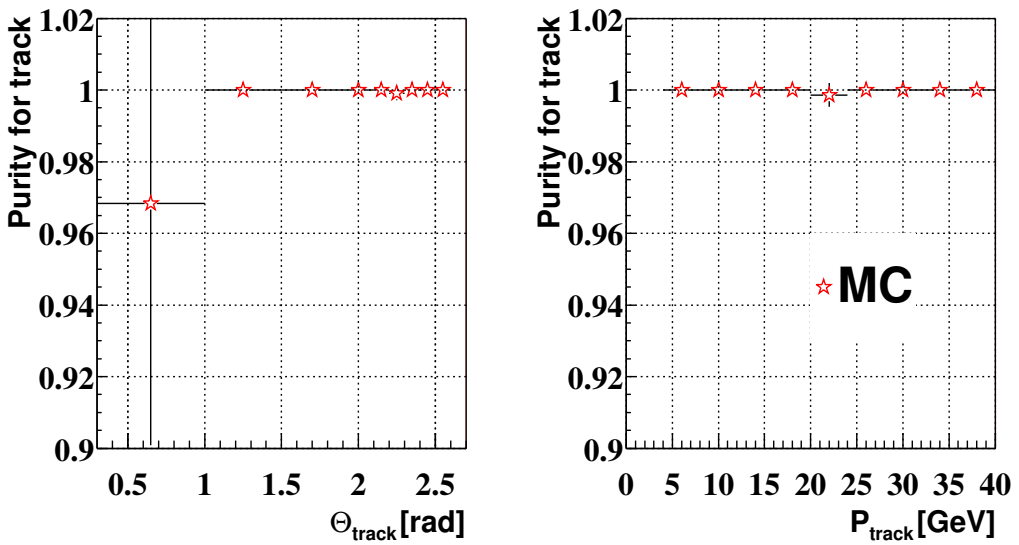

Figure 9.3: Purity of the sample of well isolated tracks. In more than 99.9% of the cases the isolated track coincides with the scattered lepton.

The purity of the sample of events with isolated tracks can be tested using Monte Carlo events: the track is considered correctly identified if it lies within 30^0 in Θ and ϕ from the scattered

lepton. In Monte Carlo simulations the scattered lepton can be easily tagged since one possesses the information of all the produced particles. Figure 9.3 shows that the purity is 99.9% for all Θ_e and P_{trk} values.

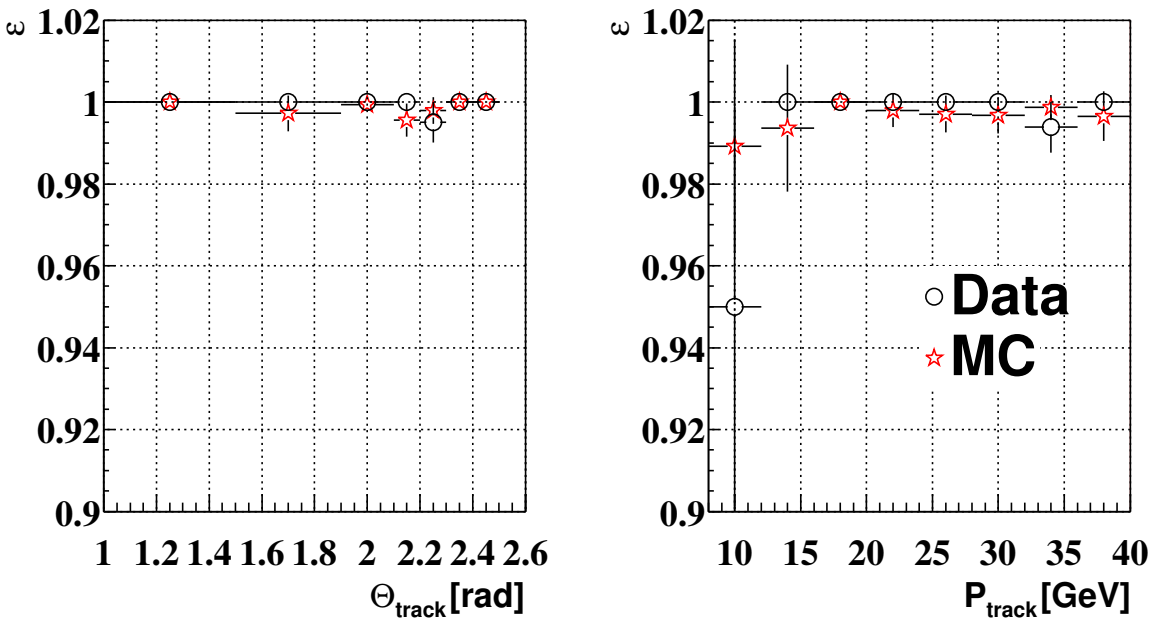

Figure 9.4: Efficiency of the electron-finder SIRA 5. The left plot shows the efficiency versus the scattered lepton angle. For the super-crack region there is a small loss in the efficiency. The right plot shows the efficiency versus the momentum of the track. Due to resolution problems in the KP region the momentum of the track can be mismeasured therefore no conclusions about the efficiency can be made in this region. The agreement between data and Monte Carlo results is within $\approx 0.5\%$.

Once one has a pure sample of isolated tracks, the efficiency of the electron-finder in data and Monte Carlo events can be determined by the rate by which the electron-finder candidate and the isolated track lie within 30^0 in Θ and ϕ from each other. The result is shown in Fig. 9.4. The efficiency is higher than 99.9% and data and Monte Carlo results agree within 0.5%. In the Θ_e variable one can see the effect of the super-crack region between the RCAL and the BCAL situated at $\Theta \approx 2.2$ rad. In this region the efficiency, both for data and Monte Carlo points, drops. This level of agreement between data and Monte Carlo results, no corrections for data neither for Monte Carlo simulation is applied.

The comparison is only valid for a small range in Θ_e and P_{trk}, but this method does only intend to show the agreement between data and Monte Carlo results. In Fig. 9.5 the probability of SIRA 5 is plotted in bins of Θ. With the agreement found in all the regions, one can calculate the efficiency for Monte Carlo events for a wider range and extrapolate the results to the data.

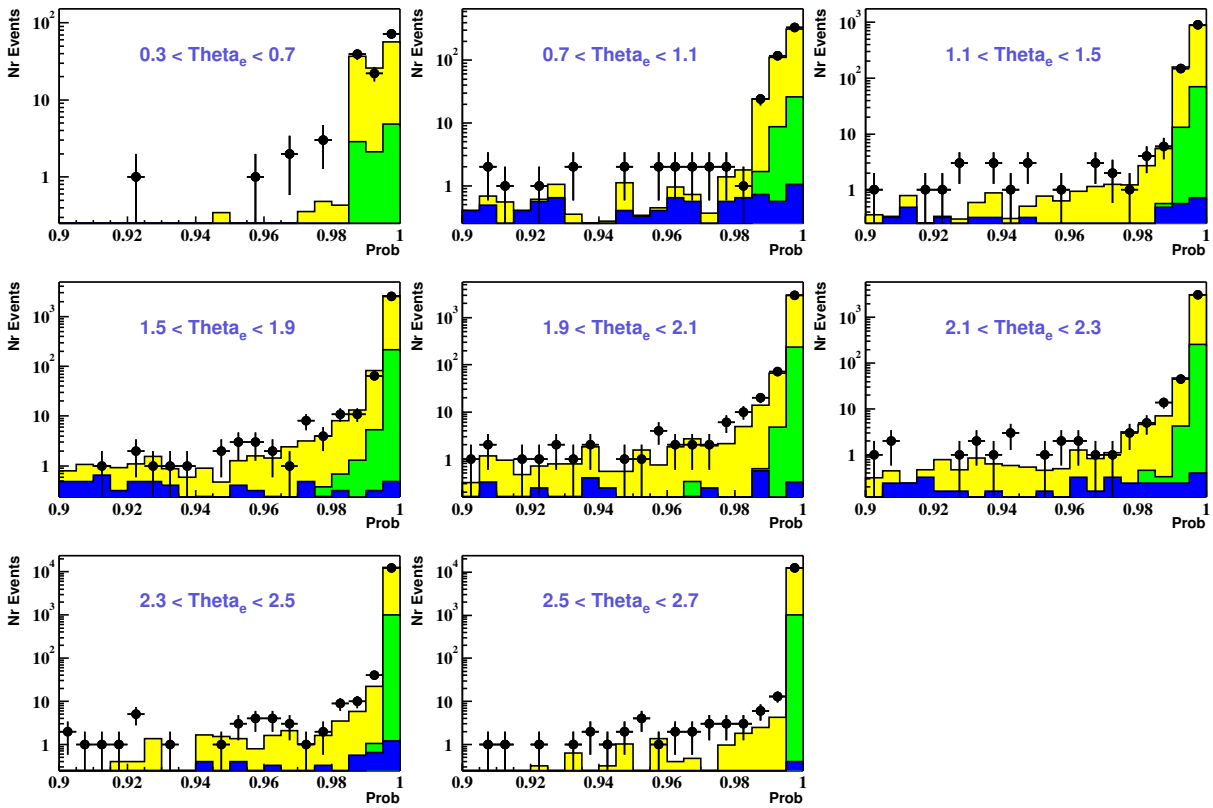

Figure 9.5: Comparison of the SIRA 5 probability in bins of the scattered lepton angle for data and Monte Carlo simulation.

9.2.2 Determination of SIRA 5 efficiency for Monte Carlo events

The study of the electron-finder efficiencies using only Monte Carlo events can be more precise and extended than the previous one. In Monte Carlo simulations the scattered lepton can be easily tagged and one does not depend on other mechanisms to identify it. Therefore all calorimeter and kinematic regions can be explored.

Estimation of the efficiency

The electron-finder SIRA 5 does the identification of the scattered lepton in two steps. In the first step, the neural network SINISTRA95 makes a list of candidates. In the second step FINDIS95 with option 5 selects the DIS candidate among all applying a probability cut of $P_e > 0.9$, a y_e cut of $y_e < 0.95$ and requiring a track for the candidate if it is inside the CTD acceptance region.

The efficiency study is also divided in two. The first efficiency, ε^{found} , shows the rate at which SINISTRA95 finds an electromagnetic candidate with $P_e > 0.9$. The second efficiency, ε^{DIS} , shows the rate at which FINDIS95 option 5 selects the scattered lepton.

The definition of ε^{found} is:

$$\varepsilon^{found}_{SINISTRA95} = \frac{\#\text{ candidate found}}{\#\text{generated}},$$

where "# candidate found" is the number of events in which at least one electromagnetic candidate was found by SINISTRA95, and "# generated" is the number of DIS events generated.

The definition of ε^{DIS} is:

$$\varepsilon^{DIS}_{SIRA5} = \frac{\#\text{DIS candidate found}}{\#\text{generated}},$$

where "# DIS candidate found" is the number of events in which the electromagnetic candidate selected by FINDIS95 was the true DIS electron.

Determination of the efficiency

When trying to apply the angular cuts to determine the matching between the true scattered lepton and the found candidate, one is faced with a problem. The resolution with which the angular position is measured varies along the calorimeter. It is better if the position is determined with the CTD and degrades when is done it with the calorimeter. Therefore, the angular cuts in Θ and ϕ are parameterized as a function of Θ: the whole Θ range $(0,\pi)$ has been divided into 15 slices, 5 slices in each calorimeter.

Another problem when applying the ϕ cut is that magnetic fields inside the detector bend the trajectories in the ϕ direction. This effect is higher for low energetic particles. Four bins in true scattered lepton energy have been made.

In each of the Θ and E_e bins, the angular differences, $\Delta\Theta$ and $\Delta\phi$, between the measured candidate and the scattered lepton variables are calculated. Θ_e and ϕ_e were calculated using calorimeter and when possible track information.

Gaussian functions are fitted to the $\Delta\Theta$ and $\Delta\phi$ distributions. From the fit of the distribution one obtains a parameterization for the mean and the width as a function of Θ_{true} for different scattered lepton energy bins (see Fig 9.6).

The dots are the track variables and the triangles represent the calorimeter variables. The vertical dashed lines show the boundaries of the calorimeters while the vertical dotted lines show the CTD acceptance region.

The mean and sigma values in Fig. 9.6 were fitted by using different polynomial functions in order to get a smooth distribution as a function on the scattered lepton energy. The fits are also plotted; the full line belongs to the track variables' fit and the dashed line to the calorimeter variables' fit.

From the plots one can see that the mean value of the Gaussian distribution for $\Delta\Theta$ is very close to zero for all scattered leptons energies and angles. The width of the distribution is smaller for track variables than for calorimeter variables inside the CTD region, around 2 mrad in the RCAL and FCAL side of the CTD away from its end, and around 4 mrad in the middle of the BCAL. It is smaller for calorimeter variables outside this region, between 6 and 8 mrad in the RCAL and 2 mrad in the FCAL. In the transition region between calorimeter and track variables the width of the track and calorimeter distributions is the same, between 6 and 8 mrad.

In the case of the $\Delta\phi$ distribution, the mean value is always shifted towards positive values due to the magnetic fields, i.e. the true value is always bigger than the measured one. The shift is 6 mrad in the BCAL for scattered leptons with energies lower than 15 GeV , smaller (2 mrad) for scattered leptons with energies higher than 25 GeV (track variables), and up to 20 mrad for calorimeter variables in the RCAL for low energies, 10 mrad for high energies. The width of the $\Delta\phi$ distribution is smaller than the width of the $\Delta\Theta$ distribution. It is below 2

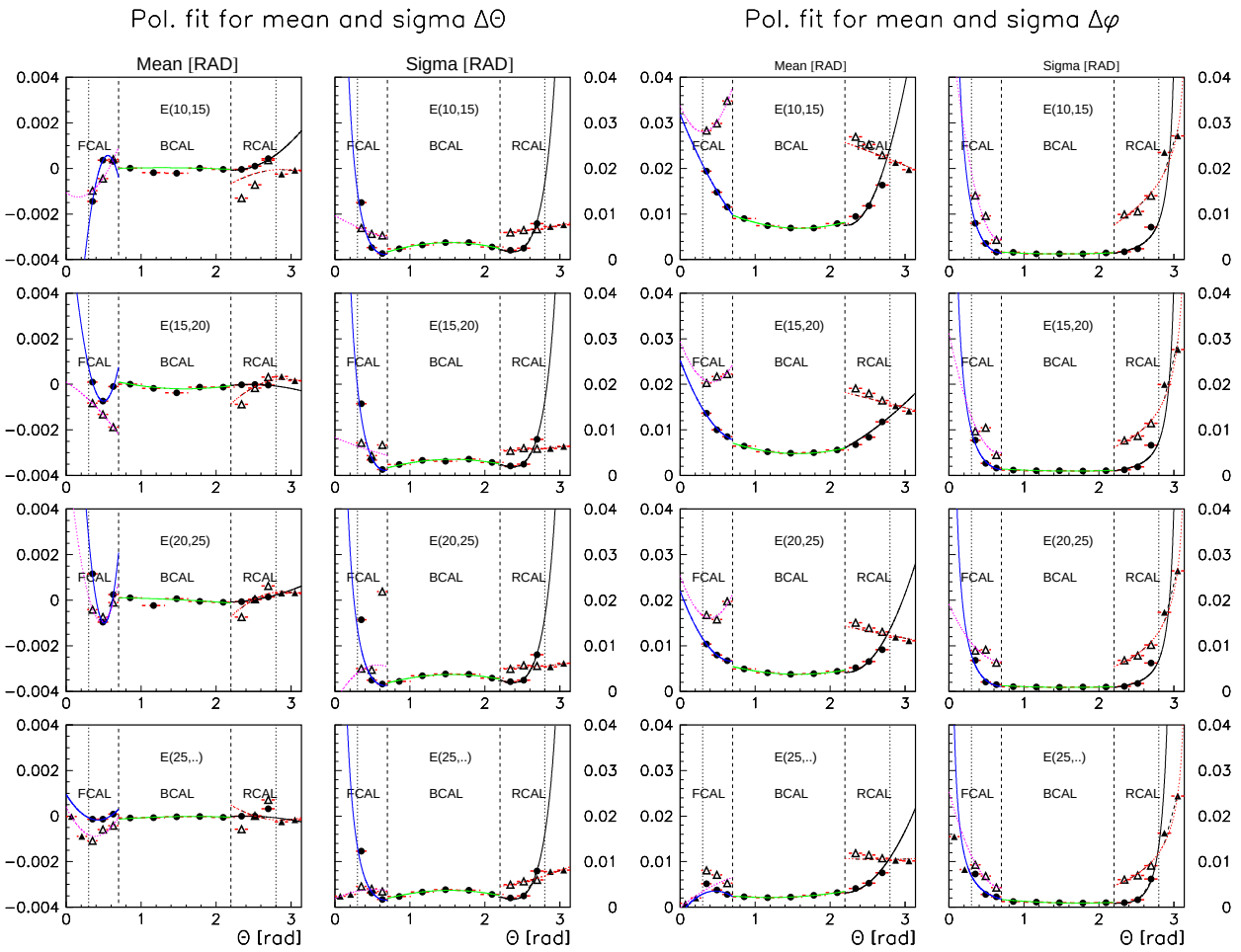

Figure 9.6: Fit of mean and sigma for $\Delta\Theta$ and $\Delta\varphi$ for all calorimeter regions in 4 different energy bins. The dotted vertical lines represent the region in which a track can be reconstructed. Different fits have been performed on different regions of the calorimeter, for the RCAL, $2.2 \leq \Theta \leq \pi$, track (dots) and non track (stars) variables have been used, as well as for the FCAL $0.0 \leq \Theta \leq 0.7$, while for the BCAL only track variables have been used. All the points are included in the fit, but closed stars/dots are the variables used to calculate ε^{DIS} .

mrad for track variables, and bigger for calorimeter variables starting at 30 mrad for low energy scattered leptons to 25 mrad for high energy ones.

Once obtained the parameterizations of the mean and the sigma of the $\Delta\Theta$ and the $\Delta\phi$ distributions, one can perform a simultaneous cut on the latter variables. Knowing Θ_{true}, φ_{true}, the measured candidate will be considered to be the DIS one if it lies within 10 sigma[1] from the nominal mean value for both variables Θ_{true} and ϕ_{true}. The region in which one or the other parameterization is used to calculate ε^{DIS} is marked with the filled dots for track variables, and filled triangles for calorimeter variables.

[1]The value of 10 sigma is chosen to take into account the tails of the distributions.

Efficiency results

The efficiency has been plotted against the true energy, angle and Q^2 of the scattered lepton in Fig. 9.7.

On each plot two horizontal lines have been drawn, the upper one represents a 2(5)% loss in ε^{found} (ε^{DIS}), and the lower one a 5(10)% loss respectively. Vertical lines have also been drawn on the Θ_{true} and Q^2_{true} plots to indicate the limits of the calorimeters (full line) as well as the limits of the CTD (dashed line) in which a track can be reconstructed (assuming $V_z = 0$). It should be noted that in the Q^2 plot the position of the lines is only approximate and are plotted.

The behavior of the electron-finders depends mostly on the position of the scattered lepton in the calorimeter, especially at the:

- R/BCAL crack: $\Theta_{true} \sim 2.2$ rad, $\log_{10}(Q^2_{true}) \sim 2$, $E_e \sim 30$ GeV
- CTD end on the RCAL side: $\Theta_{true} \sim 2.8$ rad, $\log_{10}(Q^2_{true}) \sim 2.8$
- F/BCAL crack: $\Theta_{true} \sim 0.7$ rad, $\log_{10}(Q^2_{true}) \sim 4.2$
- CTD end on the FCAL side: $\Theta_{true} \sim 0.3$ rad, $\log_{10}(Q^2_{true}) \sim 4.7$.

In the region of the cracks between calorimeters one observes a big drop of ε^{found} for SIRA 5. A drop at the CTD end at the RCAL side is also present.

Analyzing ε^{DIS} one sees a drop in the efficiency compared to ε^{found} . A falling tendency of the efficiency versus Θ_{true} starting in the middle of the BCAL continuing until the end of the FCAL should be noted. A detailed study of this inefficiency can be found in Appendix C.

9.3 Efficiency of the Track Requirement Cuts

In the CTD acceptance region the scattered lepton is required to have a track. The measured track has to fulfill two conditions. One is that the distance of closest approach (left plot of Fig. 9.8) between the extrapolated track position to the calorimeter and the calorimeter cluster has to be $DCA \leq 10$ cm. For the second condition the momentum of the track (right plot of Fig. 9.8) has to be $P_{trk} \geq 5$ GeV. These two cuts help to reduce background and ensure a good quality for the track.

It has be ensured that the number of data and Monte Carlo events rejected by these cuts is the same.

The rejection efficiency is given as a function of the scattered lepton angle energy determined from calorimeter. Since the two cuts, as said before, reject a lot of PHP background the study is done in terms of the $E - p_z$ variable without applying any cut to it. To reduce PHP effects that may appear when removing this cut, another cut was used instead $P_T/E_T \geq 0.6$ (Fig. 9.9). This cut is used in charged current analysis [B+00] to reduce PHP background.

The variable $E - p_Z$ is plotted in bins of Θ_e and E_e for all events in the CTD acceptance region[2]. These events have a track associated to the scattered lepton reconstructed with more

[2]The plots not found in this section can be found in Appendix F

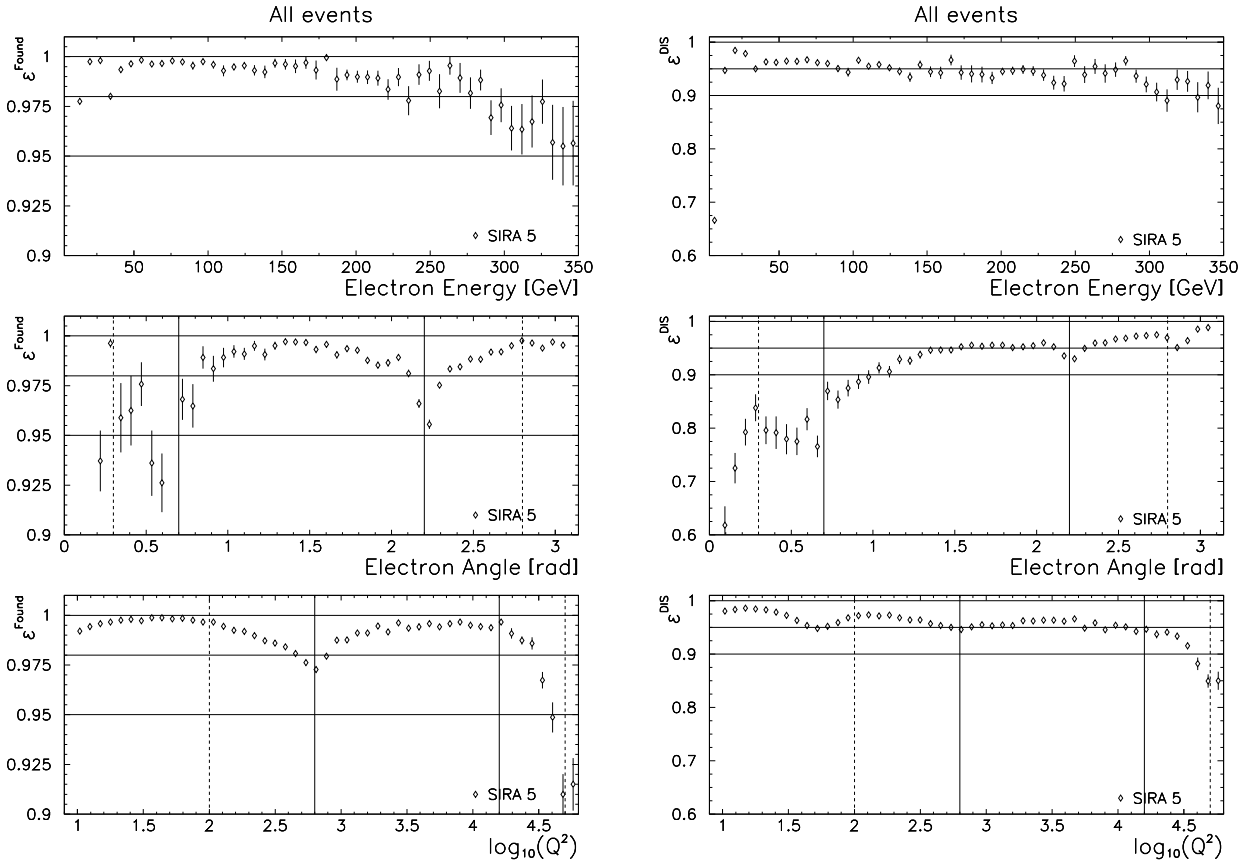

Figure 9.7: ε^{found} and ε^{DIS} plotted versus the energy, angle and $\log_{10}(\mathrm{Q}^2)$ of the true scattered lepton for SIRA 5. Horizontal lines represent 2% loss (upper line) and 5% loss (lower line), vertical full lines indicate CAL limits and vertical dashed lines represent CTD end. On the $\log_{10}(\mathrm{Q}^2)$ plot the positions of the calorimeters are approximate.

than 4 super-layers. The ratio of this distribution with the cuts $DCA \leq 10$ cm and $P_{trk} \geq 5$ GeV divided by the same distribution with no cuts will give an idea of the efficiency of the cuts in data and Monte Carlo events.

The ratio between data and Monte Carlo efficiencies for each Θ and E_e bin is obtained by fitting constant line. To get rid of PHP effects present at low $E - p_Z$ values only the central region of the $E - p_Z$ distribution has been fitted. The result of this fit is plotted for every bin in Θ_e and E_e in Fig. 9.10.

To obtain the relative difference the efficiency over the whole Θ and E_e has been fitted to a constant line. In the Θ case the assumption that the CTD is symmetric has been done to overcome the low statistics on the low angle region.

Observing the region of high Θ_e values, one can see that the agreement between data and Monte Carlo efficiencies is within 0.5%. In the lower part of the plot the results against the E_e variable are shown. They are obtained in the same way as for the Θ_e variable. The results obtained are compatible with each other within errors. Due to the good agreement between data and Monte Carlo results no corrections are foreseen.

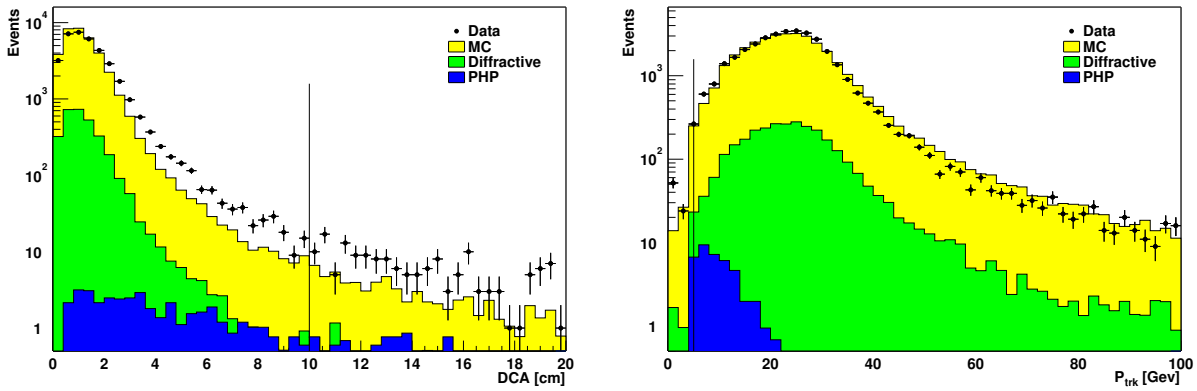

Figure 9.8: (left) Distance of closest approach and (right) momentum of the track distributions. The vertical lines show the analysis cuts (see text for details).

9.4 Electromagnetic Energy Studies

It has been shown in the preceding chapter that several corrections are applied to the scattered lepton energy so that the measured value approaches the expected value. Nevertheless the understanding of the energy scale is not perfect due to detector effects or bad Monte Carlo simulation. Therefore an electromagnetic energy scale uncertainty has to be quoted. For this analysis the electromagnetic energy scales for the RCAL and the BCAL have been studied. The FCAL is not considered independently in the analysis due to lack of statistics.

9.4.1 RCAL studies

In this study the measured energy after dead material, non-uniformity corrections and smearing is compared to the predicted energy calculated with the double angle method. This has been done in bins of the double angle energy. The distribution of the $1 - E_e/E_{DA}$ variable in bins of E_{DA} has bin fitted to a Gaussian independently for data and Monte Carlo samples[3]. The comparison of the obtained mean value for data and Monte Carlo fits (first plot of Fig. 9.11) will give the electromagnetic energy scale uncertainty.

9.4.2 BCAL studies

In the BCAL three different samples of scattered leptons have been made according to their purity. The first sample corresponds to the scattered leptons used for the analysis. For the second sample two extra cuts were added to enhance the purity of the sample. The first cut rejects scattered leptons that have an energy in cone not belonging to them ≥ 1.5 GeV. This cut selects scattered leptons that are very collimated and do not have any background contamination. Secondly the $E - p_z$ cut has been raised to further reduce PHP background to 44 GeV $\leq E - Pz \leq$ 65 GeV.

The last sample consists of high-energy scattered leptons. These are usually less affected by corrections due to inactive material or smearing of the Monte Carlo energy and one expects the Monte Carlo simulation to describe them better.

[3]The plots not found in this section can be found in Appendix E.

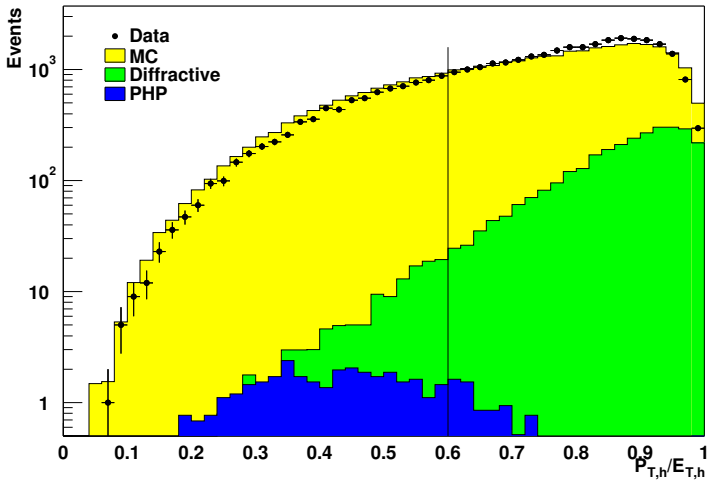

Figure 9.9: $P_{T,h}/E_{T,h}$ distribution. The vertical line shows the cut at $P_{T,h}/E_{T,h} > 0.6$.

The same procedure of plotting and fitting used for the RCAL studies (Appendix E) has been applied to the three sets of BCAL scattered leptons.

The mean values obtained from the fits for data and Monte Carlo samples are shown in the last three plots of Fig. 9.11. It should be noticed the tendency of the data and Monte Carlo points to approach the nominal value when the purity of the sample increases.

9.4.3 Conclusion

Figure 9.12 resumes all the studies performed in the RCAL and the BCAL. The difference between the data and Monte Carlo mean values obtained from the Gaussian fits is plotted against the double angle energy. One can see that for energies bigger than 20 GeV the difference between the values is within 1%. For lower values of the energy the difference can get as big as 1.5%. This is in good agreement with the results presented in [Liu]. To calculate the systematic uncertainty in the cross section associated to the electromagnetic energy scale uncertainty, the Monte Carlo energy has been varied for all calorimeters, RCAL, BCAL and FCAL by 2%. The difference in the results has been quoted as the uncertainty error.

9.5 Other Scattered Lepton Systematic Studies

9.5.1 Scattered lepton isolation

As explained in Appendix C, one of the reasons for the inefficiency of the electron finders is the choice of an electromagnetic candidate that belongs to the jet as the scattered lepton. To solve this problem a cut to reject these type of events is used. A cone in η and ϕ is built around the scattered lepton with radius $R = 1$. The amount of energy inside the cone that does not belong to the scattered lepton is shown in Fig. 9.13.

A cut on the amount of energy inside the cone that does not belong to the scattered lepton of $E_{not\,in\,cone} \leq 5$ GeV is applied. It has also been shown (Section 9.4.2) that the rise of this cut improves the purity of the scattered leptons. The change of this cut can affect the measurement

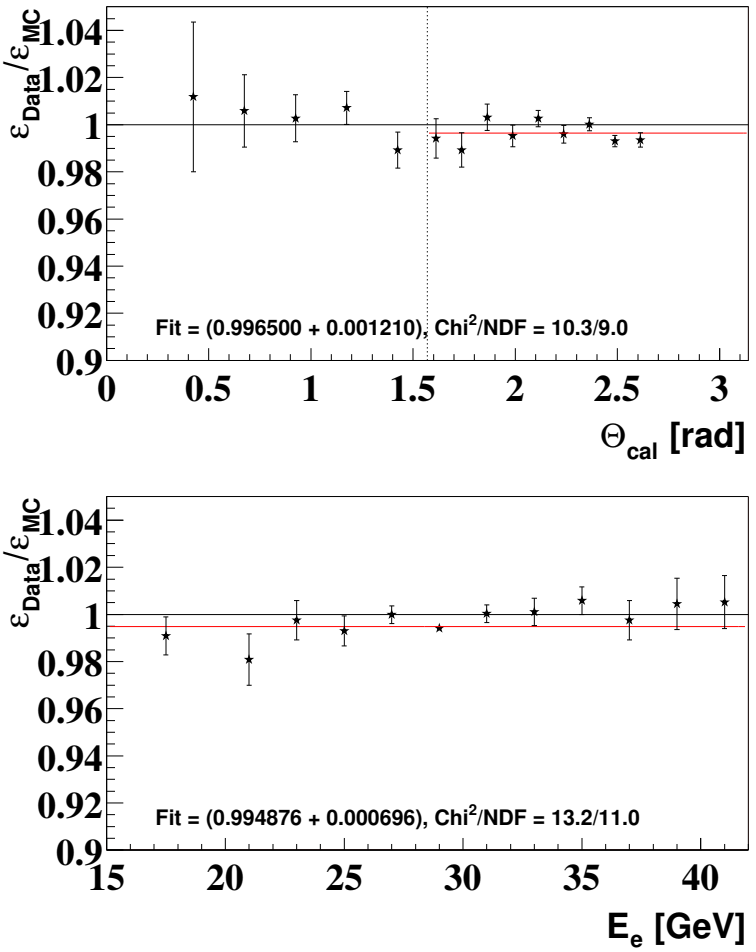

Figure 9.10: Comparison of the efficiency rejecting data and Monte Carlo events with track cuts. Due to lack of statistic for the theta variable only the right region is used to perform the fit. The results versus Θ and E_e are consistent within errors. Data and Monte Carlo results agree within 99.5%.

of the cross section, therefore several cuts have been tested and the systematic uncertainty is quoted as the difference between the results (see Chapter 10).

9.5.2 Electron energy smearing

In Section 8.2.4 smearing of the Monte Carlo energy has been presented. The constant value by which the energy is smeared has an error that affects the cuts applied to variables that depend on the scattered lepton energy. To calculate the systematic uncertainty coming from this effect, the constant value has been raised and lowered (by 0.1% up and no smearing) and the cross section has been recalculated with this new values.

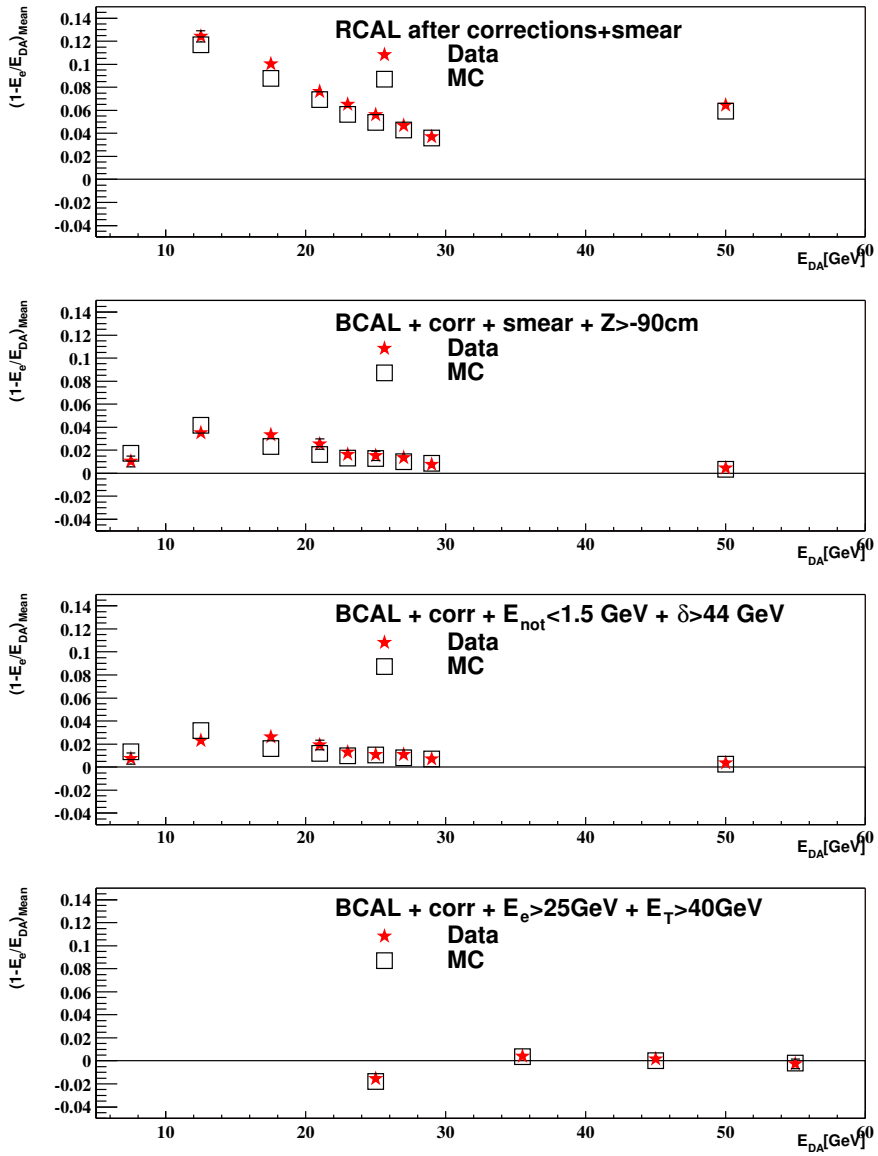

Figure 9.11: Mean value of the Gaussian fit of the $1 - E_e/E_{DA}$ distribution for data and Monte Carlo sample. Upper plot is for scattered leptons on the RCAL. Next plots are for scattered leptons on the BCAL in increasing order of purity (see text for full explanation).

9.6 Hadronic Final State Studies

9.6.1 Diffractive sample

The estimation of the diffractive fraction for the Monte Carlo simulation was illustrated in Section 8.1.7. The error associated to the estimation enters the extraction of the double differential cross section as a systematic uncertainty. To calculate it, the diffractive fraction has been varied by 50% and the double differential cross section has been extracted again. The difference between the obtained results will be quoted as the systematic uncertainty.

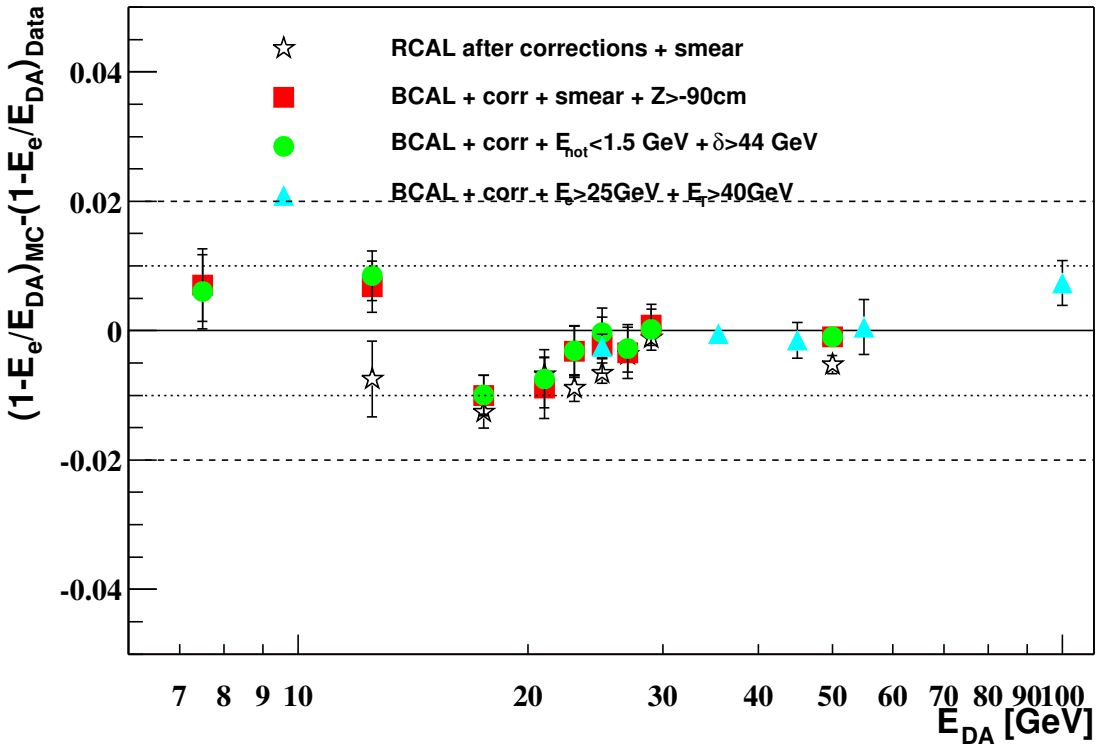

Figure 9.12: Mean value of the $1 - E_e/E_{DA}$ distribution in data minus mean value of the Monte Carlo distribution. Stars are scattered leptons in the RCAL, squares scattered leptons in the BCAL, sample used for the analysis. Dots and triangles are for scattered leptons on the BCAL with different cuts (see text for full explanation).

9.6.2 Hadronic energy scale

As in the electromagnetic case, the hadronic variables have been corrected to obtain a result as close as possible to the true one. The remaining scale uncertainty has to be quoted as a systematic uncertainty.

One method to evaluate the hadronic energy scale is based on the fact that the scattered lepton and the hadronic system have to balanced in p_T. Knowing the scattered lepton energy one can estimate what the hadronic energy should be. This is illustrated in detail in [B$^+$99].

An alternative method using diffractive events has been used [Cor]. The advantage of using these kind of events, compared to the the previous method, is that there is no proton remnant to carry any p_T and the p_T carried by the proton is negligible [B$^+$98]. One can be sure that all the p_T from the scattered lepton is balanced by the hadronic jet. Another advantage of this method is that knowing the pseudo-rapidity of the most forward and most backward particle in the jet, one can determined in which calorimeter the hadronic jet is contained. In this way one can estimate the hadronic energy scale independently for each calorimeter.

The result of the study is that the energy scale uncertainty is known better than 2% for all calorimeters and EMC and HAC sections.

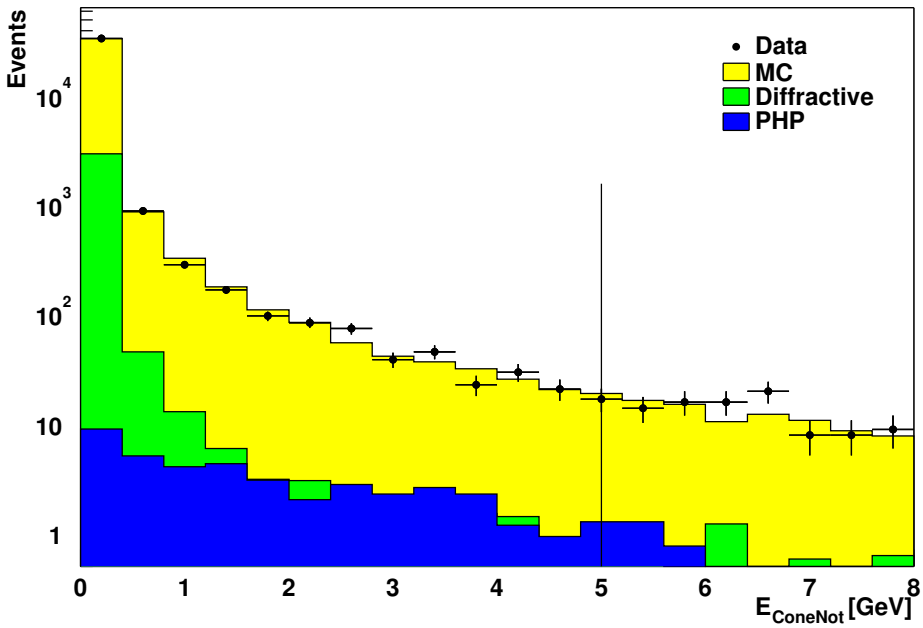

Figure 9.13: Energy in an $\eta - \phi$ cone of radius $R = 1$ around the scattered lepton, that does not belong to it. The vertical line shows the analysis cut $E_{ConeNot} < 5$ GeV .

9.7 Background Studies

9.7.1 Estimation of the PHP background

To estimate the PHP background 5 million PHP Monte Carlo events have been used. The distribution of the remaining events after all the analysis cuts in the kinematic variables can be seen in Fig. 9.14. Almost all events are concentrated in the low Q^2 and high y_e region. These small number of events is subtracted from the data in each bin to calculate the cross section.

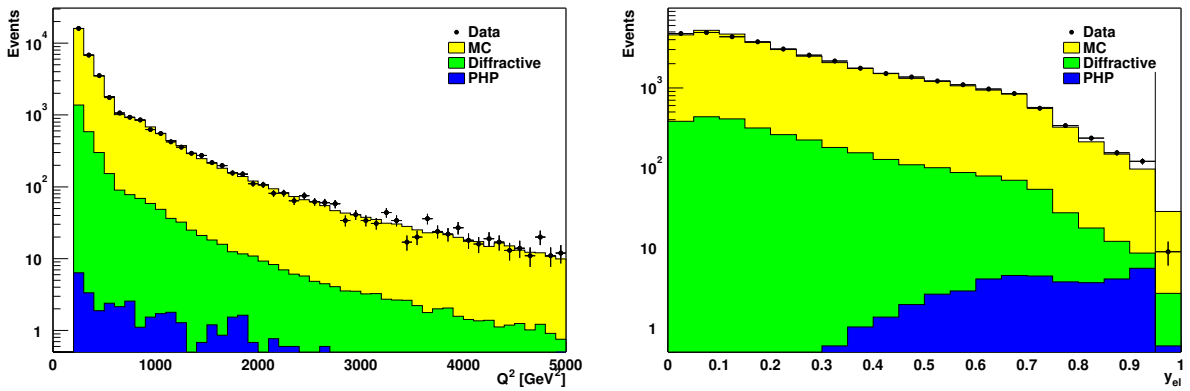

Figure 9.14: Photoproduction background in the Q^2 and y_e variables. A cut $y_e < 0.95$ is already placed in SIRA 5, this is the reason why there are so few events in this region.

The systematic associated to PHP background has been calculated by varying the number of PHP events in one bin by $3 \cdot \sigma$.

9.7.2 PHP background rejection with y_e cut

One can see from the Fig. 9.14 that almost all PHP background is concentrated on the high y region. To remove the PHP events a cut on the y_e variable was placed. The number of events in our sample at high Q^2 is almost negligible, nevertheless a change in the y_e will affect the estimation of the PHP background. To get an idea of the change a tighter cut ($y_e < 0.9$) on this variable was made and the analysis was repeated with the new cut.

9.7.3 Estimation of the beam-gas background

In Section 8.3.2, it was explained how to estimate the contamination of the beam-gas background in the sample. One looks how may events from e- and p-pilot bunches survive the DIS cuts. The obtained results show that there are no p-pilot events in the sample, and 18 e-pilot events. Fig 9.15 shows the distribution in x, y and Q^2 of these events. The maximum Q^2 value a e-pilot event can reach is $Q^2 \leq 55\,\mathrm{GeV}^2$. None of these events can be a beam-gas event. After scanning them all, it was found that these events are DIS events and no beam-gas events. Events flagged as e-pilot events are events in which the proton beam current falls below a certain threshold: so, although very small, there is still a possibility that the leptons collide with protons resulting in DIS events.

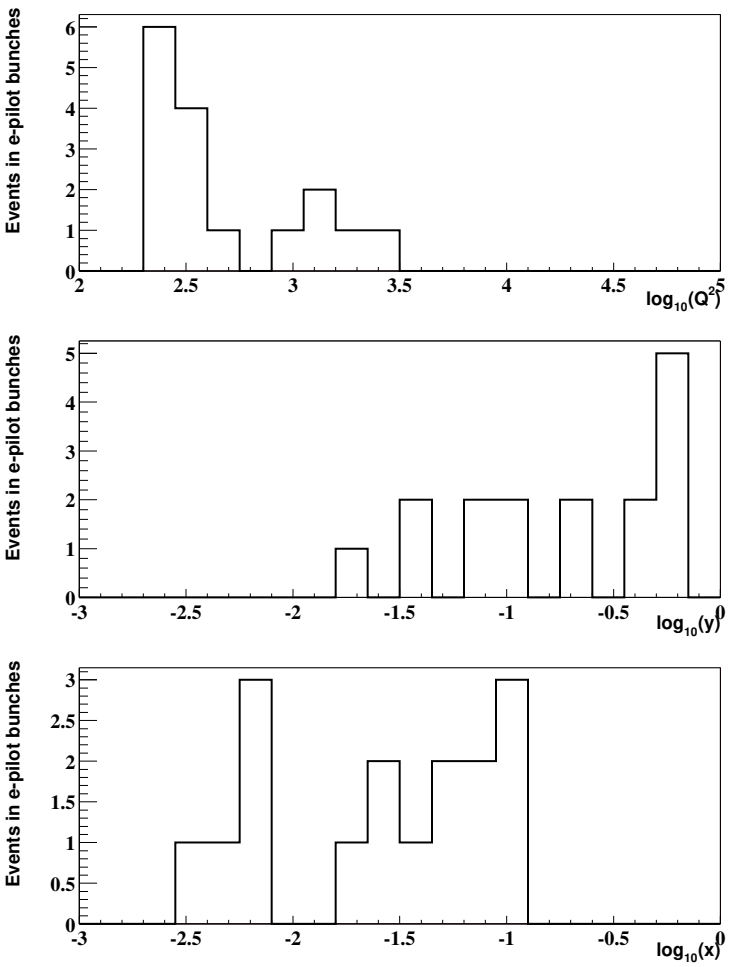

Figure 9.15: Distribution in the kinematic variables of the e-pilot bunches events.

Since no beam-gas was found, no background subtraction of this kind was done.

9.8 Luminosity uncertainty

There is an uncertainty associated to the luminosity estimation. The uncertainty has already been shown in Table 5.1. This uncertainty has not been included in the total systematic uncertainty.

9.9 Extraction of the Cross Sections and $xF_3(x, Q^2)$

9.9.1 Statistical error

As explained in Chapter 5 the bin by bin unfolding has been chosen to extract the double differential cross section. The advantage of this method is that the error between bins are uncorrelated. The disadvantage this method has is that the migrations between bins is not taken into account. Still, the use of bin by bin unfolding is justified if the Monte Carlo simulation is able to describe the data well. Since in this and the preceding chapter it has been shown that the level of agreement is very high, the bin by bin unfolding is used. The statistical error is given by the number of data and Monte Carlo events in each bin.

As shown in Section 6.6 each Monte Carlo event is reweighted so that is is normalized to the data and can be compared to them. For each bin i the sum of weights $(\sum_j w_j)_i$ and the sum of the squared weights $(\sum_j w_j^2)_i$, is determined. The measured Monte Carlo events and the statistical error is given by:

$$\begin{aligned} N^{MC}_{meas,i} &= (\sum_j w_j)_i \\ \Delta N^{MC}_{meas,i} &= \left(\sqrt{(\sum_j w_j^2)_i}\right). \end{aligned}$$

Taking $N^{Data}_{obs,i}$ as the total number of events observed in the bin i the statistical error is taken to be Gaussian if more than 12 events are found in the bin. Poisson errors are used otherwise.

Taking these into account, the statistical error on the cross section is given by:

$$\left(\frac{\Delta\sigma}{\sigma}\right)_i = \sqrt{\left(\frac{\Delta N^{Data}_{obs,i}}{N^{Data}_{obs,i}}\right) + \left(\frac{\Delta N^{MC}_{meas,i}}{N^{MC}_{meas,i}}\right)}.$$

For a large number of Monte Carlo events, $N^{MC_{gen}} \to \infty$, the contribution of the statistical error from the Monte Carlo sample to the measurement is negligible. The remaining statistical error depends on the data luminosity collected for the analysis.

9.9.2 Systematic uncertainty

As seen along this chapter the understanding of the detector, the Monte Carlo simulation and the remaining background is not perfect. A way to quantify the precision with which the

measurement is done is given by the systematic uncertainty. This uncertainty gives an idea of the stability of the measurement with respect to the variation of not well known quantities involved in the measurement.

The variation of each quantity is done in a range given by the uncertainty of itself. Then the measurement of the cross section is repeated. The difference between the new and the nominal value is quoted as the systematic uncertainty.

The systematic uncertainties have been chosen so that there are independent of each other, i.e. no uncertainty is double counted. Therefore the total systematic uncertainty is the sum of the individual uncertainties added in quadrature.

The effect of the systematic checks that have been explained in this chapter will be shown in Chapter 10.

9.9.3 Quality of the bins

To estimate the quality of the bins one can calculate the acceptance, efficiency and purity of each bin.

The efficiency of a bin is defined as:

$$\varepsilon = \frac{\#\text{Events generated and measured in bin}}{\#\text{Events generated in bin}},$$

its purity is:

$$P = \frac{\#\text{Events generated and measured in bin}}{\#\text{Events measured in bin}},$$

and from the acceptance:

$$A = \frac{P}{\varepsilon} = \frac{\#\text{Events measured in bin}}{\#\text{Events generated in bin}}.$$

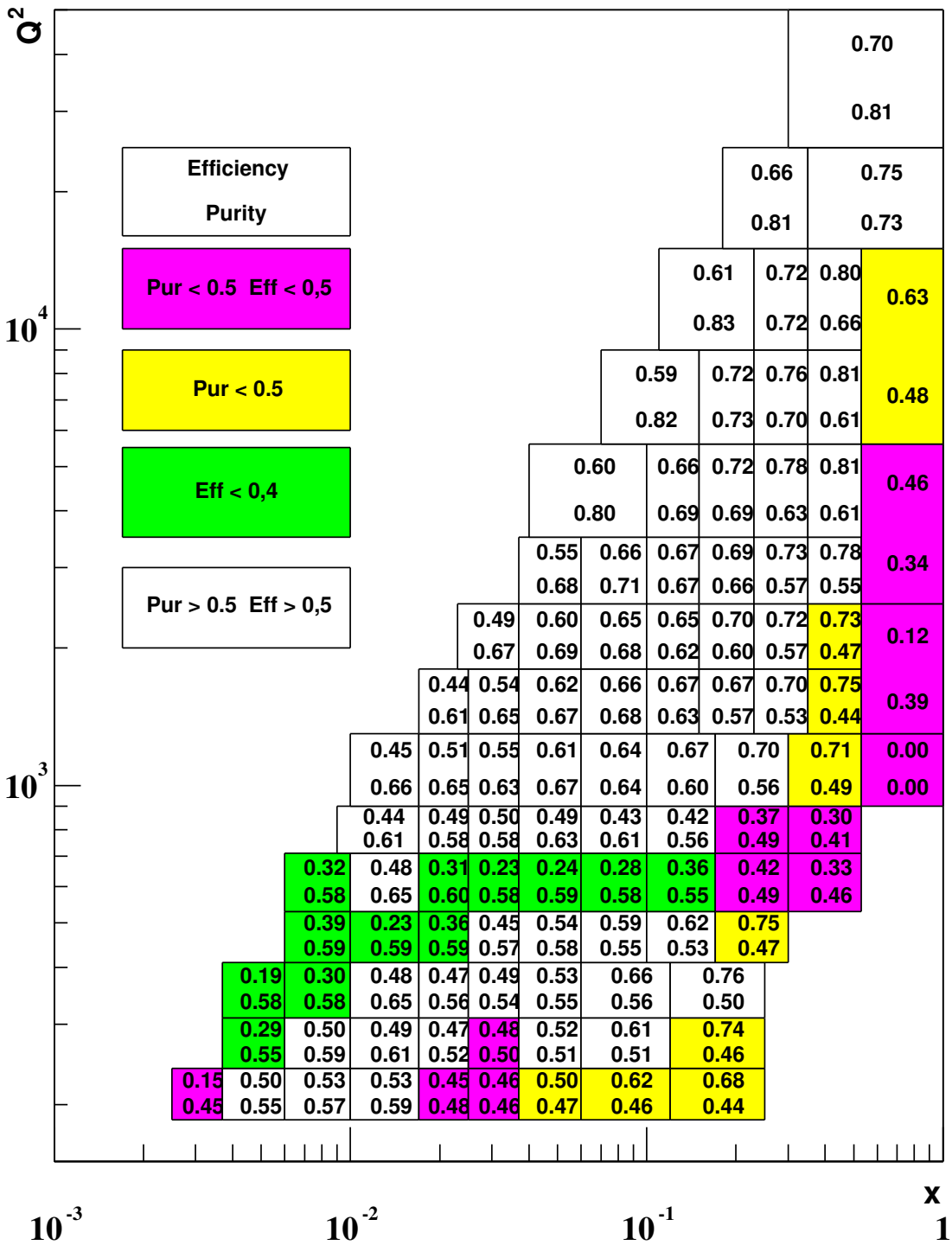

Figure 9.16: Purity and efficiency of the double differential bins.

The efficiency and purity for the double differential bins is shown in Fig. 9.16. Only bins with an efficiency greater than 40% and a purity greater than 50% are used.

Chapter 10

Measurement of Cross Sections

In this chapter the results of the measurement of the single and double differential cross sections are presented. Results are given with statistical errors and systematic uncertainties. The measured values have been compared to the Standard Model predictions evaluated with the CTEQ5D parton density functions.

The data samples shown are 29.5 pb^{-1} of $(e^+p)^{820}$ data, 15.8 pb^{-1} of $(e^-p)^{920}$ data and 56.9 pb^{-1} of $(e^+p)^{920}$ data. All data samples have been treated as explained in Chapters 5 to 9. The values with statistical errors and systematic uncertainties can be found in Appendix J.

All single differential cross sections $d\sigma/dQ^2$, $d\sigma/dx$ and $d\sigma/dy$ have been measured for $Q^2 > 200$ GeV^2 . The cross section $d\sigma/dx$ for $Q^2 > 10000$ GeV^2 has also been measured. The double differential cross section $d^2\sigma/dx\,dQ^2$ has been measured in the x and Q^2 bins shown in Fig. 9.16.

10.1 Measurement of the Single Differential Cross Section dσ/dQ^2

Figure 10.1 shows the single differential cross section $d\sigma/dQ^2$ both for electrons and positrons for different proton energies.

The cross section is observed to fall more than 6 orders of magnitude. For $Q^2 < 1000$ GeV^2 the positrons' cross section is observed to be approximately equal to the electrons' cross section. In this kinematic domain NC $e^\pm$ DIS is mediated by single photon exchange and the Q^2 dependence of $d\sigma/dQ^2$ reflects the $1/Q^4$ dependence of the photon propagator.

As Q^2 approaches the Z-boson mass squared ($Q^2 \sim M_Z^2$) the positrons' cross section falls below that for electrons. At such large Q^2 both photon- and Z-exchange contributions must be taken into account. The interference between the two contributions suppresses the positrons' cross section and enhances the electrons' cross section. The SM, which incorporates all these effects, gives a good description of the data.

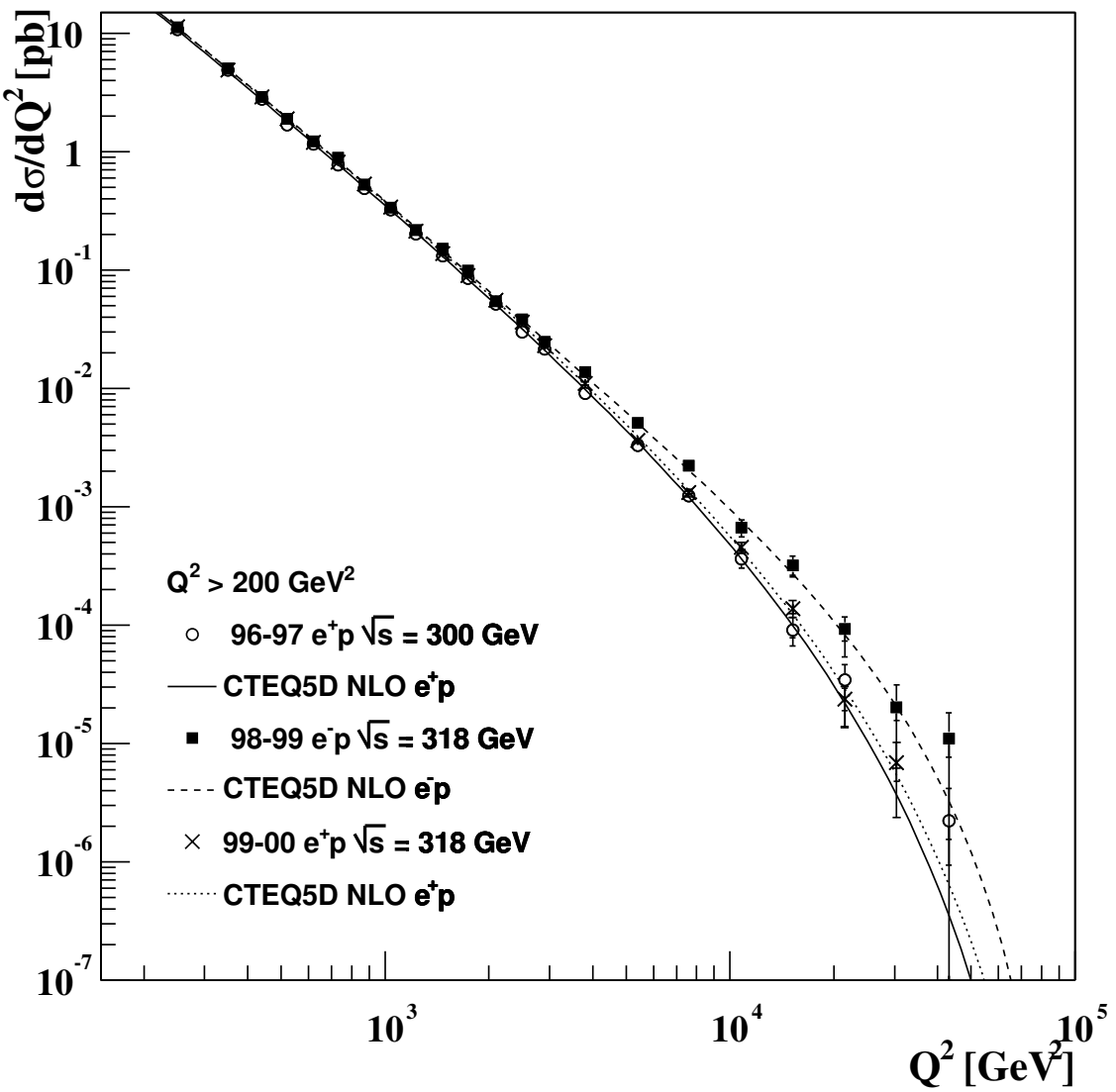

Figure 10.1: Single differential cross section $d\sigma/dQ^2$ for the 96/97 positron (open circles), 98/99 electron (closed squares) and 99/00 positron (crosses) data samples. The comparison to the Standard Model prediction calculated using the CTEQ5D parameterization is also shown for all data samples.

10.2 Measurement of the Single Differential Cross Section dσ/dx

The single differential cross section $d\sigma/dx$ for $Q^2 > 200$ GeV^2 for the all data samples is shown in Fig. 10.2. On the top part the measured cross section is shown for all data samples. The cross section is $\mathcal{O}(10^4)$ for lower values of x and double decreased almost five orders of magnitude for $x \sim 0.8$.

On the bottom part the ratio of the obtained values to the predicted is shown. The ratio shows good agreement between the obtained values and the theory, except for one bin at $x = 0.31$

where the $(e^+p)^{920}$ point seems to be underneath the theory. In the highest x bin the $(e^-p)^{920}$ sample has run out of statistics.

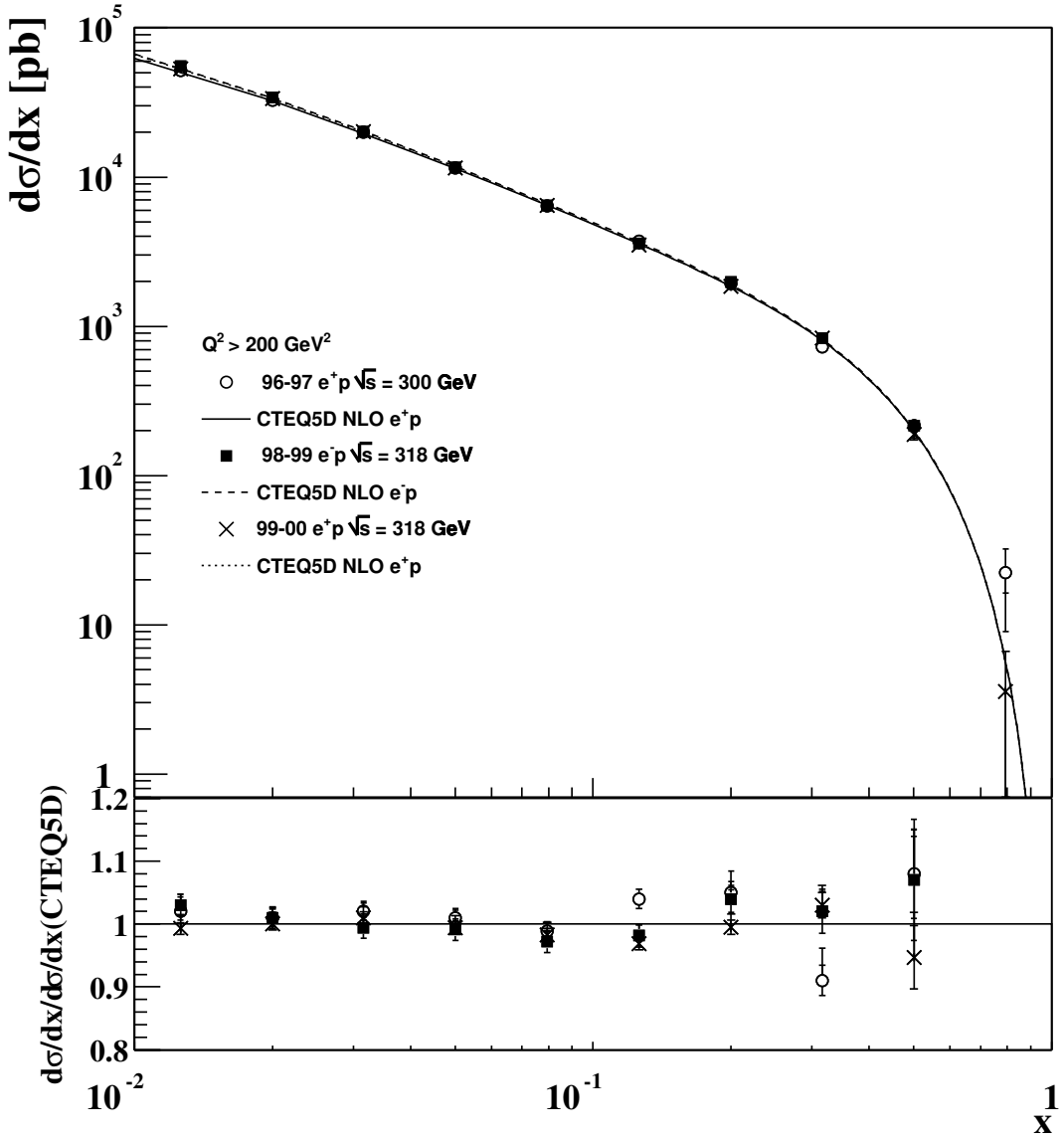

Figure 10.2: Single differential cross section $d\sigma/dx$ for $Q^2 > 200$ GeV^2 for the 96/96 positron (open circles), 98/99 electron (closed squares) and 99/00 positron (crosses) data sample. The comparison to the Standard Model prediction calculated using the CTEQ5D parameterization is also shown for all data samples.

In Fig. 10.3 the measured single cross section $d\sigma/dx$ for $Q^2 > 10000$ GeV^2 for all data samples is shown. At such high Q^2 value the contribution from the Z-boson exchange becomes visible, i.e. the single differential cross section for electrons is larger than for positrons for lower values of x.

The cross section for this Q^2 value is in general two orders of magnitude smaller than for $Q^2 > 200$ GeV^2 . As seen in the figure the cross section reaches a maximum at $x \sim 0.11$ for electrons and at a slightly smaller x value for the positrons. All data samples seem to agree

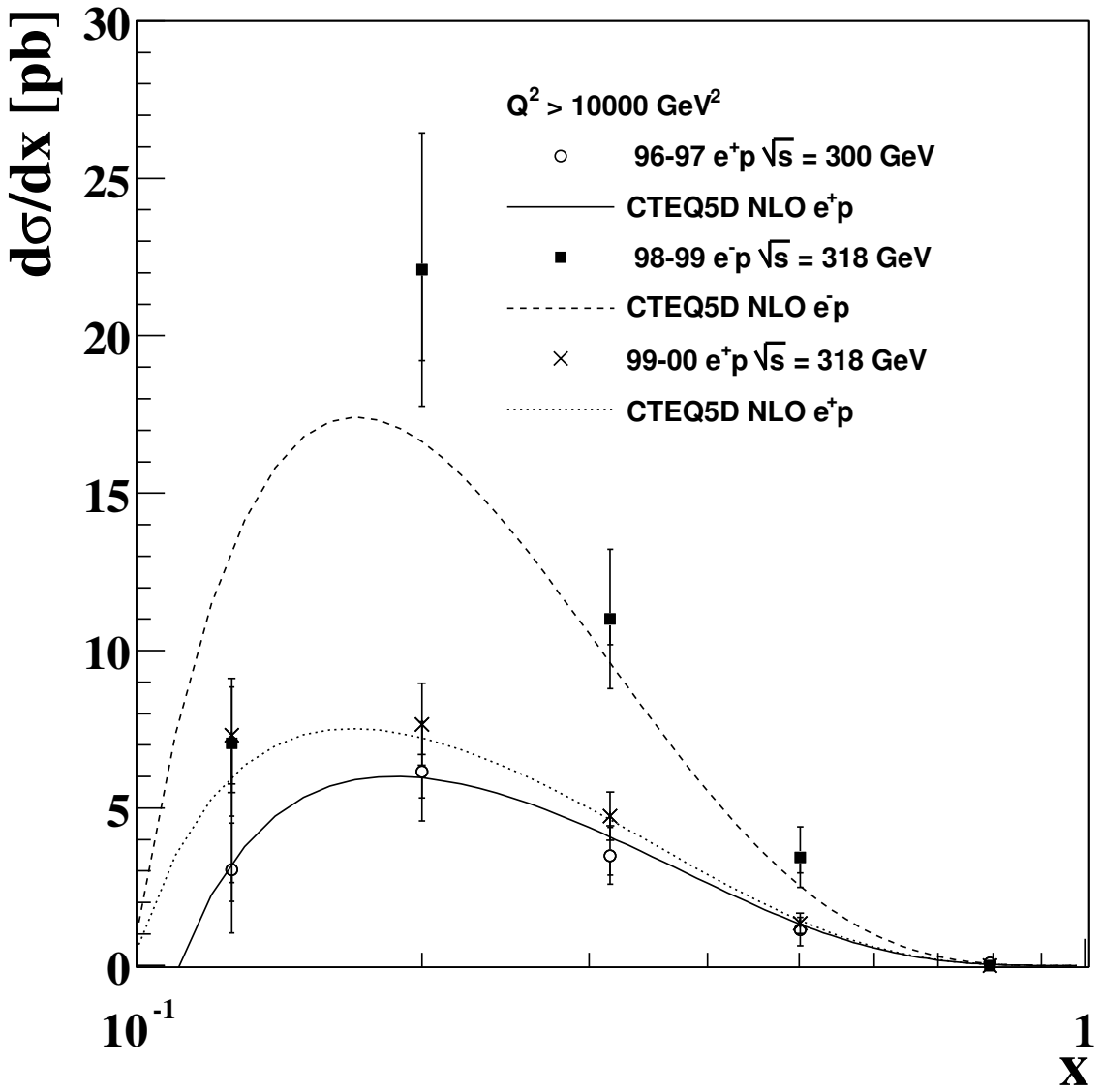

Figure 10.3: Single differential cross section $d\sigma/dx$ for $Q^2 > 10000$ GeV^2 for the 96/97 positron (open circles), 98/99 electron (closed squares) and 99/00 positron (crosses) data samples. The comparison to the Standard Model prediction calculated using the CTEQ5D parameterization is also shown for all data samples.

with the theory within the errors.

10.3 Measurement of the Single Differential Cross Section dσ/dy

The single differential cross section $d\sigma/dy$ has been calculated for $Q^2 > 200$ GeV^2 and plotted in Fig. 10.4 for all data samples. The cross section decreases one order of magnitude from the low y to the high y region. The behavior of the cross section seems to follow a $1/y^2$ slope, as

expected from its definition.

In the lower plot the ratio of the measured single differential cross section to the theory is shown for the all data samples. The $(e^+p)^{820}$ sample seems to be lower than the expectation. In the high y region, except for the last bin, it seems to agree better with the theory, while the other two samples seem to overshot the expected value.

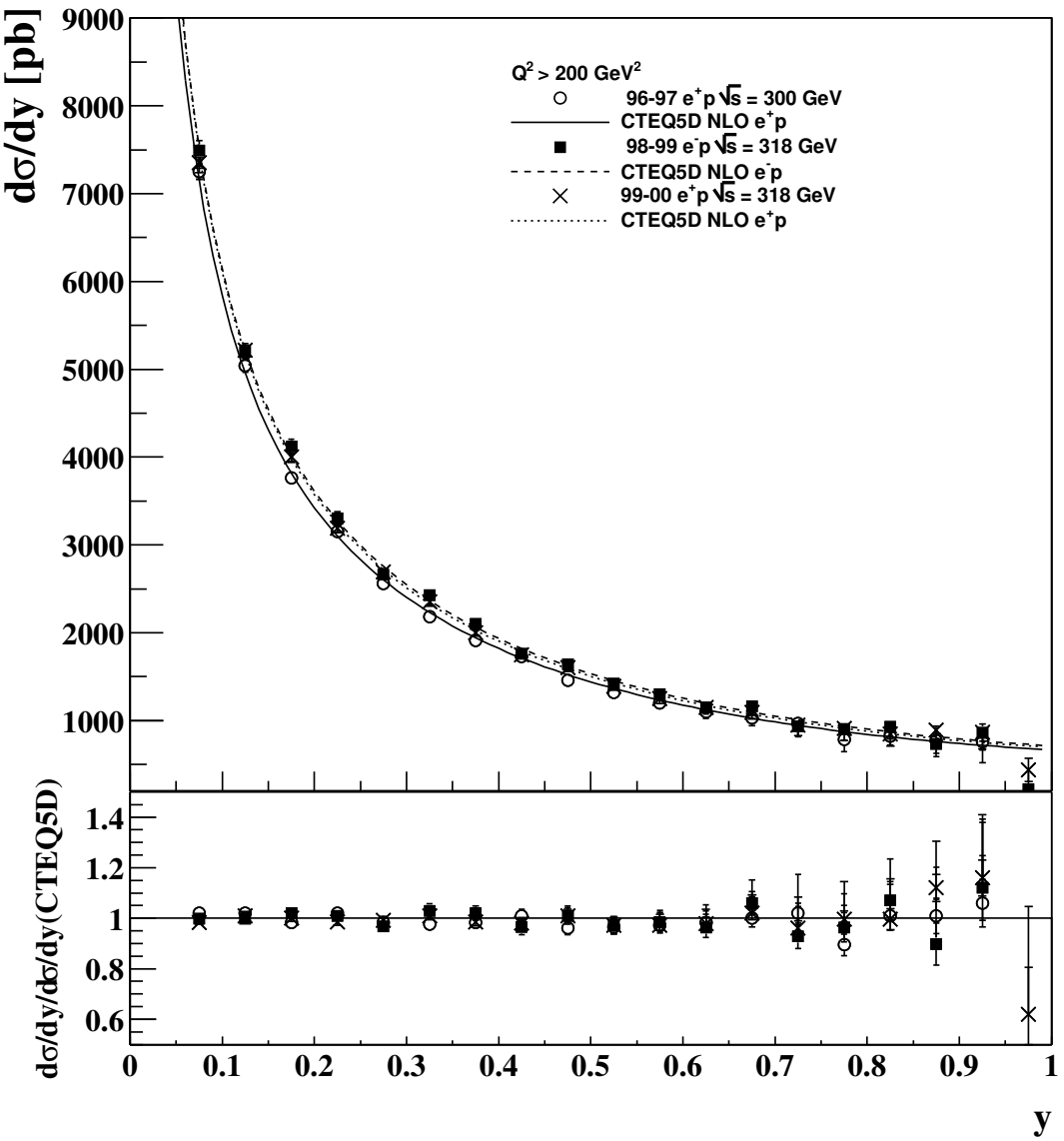

Figure 10.4: Single differential cross section $d\sigma/dy$ for $Q^2 > 200$ GeV^2 for the 96/97 positron (open circles), 98/99 electron (closed squares) and 99/00 positron (crosses) data samples. The comparison to the Standard Model prediction calculated using the CTEQ5D parameterization is also shown for all data samples.

10.4 Measurement of the Double Differential Cross Section $\mathrm{d}\sigma/\mathrm{dx}\,\mathrm{dQ}^2$

In Fig. 10.5 and Fig. 10.6 the reduced cross section for all data samples is shown. The reduced cross section is related to the double differential cross section via:

$$\tilde{\sigma^{\pm}} = \frac{xQ^4}{2\pi\alpha^2}\frac{1}{Y_+}\frac{d^2\sigma^{\pm}}{dx\,dQ^2}.$$

From the definition of the double differential cross section (Eq. (2.11)), the reduced cross section follows the form of $F_2(x, Q^2)$, small for high values of Q^2 and rising towards lower values of x.

For low values of Q^2 ($Q^2 < 1200$ GeV^2) the double differential cross section for both electrons and positrons is the same. Only when going to higher values of Q^2 the contribution of the Z-boson exchange starts to become visible. The cross section for electrons is larger than the one for positrons. This difference is exploited to extract the structure function of the proton $xF_3(x, Q^2)$. All data samples agree with the predicted theory values.

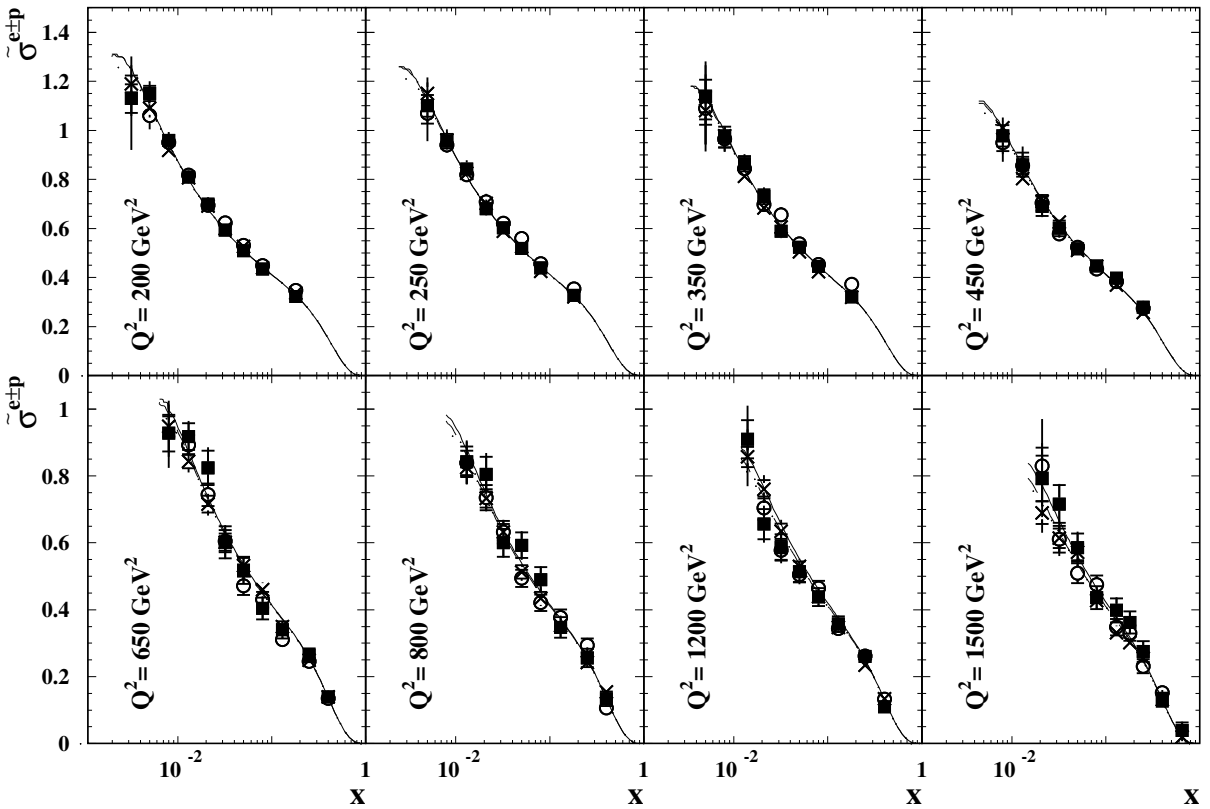

Figure 10.5: Reduced cross section $\tilde{\sigma}$ for $Q^2 > 200$ GeV^2 for the 96/97 positron (open circles), 98/99 electron (closed squares) and 99/00 positron (crosses) data samples. The comparison to the Standard Model prediction calculated using the CTEQ5D parameterization is also shown for all data samples.

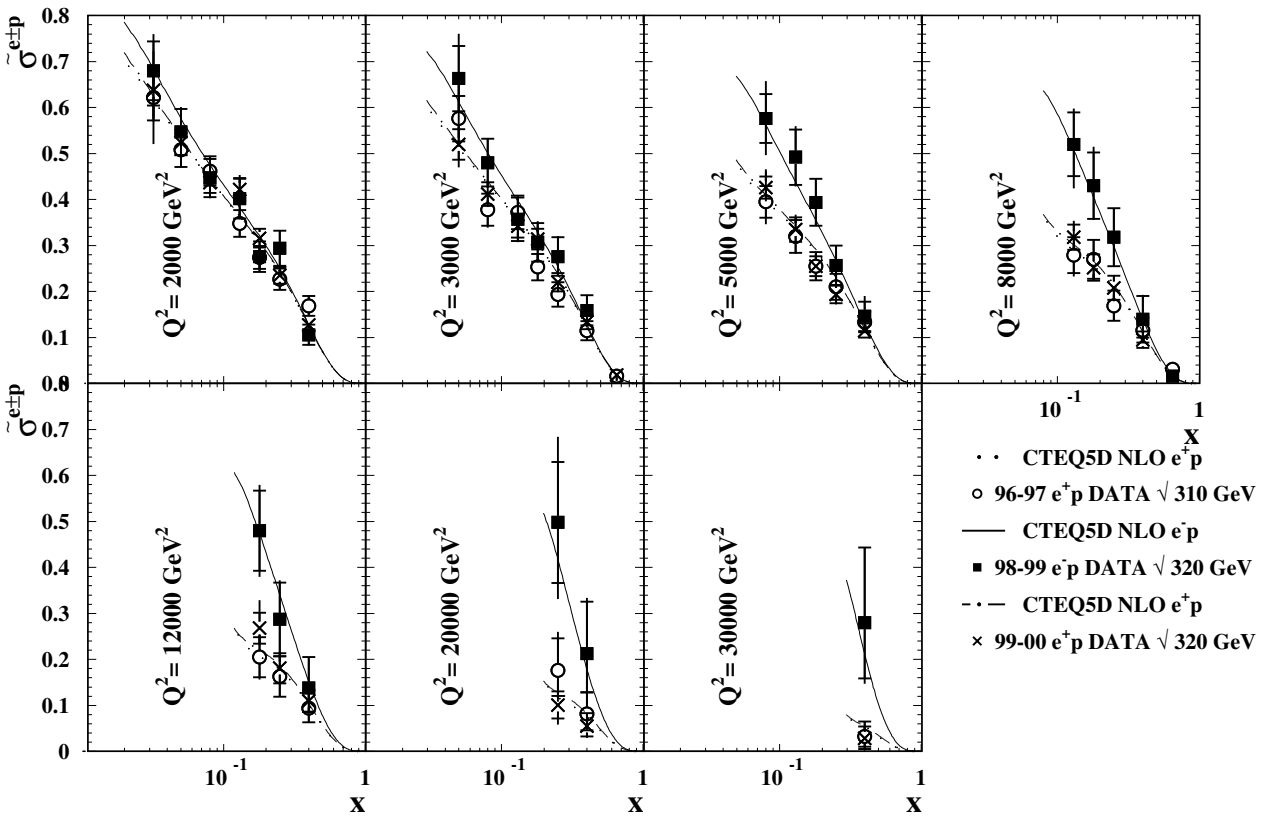

Figure 10.6: Reduced cross section $\tilde{\sigma}$ for $Q^2 > 200$ GeV^2 for the 96/97 positron (open circles), 98/99 electron (closed squares) and 99/00 positron (crosses) data samples. The comparison to the Standard Model prediction calculated using the CTEQ5D parameterization is also shown for all data samples.

Chapter 11

Results of the Extraction of the Structure Function $xF_3(x, Q^2)$

11.1 Extraction of the Structure Function $xF_3(x, Q^2)$

The extraction of the structure function of the proton $xF_3(x, Q^2)$ has been performed as explained in Chapter 5. All data samples, $(e^+p)^{820}$ $(e^-p)^{920}$ and $(e^+p)^{920}$, have been analyzed to obtain the $xF_3(x, Q^2)$ value from the double differential cross section, as presented in Chapter 10.

The statistical error on the extraction of $xF_3(x, Q^2)$ is clearly dominated by the electron sample (see Appendix A) therefore only the results of the combination of $(e^+p)^{820}$ and $(e^-p)^{920}$ is shown in this chapter.

The method to add the the $(e^+p)^{920}$ sample to the value obtained in this chapter and the final result can be found in Appendix A.

Due to the low statistics in the electron sample the double differential bins (Fig. 9.16) have been combined to reduce the statistical error. The new bins are shown in Fig. 11.1. Bins have been combined in x, keeping the Q^2 bins, only the two highest Q^2 bins have been combined.

The extracted values[1] of $xF_3(x, Q^2)$ are shown in Fig. 11.2. They are compared to the theoretical value of $xF_3(x, Q^2)$ obtained using the CTEQ5D parameterization for the parton density functions. The total error is dominated by the statistical error of the electron data sample. Within errors the extracted values are in agreement with the theory.

The shaded band corresponds to the contribution of $F_L(x, Q^2)$ which comes due to the different proton beam energies used to extract $xF_3(x, Q^2)$ (see Chapter 5). The contribution has been multiplied by 10 so that it can be seen in the figure. The contribution of $F_L(x, Q^2)$ is negligible and will be neglected from now on.

Observing the form of the theoretical prediction one can see that $xF_3(x, Q^2)$ follows the valence quark densities shown in Fig. 2.11. It is small for low x values, increases until its maximum is reached at $x \approx 0.1$ and decreases to zero for x tending to one.

Figure 11.3 shows $xF_3(x, Q^2)$ in bins of fixed x. Although only four bins for x are shown and the statistical errors are big, the data are consistent with the scaling violation already measured

[1] The values with statistical errors and systematic uncertainties can be found in Appendix J.

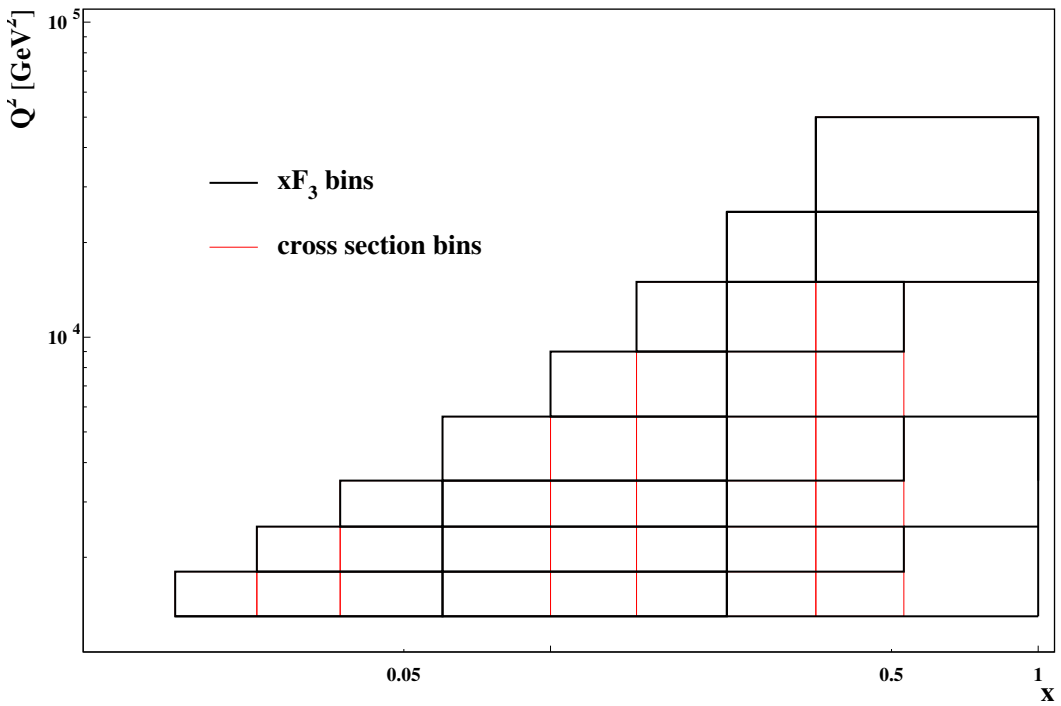

Figure 11.1: xF_3 bins in the $x\,Q^2$ kinematic plane. The bins used to measure the double differential cross sections (dotted line) have been combined (full line) in order to rise the statistics.

in $F_2(x, Q^2)$ (see Chapter 2). For different values of x the dependence of the structure function on Q^2 is different. For the low x value the slope of the curve rises faster than for the higher x value. The first three Q^2 bins for $x = 0.4$ have been combined weighted by the error.

11.2 Extraction of $xG_3(x, Q^2)$

Figure 11.4 shows the first $xG_3(x, Q^2)$ extraction made with ZEUS data. The values have been obtained using the relation $xF_3(x, Q^2) \approx -2a_e\chi_z(Q^2)xG_3(x, Q^2)$ already explained in Section 2.6. The x values at which the extraction is quoted have been shifted so that all the points become visible. From the data it is not possible to see the small Q^2 dependency of the structure function xG_3.

11.3 Comparison with other experiments

The statistical errors of the electron sample dominate the total error on $xG_3(x, Q^2)$. To reduce the statistical errors, the Q^2 bins have been combined. Weighted means have been taken of the measurements corrected to $Q^2 = 1500$ GeV^2 . The result is shown as black squares in Fig. 11.5.

The structure function $xG_3(x, Q^2)$ of the proton in neutral current events was first measured with polarized muon beams by the BCDMS collaboration [A$^+$84]. They measured $xG_3(x, Q^2)$ for 40 GeV^2 $< Q^2 <$ 180 GeV^2 . The use of polarized beams allows a measurement of the

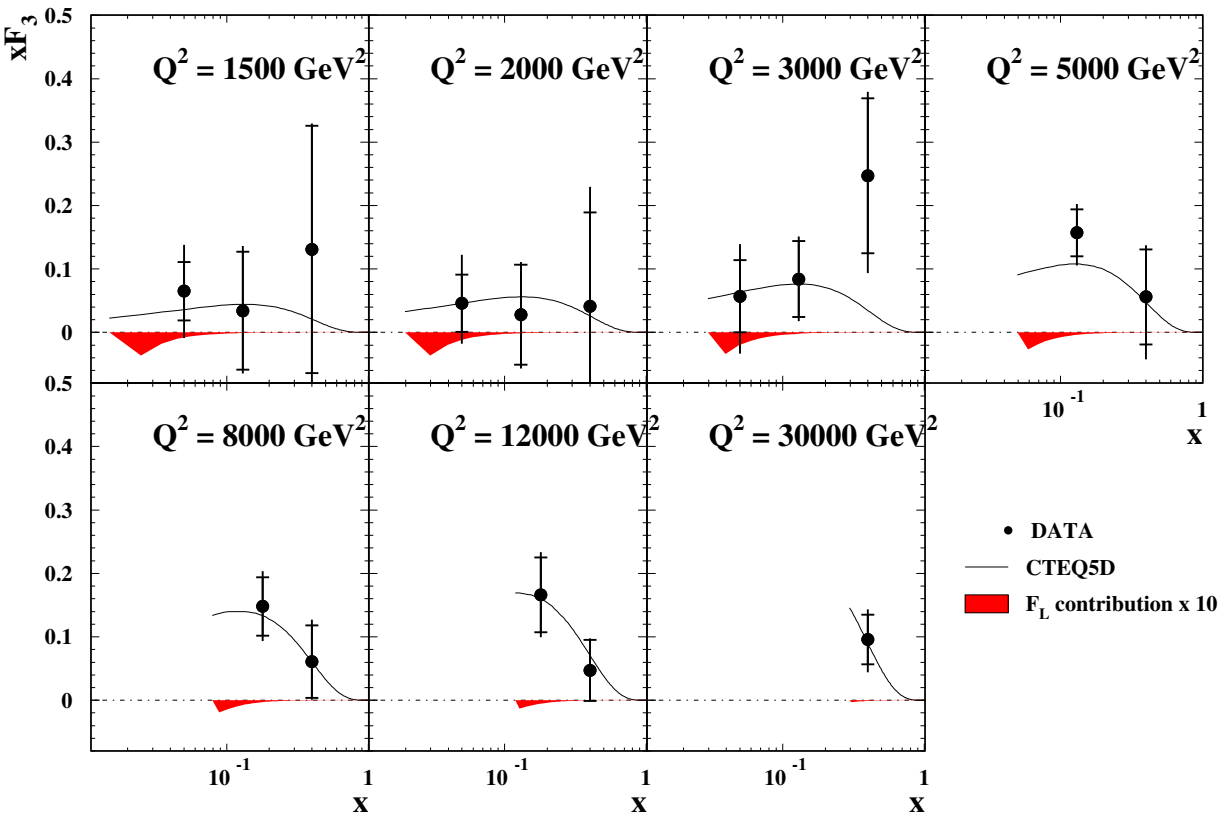

Figure 11.2: Structure function $xF_3(x, Q^2)$ of the proton extracted for the $(e^+p)^{820}$ and $(e^-p)^{920}$ data samples. The result is shown in fixed bins of Q^2.

structure function at such low Q^2 values. The results from the BCDMS collaboration are shown in Fig. 11.5 as open dots.

Also the comparison to data from other experiments is shown. Crosses and stars show the data obtained by the H1 collaboration [A+01] at $Q^2 = 5000\ \mathrm{GeV}^2$ and $Q^2 = 12000\ \mathrm{GeV}^2$ respectively. The neutral current data from HERA is in good agreement with the theoretical values within the big statistical errors.

The latest neutrino data from the CCFR experiment [S+97] is also shown (statistical errors only). Only two values of Q^2 from the 12 available have been shown. The first value, $Q^2 = 12.6\ \mathrm{GeV}^2$, is taken because it is the average Q^2 of the sample. The second value, $Q^2 = 125\ \mathrm{GeV}^2$, is the highest Q^2 bin with more than three bins in x. The $xF_3(x, Q^2)^{CC}$ values have been corrected using Eq. (2.21), to be compared to $xG_3(x, Q^2)$ values. The neutrino experiments have the smallest statistical errors of all data samples.

11.4 Sum rule for $\mathbf{xF_3(x, Q^2)}$

In Section 2.8 the sum rule for the structure functions $xF_3(x, Q^2)$ and $xG_3(x, Q^2)$ was derived.

It was also studied that, in principle, one could obtain the number of valence quarks, i.e. N_u and N_d, inside the proton by fitting the integral of $F_3(x, Q^2)$. Since the extraction of this

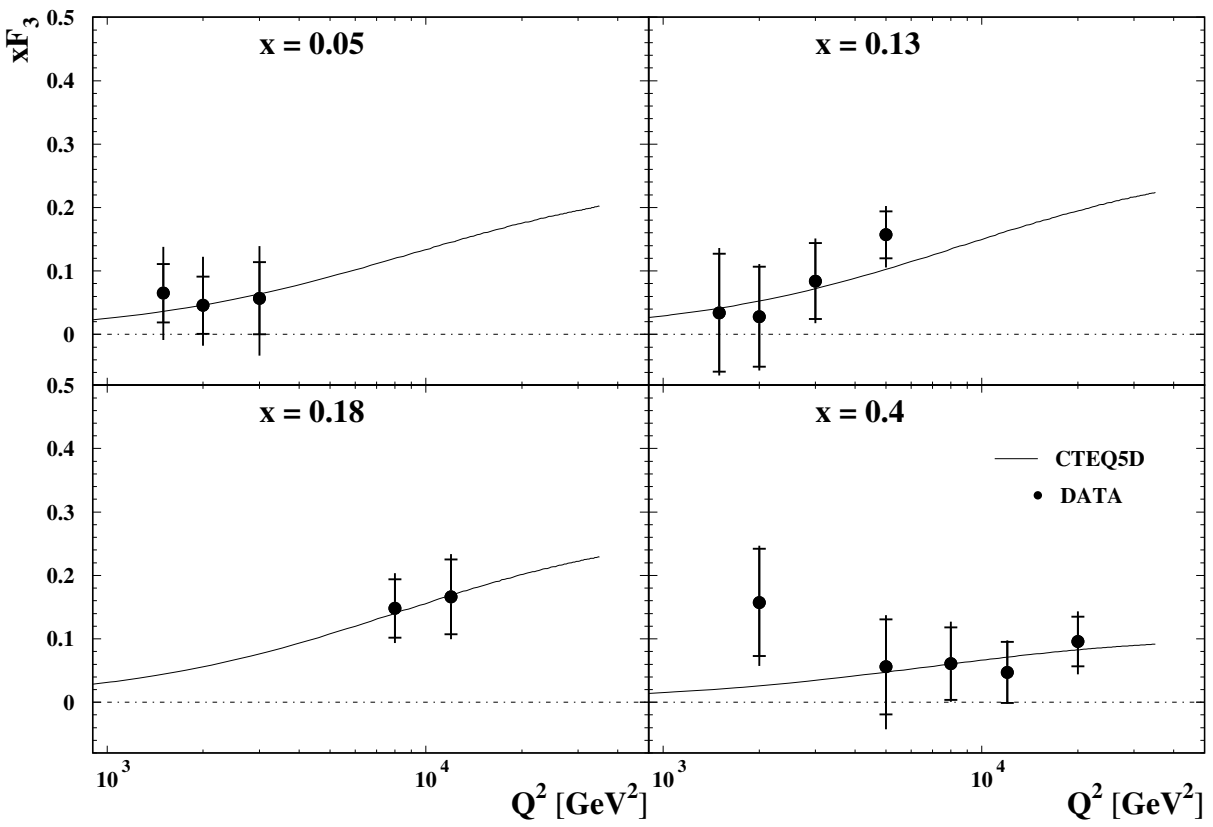

Figure 11.3: Structure function of the proton $xF_3(x, Q^2)$ extracted for the $(e^+p)^{820}$ and $(e^-p)^{920}$ data samples. The result is shown in fixed bins of x. The first three Q^2 bins for $x = 0.4$ have been combined weighted by the error.

structure function is clearly dominated by the statistical errors of the electron sample $(e^-p)^{920}$ this measurement can only be used as a test of the theory.

Figure 11.6 shows the integral:

$$J(Q^2) = \int_{x_{min}(Q^2)}^{1} \frac{dx}{x}\, xG_3$$

for the $xG_3(x, Q^2) = xF_3(x, Q^2)/[-2a_e\chi_z(Q^2)]$ value extracted form the data samples $(e^+p)^{820}$ and $(e^-p)^{920}$. The values of the theoretical prediction for the integral over the total interval $[0, 1]$ and over the interval $[x_{min}(Q^2), 1]$ are also given. The Q^2 dependency introduced by the integration over a limited range in x is clearly visible. It can be seen that when the integration range gets smaller, the integral departs from the nominal value at 5/3 and tends to zero.

The integral over $G_3(x, Q^2)$ is done as in [RS00] for the combined data at $Q^2 = 1500\,\mathrm{GeV}^2$. The obtained value for the integral Eq. (2.19) is:

$$J(Q^2) = \int_{0.017}^{0.65} dx\, G_3(x, Q^2) = 1.17 \pm 0.44\,\mathrm{stat.}\, {}^{+0.45}_{-0.44}\,\mathrm{sys.}$$

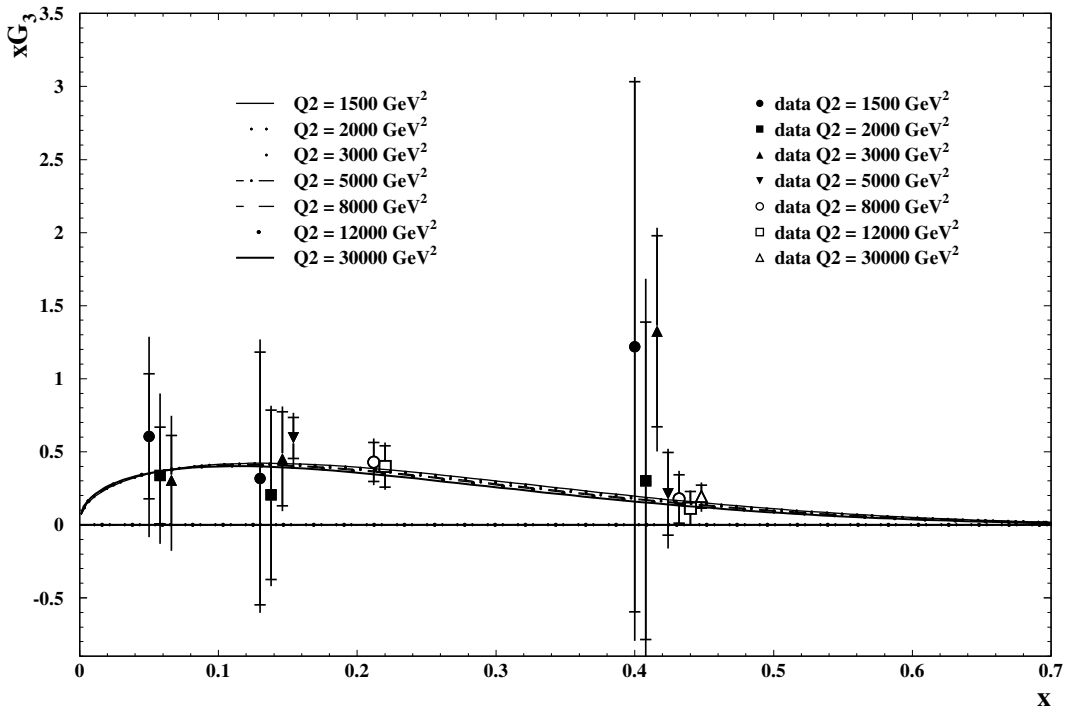

Figure 11.4: Extraction of the structure function $xG_3(x, Q^2)$ for different x and Q^2 bins.

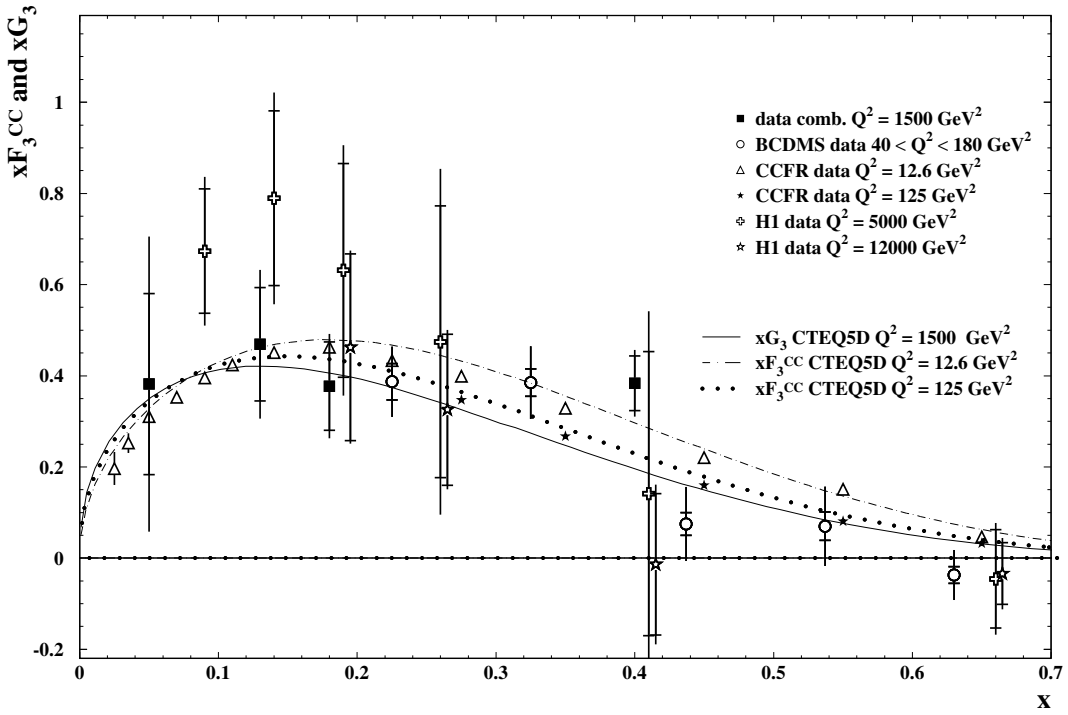

Figure 11.5: Comparison of xG_3 and xF_3^{CC} values for different experiments.

The value obtained is in good agreement with the expected value $J(Q^2) = 1.16$ calculated using the CTEQ5D parameterization. Due to the big statistical errors and systematic uncertainties the obtained value cannot be used to see the preference of the data for one parameterization or other (see Chapter 2).

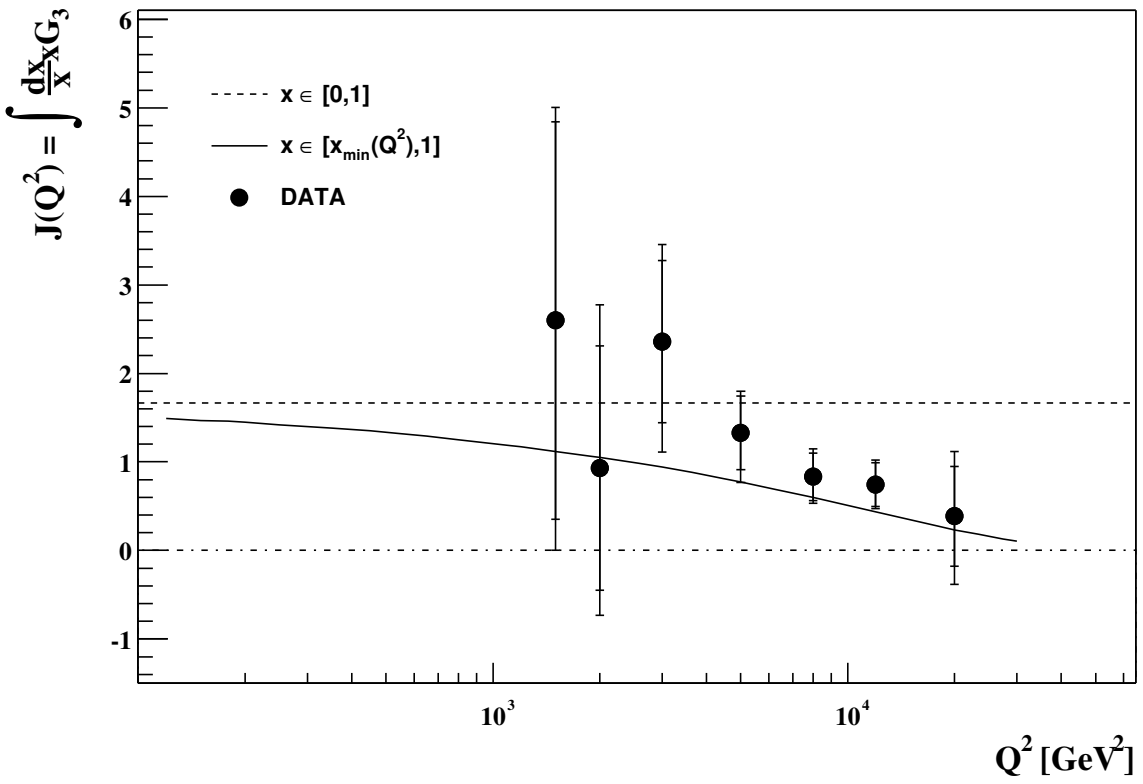

Figure 11.6: Integral of G_3 for different values of Q^2. The full line shows the integral over the restricted range $x \in [x_{min}(Q^2), 1]$. The dotted line shows the integral for the whole range $x \in [0, 1]$.

The result obtained with H1 data [RS00] is $J(Q^2) = 1.88 \pm 0.35\,(\text{stat.}) \pm 0.27\,(\text{sys.})$, which is, within the errors, also in good agreement.

Chapter 12

Summary and Outlook

This thesis has presented the first test of parity violation effects due to weak interactions in neutral current events using ZEUS data.

Parity violation has already been tested in neutrino–nucleon scattering experiments in charged current events where the exchanged weak bosons are the $W^{\pm}$ bosons. The region covered by these experiments is $Q^2 < 200$ GeV^2. The structure function $xG_3(x, Q^2)$ has also been measured before in neutral current events in muon–nucleon experiments. The region covered by this experiment is $40 < Q^2 < 180$ GeV^2 . In this work the explored region starts at $Q^2 > 1500$ GeV^2.

The structure function of the proton $xF_3(x, Q^2)$ has been extracted with the aim to test the parity violation effect introduced by the exchange of the weak Z-boson in deep inelastic neutral current events. In order to extract the structure function the data samples 96/97 positron, 98/99 electron and 99/00 positron data samples have been analyzed.

During the study, the Monte Carlo simulation and the existing algorithms have been tested, and the precision of the detector has been measured. The final results show a very good agreement, for all data samples, between the data and the Monte Carlo simulation. This agreement is afterwards confirmed again in the extraction of the cross sections.

Single and double differential cross sections have been measured and shown with statistical errors and systematic uncertainties. The data at high Q^2 shows the parity violation effect introduced by the exchange of the weak boson Z. The Standard Model, in which left- and right-handed fermions are treated differently, is able to describe the data over a wide range in x and Q^2.

The structure function $xF_3(x, Q^2)$ has been obtained from the subtraction of the double differential cross section for electrons and positrons at high Q^2. A special method has been developed in the framework of this work in order to extract $xF_3(x, Q^2)$ with the smallest possible statistical error. Nevertheless the total error of the structure function is dominated by the statistical error of the electron sample.

The result has been presented in bins of fixed Q^2 as a function of x, and in bins of fixed x as a function of Q^2. In the first case the sensitivity to the valence quarks could be observed, in the second case, the scaling violation already seen in $F_2(x, Q^2)$ could be confirmed.

A phenomenological study on $xF_3(x, Q^2)$ has been performed. A new sum rule for the structure function $xF_3(x, Q^2)$ has been derived in the same way as the Lewellyn-Smith sum rule for

$xF_3(x,Q^2)^{CC}$ [GS69]. This measurement could be used to extract the number of valence quarks inside the proton. Unfortunately, due to the big errors, it could only be used as a test of the already postulated and confirmed numbers. The obtained results are in good agreement, within the errors, with the Standard Model predictions.

The structure function $xG_3(x,Q^2)$ has been obtained from $xF_3(x,Q^2)$ neglecting the contribution from $xH_3(x,Q^2)$ and has been compared to other values of $xG_3(x,Q^2)$ measured using NC DIS events, as well as to xF_3^{CC} data obtained from neutrino-nucleon DIS experiments.

The measurement of $xF_3(x,Q^2)$ or $xG_3(x,Q^2)$ performed in this analysis is clearly dominated by the statistical error. A way to improve the measurement is to use the data that will be taken after the luminosity upgrade. Figure 12.1 shows the statistical errors from the measurement shown here, outer bars, compared to the statistical errors that one could achieve with 150 pb^{-1} of electrons and the same quantity of positrons.

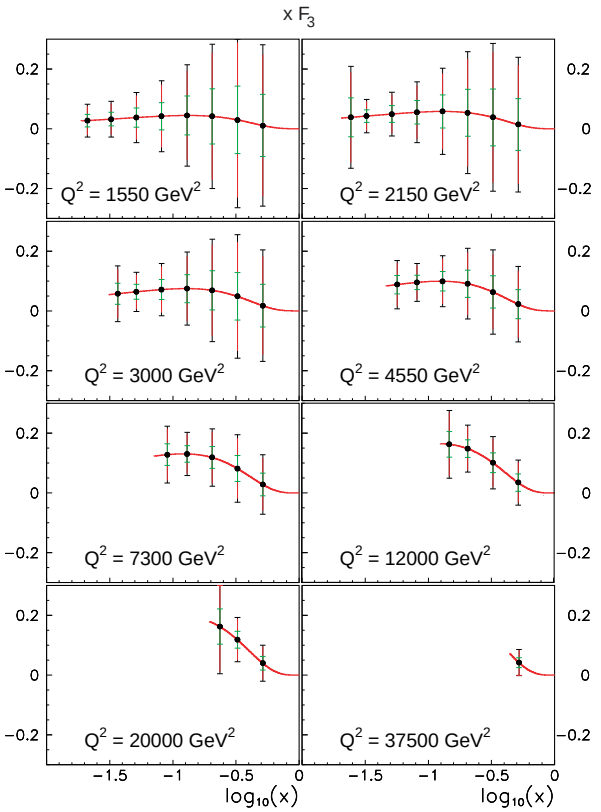

Figure 12.1: Change of the statistical error of $xF_3(x,Q^2)$ with increasing luminosity. The outer error bar corresponds to the statistical error of this measurement. The inner error bar shows the statistical error with 150 pb^{-1} of e^+p and 150 pb^{-1} of e^-p data.

For the high x and high Q^2 region there is a big improvement. This is the region in which a precise measurement of $xF_3(x,Q^2)$ could help to constrain the valence quark densities.

After the luminosity upgrade, HERA will be running with polarized beams [Lon99, Beh]. As seen from the data of the BCDMS collaboration, having polarized beams increases the sensitivity to $xF_3(x,Q^2)$ at lower values of Q^2. This means that HERA would be able to measure $xF_3(x,Q^2)$ in a region that overlaps with the neutrino experiments.

Figure 12.2 shows the coefficients $-a_e\chi_z(Q^2)$, $-v_e\chi_z(Q^2)$, $(a_e^2+v_e^2)\chi_z^2(Q^2)$ and $2a_ev_e\chi_z^2(Q^2)$ as in Fig. 2.12 but now with different polarizations (λ). The polarization can be chosen in such

a way that the sensitivity to $xF_3(x, Q^2)$ is maximal. Taking $\lambda = +1$ for positrons and $\lambda = -1$ for electrons one can calculate the difference of the cross sections for electrons and positrons from Eq. (2.12).

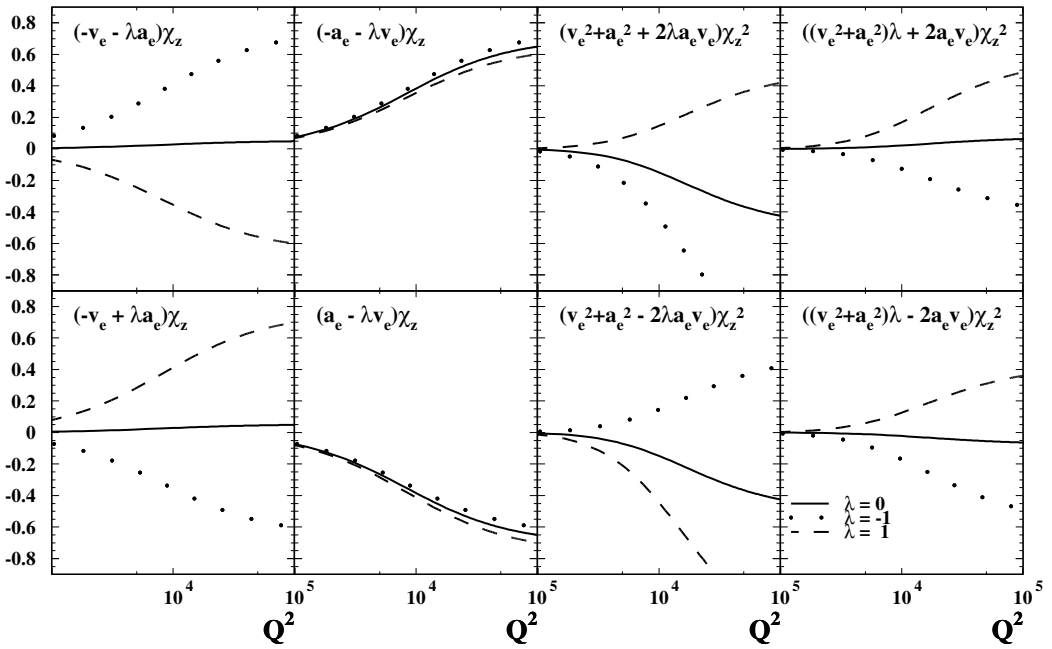

Figure 12.2: Electroweak couplings multiplied by the Z propagator for positrons (top) and electrons (bottom), for different polarizations as a function of Q^2.

Comparing the obtained value with the result one would obtain with no polarization ($\lambda = 0$) one sees that the sensitivity to $xF_3(x, Q^2)$ increases by $(a_e + v_e)/a_e \approx 45\%$.

Acknowledgments

The achievement of this thesis has only been possible with the help of many people. I would like to take this opportunity to thank them all.

First of all I would like to thank my supervisor Dr. Stefan Schlenstedt for giving me the opportunity to do my Ph.D. at DESY Zeuthen, and for his good advises. I also would like to thank the referees Prof. Thomas Lohse, Prof. Paul Söding and Prof. Ulrich Katz, for reading and evaluating this thesis.

Special thanks to Dr. Ken Long and Dr. Antonio Pellegrino for the useful comments and corrections to the written work. I will like to thank Dr. Juan Terrón and Dr. Tancredi Carli for helping me to prepare the thesis defense.

The achievement of the results presented in this thesis has been possible due to the hard work of my colleagues' group Matthias Moritz, Henning Schnurbusch, Alexander Kappes, and Ricardo Gonçalo.

Living in a foreign country has been made easier thanks to the warm welcome of the ZEUS students, Dr. Margherita Milite, Dr. Florian Goebel, Monica Vazquez, Dr. Ignacio Redondo, Oscar Gonzalez, Dr. Stefan Stonjek, Sven Schagen, Jaap Velthuis, Dr. Dorian Kçira and the already mentioned.

Agradezco a mis amigos y familia en España por su apoyo a pesar de los 2200 km de distancia que nos separan. Un agradecimiento especial a Laura López por estar siempre al otro lado y por haber compartido confidencias conmigo por mail, teléfono y en vivo a los dos lados de los Pirineos.

Dedico esta tesis a mis padres Gloria y Luis, a mis hermanos Lola y Luis y a mis abuelas Gertrud Stern y Maria Urreiztieta por haber hecho el largo camino conmigo y sin ayuda de los cuales nunca habria podido terminar esta tesis. Tambien dedico esta tesis a Benedikt Plümper, compartir mi vida con él ha sido lo mejor que he obtenido de este doctorado.

Appendix A

Adding the $(e^+p)^{920}$ Data for the Extraction of $xF_3(x, Q^2)$

After operating with electrons, HERA decided to switch back to positrons. ZEUS acquired then a great amount of positron data with proton beam energy $E_p = 920$ GeV. With the possibility of doubling the positron data, the wish came to combine all three data samples to calculate $xF_3(x, Q^2)$ with statistical errors as small as possible. Then as before, the question of how to combine data samples with different proton energy arose.

Mathematically it is allowed to combine the two positron data samples $(e^+p)^{820}$ and $(e^-p)^{920}$ in one and extract, together with the electron sample $(e^-p)^{920}$, $xF_3(x, Q^2)$. This easy solution cannot be considered since the double differential cross section calculated for both positron samples together at the same x and Q^2 point would have different values of y yielding to a non physical result.

The only solution left is to extract $xF_3(x, Q^2)$ from each positron data sample together with the electron data sample, and then combine the two obtained values. When doing that one should take special care in the combination, since the two $xF_3(x, Q^2)$ values are correlated through the electron sample.

The extraction of $xF_3(x, Q^2)^{820}$ with the data samples $(e^+p)^{820}$ and $(e^-p)^{920}$ has already been presented in Section 5.4.

When combining the data samples $(e^+p)^{920}$ and $(e^-p)^{920}$ both data samples have the same proton beam energy ($E_p = 920$GeV) and $xF_3(x, Q^2)^{920}$ can be calculated by simply subtracting the double differential cross sections for electrons and positrons as shown below:

$$xF_3(x, Q^2)^{920} = \left(\frac{xQ^4}{2\pi\alpha^2}\right)\left(\frac{1}{2Y_-^{920}}\right)\left(\frac{d^2\sigma^-}{dx\,dQ^2} - \frac{d^2\sigma^+}{dx\,dQ^2}\right).$$

The statistical error on this quantity is:

$$\delta^2(xF_3(x, Q^2)^{920}) = \left(\frac{xQ^4}{2\pi\alpha^2}\right)^2\left(\frac{1}{2Y_-^{920}}\right)^2\left\{\left[\delta\left(\frac{d^2\sigma^-}{dx\,dQ^2}\right)\right]^2 + \left[\delta\left(\frac{d^2\sigma^+}{dx\,dQ^2}\right)\right]^2\right\}.$$

Having obtained the two $xF_3(x, Q^2)$ values, now the combination of these two follows.

A.1 Combination of the Data Samples

The presence of a correlation term prevents the two results from being combined with the usual formula of the average weighted with the inverse of the variance.

A way to overcome this problem is given by the fact that the correlation:

$$\rho(xF_3^{820}, xF_3^{920}) = \frac{cov(xF_3^{820}, xF_3^{920})}{\delta(xF_3^{820})\delta(xF_3^{920})},$$

is positive, where the covariance is defined as:

$$cov(xF_3^{820}, xF_3^{920}) = \frac{\partial\left(xF_3^{820}\right)}{\partial\left(\frac{d^2\sigma^-}{dxdQ^2}\right)}\frac{\partial\left(xF_3^{920}\right)}{\partial\left(\frac{d^2\sigma^-}{dxdQ^2}\right)}\delta^2\left(\frac{d^2\sigma^-}{dxdQ^2}\right).$$

Then the correlation between the two results is equal to that introduced by an uncertainty on a common offset [D'A94].

The variances associated to each $xF_3(x,Q^2)$ value may be considered as being formed of two parts: one of these parts is common to both variances, while the other is individual. The common part is given by the covariance. The individual contribution to each variance is then evaluated subtracting the covariance. This procedure allows the expected value $xF_3(x,Q^2)$ to be evaluated as the average of xF_3^{820} and xF_3^{920}, weighted with the inverse of the individual variance. We have then:

$$xF_3 = \frac{1}{W}\left(\frac{xF_3^{820}}{w^{820}} + \frac{xF_3^{920}}{w^{920}}\right),$$

where W, w^{820} and w^{920} are defined in terms of the covariance as follows:

$$W = \frac{1}{w^{820}} + \frac{1}{w^{920}},$$

$$w^{820} = \delta^2\left(xF_3^{820}\right) - cov\left(xF_3^{820}, xF_3^{920}\right),$$

$$w^{920} = \delta^2\left(xF_3^{920}\right) - cov\left(xF_3^{820}, xF_3^{920}\right).$$

The statistical error for the new $xF_3(x,Q^2)$ value is given by:

$$\delta^2(xF_3) = \frac{1}{W} + cov(xF_3^{820}, xF_3^{920}).$$

A.2 Reduction of the Statistical Error with Increasing Luminosity.

Now that one has an expression for the new combined value and its error, one could in principle do an academic study to see the change in the relative statistical error of $xF_3(x,Q^2)$ when adding new luminosity. The cross section is related to the number of events normalized to the luminosity. Considering Gaussian errors on xF_3^{820} and xF_3^{920}, one can substitute the errors on the double differential cross sections and by the Gaussian error given by:

$$N = \sigma \cdot \mathcal{L} \rightarrow \delta^2(N) = \frac{1}{N} = \frac{1}{\sigma\mathcal{L}}.$$

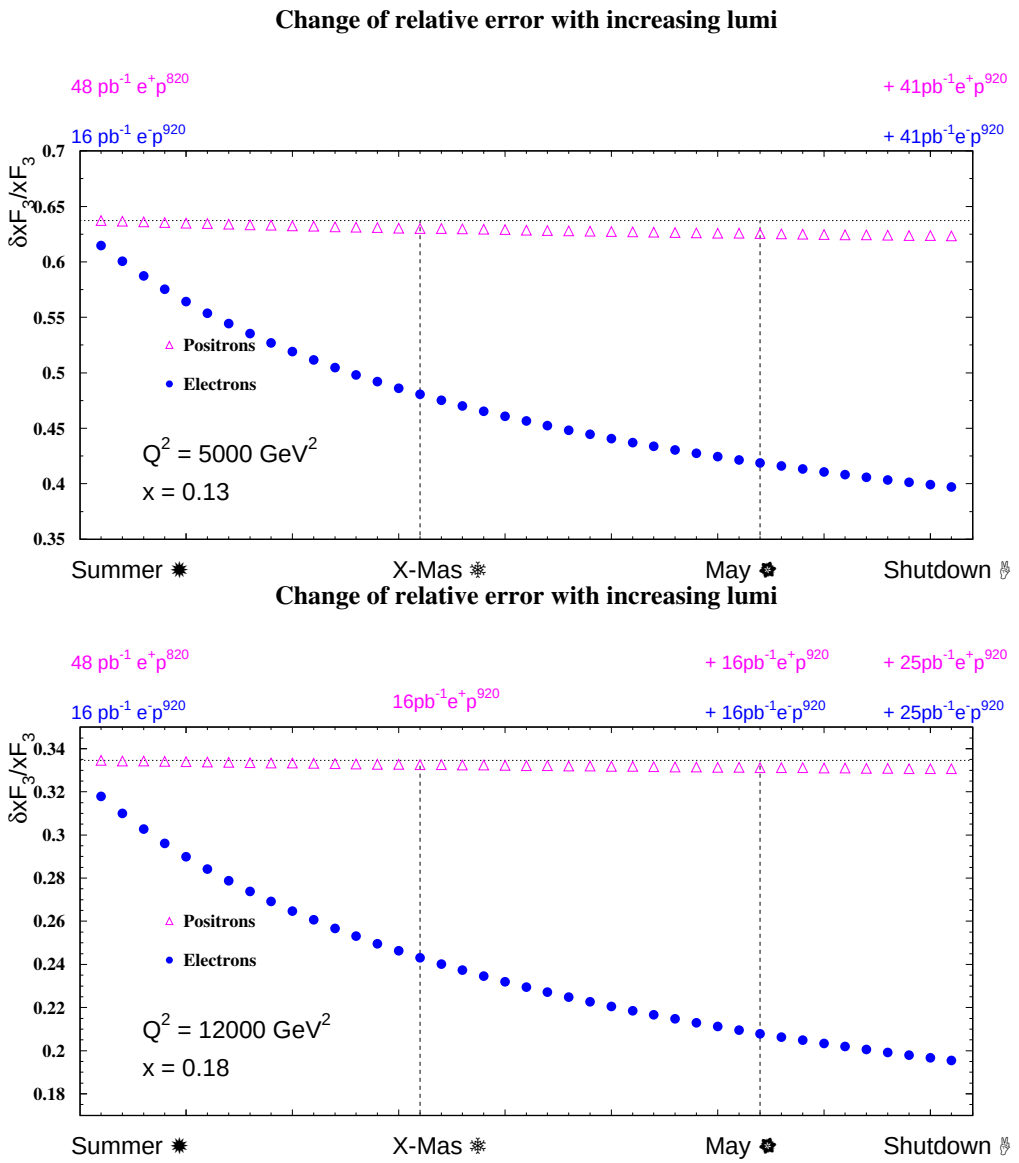

Figure A.1: Change of the relative $xF_3(x, Q^2)$ errors with increasing luminosity for $x = 0.13$ and $Q^2 = 5,000$ GeV^2 bin (top) and the $x = 0.18$ and $Q^2 = 12,000$ GeV^2 bin (bottom). On the x axis Summer corresponds to the 99 Summer and it has been supoused a luminosity average of 3 pb^{-1} per month.

It is clear that increasing the luminosity will reduce the statistical error.

One can see in Fig. A.1 that when increasing the positron data sample, the relative error does not change at all. On the other hand, when increasing the electron data sample, the relative error reduces considerably, giving the prove that the statistical errors in the $xF_3(x, Q^2)$ measurement are dominated by the small luminosity of the electron sample, and adding more positron data does not help to bring them down.

Figure A.2 shows the combined value of $xF_3(x, Q^2)$ for all data samples. The value has been obtained as explained in section A.1 using the obtained values shown in Fig 11.2.

If one compares the results shown here with the results shown in Fig. 11.2 one can hardly see any difference in the size of the errors. Even adding almost 60 pb^{-1} of positron data the statistical error does not decrease, since it is dominated by the statistical error of the electron

sample.

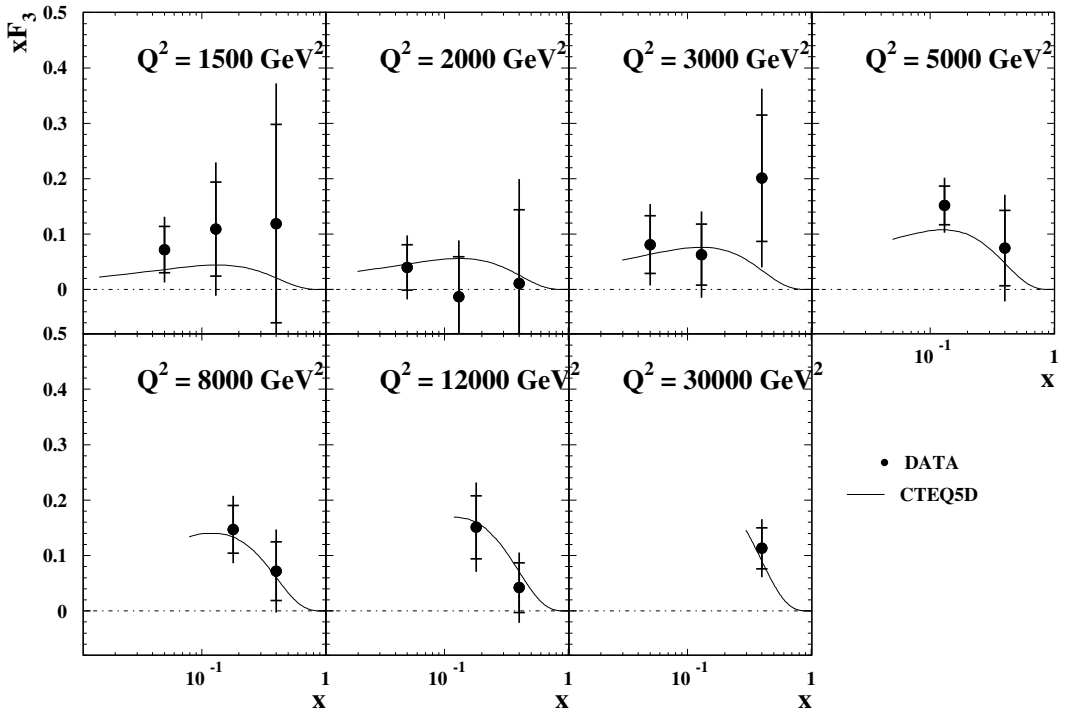

Figure A.2: Structure function of the proton $xF_3(x, Q^2)$ extracted for all data samples. The result is shown in fixed bins of Q^2.

Appendix B

Plots to the Monte Carlo Energy Smearing Estimation

As seen in Section 8.2.4 the Monte Carlo energy has to be smeared so that the data and Monte Carlo energy resolution agree. The value by which the Monte Carlo energy has to be smeared is calculated in bins of the measured energy E_e independently for the RCAL and the BCAL because the range of scattered lepton energies in both calorimeters is different.

The RCAL is divided in 9 bins. The boundaries of these bins are [8.0, 15.0, 18.0, 20.0, 22.0, 24.0, 26.0, 28.0, 30.0, 35.0] GeV. This binning has been chosen to expand the Kinematic Peak region. For each bin the distribution E_e/E_{DA} is plotted as shown in Fig. B.1. E_e is the energy of the scattered lepton after non-uniformity and dead-material corrections. The data and Monte Carlo distributions are fitted to a Gaussian function, the results of the fit are also shown in the figure. One can see that the distributions in the middle energy region, present tails towards smaller values of one. These tails come from radiative events. So that the measurement does not get distort, only the central peak of the distribution has been fitted.

In the BCAL the same procedure is done this time with the bin boundaries [8.0, 15.0, 20.0, 25.0, 30.0, 35.0, 40.0, 50.0, 80.0, 500.0] GeV. The binning has been chosen so that high energetic scattered leptons are also considered. The distributions and the result of the Gaussian fits from the central part of the distribution is shown in Fig. B.2.

the complete study and the results can be found in Section 8.2.4.

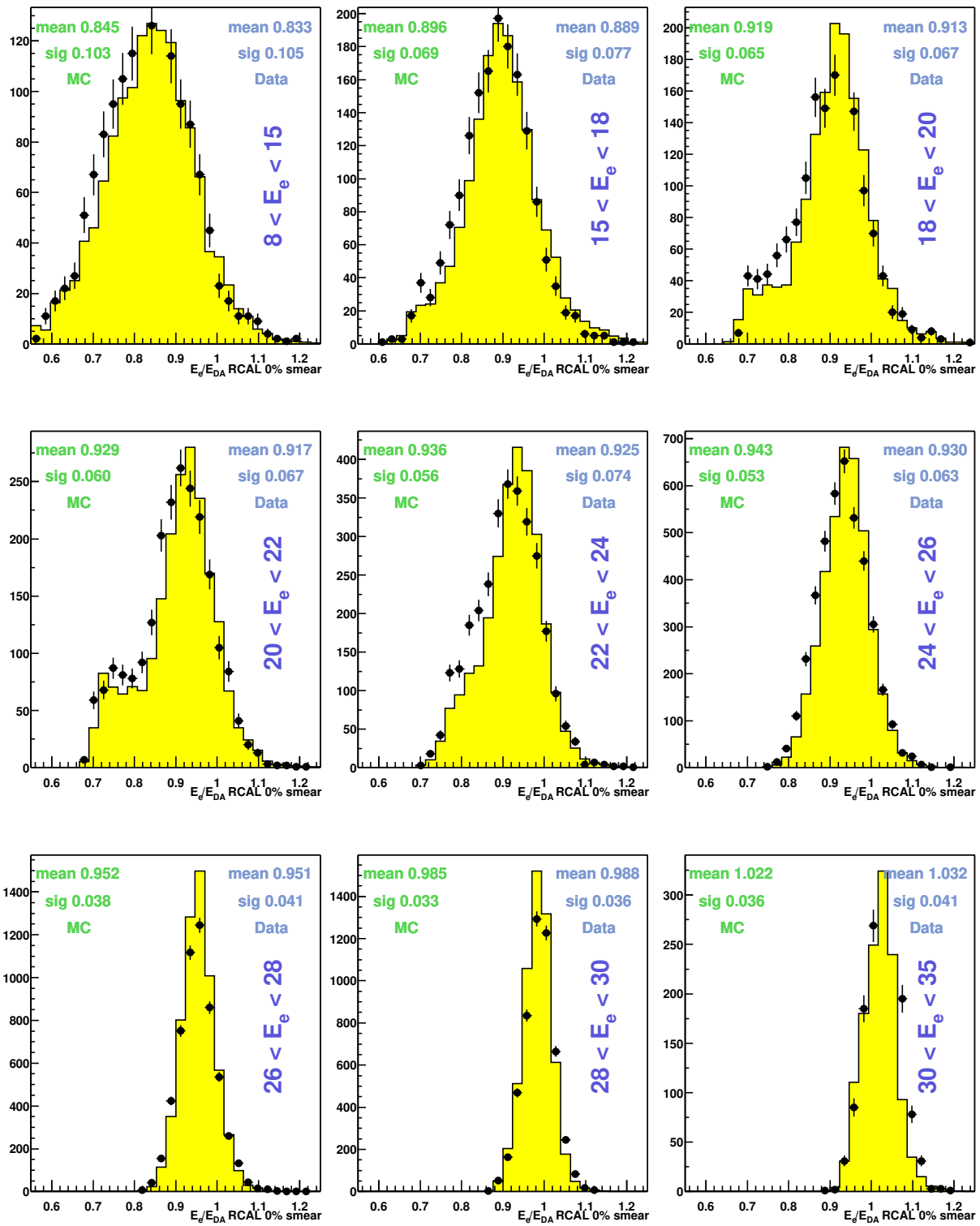

Figure B.1: E_e/E_{DA} in different bins of E_e for scattered leptons in the RCAL.

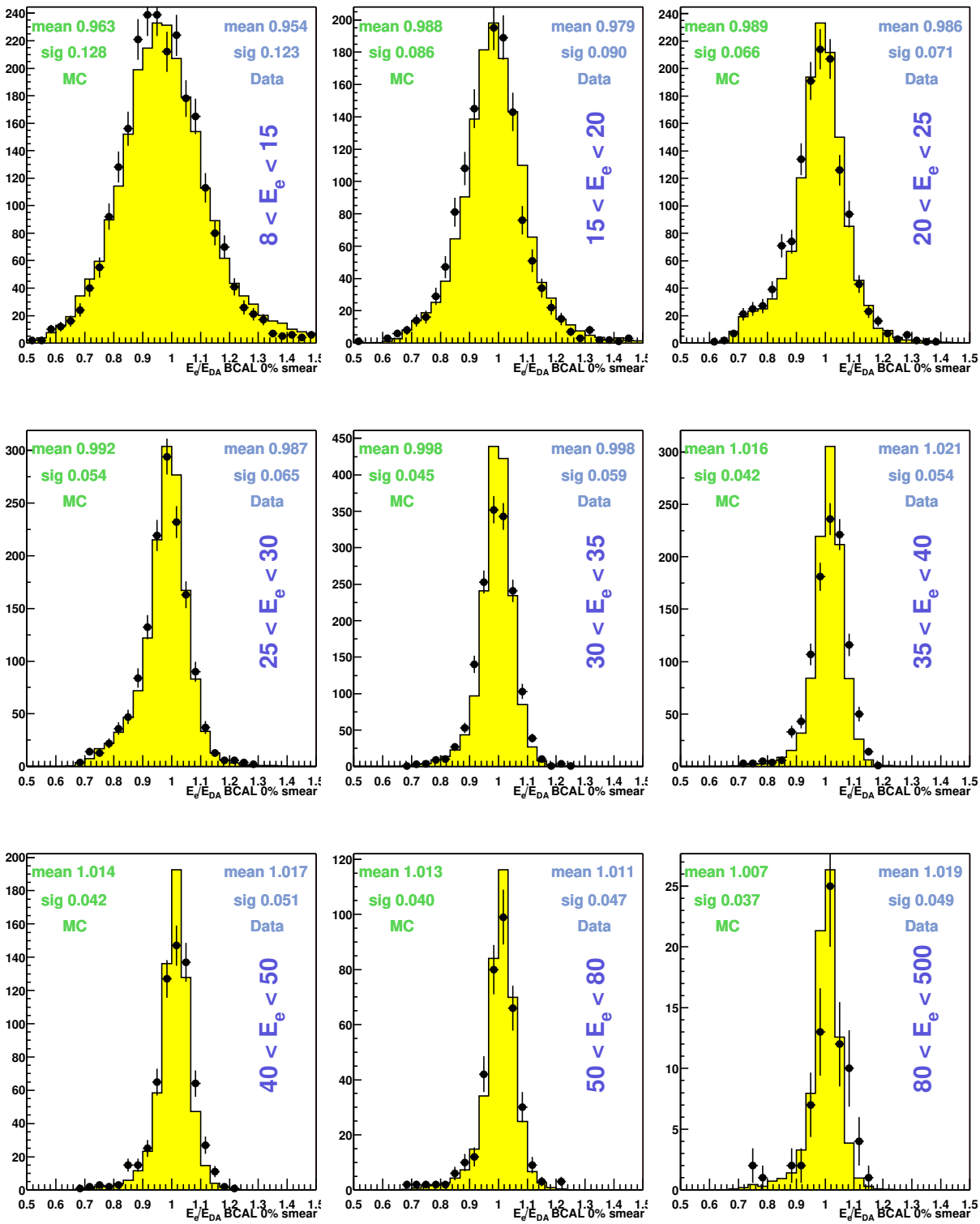

Figure B.2: E_e/E_{DA} in different bins of E_e for scattered leptons in the BCAL. The events correspond to the sample used to perform the analysis.

Appendix C

Causes of Inefficiency of the Electron-Finder SINISTRA95

There are different reasons leading to inefficiencies of SIRA 5. One is the fact that there is a number of events in which the vertex is mismeasured, another big problem are events with QED radiation that are difficult to tag. There are also minor problems not treated in detail in this appendix.

C.1 Wrong Vertex Measurement

In cases in which the vertex is not properly reconstructed the difference between Θ_{true} and the wrongly reconstructed Θ_e might become large and therefore the candidate is not considered as the scattered lepton. This is, of course, not a problem of the electron-finder but of the vertex package (with implications on the analysis presented here). ε^{DIS} has been calculated again using only events in which the reconstructed vertex is not further away than 5 cm from the real vertex.

The improvement in the efficiency is expected to be outside the CTD region where the angles are calculated using calorimeter information. One can observe in Fig. C.1 that in the case of SIRA there is an improvement of the efficiency of 3% in the RCAL region and the drop in the efficiency at the end of the CTD disappears.

To solve this problem one makes use the track of the scattered lepton to reconstruct the vertex.

C.2 Radiative Events

There is still a big difference between ε^{found} and ε^{DIS} . The main difference comes from a possible misidentification of the scattered lepton in radiative events. In some cases the scattered lepton is contained in the list of candidates but the candidate chosen as the scattered lepton is a radiated photon. The radiative events considered are Compton events, initial state radiation (ISR) events and final state radiation (FSR) events.

Compton events are quasi-elastic events and the signature is two electromagnetic clusters in the calorimeter, one belonging to the scattered lepton and one to the photon. If the photon is

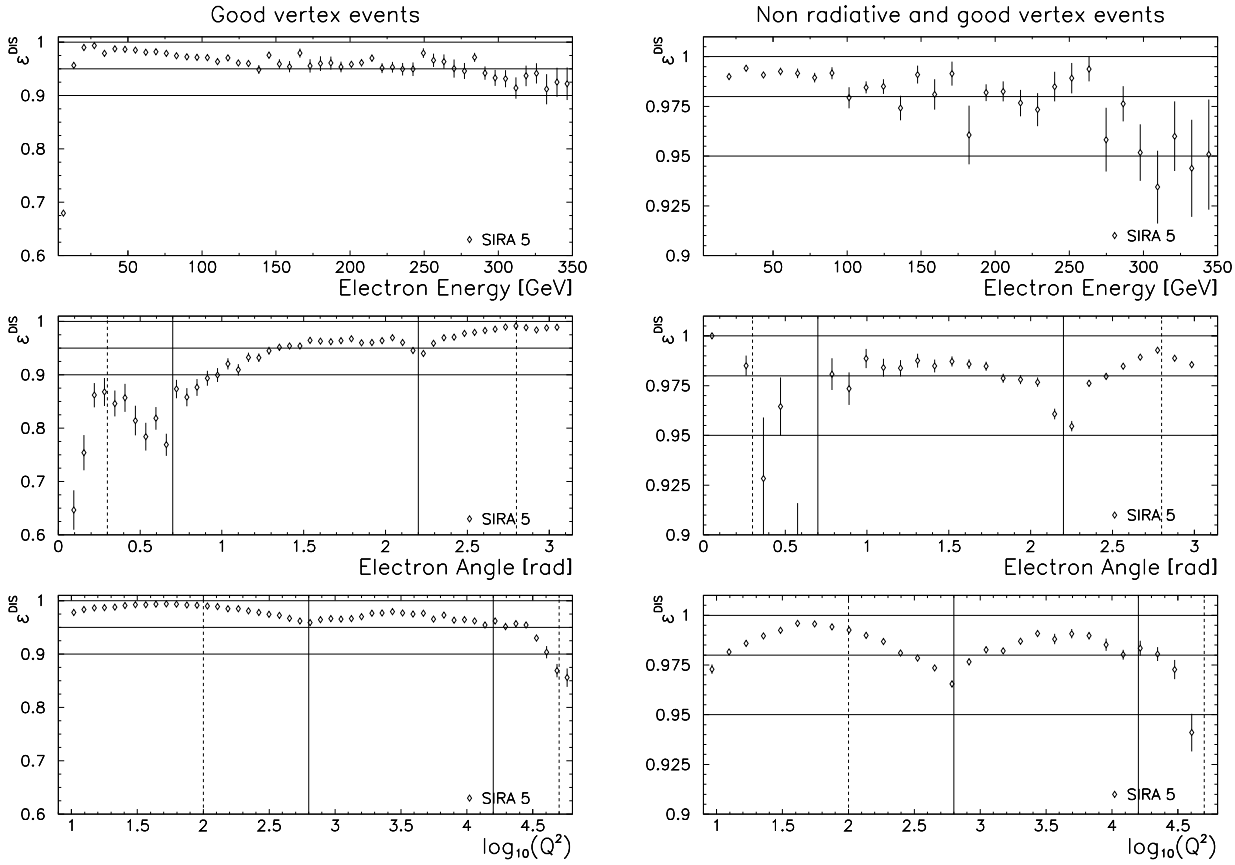

Figure C.1: ε^{DIS} plotted versus the energy, angle and $\log_{10}(\mathrm{Q}^2)$ of the true scattered lepton variables for SIRA 5, only for events in which $|V_z^{true} - V_z^{meas.}| \leq 5$ cm and only for non radiative events.

located in the RCAL outside the CTD region it is possible that the electron-finder takes this candidate as the scattered lepton.

Nevertheless the major problem are ISR events. In this case the incoming lepton radiates a photon with a very small angle with respect to itself. In most of the cases the photon goes down the beam pipe but it can happen that the photon hits the calorimeter near the beam hole, i.e. outside the CTD region. This causes in almost all the cases a misidentification of the scattered lepton.

FSR events are events in which the scattered lepton radiates a collinear photon, both particles are very close in the calorimeter making it difficult to distinguish between them. The error made in the angular reconstruction of the scattered lepton is very small compared with the other two processes. The results of recalculating ε^{DIS} for non radiative events with a good vertex are shown in Fig. C.1 . The falling tendency of the efficiency as a function of Θ_{true} disappears and the efficiencies for the electron-finders lie all above 95% away from calorimeter cracks and in the FCAL region. In this case ε^{DIS} is very close to ε^{found} and the main problem for identifying scattered leptons are the cracks between the calorimeters and the CTD end on the RCAL side.

C.3 Other Inefficiencies

There are also other minor inefficiencies, not investigated here in detail. One example are events in which the scattered lepton is located between two calorimeter cells giving a much too big deposit of energy that enters the HAC region. In this cases the scattered lepton is considered as a hadronic cluster.

Another inefficiency is the identification of the hadronic jet as the scattered lepton. This problem can be solved using cone isolation.

Appendix D

Comparison Between Different Electron-Finders

The identification of the scattered lepton is done in this analysis using SINISTRA95 with option 5 of FINDIS95 as electron finder. Nevertheless there is also a commonly used electron finder in ZEUS called EM [Str].

EM is based on detailed parameterizations of the detector response for electrons. Seven variables (four calorimeter and three track variables) are used to evaluate whether or not a calorimeter cluster is an electron. EM is optimized for each calorimeter BCAL and FCAL separately to avoid the crack between both calorimeters.

The efficiency study performed in SINISTRA95, Section 9.2, is also done for EM. The results obtained for both electron-finders are compared in this appendix.

In this case we only show ε^{DIS} for all events and for non-radiative events with good vertex.

In Fig. D.1 ε^{found} is shown, SIRA 5 efficiency is higher than EM's in the BCAL region. In the RCAL region the SIRA 5 performance is superior due to the drop EM suffers at the end of the CTD. In the FCAL region SIRA 5 efficiency still remains higher than EM's.

For non-radiative and good-vertex events the efficiency of both electron-finders is comparable in the BCAL and FCAL regions. In the RCAL region, where EM was not optimized for, the efficiency of SIRA 5 is considerably higher.

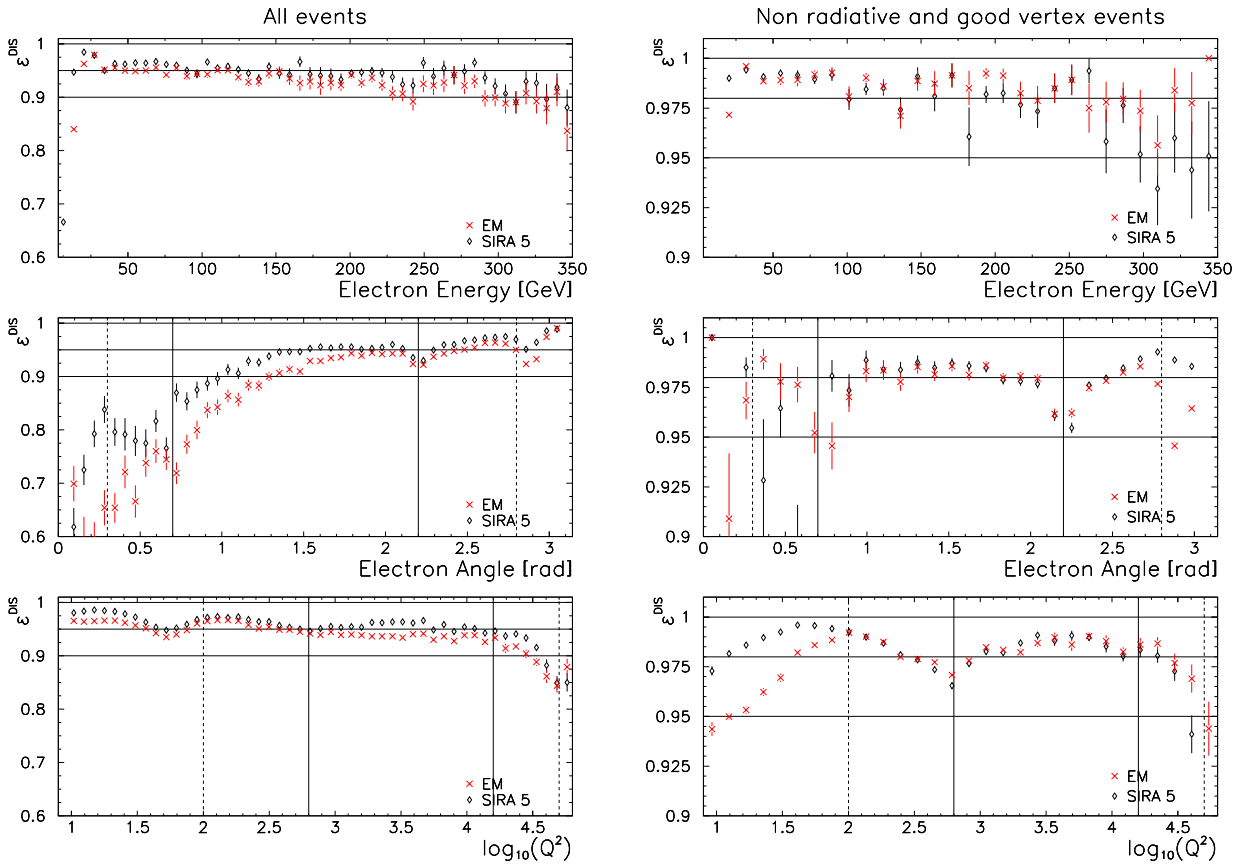

Figure D.1: ε^{DIS} plotted versus the energy, angle and $\log_{10}(Q^2)$ of the true scattered lepton variables for SIRA 5 (diamonds) and EM (crosses), for all events (left) and only for non radiative events and $|V_z^{true} - V_z^{meas.}| \leq 5$ cm (right).

Appendix E

Plots to the Electromagnetic Energy Scale

The electromagnetic energy scale is calculated separately for the RCAL and the BCAL. It is done in bins of the scattered lepton energy predicted with the double angle method E_{DA}. The scattered leptons in the BCAL have also been separated in three samples according to their purity (see Section 9.4.2). The bins boundaries used in the RCAL and the two first samples of the BCAL are [10.0, 15.0, 20.0, 22.0, 25.0, 27.0, 30.0, 35.0, 45.0, 500.0] GeV, for the sample of high energy scattered leptons the bin boundaries are [20.0, 30.0, 40.0, 50.0, 60.0, 120.0, 500.0] GeV.

The distribution $1-E_e/E_{DA}$ is fitted in different bins of E_{DA} for scattered leptons in the RCAL (Fig. E.1) in the BCAL first sample (Fig. E.2) second sample (Fig. E.3) and the high purity sample (Fig. E.4).

The results of the fits performed on the data and Monte Carlo distributions is also shown in each corresponding figure.

The final results of the study can be found in Section 9.4.

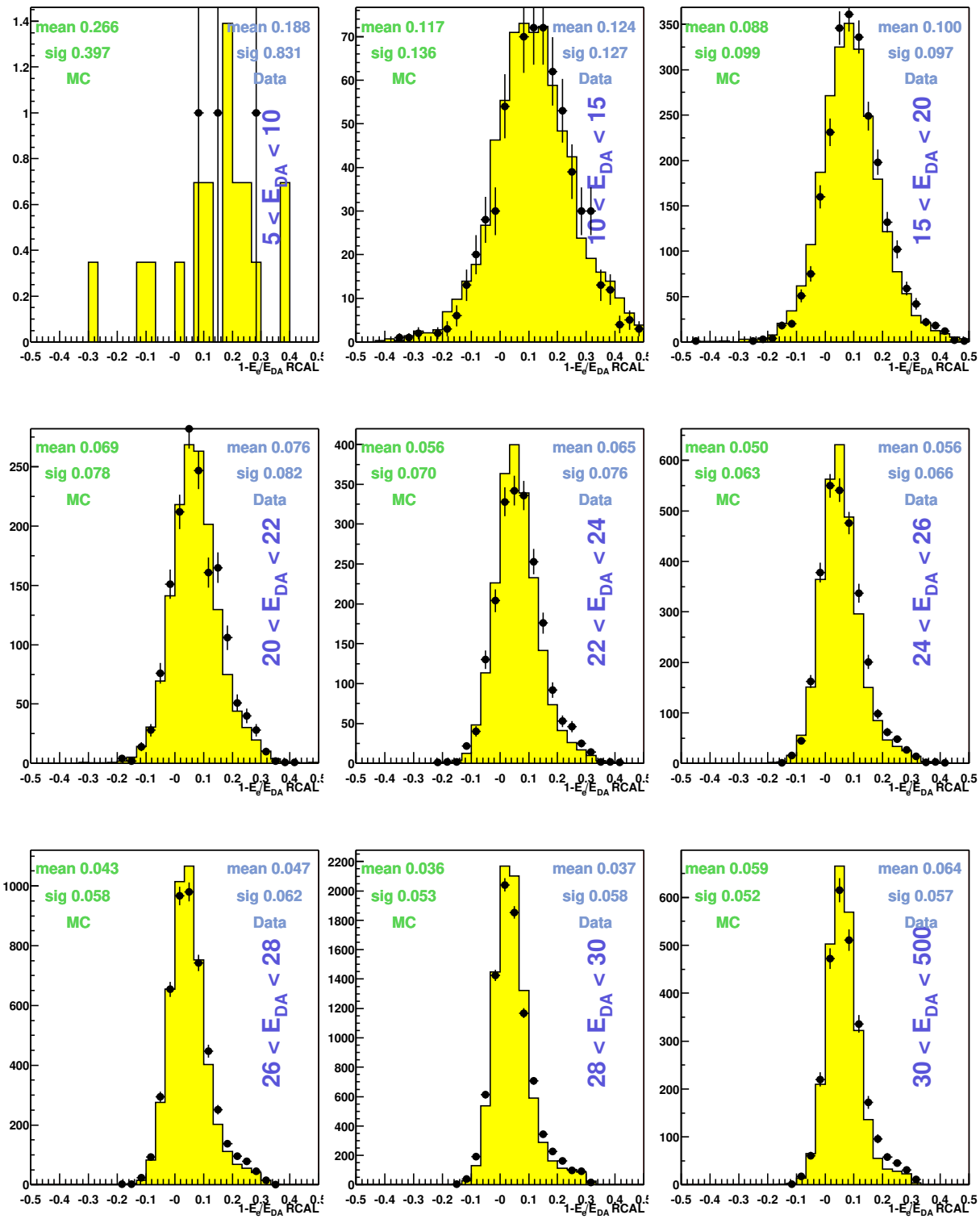

Figure E.1: $1 - E_e/E_{DA}$ in different bins of E_{DA} for scattered leptons in the RCAL.

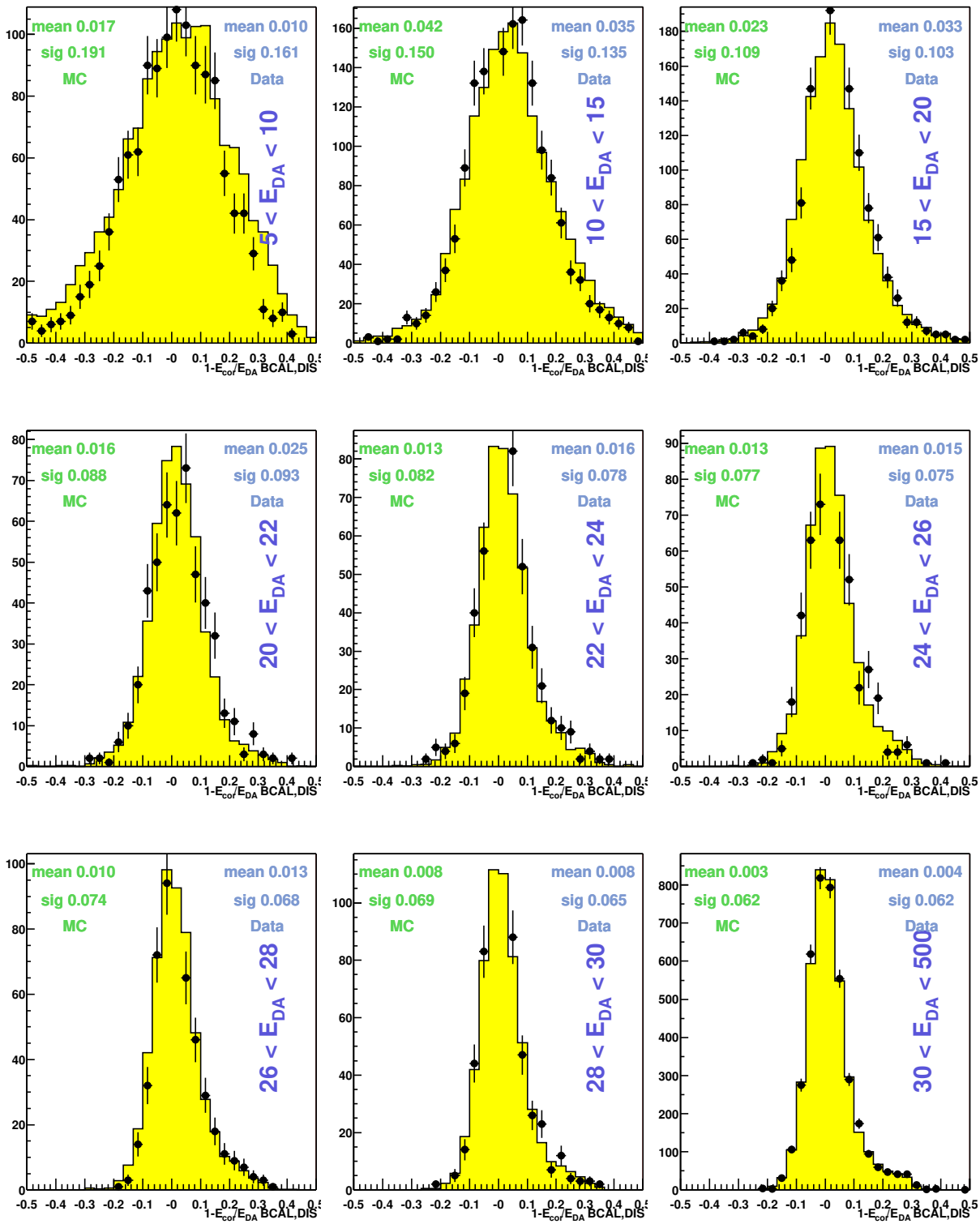

Figure E.2: $1 - E_e/E_{DA}$ in different bins of E_{DA} for scattered leptons in the BCAL. The events correspond to the sample used to perform the analysis.

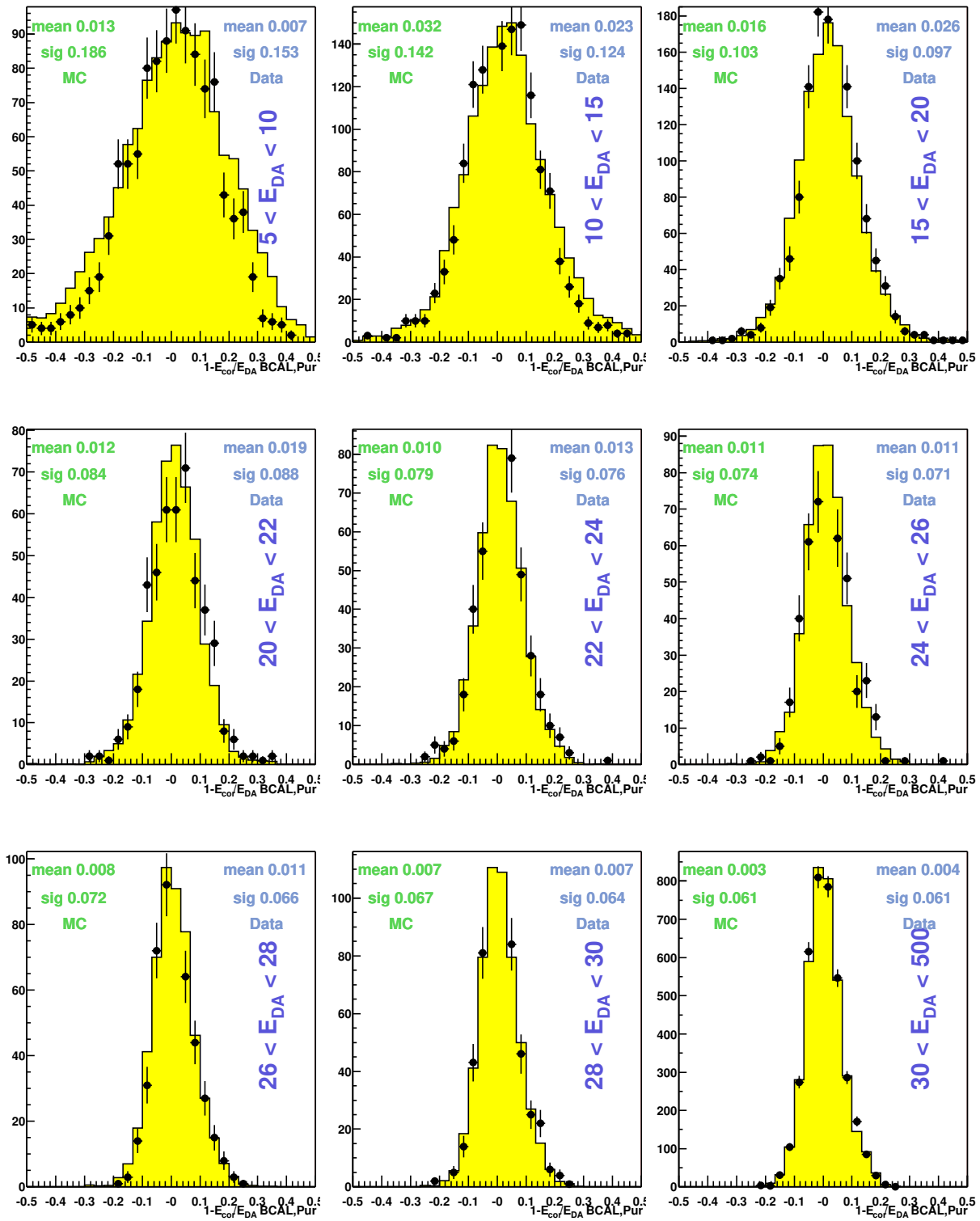

Figure E.3: $1 - E_e/E_{DA}$ in different bins of E_{DA} for scattered leptons in the BCAL. The events correspond to the sample with tighter cuts on the $E - p_Z$ and the $E_{EnotinCone}$ variable (see Section 9.4 for complete description.).

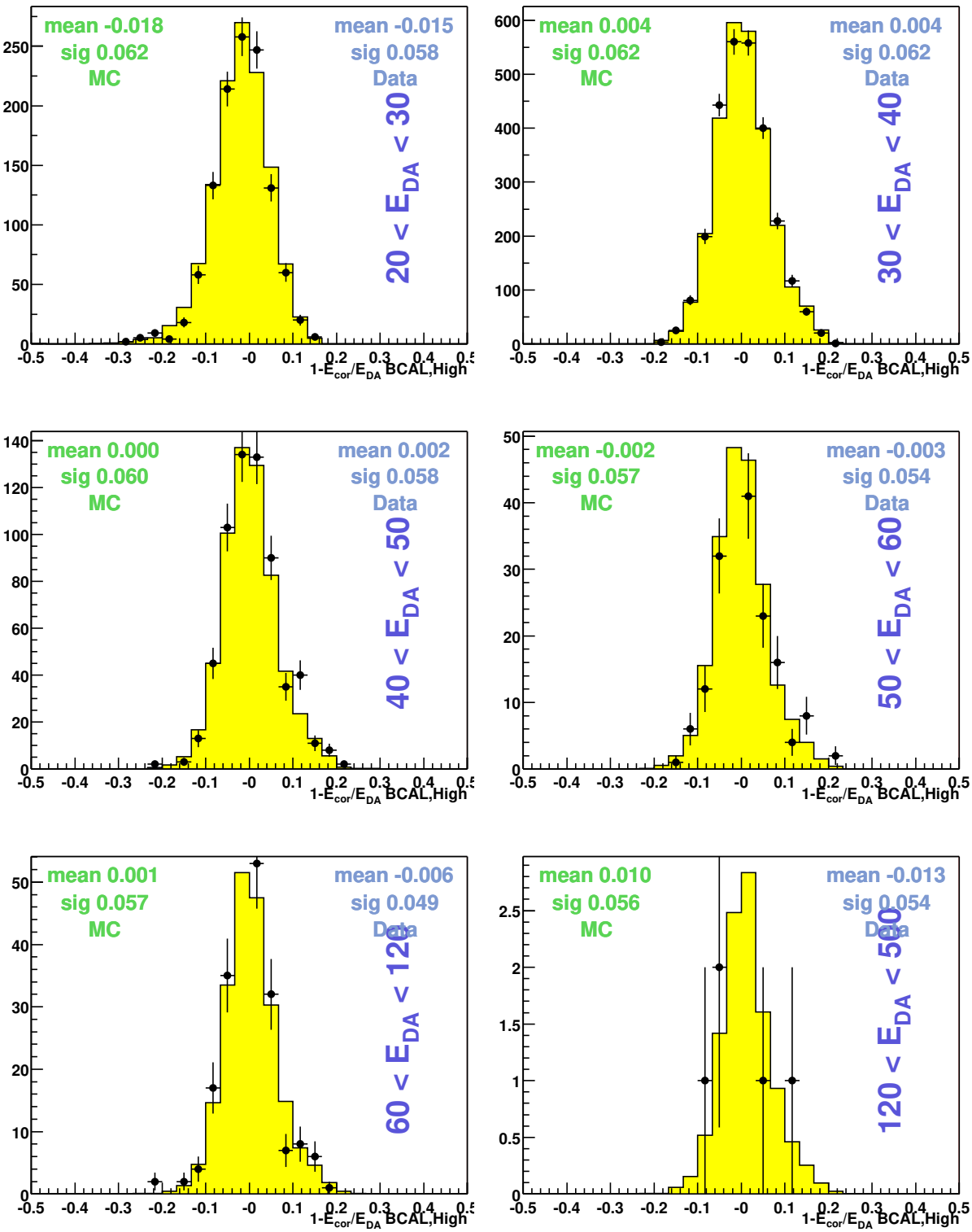

Figure E.4: $1 - E_e/E_{DA}$ in different bins of E_{DA} for scattered leptons in the BCAL. The events correspond to the high purity sample (see Section 9.4 for complete description.).

Appendix F

Plots to the Efficiency of the Track Requirement Cuts Study

In this appendix the plots to the study presented in Section 9.3 are shown.

Figure F.1 shows the $E - p_Z$ distribution in bins of scattered lepton angle Θ measured with the calorimeter where no cuts on the distance of closest approach variable or the momentum of the track are applied.

Figure F.2 shows the same distributions but with the cuts $DCA < 10$ cm and $P_{track} > 5$ GeV applied.

Figure F.3 shows the ratio from the distributions with cuts divided by the distributions with no cuts in bins of Θ. As expected for low values of $E - p_z$ the data shows a strong falling due to rejected PHP events not present in the Monte Carlo distribution.

Finally Fig. F.4 shows the ratio data to Monte Carlo distributions fitted in the central region if the $E - p_Z$ distributions.

The results of the fit are shown in Section 9.3.

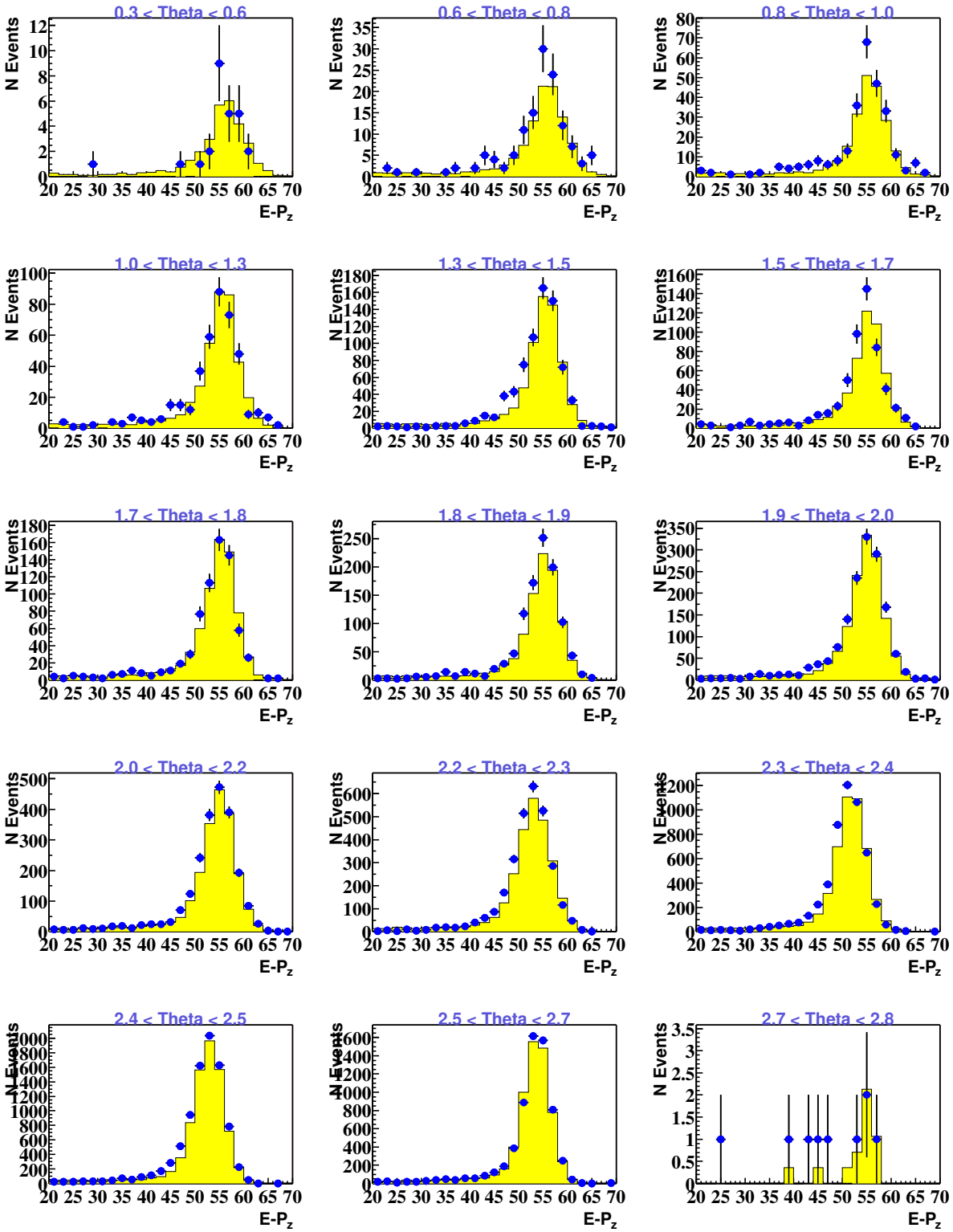

Figure F.1: $E - p_z$ variable in bins of the scattered lepton angle Θ. This sample has no track cuts.

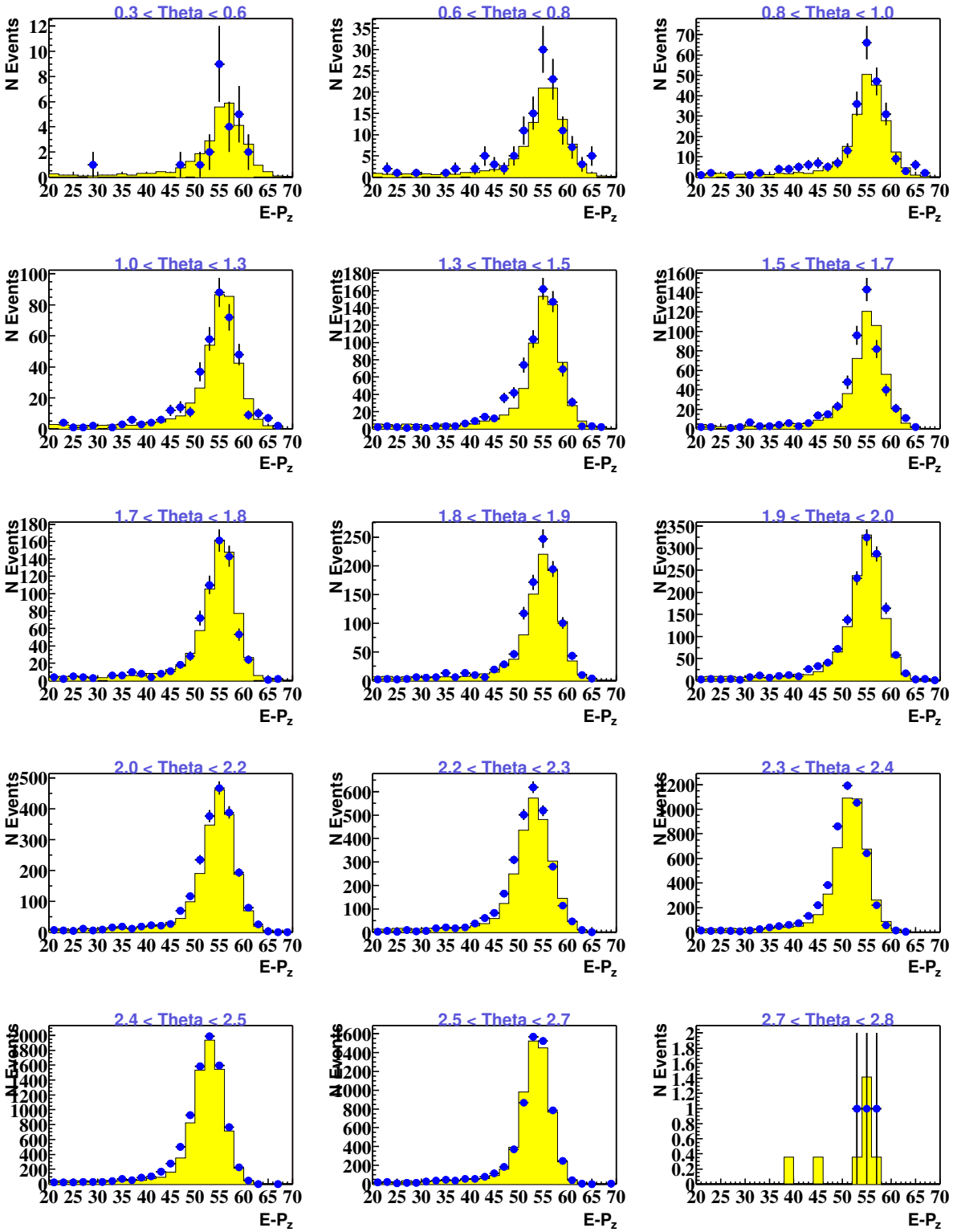

Figure F.2: $E - p_Z$ variable in bins of the scattered lepton angle Θ. This sample has cuts on the track variables, i.e. $P_{trk} > 5\,GeV$ and $DCA < 10\,cm$.

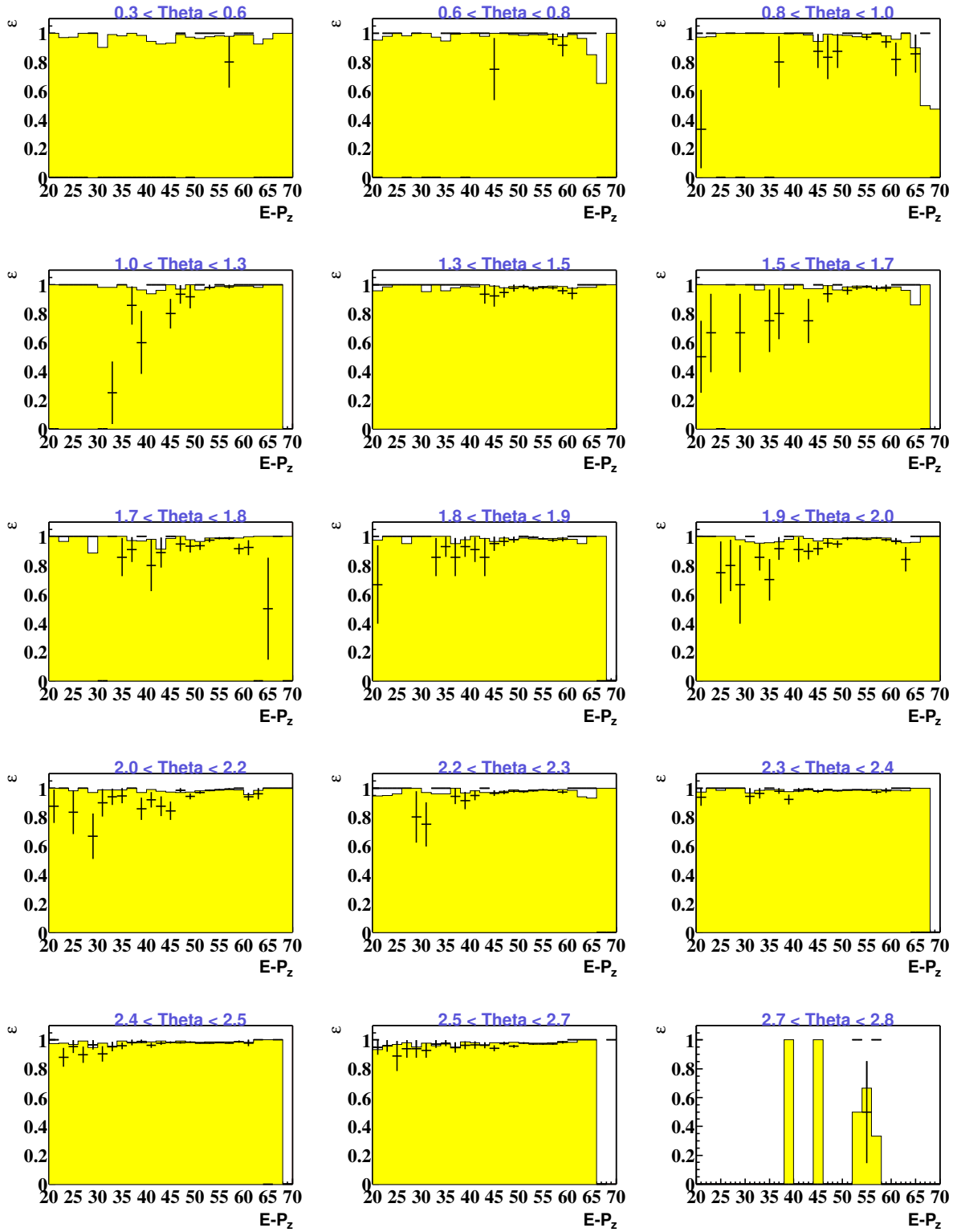

Figure F.3: Ratio from the $E - p_Z$ distributions with applied cuts divided by the distributions with no cuts in bins of the scattered lepton angle Θ.

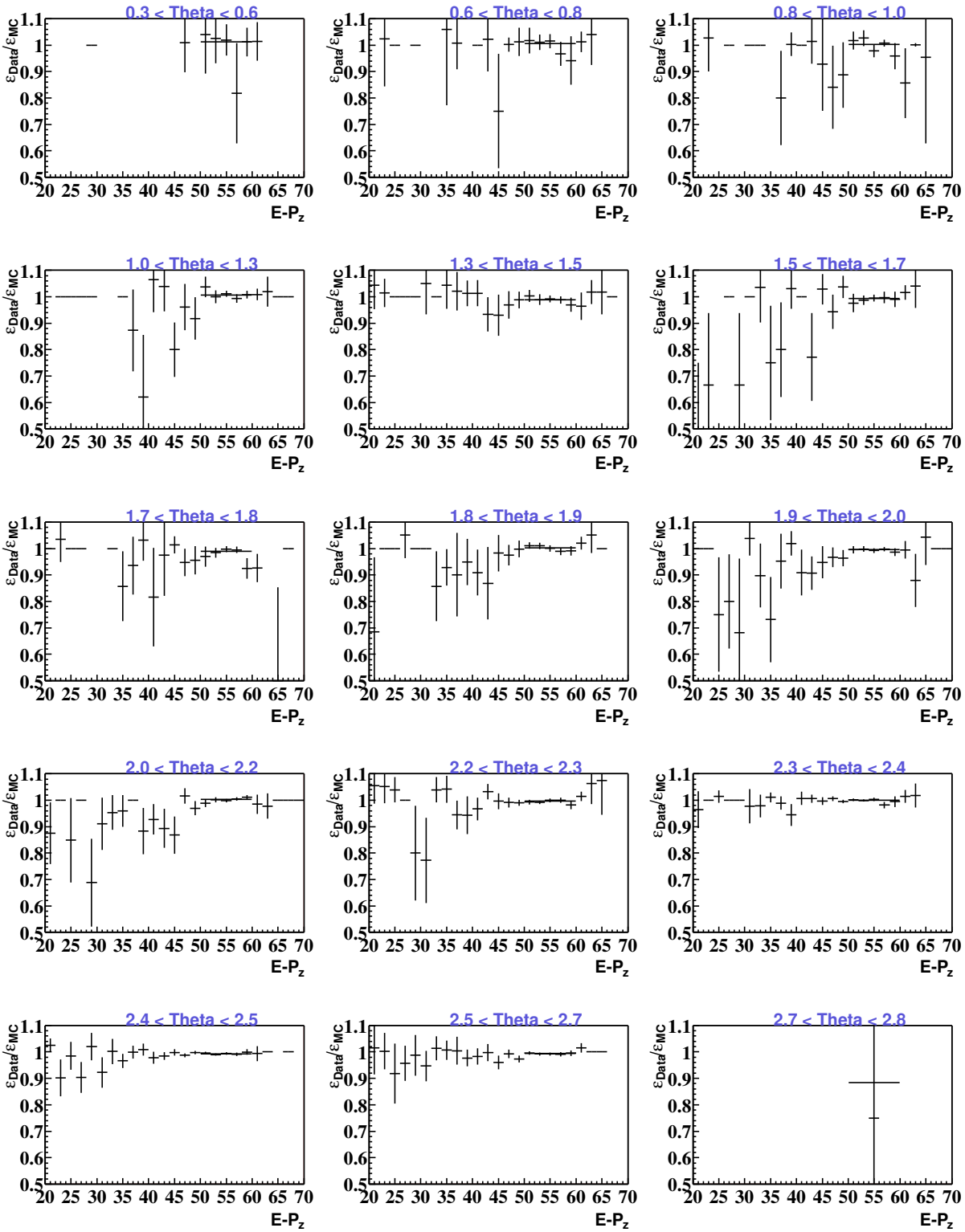

Figure F.4: Double ratio of the two distributions with and without cuts, data over Monte Carlo simulation, in bins of the scattered lepton angle Θ.

Appendix G

Different Reconstruction Methods of the Hadronic Variables

For the extraction of the cross section we have use CORANDCUT to reconstruct the hadronic variables. There is a second commonly used algorithm in ZEUS called ZUFOSNT.

In CORANDCUT the hadronic variables are calculated from the calorimeter information only. Nevertheless it is possible that some particles do not reach the calorimeter obtaining then a bad estimation of the energy. To solve this problem ZUFOSNT uses the information of the CTD to calculate the energy of the hadrons.

First the cone algorithm, described in Section 8.1.3, forms islands as in the CORANDCUT case. In case there is a track pointing to the island, each island is matched to it. After this process three different types of objects are found:

- Calorimeter islands with no track associated. These clusters come from neutral particles with an energy $E^2 = p^2$.
- Tracks not associated to any energy cluster in calorimeter. This tracks are counted as pions.
- Calorimeter clusters that have more than three tracks associated. They are the so called "jet" clusters and are given a mass[1] $E^2 = p^2$.

Complex rules [Bri98] have been developed to decide how to combine the track and the calorimeter information. In average the contribution from the tracks to the jet energy is 11% [Tun01b].

The advantage of this method is that taking into account the information of the tracks the description of the energy of the jet should be better. This is of special interest when part of the jet is falling into a super-crack. The badly measured energy of the particles in the crack can be replaced by the track information.

ZUFOSNT has also a γ_{max} cut implemented [Tun01b]. The γ_{max} is a tuned parameter, it depends on the sample of events chosen to calculate it. For CORANDCUT the events used to tune γ_{max} were mainly high Q^2 events, while ZUFOSNT was tuned with low Q^2 events. The definition of the γ_{max} cut in ZUFOSNT is therefore different:

[1] The jet contains usually enough energy so that the approximation of massless particles is valid.

- $\gamma_{max} = \gamma_h + 50^0$
- All energy clusters with $E \leq 3$ GeV, $\Theta \geq \gamma_{max}$ are only removed if they have a bad timing.

The differences with CORANDCUT are:

- Because of the γ_{max} cut definition no islands in FCAL are removed in ZUFOSNT.
- γ_{max} is not applied to tracks.
- Islands with good timing are not removed even if they have low energy and an angle greater than γ_{max}.

Since we would like to consider the use of ZUFOSNT for our analysis we have implemented the γ_{max} cut from CORANDCUT into it. The only exception is that the cut is not applied to tracks.

Now we want to compare the resolution and the bias of the two algorithms as a function of the hadronic variables $E - p_Z$ and P_T in terms of γ_h and y_{true}. Results are shown in Fig. G.1. On each row the resolution and bias of each of the algorithms CORANDCUT, ZUFOSNT and ZUFOSNT+CORANDCUT are plotted. The results are plotted for the $E-p_Z$ and P_T variables as a function of γ_h (rows one and two) and as a function of y_{true} (rows three and four). The high γ_h region corresponds to the low y_{true} region, therefore the results obtained in both regions would need to be consistent.

In general the hadronic variables calculated with CORANDCUT are closer to the true variables than the ones calculated with ZUFOSNT. While the resolution and bias of the P_T variable remains quite constant over the whole $\gamma/\log_{10}(y_{true})$ range, the bias of the δ variable increases dramatically for high γ_h values. This is due to the fact that the δ isolines in the kinematic plane Fig. 7.4 are almost parallel to the γ_h isolines Fig. 7.7. A small mismeasurement of the δ variable will directly translate in a bad estimation of the γ_h variable. In this region the implementation of the new γ_{max} cut in ZUFOSNT shown an improvement in the region $-2.5 \leq \log_{10}(y_{true}) \leq -1.5$.

The calculation of the hadronic variables in both cases is better for low γ_h values where the hadronic energy is mostly contained in the FCAL region. The results remain quite constant until the hadronic jet reaches the RCAL region. In this case the lack of statistics cannot predict much, but it is clear that the measured variables lie far apart from the true ones.

This study allows us to prove that the chosen algorithm to reconstruct the hadronic final state, CORANDCUT, is able to describe the true variables for almost all the γ_h regions that are statistically significant.

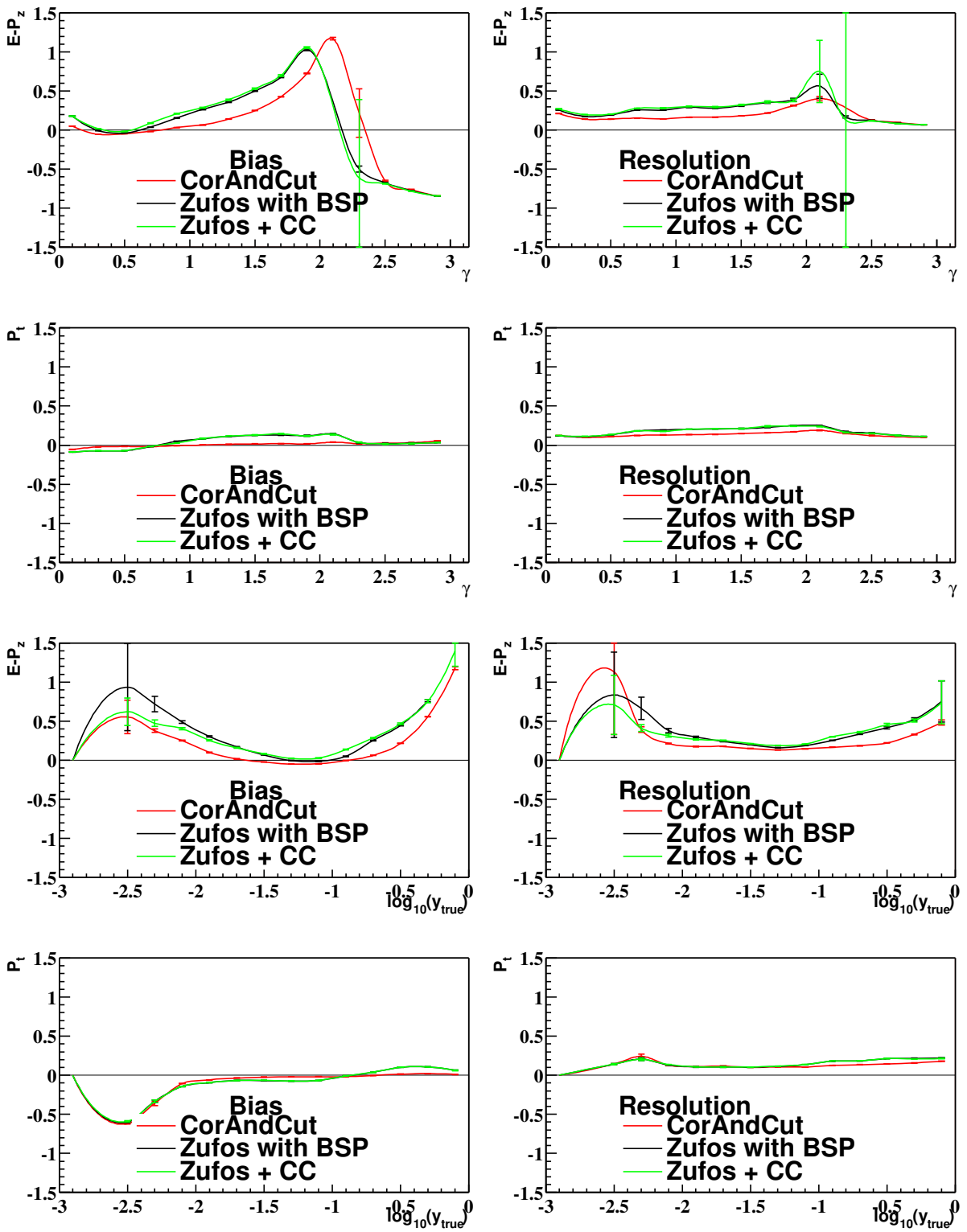

Figure G.1: Resolution and bias for ZUFOSNT, CORANDCUT and ZUFOSNT with CORANDCUT γ_{max} cut implemented. Left plots show the resolution and right plots the bias.

Appendix H

Control Plots for the Data Samples $(e^+p)^{820}$ and $(e^+p)^{920}$

The figures in this appendix show the comparison between data and Monte Carlo distributions for the main variables involved in the extraction of the cross sections for the data samples 1996/97 and 1999/2000.

H.1 Data Sample 1996/1997

Figure H.1 shows the reweighted electron z-coordinate of the vertex. Figure H.2 shows the energy of the scattered lepton after non-uniformity corrections, dead-material corrections and Monte Carlo energy smearing according to Section 8.1.5.

Figure H.3 shows the scattered lepton angle determined with the track in the CTD acceptance region and with the calorimeter otherwise. Figures H.4 and H.5 show the hadronic variables, γ_h and δ_h, obtained with the algorithm CORANDCUT.

The vertical lines shown in the plots correspond to the analysis cuts. A description of them can be found in Section 8.4.

H.2 Data Sample 1999/2000

Figure H.6 shows the reweighted electron z-coordinate of the vertex. Figure H.7 shows the energy of the scattered lepton after non-uniformity corrections, dead-material corrections and Monte Carlo energy smearing according to Section 8.1.5.

Figure H.8 shows the scattered lepton angle determined with the track in the CTD acceptance region and with the calorimeter otherwise. Figures H.9 and H.10 show the hadronic variables, γ_h and δ_h, obtained with the algorithm CORANDCUT.

For both data samples the data and the Monte Carlo simulation show good agreement.

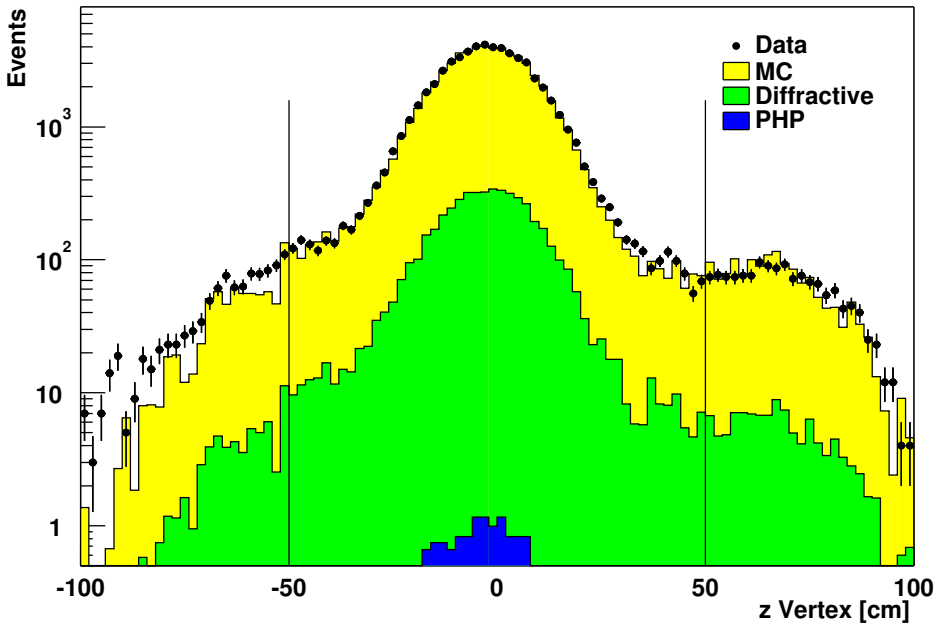

Figure H.1: Reweighted z-Vertex for the 1996/97 data sample

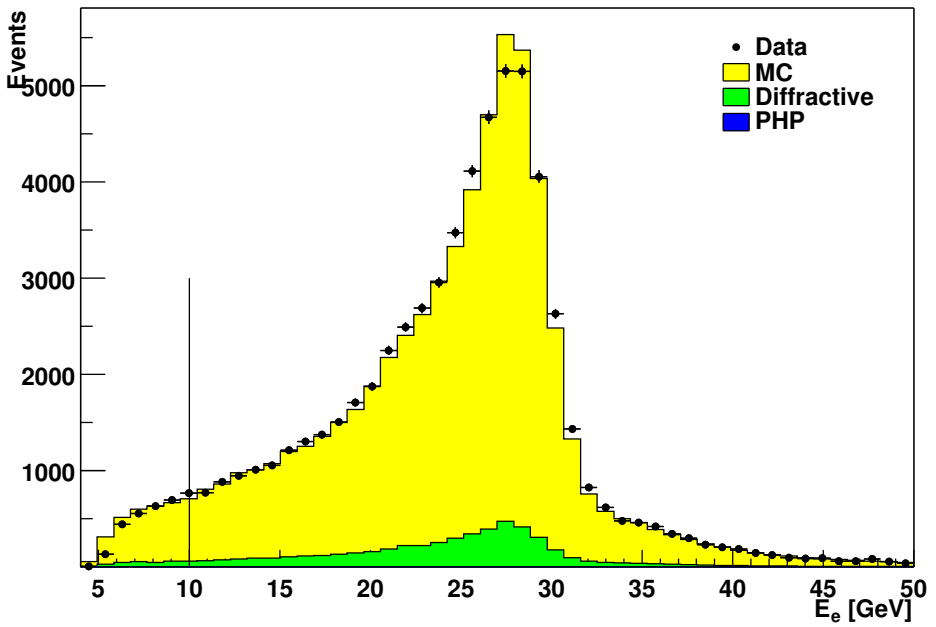

Figure H.2: Corrected scattered lepton energy E_e for the 1996/97 data sample

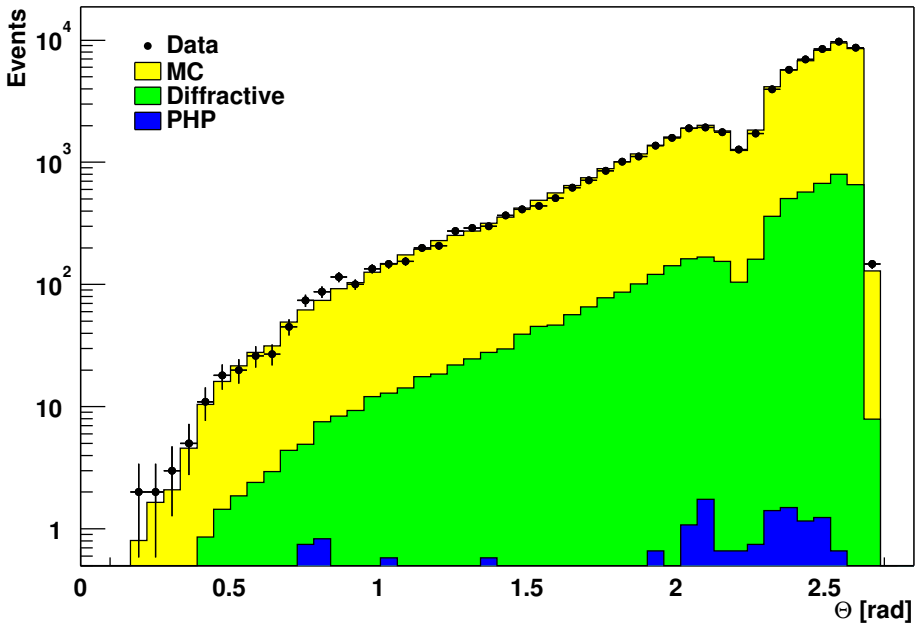

Figure H.3: Scattered lepton angle Θ for the 1996/97 data sample

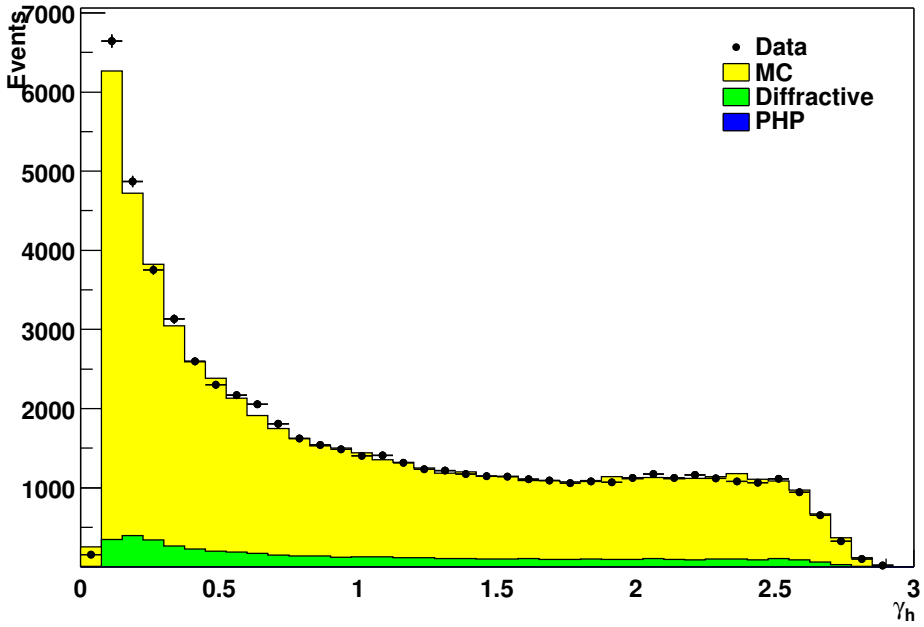

Figure H.4: Hadronic γ_h angle for the 1996/97 data sample

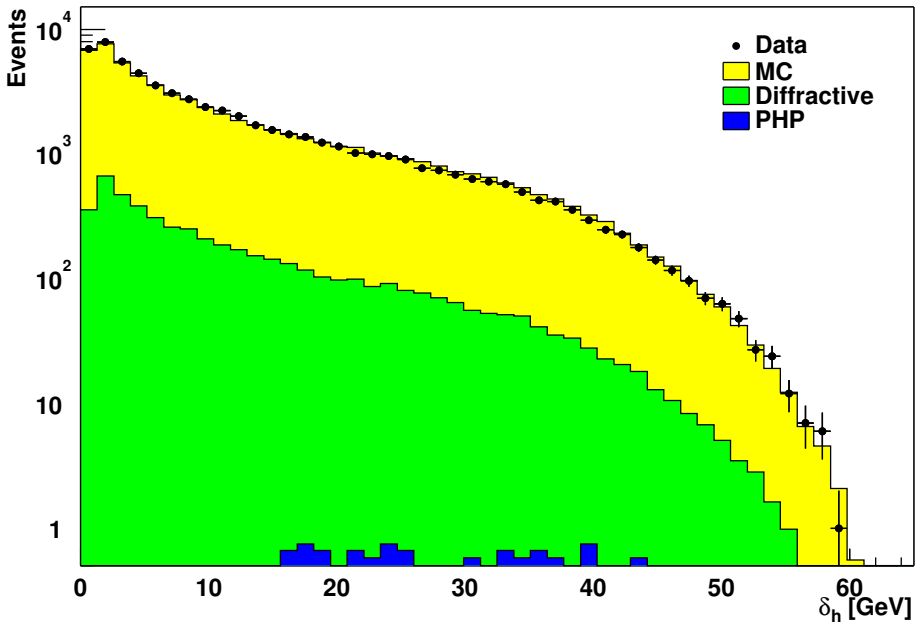

Figure H.5: Hadronic δ_h distribution for the 1996/97 data sample

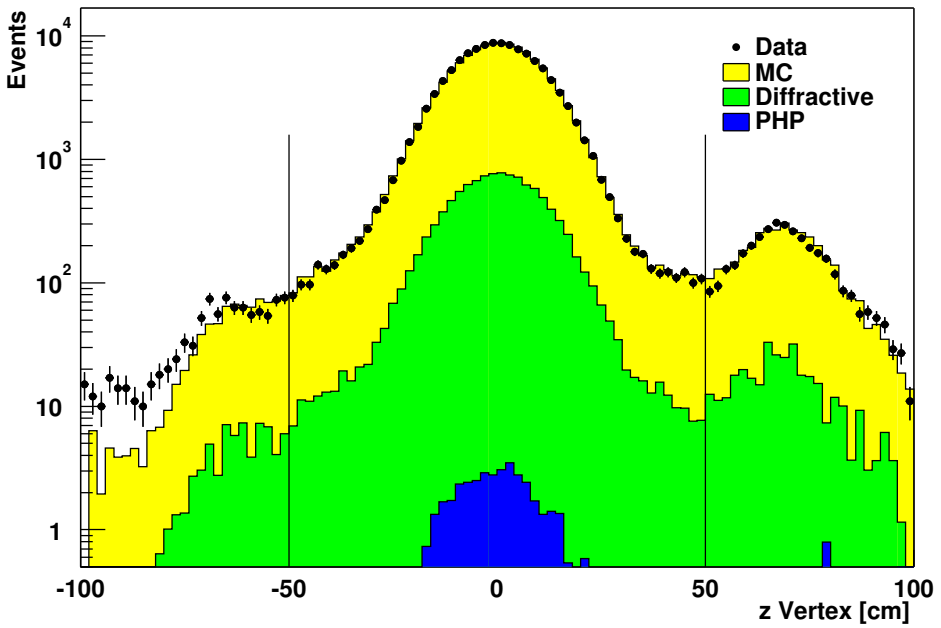

Figure H.6: Reweighted z-Vertex for the 1999/2000 data sample

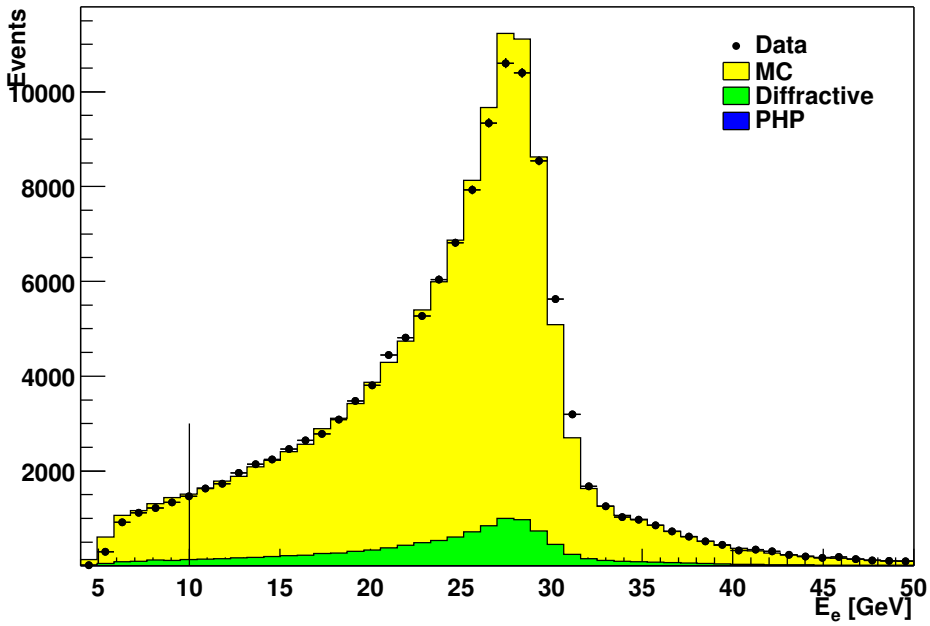

Figure H.7: Corrected scattered lepton energy E_e for the 1999/2000 data sample

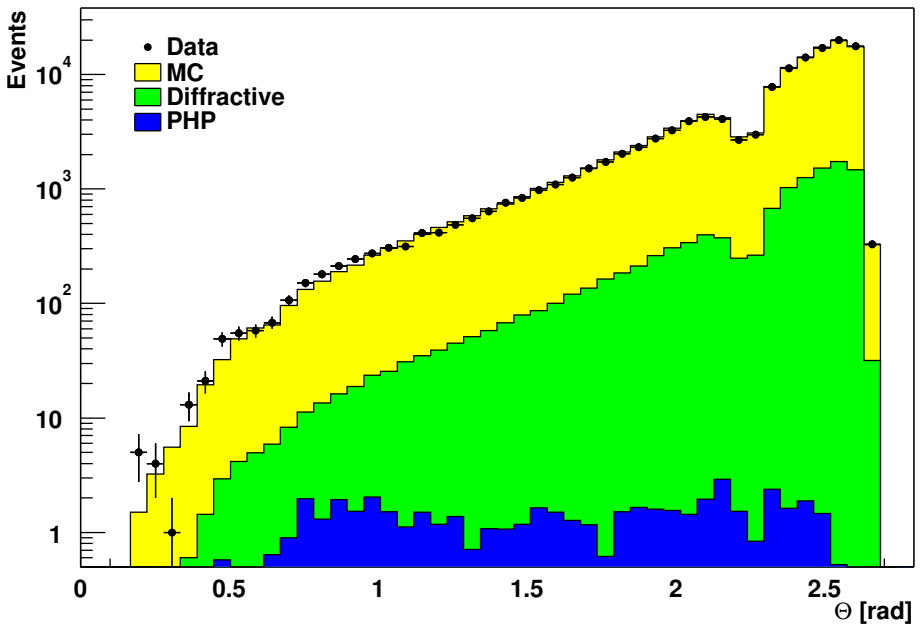

Figure H.8: Scattered lepton angle Θ for the 1999/2000 data sample

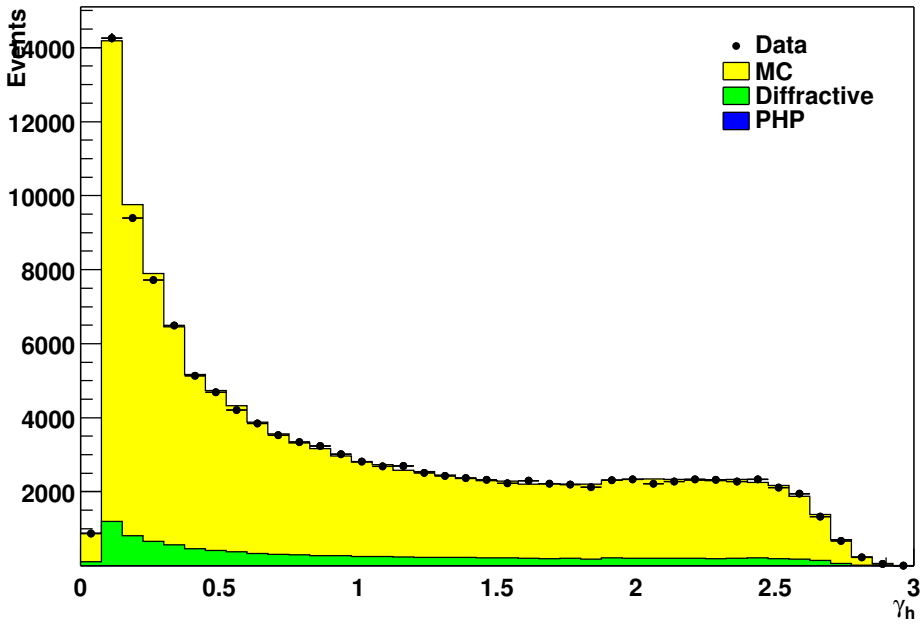

Figure H.9: Hadronic γ_h angle for the 1999/2000 data sample

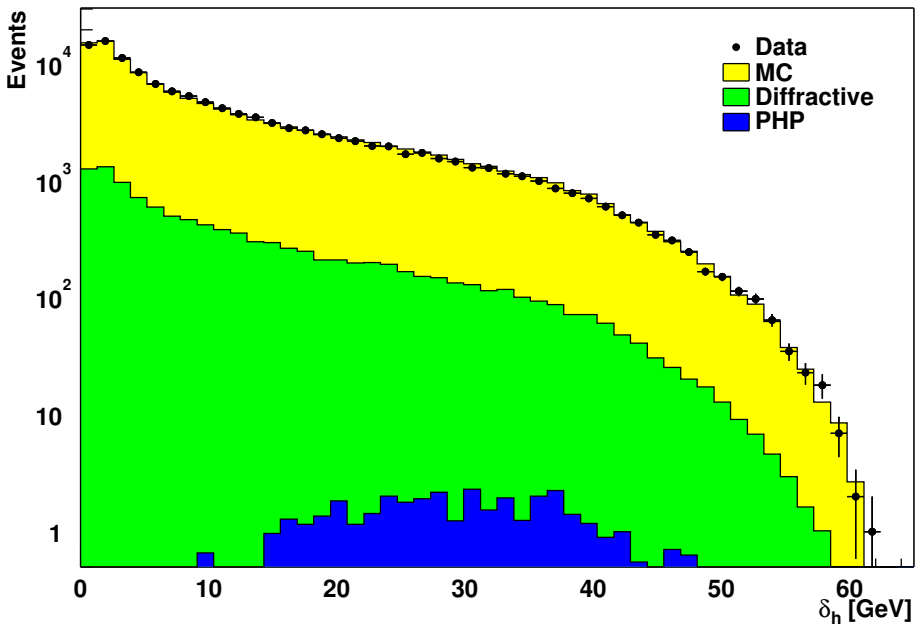

Figure H.10: Hadronic δ_h distribution for the 1999/2000 data sample

Appendix I

Systematic Uncertainties for the Cross Section Measurement

This appendix contains the study of the systematic uncertainties that enter the measurement of the single and double differential cross sections. The contribution of each systematic uncertainty is shown separately, and this is done for every cross section. The systematic uncertainties are calculated according to Chapter 9.

For uncertainties in which a cut has been varied up and down the contribution is shown in the same plot. If the cut is varied by a positive quantity the uncertainty is shown with a circle. A square is used otherwise.

Only the uncertainties on the electrons 1998/99 data sample is shown. The tendency followed by each uncertainty is expected to be the same for all data samples.

I.1 Systematic Uncertainty for the Single Differential Cross Section $d\sigma/dQ^2$

In this section the systematic uncertainty for the single differential cross section $d\sigma/dQ^2$ is shown. It can be seen in Fig. I.1 that except for the high Q^2 region all the uncertainties are smaller than 2%. In the high Q^2 region the uncertainty is dominated by statistics.

The biggest contribution comes from cuts like y_{el}, $E - p_Z$, the momentum of the track and the cone isolation that reduce the PHP background.

I.2 Systematic Uncertainty for the Single Differential Cross Section $d\sigma/dx$

In this section the systematic uncertainty for the single differential cross section $d\sigma/dx$ is for the different Q^2 cuts is shown.

For $Q^2 > 200$ GeV^2 Fig. I.2 shows that all the uncertainties are smaller than 2%.

The biggest contribution may come from the cut on the momentum of the track that rejects PHP background at high y values, i.e low x region.

When going to higher Q^2 cuts, i.e $Q > 10000$ GeV^2, the systematic uncertainties (Fig. I.3) become bigger but still inside the 2% range. Again the low x region has bigger uncertainties due to the PHP rejection cuts.

I.3 Systematic Uncertainty for the Single Differential Cross Section $d\sigma/dy$

The tendency found in the systematic uncertainties for the single differential cross section $d\sigma/dx$ is clearly seen for $d\sigma/dy$. The biggest systematic uncertainties (Fig. I.4) are located on the region where most of the PHP background is located. This is the high y region. Nevertheless, for lower values of y the systematic uncertainty is negligible.

I.4 Systematic Uncertainty for the Double Differential Cross Section $d\sigma^2/dx\,dQ^2$

The systematic uncertainties for the double differential cross section show a trend which is the combination of what has been seen in the single differential cross sections $d\sigma/dQ^2$ and $d\sigma/dx$. For high values of Q^2 the systematic uncertainty is dominated by statistics. This can be seen in Fig. I.5 where the statistical uncertainty increases with the bin number. The bin number increases first in Q^2 and within this bin, in x. For low values of x, i.e. beginning of a new Q^2 bin, the systematic uncertainty is higher than for other values due to the PHP rejection cuts. Almost all the values lie within 2%

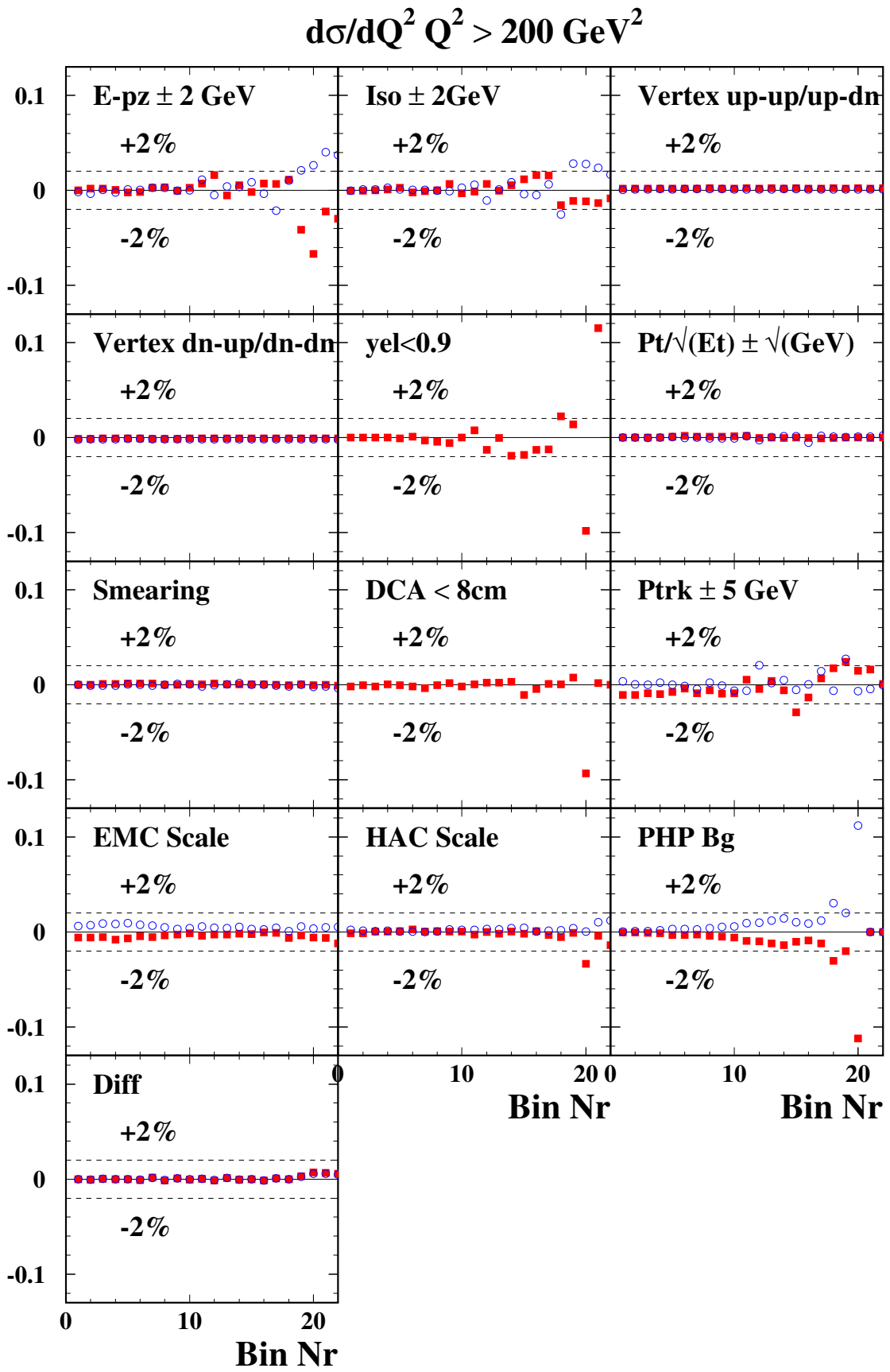

Figure I.1: Systematic uncertainties for the single differential cross section $d\sigma/dQ^2$ measured for $Q^2 > 200$ GeV^2 for the electron data sample 1998/99.

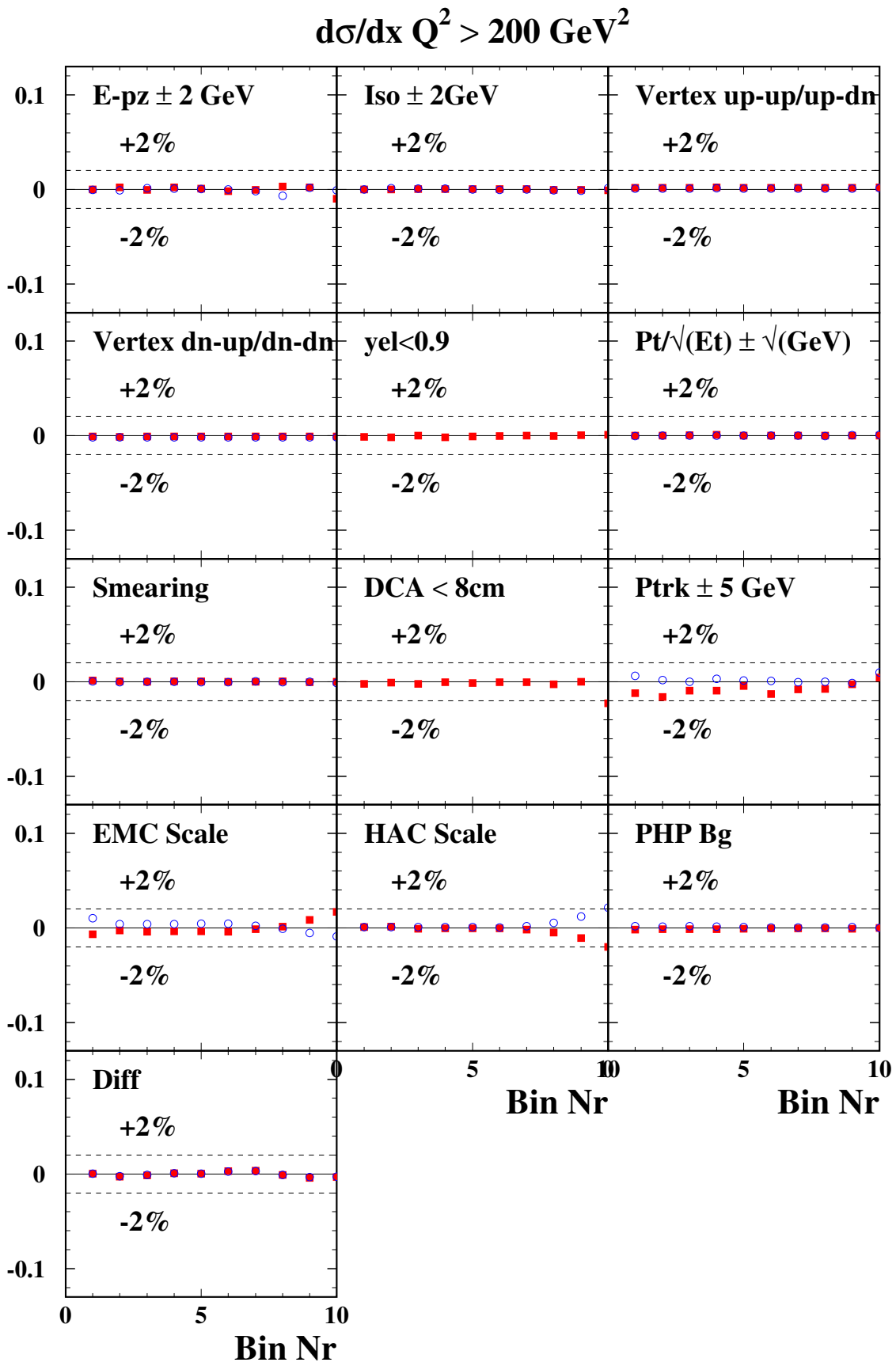

Figure I.2: Systematic uncertainties for the single differential cross section $d\sigma/dx$ measured for $Q^2 > 200$ GeV^2 for the electron data sample 1998/99.

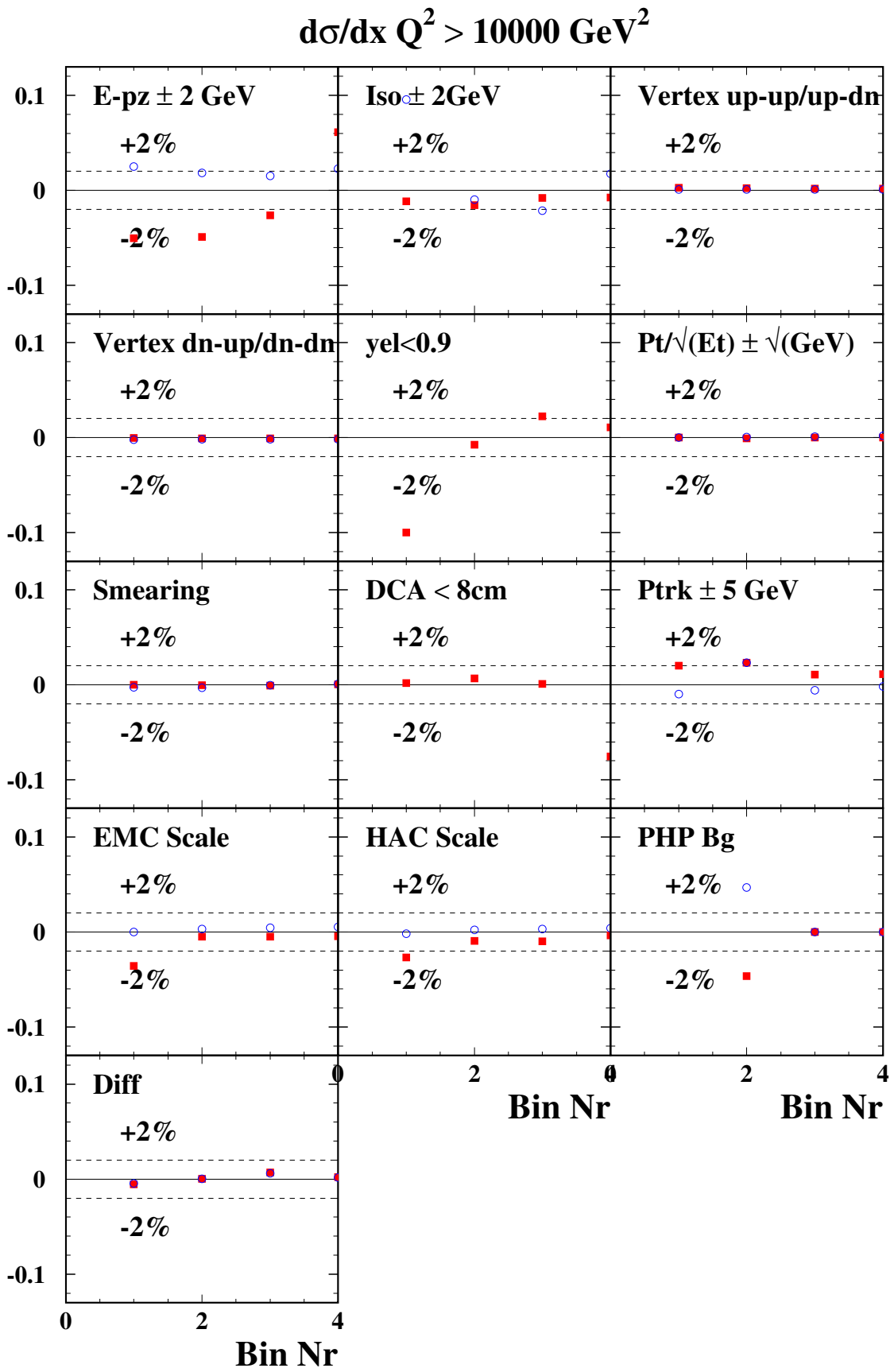

Figure I.3: Systematic uncertainties for the single differential cross section $d\sigma/dx$ measured for $Q^2 > 10000$ GeV^2 for the electron data sample 1998/99.

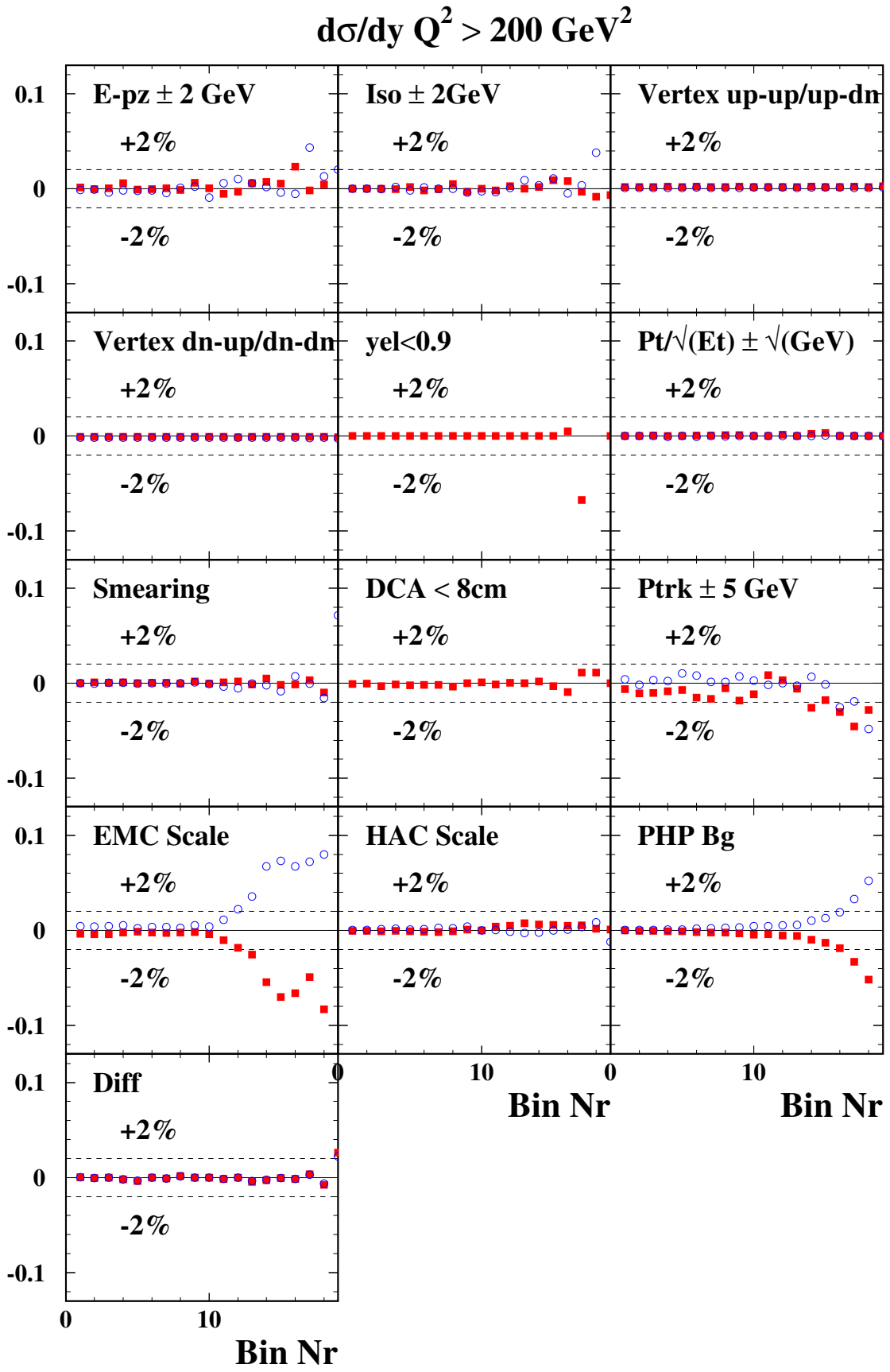

Figure I.4: Systematic uncertainties for the single differential cross section $d\sigma/dy$ measured for $Q^2 > 200$ GeV^2 for the electron data sample 1998/99.

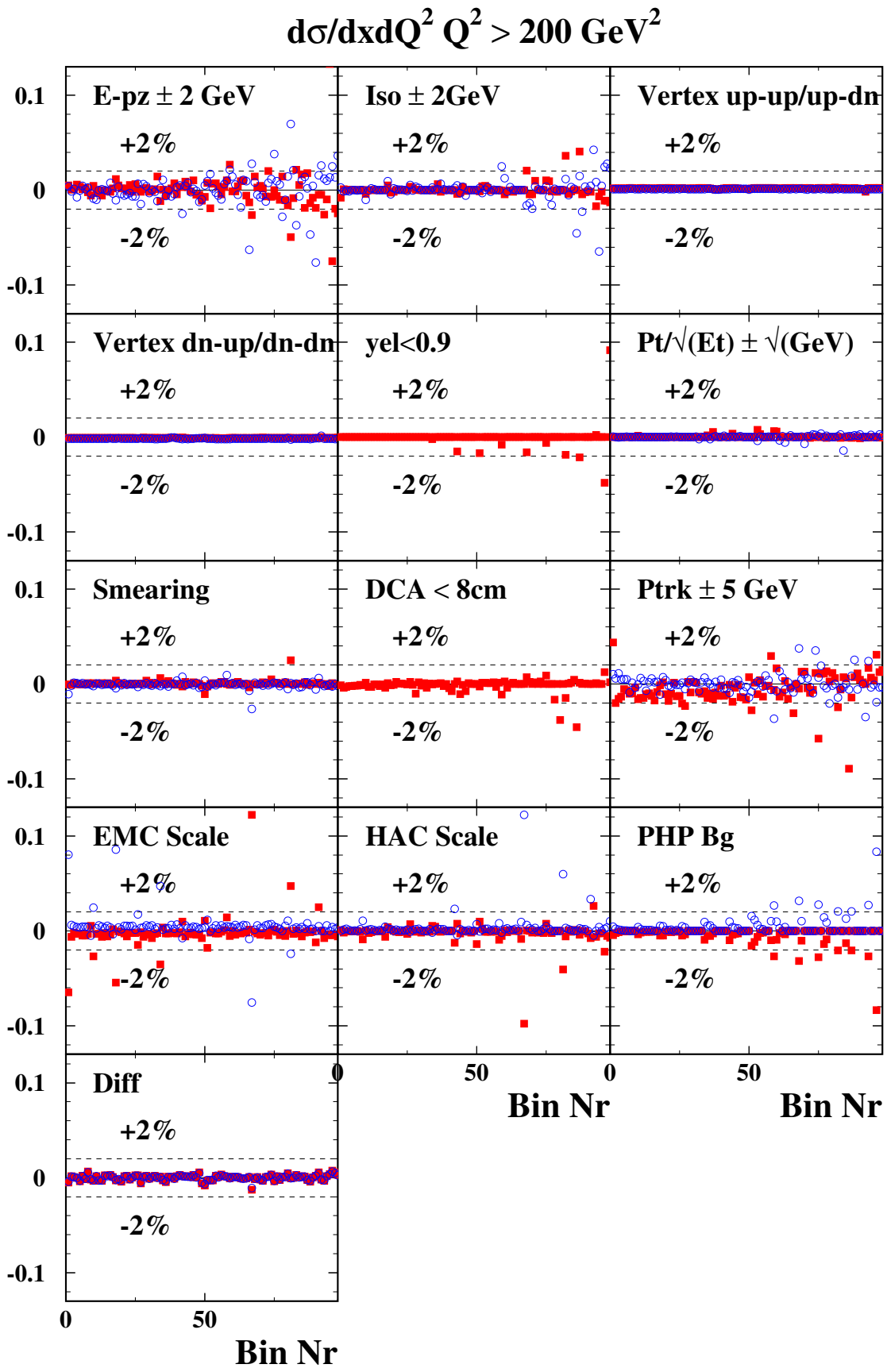

Figure I.5: Systematic uncertainty for the double differential cross section $d^2\sigma/dx\,dQ^2$ for $Q^2 > 200$ GeV^2 for the 98/99 electron data sample.

Appendix J

Data tables

x	$\frac{d\sigma^{820}}{dx}$	$\%\delta_{sta.Up}$	$\%\delta_{sta.Dn}$	$\%\delta_{sys.Up}$	$\%\delta_{sys.Dn}$
$0.794 \cdot 10^{-02}$	$0.719 \cdot 10^{+05}$	$0.155 \cdot 10^{-01}$	$0.155 \cdot 10^{-01}$	$0.335 \cdot 10^{-01}$	$-0.266 \cdot 10^{-01}$
$0.126 \cdot 10^{-01}$	$0.519 \cdot 10^{+05}$	$0.138 \cdot 10^{-01}$	$0.138 \cdot 10^{-01}$	$0.225 \cdot 10^{-01}$	$-0.318 \cdot 10^{-01}$
$0.200 \cdot 10^{-01}$	$0.327 \cdot 10^{+05}$	$0.137 \cdot 10^{-01}$	$0.137 \cdot 10^{-01}$	$0.164 \cdot 10^{-01}$	$-0.300 \cdot 10^{-01}$
$0.316 \cdot 10^{-01}$	$0.199 \cdot 10^{+05}$	$0.136 \cdot 10^{-01}$	$0.136 \cdot 10^{-01}$	$0.160 \cdot 10^{-01}$	$-0.196 \cdot 10^{-01}$
$0.501 \cdot 10^{-01}$	$0.115 \cdot 10^{+05}$	$0.143 \cdot 10^{-01}$	$0.143 \cdot 10^{-01}$	$0.119 \cdot 10^{-01}$	$-0.191 \cdot 10^{-01}$
$0.794 \cdot 10^{-01}$	$0.640 \cdot 10^{+04}$	$0.148 \cdot 10^{-01}$	$0.148 \cdot 10^{-01}$	$0.133 \cdot 10^{-01}$	$-0.168 \cdot 10^{-01}$
$0.126 \cdot 10^{+00}$	$0.372 \cdot 10^{+04}$	$0.151 \cdot 10^{-01}$	$0.151 \cdot 10^{-01}$	$0.890 \cdot 10^{-02}$	$-0.178 \cdot 10^{-01}$
$0.200 \cdot 10^{+00}$	$0.194 \cdot 10^{+04}$	$0.168 \cdot 10^{-01}$	$0.168 \cdot 10^{-01}$	$0.323 \cdot 10^{-01}$	$-0.133 \cdot 10^{-01}$
$0.316 \cdot 10^{+00}$	$0.729 \cdot 10^{+03}$	$0.265 \cdot 10^{-01}$	$0.265 \cdot 10^{-01}$	$0.566 \cdot 10^{-01}$	$-0.391 \cdot 10^{-01}$
$0.501 \cdot 10^{+00}$	$0.215 \cdot 10^{+03}$	$0.658 \cdot 10^{-01}$	$0.658 \cdot 10^{-01}$	$0.644 \cdot 10^{-01}$	$-0.345 \cdot 10^{-01}$
$0.794 \cdot 10^{+00}$	$0.223 \cdot 10^{+02}$	$0.449 \cdot 10^{+00}$	$0.595 \cdot 10^{+00}$	$0.267 \cdot 10^{+00}$	$-0.555 \cdot 10^{+00}$

Table J.1: $d\sigma/dx$ values for $Q^2 > 200$ GeV^2 for the $(e^+p)^{820}$ sample

x	$\frac{d\sigma^{920}}{dx}$	$\%\delta_{sta.Up}$	$\%\delta_{sta.Dn}$	$\%\delta_{sys.Up}$	$\%\delta_{sys.Dn}$
$0.794 \cdot 10^{-02}$	$0.792 \cdot 10^{+05}$	$0.180 \cdot 10^{-01}$	$0.180 \cdot 10^{-01}$	$0.272 \cdot 10^{-01}$	$-0.243 \cdot 10^{-01}$
$0.126 \cdot 10^{-01}$	$0.554 \cdot 10^{+05}$	$0.166 \cdot 10^{-01}$	$0.166 \cdot 10^{-01}$	$0.171 \cdot 10^{-01}$	$-0.275 \cdot 10^{-01}$
$0.200 \cdot 10^{-01}$	$0.340 \cdot 10^{+05}$	$0.168 \cdot 10^{-01}$	$0.168 \cdot 10^{-01}$	$0.152 \cdot 10^{-01}$	$-0.228 \cdot 10^{-01}$
$0.316 \cdot 10^{-01}$	$0.201 \cdot 10^{+05}$	$0.167 \cdot 10^{-01}$	$0.167 \cdot 10^{-01}$	$0.217 \cdot 10^{-01}$	$-0.179 \cdot 10^{-01}$
$0.501 \cdot 10^{-01}$	$0.116 \cdot 10^{+05}$	$0.176 \cdot 10^{-01}$	$0.176 \cdot 10^{-01}$	$0.145 \cdot 10^{-01}$	$-0.140 \cdot 10^{-01}$
$0.794 \cdot 10^{-01}$	$0.647 \cdot 10^{+04}$	$0.182 \cdot 10^{-01}$	$0.182 \cdot 10^{-01}$	$0.164 \cdot 10^{-01}$	$-0.230 \cdot 10^{-01}$
$0.126 \cdot 10^{+00}$	$0.360 \cdot 10^{+04}$	$0.188 \cdot 10^{-01}$	$0.188 \cdot 10^{-01}$	$0.165 \cdot 10^{-01}$	$-0.164 \cdot 10^{-01}$
$0.200 \cdot 10^{+00}$	$0.198 \cdot 10^{+04}$	$0.206 \cdot 10^{-01}$	$0.206 \cdot 10^{-01}$	$0.139 \cdot 10^{-01}$	$-0.280 \cdot 10^{-01}$
$0.316 \cdot 10^{+00}$	$0.830 \cdot 10^{+03}$	$0.344 \cdot 10^{-01}$	$0.344 \cdot 10^{-01}$	$0.315 \cdot 10^{-01}$	$-0.351 \cdot 10^{-01}$
$0.501 \cdot 10^{+00}$	$0.215 \cdot 10^{+03}$	$0.901 \cdot 10^{-01}$	$0.901 \cdot 10^{-01}$	$0.649 \cdot 10^{-01}$	$-0.753 \cdot 10^{-01}$
$0.794 \cdot 10^{+00}$	$0.000 \cdot 10^{+00}$	$0.000 \cdot 10^{+00}$	$0.000 \cdot 10^{+00}$	$0.000 \cdot 10^{+00}$	$0.000 \cdot 10^{+00}$

Table J.2: $d\sigma/dx$ values for $Q^2 > 200$ GeV^2 for the $(e^-p)^{920}$ sample

x	$\frac{d\sigma^{920}}{dx}$	$\%\delta_{sta.Up}$	$\%\delta_{sta.Dn}$	$\%\delta_{sys.Up}$	$\%\delta_{sys.Dn}$
$0.794 \cdot 10^{-02}$	$0.794 \cdot 10^{+05}$	$0.101 \cdot 10^{-01}$	$0.101 \cdot 10^{-01}$	$0.270 \cdot 10^{-01}$	$-0.294 \cdot 10^{-01}$
$0.126 \cdot 10^{-01}$	$0.533 \cdot 10^{+05}$	$0.936 \cdot 10^{-02}$	$0.936 \cdot 10^{-02}$	$0.224 \cdot 10^{-01}$	$-0.251 \cdot 10^{-01}$
$0.200 \cdot 10^{-01}$	$0.336 \cdot 10^{+05}$	$0.947 \cdot 10^{-02}$	$0.947 \cdot 10^{-02}$	$0.189 \cdot 10^{-01}$	$-0.216 \cdot 10^{-01}$
$0.316 \cdot 10^{-01}$	$0.201 \cdot 10^{+05}$	$0.940 \cdot 10^{-02}$	$0.940 \cdot 10^{-02}$	$0.175 \cdot 10^{-01}$	$-0.202 \cdot 10^{-01}$
$0.501 \cdot 10^{-01}$	$0.115 \cdot 10^{+05}$	$0.998 \cdot 10^{-02}$	$0.998 \cdot 10^{-02}$	$0.192 \cdot 10^{-01}$	$-0.155 \cdot 10^{-01}$
$0.794 \cdot 10^{-01}$	$0.643 \cdot 10^{+04}$	$0.102 \cdot 10^{-01}$	$0.102 \cdot 10^{-01}$	$0.203 \cdot 10^{-01}$	$-0.202 \cdot 10^{-01}$
$0.126 \cdot 10^{+00}$	$0.349 \cdot 10^{+04}$	$0.106 \cdot 10^{-01}$	$0.106 \cdot 10^{-01}$	$0.207 \cdot 10^{-01}$	$-0.189 \cdot 10^{-01}$
$0.200 \cdot 10^{+00}$	$0.185 \cdot 10^{+04}$	$0.118 \cdot 10^{-01}$	$0.118 \cdot 10^{-01}$	$0.207 \cdot 10^{-01}$	$-0.217 \cdot 10^{-01}$
$0.316 \cdot 10^{+00}$	$0.831 \cdot 10^{+03}$	$0.195 \cdot 10^{-01}$	$0.195 \cdot 10^{-01}$	$0.309 \cdot 10^{-01}$	$-0.398 \cdot 10^{-01}$
$0.501 \cdot 10^{+00}$	$0.188 \cdot 10^{+03}$	$0.534 \cdot 10^{-01}$	$0.534 \cdot 10^{-01}$	$0.756 \cdot 10^{-01}$	$-0.537 \cdot 10^{-01}$
$0.794 \cdot 10^{+00}$	$0.358 \cdot 10^{+01}$	$0.846 \cdot 10^{+00}$	$0.100 \cdot 10^{+01}$	$0.142 \cdot 10^{+01}$	$-0.289 \cdot 10^{+00}$

Table J.3: $d\sigma/dx$ values for $Q^2 > 200$ GeV^2 for the $(e^+p)^{920}$ sample

x	$\frac{d\sigma^{820}}{dx}$	$\%\delta_{sta.Up}$	$\%\delta_{sta.Dn}$	$\%\delta_{sys.Up}$	$\%\delta_{sys.Dn}$
$0.794 \cdot 10^{-02}$	$0.719 \cdot 10^{+05}$	$0.155 \cdot 10^{-01}$	$0.155 \cdot 10^{-01}$	$0.335 \cdot 10^{-01}$	$-0.266 \cdot 10^{-01}$
$0.126 \cdot 10^{-01}$	$0.519 \cdot 10^{+05}$	$0.138 \cdot 10^{-01}$	$0.138 \cdot 10^{-01}$	$0.225 \cdot 10^{-01}$	$-0.318 \cdot 10^{-01}$
$0.200 \cdot 10^{-01}$	$0.327 \cdot 10^{+05}$	$0.137 \cdot 10^{-01}$	$0.137 \cdot 10^{-01}$	$0.164 \cdot 10^{-01}$	$-0.300 \cdot 10^{-01}$
$0.316 \cdot 10^{-01}$	$0.199 \cdot 10^{+05}$	$0.136 \cdot 10^{-01}$	$0.136 \cdot 10^{-01}$	$0.160 \cdot 10^{-01}$	$-0.196 \cdot 10^{-01}$
$0.501 \cdot 10^{-01}$	$0.115 \cdot 10^{+05}$	$0.143 \cdot 10^{-01}$	$0.143 \cdot 10^{-01}$	$0.119 \cdot 10^{-01}$	$-0.191 \cdot 10^{-01}$
$0.794 \cdot 10^{-01}$	$0.640 \cdot 10^{+04}$	$0.148 \cdot 10^{-01}$	$0.148 \cdot 10^{-01}$	$0.133 \cdot 10^{-01}$	$-0.168 \cdot 10^{-01}$
$0.126 \cdot 10^{+00}$	$0.372 \cdot 10^{+04}$	$0.151 \cdot 10^{-01}$	$0.151 \cdot 10^{-01}$	$0.890 \cdot 10^{-02}$	$-0.178 \cdot 10^{-01}$
$0.200 \cdot 10^{+00}$	$0.194 \cdot 10^{+04}$	$0.168 \cdot 10^{-01}$	$0.168 \cdot 10^{-01}$	$0.323 \cdot 10^{-01}$	$-0.133 \cdot 10^{-01}$
$0.316 \cdot 10^{+00}$	$0.729 \cdot 10^{+03}$	$0.265 \cdot 10^{-01}$	$0.265 \cdot 10^{-01}$	$0.566 \cdot 10^{-01}$	$-0.391 \cdot 10^{-01}$
$0.501 \cdot 10^{+00}$	$0.215 \cdot 10^{+03}$	$0.658 \cdot 10^{-01}$	$0.658 \cdot 10^{-01}$	$0.644 \cdot 10^{-01}$	$-0.345 \cdot 10^{-01}$
$0.794 \cdot 10^{+00}$	$0.223 \cdot 10^{+02}$	$0.449 \cdot 10^{+00}$	$0.595 \cdot 10^{+00}$	$0.267 \cdot 10^{+00}$	$-0.555 \cdot 10^{+00}$

Table J.4: $d\sigma/dx$ values for $Q^2 > 200$ GeV^2 for the $(e^+p)^{820}$ sample

x	$\frac{d\sigma^{920}}{dx}$	$\%\delta_{sta.Up}$	$\%\delta_{sta.Dn}$	$\%\delta_{sys.Up}$	$\%\delta_{sys.Dn}$
$0.794 \cdot 10^{-02}$	$0.792 \cdot 10^{+05}$	$0.180 \cdot 10^{-01}$	$0.180 \cdot 10^{-01}$	$0.272 \cdot 10^{-01}$	$-0.243 \cdot 10^{-01}$
$0.126 \cdot 10^{-01}$	$0.554 \cdot 10^{+05}$	$0.166 \cdot 10^{-01}$	$0.166 \cdot 10^{-01}$	$0.171 \cdot 10^{-01}$	$-0.275 \cdot 10^{-01}$
$0.200 \cdot 10^{-01}$	$0.340 \cdot 10^{+05}$	$0.168 \cdot 10^{-01}$	$0.168 \cdot 10^{-01}$	$0.152 \cdot 10^{-01}$	$-0.228 \cdot 10^{-01}$
$0.316 \cdot 10^{-01}$	$0.201 \cdot 10^{+05}$	$0.167 \cdot 10^{-01}$	$0.167 \cdot 10^{-01}$	$0.217 \cdot 10^{-01}$	$-0.179 \cdot 10^{-01}$
$0.501 \cdot 10^{-01}$	$0.116 \cdot 10^{+05}$	$0.176 \cdot 10^{-01}$	$0.176 \cdot 10^{-01}$	$0.145 \cdot 10^{-01}$	$-0.140 \cdot 10^{-01}$
$0.794 \cdot 10^{-01}$	$0.647 \cdot 10^{+04}$	$0.182 \cdot 10^{-01}$	$0.182 \cdot 10^{-01}$	$0.164 \cdot 10^{-01}$	$-0.230 \cdot 10^{-01}$
$0.126 \cdot 10^{+00}$	$0.360 \cdot 10^{+04}$	$0.188 \cdot 10^{-01}$	$0.188 \cdot 10^{-01}$	$0.165 \cdot 10^{-01}$	$-0.164 \cdot 10^{-01}$
$0.200 \cdot 10^{+00}$	$0.198 \cdot 10^{+04}$	$0.206 \cdot 10^{-01}$	$0.206 \cdot 10^{-01}$	$0.139 \cdot 10^{-01}$	$-0.280 \cdot 10^{-01}$
$0.316 \cdot 10^{+00}$	$0.830 \cdot 10^{+03}$	$0.344 \cdot 10^{-01}$	$0.344 \cdot 10^{-01}$	$0.315 \cdot 10^{-01}$	$-0.351 \cdot 10^{-01}$
$0.501 \cdot 10^{+00}$	$0.215 \cdot 10^{+03}$	$0.901 \cdot 10^{-01}$	$0.901 \cdot 10^{-01}$	$0.649 \cdot 10^{-01}$	$-0.753 \cdot 10^{-01}$
$0.794 \cdot 10^{+00}$	$0.000 \cdot 10^{+00}$	$0.000 \cdot 10^{+00}$	$0.000 \cdot 10^{+00}$	$0.000 \cdot 10^{+00}$	$0.000 \cdot 10^{+00}$

Table J.5: $d\sigma/dx$ values for $Q^2 > 200$ GeV^2 for the $(e^-p)^{920}$ sample

x	$\frac{d\sigma^{920}}{dx}$	$\%\delta_{sta.Up}$	$\%\delta_{sta.Dn}$	$\%\delta_{sys.Up}$	$\%\delta_{sys.Dn}$
$0.794 \cdot 10^{-02}$	$0.794 \cdot 10^{+05}$	$0.101 \cdot 10^{-01}$	$0.101 \cdot 10^{-01}$	$0.270 \cdot 10^{-01}$	$-0.294 \cdot 10^{-01}$
$0.126 \cdot 10^{-01}$	$0.533 \cdot 10^{+05}$	$0.936 \cdot 10^{-02}$	$0.936 \cdot 10^{-02}$	$0.224 \cdot 10^{-01}$	$-0.251 \cdot 10^{-01}$
$0.200 \cdot 10^{-01}$	$0.336 \cdot 10^{+05}$	$0.947 \cdot 10^{-02}$	$0.947 \cdot 10^{-02}$	$0.189 \cdot 10^{-01}$	$-0.216 \cdot 10^{-01}$
$0.316 \cdot 10^{-01}$	$0.201 \cdot 10^{+05}$	$0.940 \cdot 10^{-02}$	$0.940 \cdot 10^{-02}$	$0.175 \cdot 10^{-01}$	$-0.202 \cdot 10^{-01}$
$0.501 \cdot 10^{-01}$	$0.115 \cdot 10^{+05}$	$0.998 \cdot 10^{-02}$	$0.998 \cdot 10^{-02}$	$0.192 \cdot 10^{-01}$	$-0.155 \cdot 10^{-01}$
$0.794 \cdot 10^{-01}$	$0.643 \cdot 10^{+04}$	$0.102 \cdot 10^{-01}$	$0.102 \cdot 10^{-01}$	$0.203 \cdot 10^{-01}$	$-0.202 \cdot 10^{-01}$
$0.126 \cdot 10^{+00}$	$0.349 \cdot 10^{+04}$	$0.106 \cdot 10^{-01}$	$0.106 \cdot 10^{-01}$	$0.207 \cdot 10^{-01}$	$-0.189 \cdot 10^{-01}$
$0.200 \cdot 10^{+00}$	$0.185 \cdot 10^{+04}$	$0.118 \cdot 10^{-01}$	$0.118 \cdot 10^{-01}$	$0.207 \cdot 10^{-01}$	$-0.217 \cdot 10^{-01}$
$0.316 \cdot 10^{+00}$	$0.831 \cdot 10^{+03}$	$0.195 \cdot 10^{-01}$	$0.195 \cdot 10^{-01}$	$0.309 \cdot 10^{-01}$	$-0.398 \cdot 10^{-01}$
$0.501 \cdot 10^{+00}$	$0.188 \cdot 10^{+03}$	$0.534 \cdot 10^{-01}$	$0.534 \cdot 10^{-01}$	$0.756 \cdot 10^{-01}$	$-0.537 \cdot 10^{-01}$
$0.794 \cdot 10^{+00}$	$0.358 \cdot 10^{+01}$	$0.846 \cdot 10^{+00}$	$0.100 \cdot 10^{+01}$	$0.142 \cdot 10^{+01}$	$-0.289 \cdot 10^{+00}$

Table J.6: $d\sigma/dx$ values for $Q^2 > 200$ GeV^2 for the $(e^+p)^{920}$ sample

x	$\frac{d\sigma^{820}}{dx}$	$\%\delta_{sta.Up}$	$\%\delta_{sta.Dn}$	$\%\delta_{sys.Up}$	$\%\delta_{sys.Dn}$
$0.126 \cdot 10^{+00}$	$0.305 \cdot 10^{+01}$	$0.484 \cdot 10^{+00}$	$0.661 \cdot 10^{+00}$	$0.137 \cdot 10^{+00}$	$-0.158 \cdot 10^{+00}$
$0.200 \cdot 10^{+00}$	$0.616 \cdot 10^{+01}$	$0.256 \cdot 10^{+00}$	$0.256 \cdot 10^{+00}$	$0.136 \cdot 10^{+00}$	$-0.345 \cdot 10^{+00}$
$0.316 \cdot 10^{+00}$	$0.349 \cdot 10^{+01}$	$0.259 \cdot 10^{+00}$	$0.259 \cdot 10^{+00}$	$0.179 \cdot 10^{+00}$	$-0.643 \cdot 10^{-01}$
$0.501 \cdot 10^{+00}$	$0.113 \cdot 10^{+01}$	$0.348 \cdot 10^{+00}$	$0.448 \cdot 10^{+00}$	$0.583 \cdot 10^{-01}$	$-0.272 \cdot 10^{-01}$
$0.794 \cdot 10^{+00}$	$0.741 \cdot 10^{-01}$	$0.850 \cdot 10^{+00}$	$0.101 \cdot 10^{+01}$	$0.167 \cdot 10^{+00}$	$-0.151 \cdot 10^{+00}$
$0.794 \cdot 10^{-01}$	$0.640 \cdot 10^{+04}$	$0.148 \cdot 10^{-01}$	$0.148 \cdot 10^{-01}$	$0.133 \cdot 10^{-01}$	$-0.168 \cdot 10^{-01}$
$0.126 \cdot 10^{+00}$	$0.372 \cdot 10^{+04}$	$0.151 \cdot 10^{-01}$	$0.151 \cdot 10^{-01}$	$0.890 \cdot 10^{-02}$	$-0.178 \cdot 10^{-01}$
$0.200 \cdot 10^{+00}$	$0.194 \cdot 10^{+04}$	$0.168 \cdot 10^{-01}$	$0.168 \cdot 10^{-01}$	$0.323 \cdot 10^{-01}$	$-0.133 \cdot 10^{-01}$
$0.316 \cdot 10^{+00}$	$0.729 \cdot 10^{+03}$	$0.265 \cdot 10^{-01}$	$0.265 \cdot 10^{-01}$	$0.566 \cdot 10^{-01}$	$-0.391 \cdot 10^{-01}$
$0.501 \cdot 10^{+00}$	$0.215 \cdot 10^{+03}$	$0.658 \cdot 10^{-01}$	$0.658 \cdot 10^{-01}$	$0.644 \cdot 10^{-01}$	$-0.345 \cdot 10^{-01}$
$0.794 \cdot 10^{+00}$	$0.223 \cdot 10^{+02}$	$0.449 \cdot 10^{+00}$	$0.595 \cdot 10^{+00}$	$0.267 \cdot 10^{+00}$	$-0.555 \cdot 10^{+00}$

Table J.7: $d\sigma/dx$ values for $Q^2 > 1000$ GeV^2 for the $(e^+p)^{820}$ sample

x	$\frac{d\sigma^{920}}{dx}$	$\%\delta_{sta.Up}$	$\%\delta_{sta.Dn}$	$\%\delta_{sys.Up}$	$\%\delta_{sys.Dn}$
$0.126 \cdot 10^{+00}$	$0.705 \cdot 10^{+01}$	$0.255 \cdot 10^{+00}$	$0.711 \cdot 10^{+00}$	$0.328 \cdot 10^{+00}$	$-0.409 \cdot 10^{+00}$
$0.200 \cdot 10^{+00}$	$0.221 \cdot 10^{+02}$	$0.196 \cdot 10^{+00}$	$0.196 \cdot 10^{+00}$	$0.131 \cdot 10^{+00}$	$-0.147 \cdot 10^{+00}$
$0.316 \cdot 10^{+00}$	$0.110 \cdot 10^{+02}$	$0.201 \cdot 10^{+00}$	$0.201 \cdot 10^{+00}$	$0.744 \cdot 10^{-01}$	$-0.815 \cdot 10^{-01}$
$0.501 \cdot 10^{+00}$	$0.344 \cdot 10^{+01}$	$0.279 \cdot 10^{+00}$	$0.279 \cdot 10^{+00}$	$0.146 \cdot 10^{+00}$	$-0.982 \cdot 10^{-01}$
$0.794 \cdot 10^{+00}$	$0.000 \cdot 10^{+00}$	$0.000 \cdot 10^{+00}$	$0.000 \cdot 10^{+00}$	$0.000 \cdot 10^{+00}$	$0.000 \cdot 10^{+00}$
$0.794 \cdot 10^{-01}$	$0.647 \cdot 10^{+04}$	$0.182 \cdot 10^{-01}$	$0.182 \cdot 10^{-01}$	$0.164 \cdot 10^{-01}$	$-0.230 \cdot 10^{-01}$
$0.126 \cdot 10^{+00}$	$0.360 \cdot 10^{+04}$	$0.188 \cdot 10^{-01}$	$0.188 \cdot 10^{-01}$	$0.165 \cdot 10^{-01}$	$-0.164 \cdot 10^{-01}$
$0.200 \cdot 10^{+00}$	$0.198 \cdot 10^{+04}$	$0.206 \cdot 10^{-01}$	$0.206 \cdot 10^{-01}$	$0.139 \cdot 10^{-01}$	$-0.280 \cdot 10^{-01}$
$0.316 \cdot 10^{+00}$	$0.830 \cdot 10^{+03}$	$0.344 \cdot 10^{-01}$	$0.344 \cdot 10^{-01}$	$0.315 \cdot 10^{-01}$	$-0.351 \cdot 10^{-01}$
$0.501 \cdot 10^{+00}$	$0.215 \cdot 10^{+03}$	$0.901 \cdot 10^{-01}$	$0.901 \cdot 10^{-01}$	$0.649 \cdot 10^{-01}$	$-0.753 \cdot 10^{-01}$
$0.794 \cdot 10^{+00}$	$0.000 \cdot 10^{+00}$	$0.000 \cdot 10^{+00}$	$0.000 \cdot 10^{+00}$	$0.000 \cdot 10^{+00}$	$0.000 \cdot 10^{+00}$

Table J.8: $d\sigma/dx$ values for $Q^2 > 1000$ GeV^2 for the $(e^-p)^{920}$ sample

x	$\frac{d\sigma^{920}}{dx}$	$\%\delta_{sta.Up}$	$\%\delta_{sta.Dn}$	$\%\delta_{sys.Up}$	$\%\delta_{sys.Dn}$
$0.126 \cdot 10^{+00}$	$0.731 \cdot 10^{+01}$	$0.248 \cdot 10^{+00}$	$0.248 \cdot 10^{+00}$	$0.212 \cdot 10^{+00}$	$-0.366 \cdot 10^{+00}$
$0.200 \cdot 10^{+00}$	$0.766 \cdot 10^{+01}$	$0.170 \cdot 10^{+00}$	$0.170 \cdot 10^{+00}$	$0.126 \cdot 10^{+00}$	$-0.156 \cdot 10^{+00}$
$0.316 \cdot 10^{+00}$	$0.475 \cdot 10^{+01}$	$0.161 \cdot 10^{+00}$	$0.161 \cdot 10^{+00}$	$0.672 \cdot 10^{-01}$	$-0.174 \cdot 10^{+00}$
$0.501 \cdot 10^{+00}$	$0.134 \cdot 10^{+01}$	$0.244 \cdot 10^{+00}$	$0.244 \cdot 10^{+00}$	$0.525 \cdot 10^{-01}$	$-0.155 \cdot 10^{+00}$
$0.794 \cdot 10^{+00}$	$0.000 \cdot 10^{+00}$	$0.000 \cdot 10^{+00}$	$0.000 \cdot 10^{+00}$	$0.000 \cdot 10^{+00}$	$0.000 \cdot 10^{+00}$
$0.794 \cdot 10^{-01}$	$0.643 \cdot 10^{+04}$	$0.102 \cdot 10^{-01}$	$0.102 \cdot 10^{-01}$	$0.203 \cdot 10^{-01}$	$-0.202 \cdot 10^{-01}$
$0.126 \cdot 10^{+00}$	$0.349 \cdot 10^{+04}$	$0.106 \cdot 10^{-01}$	$0.106 \cdot 10^{-01}$	$0.207 \cdot 10^{-01}$	$-0.189 \cdot 10^{-01}$
$0.200 \cdot 10^{+00}$	$0.185 \cdot 10^{+04}$	$0.118 \cdot 10^{-01}$	$0.118 \cdot 10^{-01}$	$0.207 \cdot 10^{-01}$	$-0.217 \cdot 10^{-01}$
$0.316 \cdot 10^{+00}$	$0.831 \cdot 10^{+03}$	$0.195 \cdot 10^{-01}$	$0.195 \cdot 10^{-01}$	$0.309 \cdot 10^{-01}$	$-0.398 \cdot 10^{-01}$
$0.501 \cdot 10^{+00}$	$0.188 \cdot 10^{+03}$	$0.534 \cdot 10^{-01}$	$0.534 \cdot 10^{-01}$	$0.756 \cdot 10^{-01}$	$-0.537 \cdot 10^{-01}$
$0.794 \cdot 10^{+00}$	$0.358 \cdot 10^{+01}$	$0.846 \cdot 10^{+00}$	$0.100 \cdot 10^{+01}$	$0.142 \cdot 10^{+01}$	$-0.289 \cdot 10^{+00}$

Table J.9: $d\sigma/dx$ values for $Q^2 > 1000$ GeV^2 for the $(e^+p)^{920}$ sample

y	$\frac{d\sigma^{820}}{dy}$	$\%\delta_{sta.Up}$	$\%\delta_{sta.Dn}$	$\%\delta_{sys.Up}$	$\%\delta_{sys.Dn}$
$0.750 \cdot 10^{-01}$	$0.725 \cdot 10^{+04}$	$0.122 \cdot 10^{-01}$	$0.122 \cdot 10^{-01}$	$0.119 \cdot 10^{-01}$	$-0.164 \cdot 10^{-01}$
$0.125 \cdot 10^{+00}$	$0.504 \cdot 10^{+04}$	$0.148 \cdot 10^{-01}$	$0.148 \cdot 10^{-01}$	$0.781 \cdot 10^{-02}$	$-0.182 \cdot 10^{-01}$
$0.175 \cdot 10^{+00}$	$0.376 \cdot 10^{+04}$	$0.170 \cdot 10^{-01}$	$0.170 \cdot 10^{-01}$	$0.157 \cdot 10^{-01}$	$-0.219 \cdot 10^{-01}$
$0.225 \cdot 10^{+00}$	$0.315 \cdot 10^{+04}$	$0.189 \cdot 10^{-01}$	$0.189 \cdot 10^{-01}$	$0.147 \cdot 10^{-01}$	$-0.314 \cdot 10^{-01}$
$0.275 \cdot 10^{+00}$	$0.256 \cdot 10^{+04}$	$0.210 \cdot 10^{-01}$	$0.210 \cdot 10^{-01}$	$0.173 \cdot 10^{-01}$	$-0.249 \cdot 10^{-01}$
$0.325 \cdot 10^{+00}$	$0.218 \cdot 10^{+04}$	$0.226 \cdot 10^{-01}$	$0.226 \cdot 10^{-01}$	$0.125 \cdot 10^{-01}$	$-0.184 \cdot 10^{-01}$
$0.375 \cdot 10^{+00}$	$0.191 \cdot 10^{+04}$	$0.241 \cdot 10^{-01}$	$0.241 \cdot 10^{-01}$	$0.169 \cdot 10^{-01}$	$-0.227 \cdot 10^{-01}$
$0.425 \cdot 10^{+00}$	$0.173 \cdot 10^{+04}$	$0.257 \cdot 10^{-01}$	$0.257 \cdot 10^{-01}$	$0.193 \cdot 10^{-01}$	$-0.300 \cdot 10^{-01}$
$0.475 \cdot 10^{+00}$	$0.146 \cdot 10^{+04}$	$0.273 \cdot 10^{-01}$	$0.273 \cdot 10^{-01}$	$0.289 \cdot 10^{-01}$	$-0.214 \cdot 10^{-01}$
$0.525 \cdot 10^{+00}$	$0.132 \cdot 10^{+04}$	$0.289 \cdot 10^{-01}$	$0.289 \cdot 10^{-01}$	$0.335 \cdot 10^{-01}$	$-0.366 \cdot 10^{-01}$
$0.575 \cdot 10^{+00}$	$0.120 \cdot 10^{+04}$	$0.308 \cdot 10^{-01}$	$0.308 \cdot 10^{-01}$	$0.537 \cdot 10^{-01}$	$-0.397 \cdot 10^{-01}$
$0.625 \cdot 10^{+00}$	$0.110 \cdot 10^{+04}$	$0.332 \cdot 10^{-01}$	$0.332 \cdot 10^{-01}$	$0.703 \cdot 10^{-01}$	$-0.412 \cdot 10^{-01}$
$0.675 \cdot 10^{+00}$	$0.103 \cdot 10^{+04}$	$0.354 \cdot 10^{-01}$	$0.354 \cdot 10^{-01}$	$0.858 \cdot 10^{-01}$	$-0.638 \cdot 10^{-01}$
$0.725 \cdot 10^{+00}$	$0.967 \cdot 10^{+03}$	$0.389 \cdot 10^{-01}$	$0.389 \cdot 10^{-01}$	$0.150 \cdot 10^{+00}$	$-0.910 \cdot 10^{-01}$
$0.775 \cdot 10^{+00}$	$0.781 \cdot 10^{+03}$	$0.477 \cdot 10^{-01}$	$0.477 \cdot 10^{-01}$	$0.174 \cdot 10^{+00}$	$-0.925 \cdot 10^{-01}$
$0.825 \cdot 10^{+00}$	$0.823 \cdot 10^{+03}$	$0.567 \cdot 10^{-01}$	$0.567 \cdot 10^{-01}$	$0.123 \cdot 10^{+00}$	$-0.169 \cdot 10^{+00}$
$0.875 \cdot 10^{+00}$	$0.773 \cdot 10^{+03}$	$0.693 \cdot 10^{-01}$	$0.693 \cdot 10^{-01}$	$0.189 \cdot 10^{+00}$	$-0.311 \cdot 10^{+00}$
$0.925 \cdot 10^{+00}$	$0.760 \cdot 10^{+03}$	$0.884 \cdot 10^{-01}$	$0.884 \cdot 10^{-01}$	$0.314 \cdot 10^{+00}$	$-0.605 \cdot 10^{+00}$
$0.975 \cdot 10^{+00}$	$0.158 \cdot 10^{+03}$	$0.446 \cdot 10^{+00}$	$0.929 \cdot 10^{+00}$	$0.204 \cdot 10^{+01}$	$-0.127 \cdot 10^{+01}$

Table J.10: $d\sigma/dy$ values for $Q^2 > 200$ GeV^2 for the $(e^+p)^{820}$ sample

y	$\frac{d\sigma^{920}}{dy}$	$\%\delta_{sta.Up}$	$\%\delta_{sta.Dn}$	$\%\delta_{sys.Up}$	$\%\delta_{sys.Dn}$
$0.750 \cdot 10^{-01}$	$0.749 \cdot 10^{+04}$	$0.149 \cdot 10^{-01}$	$0.149 \cdot 10^{-01}$	$0.140 \cdot 10^{-01}$	$-0.135 \cdot 10^{-01}$
$0.125 \cdot 10^{+00}$	$0.520 \cdot 10^{+04}$	$0.180 \cdot 10^{-01}$	$0.180 \cdot 10^{-01}$	$0.101 \cdot 10^{-01}$	$-0.223 \cdot 10^{-01}$
$0.175 \cdot 10^{+00}$	$0.412 \cdot 10^{+04}$	$0.207 \cdot 10^{-01}$	$0.207 \cdot 10^{-01}$	$0.148 \cdot 10^{-01}$	$-0.237 \cdot 10^{-01}$
$0.225 \cdot 10^{+00}$	$0.330 \cdot 10^{+04}$	$0.229 \cdot 10^{-01}$	$0.229 \cdot 10^{-01}$	$0.217 \cdot 10^{-01}$	$-0.209 \cdot 10^{-01}$
$0.275 \cdot 10^{+00}$	$0.266 \cdot 10^{+04}$	$0.255 \cdot 10^{-01}$	$0.255 \cdot 10^{-01}$	$0.189 \cdot 10^{-01}$	$-0.238 \cdot 10^{-01}$
$0.325 \cdot 10^{+00}$	$0.243 \cdot 10^{+04}$	$0.270 \cdot 10^{-01}$	$0.270 \cdot 10^{-01}$	$0.206 \cdot 10^{-01}$	$-0.290 \cdot 10^{-01}$
$0.375 \cdot 10^{+00}$	$0.210 \cdot 10^{+04}$	$0.288 \cdot 10^{-01}$	$0.288 \cdot 10^{-01}$	$0.132 \cdot 10^{-01}$	$-0.322 \cdot 10^{-01}$
$0.425 \cdot 10^{+00}$	$0.176 \cdot 10^{+04}$	$0.313 \cdot 10^{-01}$	$0.313 \cdot 10^{-01}$	$0.229 \cdot 10^{-01}$	$-0.179 \cdot 10^{-01}$
$0.475 \cdot 10^{+00}$	$0.164 \cdot 10^{+04}$	$0.326 \cdot 10^{-01}$	$0.326 \cdot 10^{-01}$	$0.379 \cdot 10^{-01}$	$-0.298 \cdot 10^{-01}$
$0.525 \cdot 10^{+00}$	$0.142 \cdot 10^{+04}$	$0.354 \cdot 10^{-01}$	$0.354 \cdot 10^{-01}$	$0.163 \cdot 10^{-01}$	$-0.297 \cdot 10^{-01}$
$0.575 \cdot 10^{+00}$	$0.130 \cdot 10^{+04}$	$0.376 \cdot 10^{-01}$	$0.376 \cdot 10^{-01}$	$0.448 \cdot 10^{-01}$	$-0.398 \cdot 10^{-01}$
$0.625 \cdot 10^{+00}$	$0.115 \cdot 10^{+04}$	$0.417 \cdot 10^{-01}$	$0.417 \cdot 10^{-01}$	$0.670 \cdot 10^{-01}$	$-0.407 \cdot 10^{-01}$
$0.675 \cdot 10^{+00}$	$0.116 \cdot 10^{+04}$	$0.437 \cdot 10^{-01}$	$0.437 \cdot 10^{-01}$	$0.863 \cdot 10^{-01}$	$-0.527 \cdot 10^{-01}$
$0.725 \cdot 10^{+00}$	$0.936 \cdot 10^{+03}$	$0.507 \cdot 10^{-01}$	$0.507 \cdot 10^{-01}$	$0.128 \cdot 10^{+00}$	$-0.938 \cdot 10^{-01}$
$0.775 \cdot 10^{+00}$	$0.901 \cdot 10^{+03}$	$0.607 \cdot 10^{-01}$	$0.607 \cdot 10^{-01}$	$0.138 \cdot 10^{+00}$	$-0.107 \cdot 10^{+00}$
$0.825 \cdot 10^{+00}$	$0.930 \cdot 10^{+03}$	$0.703 \cdot 10^{-01}$	$0.703 \cdot 10^{-01}$	$0.153 \cdot 10^{+00}$	$-0.147 \cdot 10^{+00}$
$0.875 \cdot 10^{+00}$	$0.732 \cdot 10^{+03}$	$0.923 \cdot 10^{-01}$	$0.923 \cdot 10^{-01}$	$0.196 \cdot 10^{+00}$	$-0.212 \cdot 10^{+00}$
$0.925 \cdot 10^{+00}$	$0.862 \cdot 10^{+03}$	$0.114 \cdot 10^{+00}$	$0.114 \cdot 10^{+00}$	$0.232 \cdot 10^{+00}$	$-0.602 \cdot 10^{+00}$
$0.975 \cdot 10^{+00}$	$0.217 \cdot 10^{+03}$	$0.149 \cdot 10^{+00}$	$0.101 \cdot 10^{+01}$	$0.342 \cdot 10^{+01}$	$-0.671 \cdot 10^{+00}$

Table J.11: $d\sigma/dy$ values for $Q^2 > 200$ GeV^2 for the $(e^- p)^{920}$ sample

y	$\frac{d\sigma^{920}}{dy}$	$\%\delta_{sta.Up}$	$\%\delta_{sta.Dn}$	$\%\delta_{sys.Up}$	$\%\delta_{sys.Dn}$
$0.750 \cdot 10^{-01}$	$0.735 \cdot 10^{+04}$	$0.839 \cdot 10^{-02}$	$0.839 \cdot 10^{-02}$	$0.152 \cdot 10^{-01}$	$-0.176 \cdot 10^{-01}$
$0.125 \cdot 10^{+00}$	$0.522 \cdot 10^{+04}$	$0.101 \cdot 10^{-01}$	$0.101 \cdot 10^{-01}$	$0.175 \cdot 10^{-01}$	$-0.159 \cdot 10^{-01}$
$0.175 \cdot 10^{+00}$	$0.400 \cdot 10^{+04}$	$0.116 \cdot 10^{-01}$	$0.116 \cdot 10^{-01}$	$0.152 \cdot 10^{-01}$	$-0.225 \cdot 10^{-01}$
$0.225 \cdot 10^{+00}$	$0.319 \cdot 10^{+04}$	$0.130 \cdot 10^{-01}$	$0.130 \cdot 10^{-01}$	$0.165 \cdot 10^{-01}$	$-0.265 \cdot 10^{-01}$
$0.275 \cdot 10^{+00}$	$0.269 \cdot 10^{+04}$	$0.143 \cdot 10^{-01}$	$0.143 \cdot 10^{-01}$	$0.166 \cdot 10^{-01}$	$-0.198 \cdot 10^{-01}$
$0.325 \cdot 10^{+00}$	$0.235 \cdot 10^{+04}$	$0.154 \cdot 10^{-01}$	$0.154 \cdot 10^{-01}$	$0.203 \cdot 10^{-01}$	$-0.294 \cdot 10^{-01}$
$0.375 \cdot 10^{+00}$	$0.200 \cdot 10^{+04}$	$0.164 \cdot 10^{-01}$	$0.164 \cdot 10^{-01}$	$0.184 \cdot 10^{-01}$	$-0.248 \cdot 10^{-01}$
$0.425 \cdot 10^{+00}$	$0.175 \cdot 10^{+04}$	$0.175 \cdot 10^{-01}$	$0.175 \cdot 10^{-01}$	$0.217 \cdot 10^{-01}$	$-0.274 \cdot 10^{-01}$
$0.475 \cdot 10^{+00}$	$0.160 \cdot 10^{+04}$	$0.185 \cdot 10^{-01}$	$0.185 \cdot 10^{-01}$	$0.250 \cdot 10^{-01}$	$-0.258 \cdot 10^{-01}$
$0.525 \cdot 10^{+00}$	$0.139 \cdot 10^{+04}$	$0.199 \cdot 10^{-01}$	$0.199 \cdot 10^{-01}$	$0.326 \cdot 10^{-01}$	$-0.237 \cdot 10^{-01}$
$0.575 \cdot 10^{+00}$	$0.125 \cdot 10^{+04}$	$0.213 \cdot 10^{-01}$	$0.213 \cdot 10^{-01}$	$0.439 \cdot 10^{-01}$	$-0.283 \cdot 10^{-01}$
$0.625 \cdot 10^{+00}$	$0.115 \cdot 10^{+04}$	$0.233 \cdot 10^{-01}$	$0.233 \cdot 10^{-01}$	$0.573 \cdot 10^{-01}$	$-0.526 \cdot 10^{-01}$
$0.675 \cdot 10^{+00}$	$0.109 \cdot 10^{+04}$	$0.247 \cdot 10^{-01}$	$0.247 \cdot 10^{-01}$	$0.700 \cdot 10^{-01}$	$-0.854 \cdot 10^{-01}$
$0.725 \cdot 10^{+00}$	$0.948 \cdot 10^{+03}$	$0.282 \cdot 10^{-01}$	$0.282 \cdot 10^{-01}$	$0.126 \cdot 10^{+00}$	$-0.108 \cdot 10^{+00}$
$0.775 \cdot 10^{+00}$	$0.907 \cdot 10^{+03}$	$0.333 \cdot 10^{-01}$	$0.333 \cdot 10^{-01}$	$0.151 \cdot 10^{+00}$	$-0.141 \cdot 10^{+00}$
$0.825 \cdot 10^{+00}$	$0.845 \cdot 10^{+03}$	$0.413 \cdot 10^{-01}$	$0.413 \cdot 10^{-01}$	$0.161 \cdot 10^{+00}$	$-0.131 \cdot 10^{+00}$
$0.875 \cdot 10^{+00}$	$0.894 \cdot 10^{+03}$	$0.482 \cdot 10^{-01}$	$0.482 \cdot 10^{-01}$	$0.166 \cdot 10^{+00}$	$-0.186 \cdot 10^{+00}$
$0.925 \cdot 10^{+00}$	$0.865 \cdot 10^{+03}$	$0.611 \cdot 10^{-01}$	$0.611 \cdot 10^{-01}$	$0.216 \cdot 10^{+00}$	$-0.318 \cdot 10^{+00}$
$0.975 \cdot 10^{+00}$	$0.439 \cdot 10^{+03}$	$0.302 \cdot 10^{+00}$	$0.302 \cdot 10^{+00}$	$0.690 \cdot 10^{+00}$	$-0.760 \cdot 10^{+00}$

Table J.12: $d\sigma/dy$ values for $Q^2 > 200$ GeV^2 for the $(e^+ p)^{920}$ sample

x	Q^2	$\frac{d^2\sigma^{820}}{dx,dQ^2}$	$\%\delta_{sta.Up}$	$\%\delta_{sta.Dn}$	$\%\delta_{sys.Up}$	$\%\delta_{sys.Dn}$
$0.320 \cdot 10^{-02}$	$0.200 \cdot 10^{+03}$	$0.101 \cdot 10^{+01}$	$0.687 \cdot 10^{-01}$	$0.687 \cdot 10^{-01}$	$0.300 \cdot 10^{+00}$	$-0.133 \cdot 10^{+00}$
$0.500 \cdot 10^{-02}$	$0.200 \cdot 10^{+03}$	$0.106 \cdot 10^{+01}$	$0.240 \cdot 10^{-01}$	$0.240 \cdot 10^{-01}$	$0.466 \cdot 10^{-01}$	$-0.353 \cdot 10^{-01}$
$0.800 \cdot 10^{-02}$	$0.200 \cdot 10^{+03}$	$0.952 \cdot 10^{+00}$	$0.225 \cdot 10^{-01}$	$0.225 \cdot 10^{-01}$	$0.185 \cdot 10^{-01}$	$-0.286 \cdot 10^{-01}$
$0.130 \cdot 10^{-01}$	$0.200 \cdot 10^{+03}$	$0.818 \cdot 10^{+00}$	$0.224 \cdot 10^{-01}$	$0.224 \cdot 10^{-01}$	$0.134 \cdot 10^{-01}$	$-0.238 \cdot 10^{-01}$
$0.210 \cdot 10^{-01}$	$0.200 \cdot 10^{+03}$	$0.694 \cdot 10^{+00}$	$0.273 \cdot 10^{-01}$	$0.273 \cdot 10^{-01}$	$0.971 \cdot 10^{-02}$	$-0.384 \cdot 10^{-01}$
$0.320 \cdot 10^{-01}$	$0.200 \cdot 10^{+03}$	$0.623 \cdot 10^{+00}$	$0.281 \cdot 10^{-01}$	$0.281 \cdot 10^{-01}$	$0.164 \cdot 10^{-01}$	$-0.204 \cdot 10^{-01}$
$0.500 \cdot 10^{-01}$	$0.200 \cdot 10^{+03}$	$0.531 \cdot 10^{+00}$	$0.269 \cdot 10^{-01}$	$0.269 \cdot 10^{-01}$	$0.152 \cdot 10^{-01}$	$-0.122 \cdot 10^{-01}$
$0.800 \cdot 10^{-01}$	$0.200 \cdot 10^{+03}$	$0.448 \cdot 10^{+00}$	$0.234 \cdot 10^{-01}$	$0.234 \cdot 10^{-01}$	$0.983 \cdot 10^{-02}$	$-0.106 \cdot 10^{-01}$
$0.180 \cdot 10^{+00}$	$0.200 \cdot 10^{+03}$	$0.347 \cdot 10^{+00}$	$0.251 \cdot 10^{-01}$	$0.251 \cdot 10^{-01}$	$0.471 \cdot 10^{-01}$	$-0.278 \cdot 10^{-01}$
$0.500 \cdot 10^{-02}$	$0.250 \cdot 10^{+03}$	$0.107 \cdot 10^{+01}$	$0.395 \cdot 10^{-01}$	$0.395 \cdot 10^{-01}$	$0.990 \cdot 10^{-01}$	$-0.808 \cdot 10^{-01}$
$0.800 \cdot 10^{-02}$	$0.250 \cdot 10^{+03}$	$0.941 \cdot 10^{+00}$	$0.266 \cdot 10^{-01}$	$0.266 \cdot 10^{-01}$	$0.203 \cdot 10^{-01}$	$-0.236 \cdot 10^{-01}$
$0.130 \cdot 10^{-01}$	$0.250 \cdot 10^{+03}$	$0.819 \cdot 10^{+00}$	$0.265 \cdot 10^{-01}$	$0.265 \cdot 10^{-01}$	$0.166 \cdot 10^{-01}$	$-0.250 \cdot 10^{-01}$
$0.210 \cdot 10^{-01}$	$0.250 \cdot 10^{+03}$	$0.708 \cdot 10^{+00}$	$0.313 \cdot 10^{-01}$	$0.313 \cdot 10^{-01}$	$0.145 \cdot 10^{-01}$	$-0.339 \cdot 10^{-01}$
$0.320 \cdot 10^{-01}$	$0.250 \cdot 10^{+03}$	$0.621 \cdot 10^{+00}$	$0.332 \cdot 10^{-01}$	$0.332 \cdot 10^{-01}$	$0.169 \cdot 10^{-01}$	$-0.153 \cdot 10^{-01}$
$0.500 \cdot 10^{-01}$	$0.250 \cdot 10^{+03}$	$0.559 \cdot 10^{+00}$	$0.309 \cdot 10^{-01}$	$0.309 \cdot 10^{-01}$	$0.111 \cdot 10^{-01}$	$-0.261 \cdot 10^{-01}$
$0.800 \cdot 10^{-01}$	$0.250 \cdot 10^{+03}$	$0.457 \cdot 10^{+00}$	$0.270 \cdot 10^{-01}$	$0.270 \cdot 10^{-01}$	$0.112 \cdot 10^{-01}$	$-0.216 \cdot 10^{-01}$
$0.180 \cdot 10^{+00}$	$0.250 \cdot 10^{+03}$	$0.353 \cdot 10^{+00}$	$0.289 \cdot 10^{-01}$	$0.289 \cdot 10^{-01}$	$0.372 \cdot 10^{-01}$	$-0.205 \cdot 10^{-01}$
$0.500 \cdot 10^{-02}$	$0.350 \cdot 10^{+03}$	$0.109 \cdot 10^{+01}$	$0.622 \cdot 10^{-01}$	$0.622 \cdot 10^{-01}$	$0.149 \cdot 10^{+00}$	$-0.164 \cdot 10^{+00}$
$0.800 \cdot 10^{-02}$	$0.350 \cdot 10^{+03}$	$0.966 \cdot 10^{+00}$	$0.360 \cdot 10^{-01}$	$0.360 \cdot 10^{-01}$	$0.429 \cdot 10^{-01}$	$-0.325 \cdot 10^{-01}$
$0.130 \cdot 10^{-01}$	$0.350 \cdot 10^{+03}$	$0.844 \cdot 10^{+00}$	$0.308 \cdot 10^{-01}$	$0.308 \cdot 10^{-01}$	$0.236 \cdot 10^{-01}$	$-0.460 \cdot 10^{-01}$
$0.210 \cdot 10^{-01}$	$0.350 \cdot 10^{+03}$	$0.697 \cdot 10^{+00}$	$0.351 \cdot 10^{-01}$	$0.351 \cdot 10^{-01}$	$0.111 \cdot 10^{-01}$	$-0.226 \cdot 10^{-01}$
$0.320 \cdot 10^{-01}$	$0.350 \cdot 10^{+03}$	$0.655 \cdot 10^{+00}$	$0.355 \cdot 10^{-01}$	$0.355 \cdot 10^{-01}$	$0.579 \cdot 10^{-02}$	$-0.327 \cdot 10^{-01}$
$0.500 \cdot 10^{-01}$	$0.350 \cdot 10^{+03}$	$0.538 \cdot 10^{+00}$	$0.336 \cdot 10^{-01}$	$0.336 \cdot 10^{-01}$	$0.241 \cdot 10^{-01}$	$-0.183 \cdot 10^{-01}$
$0.800 \cdot 10^{-01}$	$0.350 \cdot 10^{+03}$	$0.454 \cdot 10^{+00}$	$0.308 \cdot 10^{-01}$	$0.308 \cdot 10^{-01}$	$0.106 \cdot 10^{-01}$	$-0.309 \cdot 10^{-01}$
$0.180 \cdot 10^{+00}$	$0.350 \cdot 10^{+03}$	$0.373 \cdot 10^{+00}$	$0.316 \cdot 10^{-01}$	$0.316 \cdot 10^{-01}$	$0.285 \cdot 10^{-01}$	$-0.276 \cdot 10^{-01}$
$0.800 \cdot 10^{-02}$	$0.450 \cdot 10^{+03}$	$0.950 \cdot 10^{+00}$	$0.366 \cdot 10^{-01}$	$0.366 \cdot 10^{-01}$	$0.739 \cdot 10^{-01}$	$-0.513 \cdot 10^{-01}$
$0.130 \cdot 10^{-01}$	$0.450 \cdot 10^{+03}$	$0.857 \cdot 10^{+00}$	$0.406 \cdot 10^{-01}$	$0.406 \cdot 10^{-01}$	$0.246 \cdot 10^{-01}$	$-0.877 \cdot 10^{-02}$
$0.210 \cdot 10^{-01}$	$0.450 \cdot 10^{+03}$	$0.704 \cdot 10^{+00}$	$0.451 \cdot 10^{-01}$	$0.451 \cdot 10^{-01}$	$0.223 \cdot 10^{-01}$	$-0.229 \cdot 10^{-01}$
$0.320 \cdot 10^{-01}$	$0.450 \cdot 10^{+03}$	$0.578 \cdot 10^{+00}$	$0.414 \cdot 10^{-01}$	$0.414 \cdot 10^{-01}$	$0.135 \cdot 10^{-01}$	$-0.153 \cdot 10^{-01}$
$0.500 \cdot 10^{-01}$	$0.450 \cdot 10^{+03}$	$0.523 \cdot 10^{+00}$	$0.359 \cdot 10^{-01}$	$0.359 \cdot 10^{-01}$	$0.130 \cdot 10^{-01}$	$-0.113 \cdot 10^{-01}$
$0.800 \cdot 10^{-01}$	$0.450 \cdot 10^{+03}$	$0.434 \cdot 10^{+00}$	$0.370 \cdot 10^{-01}$	$0.370 \cdot 10^{-01}$	$0.238 \cdot 10^{-01}$	$-0.134 \cdot 10^{-01}$
$0.130 \cdot 10^{+00}$	$0.450 \cdot 10^{+03}$	$0.384 \cdot 10^{+00}$	$0.375 \cdot 10^{-01}$	$0.375 \cdot 10^{-01}$	$0.169 \cdot 10^{-01}$	$-0.986 \cdot 10^{-02}$

Table J.13: $d^2\sigma/dxdQ^2$ values for the $(e^+p)^{820}$ sample

x	Q^2	$\frac{d^2\sigma^{820}}{dx,dQ^2}$	$\%\delta_{sta.Up}$	$\%\delta_{sta.Dn}$	$\%\delta_{sys.Up}$	$\%\delta_{sys.Dn}$
$0.250 \cdot 10^{+00}$	$0.450 \cdot 10^{+03}$	$0.274 \cdot 10^{+00}$	$0.395 \cdot 10^{-01}$	$0.395 \cdot 10^{-01}$	$0.104 \cdot 10^{-01}$	$-0.178 \cdot 10^{-01}$
$0.800 \cdot 10^{-02}$	$0.650 \cdot 10^{+03}$	$0.840 \cdot 10^{+00}$	$0.560 \cdot 10^{-01}$	$0.560 \cdot 10^{-01}$	$0.116 \cdot 10^{+00}$	$-0.803 \cdot 10^{-01}$
$0.130 \cdot 10^{-01}$	$0.650 \cdot 10^{+03}$	$0.893 \cdot 10^{+00}$	$0.332 \cdot 10^{-01}$	$0.332 \cdot 10^{-01}$	$0.419 \cdot 10^{-01}$	$-0.244 \cdot 10^{-01}$
$0.210 \cdot 10^{-01}$	$0.650 \cdot 10^{+03}$	$0.744 \cdot 10^{+00}$	$0.456 \cdot 10^{-01}$	$0.456 \cdot 10^{-01}$	$0.971 \cdot 10^{-02}$	$-0.138 \cdot 10^{-01}$
$0.320 \cdot 10^{-01}$	$0.650 \cdot 10^{+03}$	$0.605 \cdot 10^{+00}$	$0.554 \cdot 10^{-01}$	$0.554 \cdot 10^{-01}$	$0.188 \cdot 10^{-01}$	$-0.255 \cdot 10^{-01}$
$0.500 \cdot 10^{-01}$	$0.650 \cdot 10^{+03}$	$0.472 \cdot 10^{+00}$	$0.578 \cdot 10^{-01}$	$0.578 \cdot 10^{-01}$	$0.226 \cdot 10^{-01}$	$-0.302 \cdot 10^{-01}$
$0.800 \cdot 10^{-01}$	$0.650 \cdot 10^{+03}$	$0.430 \cdot 10^{+00}$	$0.548 \cdot 10^{-01}$	$0.548 \cdot 10^{-01}$	$0.159 \cdot 10^{-01}$	$-0.501 \cdot 10^{-01}$
$0.130 \cdot 10^{+00}$	$0.650 \cdot 10^{+03}$	$0.311 \cdot 10^{+00}$	$0.568 \cdot 10^{-01}$	$0.568 \cdot 10^{-01}$	$0.172 \cdot 10^{-01}$	$-0.231 \cdot 10^{-01}$
$0.250 \cdot 10^{+00}$	$0.650 \cdot 10^{+03}$	$0.246 \cdot 10^{+00}$	$0.562 \cdot 10^{-01}$	$0.562 \cdot 10^{-01}$	$0.208 \cdot 10^{-01}$	$-0.131 \cdot 10^{-01}$
$0.400 \cdot 10^{+00}$	$0.650 \cdot 10^{+03}$	$0.135 \cdot 10^{+00}$	$0.942 \cdot 10^{-01}$	$0.942 \cdot 10^{-01}$	$0.550 \cdot 10^{-01}$	$-0.408 \cdot 10^{-01}$
$0.130 \cdot 10^{-01}$	$0.800 \cdot 10^{+03}$	$0.839 \cdot 10^{+00}$	$0.438 \cdot 10^{-01}$	$0.438 \cdot 10^{-01}$	$0.611 \cdot 10^{-01}$	$-0.626 \cdot 10^{-01}$
$0.210 \cdot 10^{-01}$	$0.800 \cdot 10^{+03}$	$0.735 \cdot 10^{+00}$	$0.508 \cdot 10^{-01}$	$0.508 \cdot 10^{-01}$	$0.211 \cdot 10^{-01}$	$-0.486 \cdot 10^{-01}$
$0.320 \cdot 10^{-01}$	$0.800 \cdot 10^{+03}$	$0.632 \cdot 10^{+00}$	$0.526 \cdot 10^{-01}$	$0.526 \cdot 10^{-01}$	$0.337 \cdot 10^{-01}$	$-0.258 \cdot 10^{-01}$
$0.500 \cdot 10^{-01}$	$0.800 \cdot 10^{+03}$	$0.494 \cdot 10^{+00}$	$0.526 \cdot 10^{-01}$	$0.526 \cdot 10^{-01}$	$0.154 \cdot 10^{-01}$	$-0.186 \cdot 10^{-01}$
$0.800 \cdot 10^{-01}$	$0.800 \cdot 10^{+03}$	$0.421 \cdot 10^{+00}$	$0.587 \cdot 10^{-01}$	$0.587 \cdot 10^{-01}$	$0.182 \cdot 10^{-01}$	$-0.875 \cdot 10^{-02}$
$0.130 \cdot 10^{+00}$	$0.800 \cdot 10^{+03}$	$0.377 \cdot 10^{+00}$	$0.643 \cdot 10^{-01}$	$0.643 \cdot 10^{-01}$	$0.134 \cdot 10^{-01}$	$-0.188 \cdot 10^{-01}$
$0.250 \cdot 10^{+00}$	$0.800 \cdot 10^{+03}$	$0.293 \cdot 10^{+00}$	$0.723 \cdot 10^{-01}$	$0.723 \cdot 10^{-01}$	$0.103 \cdot 10^{-01}$	$-0.250 \cdot 10^{-01}$
$0.400 \cdot 10^{+00}$	$0.800 \cdot 10^{+03}$	$0.106 \cdot 10^{+00}$	$0.129 \cdot 10^{+00}$	$0.129 \cdot 10^{+00}$	$0.516 \cdot 10^{-01}$	$-0.392 \cdot 10^{-01}$
$0.140 \cdot 10^{-01}$	$0.120 \cdot 10^{+04}$	$0.839 \cdot 10^{+00}$	$0.571 \cdot 10^{-01}$	$0.571 \cdot 10^{-01}$	$0.885 \cdot 10^{-01}$	$-0.142 \cdot 10^{+00}$
$0.210 \cdot 10^{-01}$	$0.120 \cdot 10^{+04}$	$0.704 \cdot 10^{+00}$	$0.499 \cdot 10^{-01}$	$0.499 \cdot 10^{-01}$	$0.692 \cdot 10^{-01}$	$-0.442 \cdot 10^{-01}$
$0.320 \cdot 10^{-01}$	$0.120 \cdot 10^{+04}$	$0.578 \cdot 10^{+00}$	$0.499 \cdot 10^{-01}$	$0.499 \cdot 10^{-01}$	$0.263 \cdot 10^{-01}$	$-0.184 \cdot 10^{-01}$
$0.500 \cdot 10^{-01}$	$0.120 \cdot 10^{+04}$	$0.505 \cdot 10^{+00}$	$0.460 \cdot 10^{-01}$	$0.460 \cdot 10^{-01}$	$0.154 \cdot 10^{-01}$	$-0.288 \cdot 10^{-01}$
$0.800 \cdot 10^{-01}$	$0.120 \cdot 10^{+04}$	$0.465 \cdot 10^{+00}$	$0.457 \cdot 10^{-01}$	$0.457 \cdot 10^{-01}$	$0.143 \cdot 10^{-01}$	$-0.231 \cdot 10^{-01}$
$0.130 \cdot 10^{+00}$	$0.120 \cdot 10^{+04}$	$0.344 \cdot 10^{+00}$	$0.505 \cdot 10^{-01}$	$0.505 \cdot 10^{-01}$	$0.165 \cdot 10^{-01}$	$-0.279 \cdot 10^{-01}$
$0.250 \cdot 10^{+00}$	$0.120 \cdot 10^{+04}$	$0.262 \cdot 10^{+00}$	$0.543 \cdot 10^{-01}$	$0.543 \cdot 10^{-01}$	$0.294 \cdot 10^{-01}$	$-0.798 \cdot 10^{-02}$
$0.400 \cdot 10^{+00}$	$0.120 \cdot 10^{+04}$	$0.133 \cdot 10^{+00}$	$0.783 \cdot 10^{-01}$	$0.783 \cdot 10^{-01}$	$0.383 \cdot 10^{-01}$	$-0.301 \cdot 10^{-01}$
$0.650 \cdot 10^{+00}$	$0.120 \cdot 10^{+04}$	$0.000 \cdot 10^{+00}$	$0.000 \cdot 10^{+00}$	$0.000 \cdot 10^{+00}$	$0.000 \cdot 10^{+00}$	$0.000 \cdot 10^{+00}$
$0.210 \cdot 10^{-01}$	$0.150 \cdot 10^{+04}$	$0.830 \cdot 10^{+00}$	$0.660 \cdot 10^{-01}$	$0.660 \cdot 10^{-01}$	$0.109 \cdot 10^{+00}$	$-0.156 \cdot 10^{+00}$
$0.320 \cdot 10^{-01}$	$0.150 \cdot 10^{+04}$	$0.611 \cdot 10^{+00}$	$0.649 \cdot 10^{-01}$	$0.649 \cdot 10^{-01}$	$0.510 \cdot 10^{-01}$	$-0.330 \cdot 10^{-01}$
$0.500 \cdot 10^{-01}$	$0.150 \cdot 10^{+04}$	$0.509 \cdot 10^{+00}$	$0.587 \cdot 10^{-01}$	$0.587 \cdot 10^{-01}$	$0.103 \cdot 10^{-01}$	$-0.326 \cdot 10^{-01}$
$0.800 \cdot 10^{-01}$	$0.150 \cdot 10^{+04}$	$0.475 \cdot 10^{+00}$	$0.569 \cdot 10^{-01}$	$0.569 \cdot 10^{-01}$	$0.277 \cdot 10^{-01}$	$-0.161 \cdot 10^{-01}$
$0.130 \cdot 10^{+00}$	$0.150 \cdot 10^{+04}$	$0.348 \cdot 10^{+00}$	$0.707 \cdot 10^{-01}$	$0.707 \cdot 10^{-01}$	$0.179 \cdot 10^{-01}$	$-0.252 \cdot 10^{-01}$

Table J.14: $d^2\sigma/dxdQ^2$ values for the $(e^+p)^{820}$ sample

x	Q^2	$\frac{d^2\sigma^{820}}{dx,dQ^2}$	$\%\delta_{sta.Up}$	$\%\delta_{sta.Dn}$	$\%\delta_{sys.Up}$	$\%\delta_{sys.Dn}$
$0.180 \cdot 10^{+00}$	$0.150 \cdot 10^{+04}$	$0.330 \cdot 10^{+00}$	$0.700 \cdot 10^{-01}$	$0.700 \cdot 10^{-01}$	$0.298 \cdot 10^{-01}$	$-0.125 \cdot 10^{-01}$
$0.250 \cdot 10^{+00}$	$0.150 \cdot 10^{+04}$	$0.231 \cdot 10^{+00}$	$0.907 \cdot 10^{-01}$	$0.907 \cdot 10^{-01}$	$0.180 \cdot 10^{-01}$	$-0.176 \cdot 10^{-01}$
$0.400 \cdot 10^{+00}$	$0.150 \cdot 10^{+04}$	$0.152 \cdot 10^{+00}$	$0.111 \cdot 10^{+00}$	$0.111 \cdot 10^{+00}$	$0.674 \cdot 10^{-01}$	$-0.386 \cdot 10^{-01}$
$0.650 \cdot 10^{+00}$	$0.150 \cdot 10^{+04}$	$0.160 \cdot 10^{-01}$	$0.443 \cdot 10^{+00}$	$0.591 \cdot 10^{+00}$	$0.288 \cdot 10^{+00}$	$-0.337 \cdot 10^{+00}$
$0.320 \cdot 10^{-01}$	$0.200 \cdot 10^{+04}$	$0.622 \cdot 10^{+00}$	$0.805 \cdot 10^{-01}$	$0.805 \cdot 10^{-01}$	$0.142 \cdot 10^{+00}$	$-0.141 \cdot 10^{+00}$
$0.500 \cdot 10^{-01}$	$0.200 \cdot 10^{+04}$	$0.508 \cdot 10^{+00}$	$0.726 \cdot 10^{-01}$	$0.726 \cdot 10^{-01}$	$0.144 \cdot 10^{-01}$	$-0.460 \cdot 10^{-01}$
$0.800 \cdot 10^{-01}$	$0.200 \cdot 10^{+04}$	$0.462 \cdot 10^{+00}$	$0.695 \cdot 10^{-01}$	$0.695 \cdot 10^{-01}$	$0.303 \cdot 10^{-01}$	$-0.150 \cdot 10^{-01}$
$0.130 \cdot 10^{+00}$	$0.200 \cdot 10^{+04}$	$0.348 \cdot 10^{+00}$	$0.826 \cdot 10^{-01}$	$0.826 \cdot 10^{-01}$	$0.240 \cdot 10^{-01}$	$-0.388 \cdot 10^{-01}$
$0.180 \cdot 10^{+00}$	$0.200 \cdot 10^{+04}$	$0.274 \cdot 10^{+00}$	$0.917 \cdot 10^{-01}$	$0.917 \cdot 10^{-01}$	$0.188 \cdot 10^{-01}$	$-0.247 \cdot 10^{-01}$
$0.250 \cdot 10^{+00}$	$0.200 \cdot 10^{+04}$	$0.227 \cdot 10^{+00}$	$0.103 \cdot 10^{+00}$	$0.103 \cdot 10^{+00}$	$0.210 \cdot 10^{-01}$	$-0.131 \cdot 10^{-01}$
$0.400 \cdot 10^{+00}$	$0.200 \cdot 10^{+04}$	$0.169 \cdot 10^{+00}$	$0.127 \cdot 10^{+00}$	$0.127 \cdot 10^{+00}$	$0.367 \cdot 10^{-01}$	$-0.168 \cdot 10^{-01}$
$0.500 \cdot 10^{-01}$	$0.300 \cdot 10^{+04}$	$0.576 \cdot 10^{+00}$	$0.855 \cdot 10^{-01}$	$0.855 \cdot 10^{-01}$	$0.632 \cdot 10^{-01}$	$-0.143 \cdot 10^{+00}$
$0.800 \cdot 10^{-01}$	$0.300 \cdot 10^{+04}$	$0.378 \cdot 10^{+00}$	$0.927 \cdot 10^{-01}$	$0.927 \cdot 10^{-01}$	$0.453 \cdot 10^{-01}$	$-0.593 \cdot 10^{-01}$
$0.130 \cdot 10^{+00}$	$0.300 \cdot 10^{+04}$	$0.372 \cdot 10^{+00}$	$0.979 \cdot 10^{-01}$	$0.979 \cdot 10^{-01}$	$0.148 \cdot 10^{-01}$	$-0.155 \cdot 10^{-01}$
$0.180 \cdot 10^{+00}$	$0.300 \cdot 10^{+04}$	$0.253 \cdot 10^{+00}$	$0.114 \cdot 10^{+00}$	$0.114 \cdot 10^{+00}$	$0.253 \cdot 10^{-01}$	$-0.385 \cdot 10^{-01}$
$0.250 \cdot 10^{+00}$	$0.300 \cdot 10^{+04}$	$0.194 \cdot 10^{+00}$	$0.137 \cdot 10^{+00}$	$0.137 \cdot 10^{+00}$	$0.744 \cdot 10^{-02}$	$-0.562 \cdot 10^{-01}$
$0.400 \cdot 10^{+00}$	$0.300 \cdot 10^{+04}$	$0.115 \cdot 10^{+00}$	$0.179 \cdot 10^{+00}$	$0.179 \cdot 10^{+00}$	$0.369 \cdot 10^{-01}$	$-0.474 \cdot 10^{-01}$
$0.650 \cdot 10^{+00}$	$0.300 \cdot 10^{+04}$	$0.157 \cdot 10^{-01}$	$0.378 \cdot 10^{+00}$	$0.489 \cdot 10^{+00}$	$0.100 \cdot 10^{+00}$	$-0.100 \cdot 10^{+00}$
$0.800 \cdot 10^{-01}$	$0.500 \cdot 10^{+04}$	$0.395 \cdot 10^{+00}$	$0.875 \cdot 10^{-01}$	$0.875 \cdot 10^{-01}$	$0.868 \cdot 10^{-01}$	$-0.145 \cdot 10^{+00}$
$0.130 \cdot 10^{+00}$	$0.500 \cdot 10^{+04}$	$0.320 \cdot 10^{+00}$	$0.111 \cdot 10^{+00}$	$0.111 \cdot 10^{+00}$	$0.401 \cdot 10^{-01}$	$-0.628 \cdot 10^{-01}$
$0.180 \cdot 10^{+00}$	$0.500 \cdot 10^{+04}$	$0.255 \cdot 10^{+00}$	$0.119 \cdot 10^{+00}$	$0.119 \cdot 10^{+00}$	$0.383 \cdot 10^{-01}$	$-0.293 \cdot 10^{-01}$
$0.250 \cdot 10^{+00}$	$0.500 \cdot 10^{+04}$	$0.210 \cdot 10^{+00}$	$0.134 \cdot 10^{+00}$	$0.134 \cdot 10^{+00}$	$0.698 \cdot 10^{-01}$	$-0.237 \cdot 10^{-01}$
$0.400 \cdot 10^{+00}$	$0.500 \cdot 10^{+04}$	$0.134 \cdot 10^{+00}$	$0.169 \cdot 10^{+00}$	$0.169 \cdot 10^{+00}$	$0.705 \cdot 10^{-01}$	$-0.241 \cdot 10^{-01}$
$0.130 \cdot 10^{+00}$	$0.800 \cdot 10^{+04}$	$0.279 \cdot 10^{+00}$	$0.139 \cdot 10^{+00}$	$0.139 \cdot 10^{+00}$	$0.884 \cdot 10^{-01}$	$-0.146 \cdot 10^{+00}$
$0.180 \cdot 10^{+00}$	$0.800 \cdot 10^{+04}$	$0.270 \cdot 10^{+00}$	$0.156 \cdot 10^{+00}$	$0.156 \cdot 10^{+00}$	$0.594 \cdot 10^{-01}$	$-0.220 \cdot 10^{-01}$
$0.250 \cdot 10^{+00}$	$0.800 \cdot 10^{+04}$	$0.169 \cdot 10^{+00}$	$0.194 \cdot 10^{+00}$	$0.194 \cdot 10^{+00}$	$0.420 \cdot 10^{-01}$	$-0.154 \cdot 10^{-01}$
$0.400 \cdot 10^{+00}$	$0.800 \cdot 10^{+04}$	$0.116 \cdot 10^{+00}$	$0.232 \cdot 10^{+00}$	$0.232 \cdot 10^{+00}$	$0.436 \cdot 10^{-01}$	$-0.410 \cdot 10^{-01}$
$0.650 \cdot 10^{+00}$	$0.800 \cdot 10^{+04}$	$0.313 \cdot 10^{-01}$	$0.316 \cdot 10^{+00}$	$0.398 \cdot 10^{+00}$	$0.966 \cdot 10^{-01}$	$-0.141 \cdot 10^{+00}$
$0.180 \cdot 10^{+00}$	$0.120 \cdot 10^{+05}$	$0.205 \cdot 10^{+00}$	$0.212 \cdot 10^{+00}$	$0.212 \cdot 10^{+00}$	$0.109 \cdot 10^{+00}$	$-0.106 \cdot 10^{+00}$
$0.250 \cdot 10^{+00}$	$0.120 \cdot 10^{+05}$	$0.163 \cdot 10^{+00}$	$0.269 \cdot 10^{+00}$	$0.269 \cdot 10^{+00}$	$0.472 \cdot 10^{-01}$	$-0.289 \cdot 10^{-01}$
$0.400 \cdot 10^{+00}$	$0.120 \cdot 10^{+05}$	$0.939 \cdot 10^{-01}$	$0.329 \cdot 10^{+00}$	$0.420 \cdot 10^{+00}$	$0.445 \cdot 10^{-01}$	$-0.381 \cdot 10^{-01}$
$0.250 \cdot 10^{+00}$	$0.200 \cdot 10^{+05}$	$0.176 \cdot 10^{+00}$	$0.313 \cdot 10^{+00}$	$0.396 \cdot 10^{+00}$	$0.224 \cdot 10^{+00}$	$-0.262 \cdot 10^{+00}$
$0.400 \cdot 10^{+00}$	$0.200 \cdot 10^{+05}$	$0.811 \cdot 10^{-01}$	$0.434 \cdot 10^{+00}$	$0.584 \cdot 10^{+00}$	$0.633 \cdot 10^{-01}$	$-0.226 \cdot 10^{+00}$
$0.400 \cdot 10^{+00}$	$0.300 \cdot 10^{+05}$	$0.325 \cdot 10^{-01}$	$0.843 \cdot 10^{+00}$	$0.100 \cdot 10^{+01}$	$0.223 \cdot 10^{+00}$	$-0.436 \cdot 10^{-01}$

Table J.15: $d^2\sigma/dxdQ^2$ values for the $(e^+p)^{820}$ sample

x	Q^2	$\frac{d^2\sigma^{920}}{dx,dQ^2}$	$\%\delta_{sta.Up}$	$\%\delta_{sta.Dn}$	$\%\delta_{sys.Up}$	$\%\delta_{sys.Dn}$
$0.320 \cdot 10^{-02}$	$0.200 \cdot 10^{+03}$	$0.113 \cdot 10^{+01}$	$0.518 \cdot 10^{-01}$	$0.518 \cdot 10^{-01}$	$0.179 \cdot 10^{+00}$	$-0.109 \cdot 10^{+00}$
$0.500 \cdot 10^{-02}$	$0.200 \cdot 10^{+03}$	$0.115 \cdot 10^{+01}$	$0.269 \cdot 10^{-01}$	$0.269 \cdot 10^{-01}$	$0.212 \cdot 10^{-01}$	$-0.349 \cdot 10^{-01}$
$0.800 \cdot 10^{-02}$	$0.200 \cdot 10^{+03}$	$0.959 \cdot 10^{+00}$	$0.265 \cdot 10^{-01}$	$0.265 \cdot 10^{-01}$	$0.276 \cdot 10^{-01}$	$-0.241 \cdot 10^{-01}$
$0.130 \cdot 10^{-01}$	$0.200 \cdot 10^{+03}$	$0.809 \cdot 10^{+00}$	$0.270 \cdot 10^{-01}$	$0.270 \cdot 10^{-01}$	$0.207 \cdot 10^{-01}$	$-0.272 \cdot 10^{-01}$
$0.210 \cdot 10^{-01}$	$0.200 \cdot 10^{+03}$	$0.699 \cdot 10^{+00}$	$0.326 \cdot 10^{-01}$	$0.326 \cdot 10^{-01}$	$0.144 \cdot 10^{-01}$	$-0.166 \cdot 10^{-01}$
$0.320 \cdot 10^{-01}$	$0.200 \cdot 10^{+03}$	$0.594 \cdot 10^{+00}$	$0.341 \cdot 10^{-01}$	$0.341 \cdot 10^{-01}$	$0.251 \cdot 10^{-01}$	$-0.130 \cdot 10^{-01}$
$0.500 \cdot 10^{-01}$	$0.200 \cdot 10^{+03}$	$0.510 \cdot 10^{+00}$	$0.321 \cdot 10^{-01}$	$0.321 \cdot 10^{-01}$	$0.115 \cdot 10^{-01}$	$-0.319 \cdot 10^{-01}$
$0.800 \cdot 10^{-01}$	$0.200 \cdot 10^{+03}$	$0.435 \cdot 10^{+00}$	$0.280 \cdot 10^{-01}$	$0.280 \cdot 10^{-01}$	$0.260 \cdot 10^{-01}$	$-0.174 \cdot 10^{-01}$
$0.180 \cdot 10^{+00}$	$0.200 \cdot 10^{+03}$	$0.322 \cdot 10^{+00}$	$0.312 \cdot 10^{-01}$	$0.312 \cdot 10^{-01}$	$0.239 \cdot 10^{-01}$	$-0.377 \cdot 10^{-01}$
$0.500 \cdot 10^{-02}$	$0.250 \cdot 10^{+03}$	$0.110 \cdot 10^{+01}$	$0.408 \cdot 10^{-01}$	$0.408 \cdot 10^{-01}$	$0.423 \cdot 10^{-01}$	$-0.766 \cdot 10^{-01}$
$0.800 \cdot 10^{-02}$	$0.250 \cdot 10^{+03}$	$0.956 \cdot 10^{+00}$	$0.309 \cdot 10^{-01}$	$0.309 \cdot 10^{-01}$	$0.181 \cdot 10^{-01}$	$-0.402 \cdot 10^{-01}$
$0.130 \cdot 10^{-01}$	$0.250 \cdot 10^{+03}$	$0.842 \cdot 10^{+00}$	$0.312 \cdot 10^{-01}$	$0.312 \cdot 10^{-01}$	$0.194 \cdot 10^{-01}$	$-0.307 \cdot 10^{-01}$
$0.210 \cdot 10^{-01}$	$0.250 \cdot 10^{+03}$	$0.680 \cdot 10^{+00}$	$0.381 \cdot 10^{-01}$	$0.381 \cdot 10^{-01}$	$0.128 \cdot 10^{-01}$	$-0.416 \cdot 10^{-01}$
$0.320 \cdot 10^{-01}$	$0.250 \cdot 10^{+03}$	$0.602 \cdot 10^{+00}$	$0.390 \cdot 10^{-01}$	$0.390 \cdot 10^{-01}$	$0.163 \cdot 10^{-01}$	$-0.179 \cdot 10^{-01}$
$0.500 \cdot 10^{-01}$	$0.250 \cdot 10^{+03}$	$0.519 \cdot 10^{+00}$	$0.371 \cdot 10^{-01}$	$0.371 \cdot 10^{-01}$	$0.187 \cdot 10^{-01}$	$-0.239 \cdot 10^{-01}$
$0.800 \cdot 10^{-01}$	$0.250 \cdot 10^{+03}$	$0.439 \cdot 10^{+00}$	$0.329 \cdot 10^{-01}$	$0.329 \cdot 10^{-01}$	$0.231 \cdot 10^{-01}$	$-0.252 \cdot 10^{-01}$
$0.180 \cdot 10^{+00}$	$0.250 \cdot 10^{+03}$	$0.327 \cdot 10^{+00}$	$0.341 \cdot 10^{-01}$	$0.341 \cdot 10^{-01}$	$0.161 \cdot 10^{-01}$	$-0.285 \cdot 10^{-01}$
$0.500 \cdot 10^{-02}$	$0.350 \cdot 10^{+03}$	$0.114 \cdot 10^{+01}$	$0.577 \cdot 10^{-01}$	$0.577 \cdot 10^{-01}$	$0.162 \cdot 10^{+00}$	$-0.946 \cdot 10^{-01}$
$0.800 \cdot 10^{-02}$	$0.350 \cdot 10^{+03}$	$0.972 \cdot 10^{+00}$	$0.436 \cdot 10^{-01}$	$0.436 \cdot 10^{-01}$	$0.398 \cdot 10^{-01}$	$-0.183 \cdot 10^{-01}$
$0.130 \cdot 10^{-01}$	$0.350 \cdot 10^{+03}$	$0.864 \cdot 10^{+00}$	$0.358 \cdot 10^{-01}$	$0.358 \cdot 10^{-01}$	$0.133 \cdot 10^{-01}$	$-0.286 \cdot 10^{-01}$
$0.210 \cdot 10^{-01}$	$0.350 \cdot 10^{+03}$	$0.730 \cdot 10^{+00}$	$0.415 \cdot 10^{-01}$	$0.415 \cdot 10^{-01}$	$0.197 \cdot 10^{-01}$	$-0.317 \cdot 10^{-01}$
$0.320 \cdot 10^{-01}$	$0.350 \cdot 10^{+03}$	$0.589 \cdot 10^{+00}$	$0.438 \cdot 10^{-01}$	$0.438 \cdot 10^{-01}$	$0.166 \cdot 10^{-01}$	$-0.278 \cdot 10^{-01}$
$0.500 \cdot 10^{-01}$	$0.350 \cdot 10^{+03}$	$0.524 \cdot 10^{+00}$	$0.413 \cdot 10^{-01}$	$0.413 \cdot 10^{-01}$	$0.187 \cdot 10^{-01}$	$-0.124 \cdot 10^{-01}$
$0.800 \cdot 10^{-01}$	$0.350 \cdot 10^{+03}$	$0.445 \cdot 10^{+00}$	$0.362 \cdot 10^{-01}$	$0.362 \cdot 10^{-01}$	$0.127 \cdot 10^{-01}$	$-0.265 \cdot 10^{-01}$
$0.180 \cdot 10^{+00}$	$0.350 \cdot 10^{+03}$	$0.321 \cdot 10^{+00}$	$0.379 \cdot 10^{-01}$	$0.379 \cdot 10^{-01}$	$0.183 \cdot 10^{-01}$	$-0.274 \cdot 10^{-01}$
$0.800 \cdot 10^{-02}$	$0.450 \cdot 10^{+03}$	$0.978 \cdot 10^{+00}$	$0.446 \cdot 10^{-01}$	$0.446 \cdot 10^{-01}$	$0.615 \cdot 10^{-01}$	$-0.434 \cdot 10^{-01}$
$0.130 \cdot 10^{-01}$	$0.450 \cdot 10^{+03}$	$0.860 \cdot 10^{+00}$	$0.574 \cdot 10^{-01}$	$0.574 \cdot 10^{-01}$	$0.135 \cdot 10^{-01}$	$-0.644 \cdot 10^{-01}$
$0.210 \cdot 10^{-01}$	$0.450 \cdot 10^{+03}$	$0.690 \cdot 10^{+00}$	$0.574 \cdot 10^{-01}$	$0.574 \cdot 10^{-01}$	$0.282 \cdot 10^{-01}$	$-0.207 \cdot 10^{-01}$
$0.320 \cdot 10^{-01}$	$0.450 \cdot 10^{+03}$	$0.601 \cdot 10^{+00}$	$0.532 \cdot 10^{-01}$	$0.532 \cdot 10^{-01}$	$0.357 \cdot 10^{-01}$	$-0.131 \cdot 10^{-01}$
$0.500 \cdot 10^{-01}$	$0.450 \cdot 10^{+03}$	$0.517 \cdot 10^{+00}$	$0.471 \cdot 10^{-01}$	$0.471 \cdot 10^{-01}$	$0.158 \cdot 10^{-01}$	$-0.170 \cdot 10^{-01}$
$0.800 \cdot 10^{-01}$	$0.450 \cdot 10^{+03}$	$0.447 \cdot 10^{+00}$	$0.483 \cdot 10^{-01}$	$0.483 \cdot 10^{-01}$	$0.172 \cdot 10^{-01}$	$-0.142 \cdot 10^{-01}$
$0.130 \cdot 10^{+00}$	$0.450 \cdot 10^{+03}$	$0.397 \cdot 10^{+00}$	$0.502 \cdot 10^{-01}$	$0.502 \cdot 10^{-01}$	$0.115 \cdot 10^{-01}$	$-0.287 \cdot 10^{-01}$

Table J.16: $d^2\sigma/dxdQ^2$ values for the $(e^- p)^{920}$ sample

x	Q^2	$\frac{d^2\sigma^{920}}{dx,dQ^2}$	$\%\delta_{sta.Up}$	$\%\delta_{sta.Dn}$	$\%\delta_{sys.Up}$	$\%\delta_{sys.Dn}$
$0.250 \cdot 10^{+00}$	$0.450 \cdot 10^{+03}$	$0.279 \cdot 10^{+00}$	$0.515 \cdot 10^{-01}$	$0.515 \cdot 10^{-01}$	$0.253 \cdot 10^{-01}$	$-0.271 \cdot 10^{-01}$
$0.800 \cdot 10^{-02}$	$0.650 \cdot 10^{+03}$	$0.928 \cdot 10^{+00}$	$0.585 \cdot 10^{-01}$	$0.585 \cdot 10^{-01}$	$0.953 \cdot 10^{-01}$	$-0.707 \cdot 10^{-01}$
$0.130 \cdot 10^{-01}$	$0.650 \cdot 10^{+03}$	$0.918 \cdot 10^{+00}$	$0.436 \cdot 10^{-01}$	$0.436 \cdot 10^{-01}$	$0.388 \cdot 10^{-01}$	$-0.252 \cdot 10^{-01}$
$0.210 \cdot 10^{-01}$	$0.650 \cdot 10^{+03}$	$0.824 \cdot 10^{+00}$	$0.621 \cdot 10^{-01}$	$0.621 \cdot 10^{-01}$	$0.233 \cdot 10^{-01}$	$-0.431 \cdot 10^{-01}$
$0.320 \cdot 10^{-01}$	$0.650 \cdot 10^{+03}$	$0.602 \cdot 10^{+00}$	$0.795 \cdot 10^{-01}$	$0.795 \cdot 10^{-01}$	$0.295 \cdot 10^{-01}$	$-0.313 \cdot 10^{-01}$
$0.500 \cdot 10^{-01}$	$0.650 \cdot 10^{+03}$	$0.518 \cdot 10^{+00}$	$0.777 \cdot 10^{-01}$	$0.777 \cdot 10^{-01}$	$0.180 \cdot 10^{-01}$	$-0.192 \cdot 10^{-01}$
$0.800 \cdot 10^{-01}$	$0.650 \cdot 10^{+03}$	$0.404 \cdot 10^{+00}$	$0.802 \cdot 10^{-01}$	$0.802 \cdot 10^{-01}$	$0.100 \cdot 10^{-01}$	$-0.264 \cdot 10^{-01}$
$0.130 \cdot 10^{+00}$	$0.650 \cdot 10^{+03}$	$0.340 \cdot 10^{+00}$	$0.761 \cdot 10^{-01}$	$0.761 \cdot 10^{-01}$	$0.244 \cdot 10^{-01}$	$-0.172 \cdot 10^{-01}$
$0.250 \cdot 10^{+00}$	$0.650 \cdot 10^{+03}$	$0.264 \cdot 10^{+00}$	$0.763 \cdot 10^{-01}$	$0.763 \cdot 10^{-01}$	$0.243 \cdot 10^{-01}$	$-0.279 \cdot 10^{-01}$
$0.400 \cdot 10^{+00}$	$0.650 \cdot 10^{+03}$	$0.139 \cdot 10^{+00}$	$0.136 \cdot 10^{+00}$	$0.136 \cdot 10^{+00}$	$0.573 \cdot 10^{-01}$	$-0.657 \cdot 10^{-01}$
$0.130 \cdot 10^{-01}$	$0.800 \cdot 10^{+03}$	$0.842 \cdot 10^{+00}$	$0.541 \cdot 10^{-01}$	$0.541 \cdot 10^{-01}$	$0.586 \cdot 10^{-01}$	$-0.546 \cdot 10^{-01}$
$0.210 \cdot 10^{-01}$	$0.800 \cdot 10^{+03}$	$0.805 \cdot 10^{+00}$	$0.645 \cdot 10^{-01}$	$0.645 \cdot 10^{-01}$	$0.332 \cdot 10^{-01}$	$-0.467 \cdot 10^{-01}$
$0.320 \cdot 10^{-01}$	$0.800 \cdot 10^{+03}$	$0.600 \cdot 10^{+00}$	$0.696 \cdot 10^{-01}$	$0.696 \cdot 10^{-01}$	$0.226 \cdot 10^{-01}$	$-0.152 \cdot 10^{-01}$
$0.500 \cdot 10^{-01}$	$0.800 \cdot 10^{+03}$	$0.593 \cdot 10^{+00}$	$0.653 \cdot 10^{-01}$	$0.653 \cdot 10^{-01}$	$0.334 \cdot 10^{-01}$	$-0.250 \cdot 10^{-01}$
$0.800 \cdot 10^{-01}$	$0.800 \cdot 10^{+03}$	$0.490 \cdot 10^{+00}$	$0.754 \cdot 10^{-01}$	$0.754 \cdot 10^{-01}$	$0.127 \cdot 10^{-01}$	$-0.280 \cdot 10^{-01}$
$0.130 \cdot 10^{+00}$	$0.800 \cdot 10^{+03}$	$0.347 \cdot 10^{+00}$	$0.896 \cdot 10^{-01}$	$0.896 \cdot 10^{-01}$	$0.160 \cdot 10^{-01}$	$-0.527 \cdot 10^{-01}$
$0.250 \cdot 10^{+00}$	$0.800 \cdot 10^{+03}$	$0.256 \cdot 10^{+00}$	$0.108 \cdot 10^{+00}$	$0.108 \cdot 10^{+00}$	$0.606 \cdot 10^{-02}$	$-0.655 \cdot 10^{-01}$
$0.400 \cdot 10^{+00}$	$0.800 \cdot 10^{+03}$	$0.134 \cdot 10^{+00}$	$0.162 \cdot 10^{+00}$	$0.162 \cdot 10^{+00}$	$0.402 \cdot 10^{-01}$	$-0.654 \cdot 10^{-01}$
$0.140 \cdot 10^{-01}$	$0.120 \cdot 10^{+04}$	$0.910 \cdot 10^{+00}$	$0.624 \cdot 10^{-01}$	$0.624 \cdot 10^{-01}$	$0.653 \cdot 10^{-01}$	$-0.906 \cdot 10^{-01}$
$0.210 \cdot 10^{-01}$	$0.120 \cdot 10^{+04}$	$0.656 \cdot 10^{+00}$	$0.691 \cdot 10^{-01}$	$0.691 \cdot 10^{-01}$	$0.484 \cdot 10^{-01}$	$-0.475 \cdot 10^{-01}$
$0.320 \cdot 10^{-01}$	$0.120 \cdot 10^{+04}$	$0.586 \cdot 10^{+00}$	$0.672 \cdot 10^{-01}$	$0.672 \cdot 10^{-01}$	$0.427 \cdot 10^{-01}$	$-0.308 \cdot 10^{-01}$
$0.500 \cdot 10^{-01}$	$0.120 \cdot 10^{+04}$	$0.514 \cdot 10^{+00}$	$0.601 \cdot 10^{-01}$	$0.601 \cdot 10^{-01}$	$0.409 \cdot 10^{-01}$	$-0.131 \cdot 10^{-01}$
$0.800 \cdot 10^{-01}$	$0.120 \cdot 10^{+04}$	$0.438 \cdot 10^{+00}$	$0.622 \cdot 10^{-01}$	$0.622 \cdot 10^{-01}$	$0.149 \cdot 10^{-01}$	$-0.314 \cdot 10^{-01}$
$0.130 \cdot 10^{+00}$	$0.120 \cdot 10^{+04}$	$0.357 \cdot 10^{+00}$	$0.664 \cdot 10^{-01}$	$0.664 \cdot 10^{-01}$	$0.319 \cdot 10^{-01}$	$-0.220 \cdot 10^{-01}$
$0.250 \cdot 10^{+00}$	$0.120 \cdot 10^{+04}$	$0.260 \cdot 10^{+00}$	$0.729 \cdot 10^{-01}$	$0.729 \cdot 10^{-01}$	$0.305 \cdot 10^{-01}$	$-0.816 \cdot 10^{-02}$
$0.400 \cdot 10^{+00}$	$0.120 \cdot 10^{+04}$	$0.110 \cdot 10^{+00}$	$0.116 \cdot 10^{+00}$	$0.116 \cdot 10^{+00}$	$0.110 \cdot 10^{+00}$	$-0.294 \cdot 10^{-01}$
$0.650 \cdot 10^{+00}$	$0.120 \cdot 10^{+04}$	$0.000 \cdot 10^{+00}$	$0.000 \cdot 10^{+00}$	$0.000 \cdot 10^{+00}$	$0.000 \cdot 10^{+00}$	$0.000 \cdot 10^{+00}$
$0.210 \cdot 10^{-01}$	$0.150 \cdot 10^{+04}$	$0.793 \cdot 10^{+00}$	$0.856 \cdot 10^{-01}$	$0.856 \cdot 10^{-01}$	$0.118 \cdot 10^{+00}$	$-0.101 \cdot 10^{+00}$
$0.320 \cdot 10^{-01}$	$0.150 \cdot 10^{+04}$	$0.716 \cdot 10^{+00}$	$0.788 \cdot 10^{-01}$	$0.788 \cdot 10^{-01}$	$0.780 \cdot 10^{-01}$	$-0.279 \cdot 10^{-01}$
$0.500 \cdot 10^{-01}$	$0.150 \cdot 10^{+04}$	$0.586 \cdot 10^{+00}$	$0.721 \cdot 10^{-01}$	$0.721 \cdot 10^{-01}$	$0.384 \cdot 10^{-01}$	$-0.360 \cdot 10^{-01}$
$0.800 \cdot 10^{-01}$	$0.150 \cdot 10^{+04}$	$0.436 \cdot 10^{+00}$	$0.780 \cdot 10^{-01}$	$0.780 \cdot 10^{-01}$	$0.268 \cdot 10^{-01}$	$-0.182 \cdot 10^{-01}$
$0.130 \cdot 10^{+00}$	$0.150 \cdot 10^{+04}$	$0.398 \cdot 10^{+00}$	$0.902 \cdot 10^{-01}$	$0.902 \cdot 10^{-01}$	$0.280 \cdot 10^{-01}$	$-0.426 \cdot 10^{-01}$

Table J.17: $d^2\sigma/dxdQ^2$ values for the $(e^-p)^{920}$ sample

x	Q^2	$\frac{d^2\sigma^{920}}{dx,dQ^2}$	$\%\delta_{sta.Up}$	$\%\delta_{sta.Dn}$	$\%\delta_{sys.Up}$	$\%\delta_{sys.Dn}$
$0.180 \cdot 10^{+00}$	$0.150 \cdot 10^{+04}$	$0.362 \cdot 10^{+00}$	$0.929 \cdot 10^{-01}$	$0.929 \cdot 10^{-01}$	$0.332 \cdot 10^{-01}$	$-0.241 \cdot 10^{-01}$
$0.250 \cdot 10^{+00}$	$0.150 \cdot 10^{+04}$	$0.275 \cdot 10^{+00}$	$0.112 \cdot 10^{+00}$	$0.112 \cdot 10^{+00}$	$0.234 \cdot 10^{-01}$	$-0.207 \cdot 10^{-01}$
$0.400 \cdot 10^{+00}$	$0.150 \cdot 10^{+04}$	$0.131 \cdot 10^{+00}$	$0.162 \cdot 10^{+00}$	$0.162 \cdot 10^{+00}$	$0.181 \cdot 10^{-01}$	$-0.148 \cdot 10^{+00}$
$0.650 \cdot 10^{+00}$	$0.150 \cdot 10^{+04}$	$0.393 \cdot 10^{-01}$	$0.458 \cdot 10^{+00}$	$0.602 \cdot 10^{+00}$	$0.316 \cdot 10^{+00}$	$-0.281 \cdot 10^{+00}$
$0.320 \cdot 10^{-01}$	$0.200 \cdot 10^{+04}$	$0.680 \cdot 10^{+00}$	$0.935 \cdot 10^{-01}$	$0.935 \cdot 10^{-01}$	$0.133 \cdot 10^{+00}$	$-0.702 \cdot 10^{-01}$
$0.500 \cdot 10^{-01}$	$0.200 \cdot 10^{+04}$	$0.547 \cdot 10^{+00}$	$0.919 \cdot 10^{-01}$	$0.919 \cdot 10^{-01}$	$0.476 \cdot 10^{-01}$	$-0.383 \cdot 10^{-01}$
$0.800 \cdot 10^{-01}$	$0.200 \cdot 10^{+04}$	$0.447 \cdot 10^{+00}$	$0.928 \cdot 10^{-01}$	$0.928 \cdot 10^{-01}$	$0.356 \cdot 10^{-01}$	$-0.504 \cdot 10^{-01}$
$0.130 \cdot 10^{+00}$	$0.200 \cdot 10^{+04}$	$0.402 \cdot 10^{+00}$	$0.107 \cdot 10^{+00}$	$0.107 \cdot 10^{+00}$	$0.344 \cdot 10^{-01}$	$-0.215 \cdot 10^{-01}$
$0.180 \cdot 10^{+00}$	$0.200 \cdot 10^{+04}$	$0.276 \cdot 10^{+00}$	$0.120 \cdot 10^{+00}$	$0.120 \cdot 10^{+00}$	$0.143 \cdot 10^{-01}$	$-0.398 \cdot 10^{-01}$
$0.250 \cdot 10^{+00}$	$0.200 \cdot 10^{+04}$	$0.294 \cdot 10^{+00}$	$0.130 \cdot 10^{+00}$	$0.130 \cdot 10^{+00}$	$0.473 \cdot 10^{-01}$	$-0.252 \cdot 10^{-01}$
$0.400 \cdot 10^{+00}$	$0.200 \cdot 10^{+04}$	$0.106 \cdot 10^{+00}$	$0.205 \cdot 10^{+00}$	$0.205 \cdot 10^{+00}$	$0.881 \cdot 10^{-01}$	$-0.141 \cdot 10^{-01}$
$0.500 \cdot 10^{-01}$	$0.300 \cdot 10^{+04}$	$0.663 \cdot 10^{+00}$	$0.107 \cdot 10^{+00}$	$0.107 \cdot 10^{+00}$	$0.123 \cdot 10^{+00}$	$-0.100 \cdot 10^{+00}$
$0.800 \cdot 10^{-01}$	$0.300 \cdot 10^{+04}$	$0.480 \cdot 10^{+00}$	$0.108 \cdot 10^{+00}$	$0.108 \cdot 10^{+00}$	$0.672 \cdot 10^{-01}$	$-0.186 \cdot 10^{-01}$
$0.130 \cdot 10^{+00}$	$0.300 \cdot 10^{+04}$	$0.357 \cdot 10^{+00}$	$0.133 \cdot 10^{+00}$	$0.133 \cdot 10^{+00}$	$0.410 \cdot 10^{-01}$	$-0.600 \cdot 10^{-01}$
$0.180 \cdot 10^{+00}$	$0.300 \cdot 10^{+04}$	$0.307 \cdot 10^{+00}$	$0.136 \cdot 10^{+00}$	$0.136 \cdot 10^{+00}$	$0.438 \cdot 10^{-01}$	$-0.626 \cdot 10^{-01}$
$0.250 \cdot 10^{+00}$	$0.300 \cdot 10^{+04}$	$0.276 \cdot 10^{+00}$	$0.152 \cdot 10^{+00}$	$0.152 \cdot 10^{+00}$	$0.207 \cdot 10^{-01}$	$-0.511 \cdot 10^{-01}$
$0.400 \cdot 10^{+00}$	$0.300 \cdot 10^{+04}$	$0.159 \cdot 10^{+00}$	$0.205 \cdot 10^{+00}$	$0.205 \cdot 10^{+00}$	$0.491 \cdot 10^{-01}$	$-0.646 \cdot 10^{-01}$
$0.650 \cdot 10^{+00}$	$0.300 \cdot 10^{+04}$	$0.126 \cdot 10^{-01}$	$0.487 \cdot 10^{+00}$	$0.663 \cdot 10^{+00}$	$0.227 \cdot 10^{+00}$	$-0.123 \cdot 10^{+00}$
$0.800 \cdot 10^{-01}$	$0.500 \cdot 10^{+04}$	$0.576 \cdot 10^{+00}$	$0.921 \cdot 10^{-01}$	$0.921 \cdot 10^{-01}$	$0.102 \cdot 10^{+00}$	$-0.108 \cdot 10^{+00}$
$0.130 \cdot 10^{+00}$	$0.500 \cdot 10^{+04}$	$0.492 \cdot 10^{+00}$	$0.123 \cdot 10^{+00}$	$0.123 \cdot 10^{+00}$	$0.394 \cdot 10^{-01}$	$-0.597 \cdot 10^{-01}$
$0.180 \cdot 10^{+00}$	$0.500 \cdot 10^{+04}$	$0.394 \cdot 10^{+00}$	$0.129 \cdot 10^{+00}$	$0.129 \cdot 10^{+00}$	$0.247 \cdot 10^{-01}$	$-0.352 \cdot 10^{-01}$
$0.250 \cdot 10^{+00}$	$0.500 \cdot 10^{+04}$	$0.257 \cdot 10^{+00}$	$0.166 \cdot 10^{+00}$	$0.166 \cdot 10^{+00}$	$0.630 \cdot 10^{-01}$	$-0.266 \cdot 10^{-01}$
$0.400 \cdot 10^{+00}$	$0.500 \cdot 10^{+04}$	$0.146 \cdot 10^{+00}$	$0.217 \cdot 10^{+00}$	$0.217 \cdot 10^{+00}$	$0.289 \cdot 10^{-01}$	$-0.213 \cdot 10^{+00}$
$0.130 \cdot 10^{+00}$	$0.800 \cdot 10^{+04}$	$0.520 \cdot 10^{+00}$	$0.133 \cdot 10^{+00}$	$0.133 \cdot 10^{+00}$	$0.126 \cdot 10^{+00}$	$-0.678 \cdot 10^{-01}$
$0.180 \cdot 10^{+00}$	$0.800 \cdot 10^{+04}$	$0.430 \cdot 10^{+00}$	$0.168 \cdot 10^{+00}$	$0.168 \cdot 10^{+00}$	$0.429 \cdot 10^{-01}$	$-0.103 \cdot 10^{+00}$
$0.250 \cdot 10^{+00}$	$0.800 \cdot 10^{+04}$	$0.318 \cdot 10^{+00}$	$0.198 \cdot 10^{+00}$	$0.198 \cdot 10^{+00}$	$0.363 \cdot 10^{-01}$	$-0.222 \cdot 10^{-01}$
$0.400 \cdot 10^{+00}$	$0.800 \cdot 10^{+04}$	$0.140 \cdot 10^{+00}$	$0.287 \cdot 10^{+00}$	$0.358 \cdot 10^{+00}$	$0.178 \cdot 10^{+00}$	$-0.124 \cdot 10^{+00}$
$0.650 \cdot 10^{+00}$	$0.800 \cdot 10^{+04}$	$0.156 \cdot 10^{-01}$	$0.550 \cdot 10^{+00}$	$0.767 \cdot 10^{+00}$	$0.115 \cdot 10^{+00}$	$-0.162 \cdot 10^{-01}$
$0.180 \cdot 10^{+00}$	$0.120 \cdot 10^{+05}$	$0.480 \cdot 10^{+00}$	$0.182 \cdot 10^{+00}$	$0.182 \cdot 10^{+00}$	$0.105 \cdot 10^{+00}$	$-0.980 \cdot 10^{-01}$
$0.250 \cdot 10^{+00}$	$0.120 \cdot 10^{+05}$	$0.287 \cdot 10^{+00}$	$0.279 \cdot 10^{+00}$	$0.279 \cdot 10^{+00}$	$0.350 \cdot 10^{-01}$	$-0.949 \cdot 10^{-01}$
$0.400 \cdot 10^{+00}$	$0.120 \cdot 10^{+05}$	$0.138 \cdot 10^{+00}$	$0.371 \cdot 10^{+00}$	$0.484 \cdot 10^{+00}$	$0.167 \cdot 10^{+00}$	$-0.159 \cdot 10^{-01}$
$0.250 \cdot 10^{+00}$	$0.200 \cdot 10^{+05}$	$0.498 \cdot 10^{+00}$	$0.264 \cdot 10^{+00}$	$0.264 \cdot 10^{+00}$	$0.205 \cdot 10^{+00}$	$-0.264 \cdot 10^{+00}$
$0.400 \cdot 10^{+00}$	$0.200 \cdot 10^{+05}$	$0.213 \cdot 10^{+00}$	$0.398 \cdot 10^{+00}$	$0.527 \cdot 10^{+00}$	$0.787 \cdot 10^{-01}$	$-0.212 \cdot 10^{+00}$
$0.400 \cdot 10^{+00}$	$0.300 \cdot 10^{+05}$	$0.280 \cdot 10^{+00}$	$0.433 \cdot 10^{+00}$	$0.583 \cdot 10^{+00}$	$0.192 \cdot 10^{+00}$	$-0.641 \cdot 10^{-01}$

Table J.18: $d^2\sigma/dxdQ^2$ values for the $(e^-p)^{920}$ sample

x	Q^2	$\frac{d^2\sigma^{920}}{dx\,dQ^2}$	$\%\delta_{sta.Up}$	$\%\delta_{sta.Dn}$	$\%\delta_{sys.Up}$	$\%\delta_{sys.Dn}$
$0.320 \cdot 10^{-02}$	$0.200 \cdot 10^{+03}$	$0.119 \cdot 10^{+01}$	$0.288 \cdot 10^{-01}$	$0.288 \cdot 10^{-01}$	$0.107 \cdot 10^{+00}$	$-0.888 \cdot 10^{-01}$
$0.500 \cdot 10^{-02}$	$0.200 \cdot 10^{+03}$	$0.109 \cdot 10^{+01}$	$0.153 \cdot 10^{-01}$	$0.153 \cdot 10^{-01}$	$0.306 \cdot 10^{-01}$	$-0.335 \cdot 10^{-01}$
$0.800 \cdot 10^{-02}$	$0.200 \cdot 10^{+03}$	$0.918 \cdot 10^{+00}$	$0.151 \cdot 10^{-01}$	$0.151 \cdot 10^{-01}$	$0.217 \cdot 10^{-01}$	$-0.250 \cdot 10^{-01}$
$0.130 \cdot 10^{-01}$	$0.200 \cdot 10^{+03}$	$0.807 \cdot 10^{+00}$	$0.152 \cdot 10^{-01}$	$0.152 \cdot 10^{-01}$	$0.187 \cdot 10^{-01}$	$-0.288 \cdot 10^{-01}$
$0.210 \cdot 10^{-01}$	$0.200 \cdot 10^{+03}$	$0.691 \cdot 10^{+00}$	$0.185 \cdot 10^{-01}$	$0.185 \cdot 10^{-01}$	$0.162 \cdot 10^{-01}$	$-0.277 \cdot 10^{-01}$
$0.320 \cdot 10^{-01}$	$0.200 \cdot 10^{+03}$	$0.599 \cdot 10^{+00}$	$0.190 \cdot 10^{-01}$	$0.190 \cdot 10^{-01}$	$0.157 \cdot 10^{-01}$	$-0.187 \cdot 10^{-01}$
$0.500 \cdot 10^{-01}$	$0.200 \cdot 10^{+03}$	$0.526 \cdot 10^{+00}$	$0.181 \cdot 10^{-01}$	$0.181 \cdot 10^{-01}$	$0.225 \cdot 10^{-01}$	$-0.180 \cdot 10^{-01}$
$0.800 \cdot 10^{-01}$	$0.200 \cdot 10^{+03}$	$0.440 \cdot 10^{+00}$	$0.157 \cdot 10^{-01}$	$0.157 \cdot 10^{-01}$	$0.258 \cdot 10^{-01}$	$-0.211 \cdot 10^{-01}$
$0.180 \cdot 10^{+00}$	$0.200 \cdot 10^{+03}$	$0.336 \cdot 10^{+00}$	$0.175 \cdot 10^{-01}$	$0.175 \cdot 10^{-01}$	$0.319 \cdot 10^{-01}$	$-0.372 \cdot 10^{-01}$
$0.500 \cdot 10^{-02}$	$0.250 \cdot 10^{+03}$	$0.115 \cdot 10^{+01}$	$0.225 \cdot 10^{-01}$	$0.225 \cdot 10^{-01}$	$0.445 \cdot 10^{-01}$	$-0.530 \cdot 10^{-01}$
$0.800 \cdot 10^{-02}$	$0.250 \cdot 10^{+03}$	$0.960 \cdot 10^{+00}$	$0.175 \cdot 10^{-01}$	$0.175 \cdot 10^{-01}$	$0.206 \cdot 10^{-01}$	$-0.291 \cdot 10^{-01}$
$0.130 \cdot 10^{-01}$	$0.250 \cdot 10^{+03}$	$0.825 \cdot 10^{+00}$	$0.176 \cdot 10^{-01}$	$0.176 \cdot 10^{-01}$	$0.192 \cdot 10^{-01}$	$-0.205 \cdot 10^{-01}$
$0.210 \cdot 10^{-01}$	$0.250 \cdot 10^{+03}$	$0.702 \cdot 10^{+00}$	$0.214 \cdot 10^{-01}$	$0.214 \cdot 10^{-01}$	$0.125 \cdot 10^{-01}$	$-0.181 \cdot 10^{-01}$
$0.320 \cdot 10^{-01}$	$0.250 \cdot 10^{+03}$	$0.588 \cdot 10^{+00}$	$0.221 \cdot 10^{-01}$	$0.221 \cdot 10^{-01}$	$0.220 \cdot 10^{-01}$	$-0.320 \cdot 10^{-01}$
$0.500 \cdot 10^{-01}$	$0.250 \cdot 10^{+03}$	$0.527 \cdot 10^{+00}$	$0.210 \cdot 10^{-01}$	$0.210 \cdot 10^{-01}$	$0.150 \cdot 10^{-01}$	$-0.187 \cdot 10^{-01}$
$0.800 \cdot 10^{-01}$	$0.250 \cdot 10^{+03}$	$0.426 \cdot 10^{+00}$	$0.185 \cdot 10^{-01}$	$0.185 \cdot 10^{-01}$	$0.258 \cdot 10^{-01}$	$-0.140 \cdot 10^{-01}$
$0.180 \cdot 10^{+00}$	$0.250 \cdot 10^{+03}$	$0.321 \cdot 10^{+00}$	$0.192 \cdot 10^{-01}$	$0.192 \cdot 10^{-01}$	$0.245 \cdot 10^{-01}$	$-0.162 \cdot 10^{-01}$
$0.500 \cdot 10^{-02}$	$0.350 \cdot 10^{+03}$	$0.108 \cdot 10^{+01}$	$0.321 \cdot 10^{-01}$	$0.321 \cdot 10^{-01}$	$0.124 \cdot 10^{+00}$	$-0.133 \cdot 10^{+00}$
$0.800 \cdot 10^{-02}$	$0.350 \cdot 10^{+03}$	$0.977 \cdot 10^{+00}$	$0.242 \cdot 10^{-01}$	$0.242 \cdot 10^{-01}$	$0.189 \cdot 10^{-01}$	$-0.208 \cdot 10^{-01}$
$0.130 \cdot 10^{-01}$	$0.350 \cdot 10^{+03}$	$0.812 \cdot 10^{+00}$	$0.205 \cdot 10^{-01}$	$0.205 \cdot 10^{-01}$	$0.142 \cdot 10^{-01}$	$-0.278 \cdot 10^{-01}$
$0.210 \cdot 10^{-01}$	$0.350 \cdot 10^{+03}$	$0.683 \cdot 10^{+00}$	$0.237 \cdot 10^{-01}$	$0.237 \cdot 10^{-01}$	$0.166 \cdot 10^{-01}$	$-0.216 \cdot 10^{-01}$
$0.320 \cdot 10^{-01}$	$0.350 \cdot 10^{+03}$	$0.606 \cdot 10^{+00}$	$0.244 \cdot 10^{-01}$	$0.244 \cdot 10^{-01}$	$0.220 \cdot 10^{-01}$	$-0.210 \cdot 10^{-01}$
$0.500 \cdot 10^{-01}$	$0.350 \cdot 10^{+03}$	$0.504 \cdot 10^{+00}$	$0.235 \cdot 10^{-01}$	$0.235 \cdot 10^{-01}$	$0.158 \cdot 10^{-01}$	$-0.144 \cdot 10^{-01}$
$0.800 \cdot 10^{-01}$	$0.350 \cdot 10^{+03}$	$0.424 \cdot 10^{+00}$	$0.206 \cdot 10^{-01}$	$0.206 \cdot 10^{-01}$	$0.190 \cdot 10^{-01}$	$-0.147 \cdot 10^{-01}$
$0.180 \cdot 10^{+00}$	$0.350 \cdot 10^{+03}$	$0.319 \cdot 10^{+00}$	$0.214 \cdot 10^{-01}$	$0.214 \cdot 10^{-01}$	$0.212 \cdot 10^{-01}$	$-0.280 \cdot 10^{-01}$
$0.800 \cdot 10^{-02}$	$0.450 \cdot 10^{+03}$	$0.101 \cdot 10^{+01}$	$0.242 \cdot 10^{-01}$	$0.242 \cdot 10^{-01}$	$0.501 \cdot 10^{-01}$	$-0.339 \cdot 10^{-01}$
$0.130 \cdot 10^{-01}$	$0.450 \cdot 10^{+03}$	$0.803 \cdot 10^{+00}$	$0.313 \cdot 10^{-01}$	$0.313 \cdot 10^{-01}$	$0.105 \cdot 10^{-01}$	$-0.304 \cdot 10^{-01}$
$0.210 \cdot 10^{-01}$	$0.450 \cdot 10^{+03}$	$0.710 \cdot 10^{+00}$	$0.326 \cdot 10^{-01}$	$0.326 \cdot 10^{-01}$	$0.210 \cdot 10^{-01}$	$-0.238 \cdot 10^{-01}$
$0.320 \cdot 10^{-01}$	$0.450 \cdot 10^{+03}$	$0.626 \cdot 10^{+00}$	$0.299 \cdot 10^{-01}$	$0.299 \cdot 10^{-01}$	$0.202 \cdot 10^{-01}$	$-0.216 \cdot 10^{-01}$
$0.500 \cdot 10^{-01}$	$0.450 \cdot 10^{+03}$	$0.511 \cdot 10^{+00}$	$0.273 \cdot 10^{-01}$	$0.273 \cdot 10^{-01}$	$0.193 \cdot 10^{-01}$	$-0.209 \cdot 10^{-01}$
$0.800 \cdot 10^{-01}$	$0.450 \cdot 10^{+03}$	$0.446 \cdot 10^{+00}$	$0.268 \cdot 10^{-01}$	$0.268 \cdot 10^{-01}$	$0.203 \cdot 10^{-01}$	$-0.145 \cdot 10^{-01}$
$0.130 \cdot 10^{+00}$	$0.450 \cdot 10^{+03}$	$0.370 \cdot 10^{+00}$	$0.287 \cdot 10^{-01}$	$0.287 \cdot 10^{-01}$	$0.206 \cdot 10^{-01}$	$-0.217 \cdot 10^{-01}$

Table J.19: $d^2\sigma/dxdQ^2$ values for the $(e^+p)^{920}$ sample

x	Q^2	$\frac{d^2\sigma^{920}}{dx\,dQ^2}$	$\%\delta_{sta.Up}$	$\%\delta_{sta.Dn}$	$\%\delta_{sys.Up}$	$\%\delta_{sys.Dn}$
$0.250 \cdot 10^{+00}$	$0.450 \cdot 10^{+03}$	$0.257 \cdot 10^{+00}$	$0.293 \cdot 10^{-01}$	$0.293 \cdot 10^{-01}$	$0.312 \cdot 10^{-01}$	$-0.150 \cdot 10^{-01}$
$0.800 \cdot 10^{-02}$	$0.650 \cdot 10^{+03}$	$0.948 \cdot 10^{+00}$	$0.321 \cdot 10^{-01}$	$0.321 \cdot 10^{-01}$	$0.906 \cdot 10^{-01}$	$-0.745 \cdot 10^{-01}$
$0.130 \cdot 10^{-01}$	$0.650 \cdot 10^{+03}$	$0.844 \cdot 10^{+00}$	$0.250 \cdot 10^{-01}$	$0.250 \cdot 10^{-01}$	$0.305 \cdot 10^{-01}$	$-0.204 \cdot 10^{-01}$
$0.210 \cdot 10^{-01}$	$0.650 \cdot 10^{+03}$	$0.716 \cdot 10^{+00}$	$0.354 \cdot 10^{-01}$	$0.354 \cdot 10^{-01}$	$0.332 \cdot 10^{-01}$	$-0.225 \cdot 10^{-01}$
$0.320 \cdot 10^{-01}$	$0.650 \cdot 10^{+03}$	$0.602 \cdot 10^{+00}$	$0.425 \cdot 10^{-01}$	$0.425 \cdot 10^{-01}$	$0.277 \cdot 10^{-01}$	$-0.318 \cdot 10^{-01}$
$0.500 \cdot 10^{-01}$	$0.650 \cdot 10^{+03}$	$0.532 \cdot 10^{+00}$	$0.420 \cdot 10^{-01}$	$0.420 \cdot 10^{-01}$	$0.270 \cdot 10^{-01}$	$-0.136 \cdot 10^{-01}$
$0.800 \cdot 10^{-01}$	$0.650 \cdot 10^{+03}$	$0.460 \cdot 10^{+00}$	$0.413 \cdot 10^{-01}$	$0.413 \cdot 10^{-01}$	$0.242 \cdot 10^{-01}$	$-0.248 \cdot 10^{-01}$
$0.130 \cdot 10^{+00}$	$0.650 \cdot 10^{+03}$	$0.350 \cdot 10^{+00}$	$0.428 \cdot 10^{-01}$	$0.428 \cdot 10^{-01}$	$0.138 \cdot 10^{-01}$	$-0.132 \cdot 10^{-01}$
$0.250 \cdot 10^{+00}$	$0.650 \cdot 10^{+03}$	$0.249 \cdot 10^{+00}$	$0.440 \cdot 10^{-01}$	$0.440 \cdot 10^{-01}$	$0.263 \cdot 10^{-01}$	$-0.222 \cdot 10^{-01}$
$0.400 \cdot 10^{+00}$	$0.650 \cdot 10^{+03}$	$0.140 \cdot 10^{+00}$	$0.765 \cdot 10^{-01}$	$0.765 \cdot 10^{-01}$	$0.544 \cdot 10^{-01}$	$-0.554 \cdot 10^{-01}$
$0.130 \cdot 10^{-01}$	$0.800 \cdot 10^{+03}$	$0.825 \cdot 10^{+00}$	$0.299 \cdot 10^{-01}$	$0.299 \cdot 10^{-01}$	$0.520 \cdot 10^{-01}$	$-0.456 \cdot 10^{-01}$
$0.210 \cdot 10^{-01}$	$0.800 \cdot 10^{+03}$	$0.733 \cdot 10^{+00}$	$0.371 \cdot 10^{-01}$	$0.371 \cdot 10^{-01}$	$0.266 \cdot 10^{-01}$	$-0.211 \cdot 10^{-01}$
$0.320 \cdot 10^{-01}$	$0.800 \cdot 10^{+03}$	$0.632 \cdot 10^{+00}$	$0.382 \cdot 10^{-01}$	$0.382 \cdot 10^{-01}$	$0.251 \cdot 10^{-01}$	$-0.248 \cdot 10^{-01}$
$0.500 \cdot 10^{-01}$	$0.800 \cdot 10^{+03}$	$0.513 \cdot 10^{+00}$	$0.386 \cdot 10^{-01}$	$0.386 \cdot 10^{-01}$	$0.336 \cdot 10^{-01}$	$-0.191 \cdot 10^{-01}$
$0.800 \cdot 10^{-01}$	$0.800 \cdot 10^{+03}$	$0.434 \cdot 10^{+00}$	$0.428 \cdot 10^{-01}$	$0.428 \cdot 10^{-01}$	$0.306 \cdot 10^{-01}$	$-0.526 \cdot 10^{-01}$
$0.130 \cdot 10^{+00}$	$0.800 \cdot 10^{+03}$	$0.353 \cdot 10^{+00}$	$0.478 \cdot 10^{-01}$	$0.478 \cdot 10^{-01}$	$0.205 \cdot 10^{-01}$	$-0.200 \cdot 10^{-01}$
$0.250 \cdot 10^{+00}$	$0.800 \cdot 10^{+03}$	$0.242 \cdot 10^{+00}$	$0.560 \cdot 10^{-01}$	$0.560 \cdot 10^{-01}$	$0.379 \cdot 10^{-01}$	$-0.258 \cdot 10^{-01}$
$0.400 \cdot 10^{+00}$	$0.800 \cdot 10^{+03}$	$0.154 \cdot 10^{+00}$	$0.818 \cdot 10^{-01}$	$0.818 \cdot 10^{-01}$	$0.402 \cdot 10^{-01}$	$-0.495 \cdot 10^{-01}$
$0.140 \cdot 10^{-01}$	$0.120 \cdot 10^{+04}$	$0.857 \cdot 10^{+00}$	$0.352 \cdot 10^{-01}$	$0.352 \cdot 10^{-01}$	$0.955 \cdot 10^{-01}$	$-0.896 \cdot 10^{-01}$
$0.210 \cdot 10^{-01}$	$0.120 \cdot 10^{+04}$	$0.760 \cdot 10^{+00}$	$0.360 \cdot 10^{-01}$	$0.360 \cdot 10^{-01}$	$0.389 \cdot 10^{-01}$	$-0.423 \cdot 10^{-01}$
$0.320 \cdot 10^{-01}$	$0.120 \cdot 10^{+04}$	$0.635 \cdot 10^{+00}$	$0.362 \cdot 10^{-01}$	$0.362 \cdot 10^{-01}$	$0.320 \cdot 10^{-01}$	$-0.404 \cdot 10^{-01}$
$0.500 \cdot 10^{-01}$	$0.120 \cdot 10^{+04}$	$0.530 \cdot 10^{+00}$	$0.338 \cdot 10^{-01}$	$0.338 \cdot 10^{-01}$	$0.312 \cdot 10^{-01}$	$-0.268 \cdot 10^{-01}$
$0.800 \cdot 10^{-01}$	$0.120 \cdot 10^{+04}$	$0.440 \cdot 10^{+00}$	$0.345 \cdot 10^{-01}$	$0.345 \cdot 10^{-01}$	$0.238 \cdot 10^{-01}$	$-0.314 \cdot 10^{-01}$
$0.130 \cdot 10^{+00}$	$0.120 \cdot 10^{+04}$	$0.347 \cdot 10^{+00}$	$0.368 \cdot 10^{-01}$	$0.368 \cdot 10^{-01}$	$0.302 \cdot 10^{-01}$	$-0.162 \cdot 10^{-01}$
$0.250 \cdot 10^{+00}$	$0.120 \cdot 10^{+04}$	$0.234 \cdot 10^{+00}$	$0.417 \cdot 10^{-01}$	$0.417 \cdot 10^{-01}$	$0.402 \cdot 10^{-01}$	$-0.377 \cdot 10^{-01}$
$0.400 \cdot 10^{+00}$	$0.120 \cdot 10^{+04}$	$0.134 \cdot 10^{+00}$	$0.597 \cdot 10^{-01}$	$0.597 \cdot 10^{-01}$	$0.490 \cdot 10^{-01}$	$-0.440 \cdot 10^{-01}$
$0.650 \cdot 10^{+00}$	$0.120 \cdot 10^{+04}$	$0.000 \cdot 10^{+00}$	$0.000 \cdot 10^{+00}$	$0.000 \cdot 10^{+00}$	$0.000 \cdot 10^{+00}$	$0.000 \cdot 10^{+00}$
$0.210 \cdot 10^{-01}$	$0.150 \cdot 10^{+04}$	$0.690 \cdot 10^{+00}$	$0.487 \cdot 10^{-01}$	$0.487 \cdot 10^{-01}$	$0.715 \cdot 10^{-01}$	$-0.991 \cdot 10^{-01}$
$0.320 \cdot 10^{-01}$	$0.150 \cdot 10^{+04}$	$0.614 \cdot 10^{+00}$	$0.471 \cdot 10^{-01}$	$0.471 \cdot 10^{-01}$	$0.473 \cdot 10^{-01}$	$-0.257 \cdot 10^{-01}$
$0.500 \cdot 10^{-01}$	$0.150 \cdot 10^{+04}$	$0.572 \cdot 10^{+00}$	$0.415 \cdot 10^{-01}$	$0.415 \cdot 10^{-01}$	$0.144 \cdot 10^{-01}$	$-0.425 \cdot 10^{-01}$
$0.800 \cdot 10^{-01}$	$0.150 \cdot 10^{+04}$	$0.427 \cdot 10^{+00}$	$0.434 \cdot 10^{-01}$	$0.434 \cdot 10^{-01}$	$0.204 \cdot 10^{-01}$	$-0.295 \cdot 10^{-01}$
$0.130 \cdot 10^{+00}$	$0.150 \cdot 10^{+04}$	$0.331 \cdot 10^{+00}$	$0.530 \cdot 10^{-01}$	$0.530 \cdot 10^{-01}$	$0.274 \cdot 10^{-01}$	$-0.378 \cdot 10^{-01}$

Table J.20: $d^2\sigma/dxdQ^2$ values for the $(e^+p)^{920}$ sample

x	Q^2	$\frac{d^2\sigma^{920}}{dx\,dQ^2}$	$\%\delta_{sta.Up}$	$\%\delta_{sta.Dn}$	$\%\delta_{sys.Up}$	$\%\delta_{sys.Dn}$
$0.180 \cdot 10^{+00}$	$0.150 \cdot 10^{+04}$	$0.302 \cdot 10^{+00}$	$0.546 \cdot 10^{-01}$	$0.546 \cdot 10^{-01}$	$0.235 \cdot 10^{-01}$	$-0.258 \cdot 10^{-01}$
$0.250 \cdot 10^{+00}$	$0.150 \cdot 10^{+04}$	$0.255 \cdot 10^{+00}$	$0.630 \cdot 10^{-01}$	$0.630 \cdot 10^{-01}$	$0.251 \cdot 10^{-01}$	$-0.394 \cdot 10^{-01}$
$0.400 \cdot 10^{+00}$	$0.150 \cdot 10^{+04}$	$0.132 \cdot 10^{+00}$	$0.894 \cdot 10^{-01}$	$0.894 \cdot 10^{-01}$	$0.498 \cdot 10^{-01}$	$-0.298 \cdot 10^{-01}$
$0.650 \cdot 10^{+00}$	$0.150 \cdot 10^{+04}$	$0.199 \cdot 10^{-01}$	$0.369 \cdot 10^{+00}$	$0.465 \cdot 10^{+00}$	$0.295 \cdot 10^{+00}$	$-0.499 \cdot 10^{+00}$
$0.320 \cdot 10^{-01}$	$0.200 \cdot 10^{+04}$	$0.638 \cdot 10^{+00}$	$0.532 \cdot 10^{-01}$	$0.532 \cdot 10^{-01}$	$0.794 \cdot 10^{-01}$	$-0.545 \cdot 10^{-01}$
$0.500 \cdot 10^{-01}$	$0.200 \cdot 10^{+04}$	$0.524 \cdot 10^{+00}$	$0.526 \cdot 10^{-01}$	$0.526 \cdot 10^{-01}$	$0.366 \cdot 10^{-01}$	$-0.253 \cdot 10^{-01}$
$0.800 \cdot 10^{-01}$	$0.200 \cdot 10^{+04}$	$0.437 \cdot 10^{+00}$	$0.515 \cdot 10^{-01}$	$0.515 \cdot 10^{-01}$	$0.381 \cdot 10^{-01}$	$-0.298 \cdot 10^{-01}$
$0.130 \cdot 10^{+00}$	$0.200 \cdot 10^{+04}$	$0.422 \cdot 10^{+00}$	$0.582 \cdot 10^{-01}$	$0.582 \cdot 10^{-01}$	$0.137 \cdot 10^{-01}$	$-0.457 \cdot 10^{-01}$
$0.180 \cdot 10^{+00}$	$0.200 \cdot 10^{+04}$	$0.316 \cdot 10^{+00}$	$0.633 \cdot 10^{-01}$	$0.633 \cdot 10^{-01}$	$0.149 \cdot 10^{-01}$	$-0.236 \cdot 10^{-01}$
$0.250 \cdot 10^{+00}$	$0.200 \cdot 10^{+04}$	$0.235 \cdot 10^{+00}$	$0.778 \cdot 10^{-01}$	$0.778 \cdot 10^{-01}$	$0.259 \cdot 10^{-01}$	$-0.265 \cdot 10^{-01}$
$0.400 \cdot 10^{+00}$	$0.200 \cdot 10^{+04}$	$0.127 \cdot 10^{+00}$	$0.109 \cdot 10^{+00}$	$0.109 \cdot 10^{+00}$	$0.533 \cdot 10^{-01}$	$-0.265 \cdot 10^{-01}$
$0.500 \cdot 10^{-01}$	$0.300 \cdot 10^{+04}$	$0.520 \cdot 10^{+00}$	$0.641 \cdot 10^{-01}$	$0.641 \cdot 10^{-01}$	$0.708 \cdot 10^{-01}$	$-0.333 \cdot 10^{-01}$
$0.800 \cdot 10^{-01}$	$0.300 \cdot 10^{+04}$	$0.412 \cdot 10^{+00}$	$0.632 \cdot 10^{-01}$	$0.632 \cdot 10^{-01}$	$0.270 \cdot 10^{-01}$	$-0.377 \cdot 10^{-01}$
$0.130 \cdot 10^{+00}$	$0.300 \cdot 10^{+04}$	$0.342 \cdot 10^{+00}$	$0.733 \cdot 10^{-01}$	$0.733 \cdot 10^{-01}$	$0.393 \cdot 10^{-01}$	$-0.375 \cdot 10^{-01}$
$0.180 \cdot 10^{+00}$	$0.300 \cdot 10^{+04}$	$0.314 \cdot 10^{+00}$	$0.724 \cdot 10^{-01}$	$0.724 \cdot 10^{-01}$	$0.239 \cdot 10^{-01}$	$-0.541 \cdot 10^{-01}$
$0.250 \cdot 10^{+00}$	$0.300 \cdot 10^{+04}$	$0.220 \cdot 10^{+00}$	$0.914 \cdot 10^{-01}$	$0.914 \cdot 10^{-01}$	$0.351 \cdot 10^{-01}$	$-0.255 \cdot 10^{-01}$
$0.400 \cdot 10^{+00}$	$0.300 \cdot 10^{+04}$	$0.134 \cdot 10^{+00}$	$0.120 \cdot 10^{+00}$	$0.120 \cdot 10^{+00}$	$0.521 \cdot 10^{-01}$	$-0.184 \cdot 10^{-01}$
$0.650 \cdot 10^{+00}$	$0.300 \cdot 10^{+04}$	$0.181 \cdot 10^{-01}$	$0.243 \cdot 10^{+00}$	$0.243 \cdot 10^{+00}$	$0.152 \cdot 10^{+00}$	$-0.152 \cdot 10^{+00}$
$0.800 \cdot 10^{-01}$	$0.500 \cdot 10^{+04}$	$0.426 \cdot 10^{+00}$	$0.558 \cdot 10^{-01}$	$0.558 \cdot 10^{-01}$	$0.414 \cdot 10^{-01}$	$-0.740 \cdot 10^{-01}$
$0.130 \cdot 10^{+00}$	$0.500 \cdot 10^{+04}$	$0.335 \cdot 10^{+00}$	$0.791 \cdot 10^{-01}$	$0.791 \cdot 10^{-01}$	$0.114 \cdot 10^{-01}$	$-0.533 \cdot 10^{-01}$
$0.180 \cdot 10^{+00}$	$0.500 \cdot 10^{+04}$	$0.255 \cdot 10^{+00}$	$0.851 \cdot 10^{-01}$	$0.851 \cdot 10^{-01}$	$0.214 \cdot 10^{-01}$	$-0.576 \cdot 10^{-01}$
$0.250 \cdot 10^{+00}$	$0.500 \cdot 10^{+04}$	$0.194 \cdot 10^{+00}$	$0.983 \cdot 10^{-01}$	$0.983 \cdot 10^{-01}$	$0.588 \cdot 10^{-01}$	$-0.236 \cdot 10^{-01}$
$0.400 \cdot 10^{+00}$	$0.500 \cdot 10^{+04}$	$0.115 \cdot 10^{+00}$	$0.132 \cdot 10^{+00}$	$0.132 \cdot 10^{+00}$	$0.523 \cdot 10^{-01}$	$-0.549 \cdot 10^{-01}$
$0.130 \cdot 10^{+00}$	$0.800 \cdot 10^{+04}$	$0.318 \cdot 10^{+00}$	$0.860 \cdot 10^{-01}$	$0.860 \cdot 10^{-01}$	$0.232 \cdot 10^{-01}$	$-0.711 \cdot 10^{-01}$
$0.180 \cdot 10^{+00}$	$0.800 \cdot 10^{+04}$	$0.252 \cdot 10^{+00}$	$0.113 \cdot 10^{+00}$	$0.113 \cdot 10^{+00}$	$0.200 \cdot 10^{-01}$	$-0.443 \cdot 10^{-01}$
$0.250 \cdot 10^{+00}$	$0.800 \cdot 10^{+04}$	$0.208 \cdot 10^{+00}$	$0.125 \cdot 10^{+00}$	$0.125 \cdot 10^{+00}$	$0.663 \cdot 10^{-01}$	$-0.276 \cdot 10^{-01}$
$0.400 \cdot 10^{+00}$	$0.800 \cdot 10^{+04}$	$0.952 \cdot 10^{-01}$	$0.184 \cdot 10^{+00}$	$0.184 \cdot 10^{+00}$	$0.590 \cdot 10^{-01}$	$-0.455 \cdot 10^{-01}$
$0.650 \cdot 10^{+00}$	$0.800 \cdot 10^{+04}$	$0.804 \cdot 10^{-02}$	$0.435 \cdot 10^{+00}$	$0.584 \cdot 10^{+00}$	$0.264 \cdot 10^{+00}$	$-0.288 \cdot 10^{-01}$
$0.180 \cdot 10^{+00}$	$0.120 \cdot 10^{+05}$	$0.268 \cdot 10^{+00}$	$0.126 \cdot 10^{+00}$	$0.126 \cdot 10^{+00}$	$0.577 \cdot 10^{-01}$	$-0.190 \cdot 10^{+00}$
$0.250 \cdot 10^{+00}$	$0.120 \cdot 10^{+05}$	$0.181 \cdot 10^{+00}$	$0.181 \cdot 10^{+00}$	$0.181 \cdot 10^{+00}$	$0.630 \cdot 10^{-01}$	$-0.263 \cdot 10^{-01}$
$0.400 \cdot 10^{+00}$	$0.120 \cdot 10^{+05}$	$0.110 \cdot 10^{+00}$	$0.220 \cdot 10^{+00}$	$0.220 \cdot 10^{+00}$	$0.712 \cdot 10^{-01}$	$-0.158 \cdot 10^{+00}$
$0.250 \cdot 10^{+00}$	$0.200 \cdot 10^{+05}$	$0.101 \cdot 10^{+00}$	$0.291 \cdot 10^{+00}$	$0.291 \cdot 10^{+00}$	$0.305 \cdot 10^{+00}$	$-0.349 \cdot 10^{+00}$
$0.400 \cdot 10^{+00}$	$0.200 \cdot 10^{+05}$	$0.546 \cdot 10^{-01}$	$0.398 \cdot 10^{+00}$	$0.527 \cdot 10^{+00}$	$0.237 \cdot 10^{+00}$	$-0.560 \cdot 10^{-01}$
$0.400 \cdot 10^{+00}$	$0.300 \cdot 10^{+05}$	$0.283 \cdot 10^{-01}$	$0.650 \cdot 10^{+00}$	$0.914 \cdot 10^{+00}$	$0.983 \cdot 10^{-01}$	$-0.676 \cdot 10^{-01}$

Table J.21: $d^2\sigma/dxdQ^2$ values for the $(e^+p)^{920}$ sample

x	Q^2	xF_3	$\delta_{sta.Up}$	$\delta_{sta.Dn}$	$\delta_{sys.Up}$	$\delta_{sys.Dn}$
0.050	1500.000	0.065	0.046	0.046	0.057	0.058
0.130	1500.000	0.034	0.093	0.093	0.043	0.033
0.400	1500.000	0.131	0.195	0.195	0.037	0.094
0.050	2000.000	0.046	0.045	0.045	0.062	0.045
0.130	2000.000	0.028	0.079	0.079	0.026	0.032
0.400	2000.000	0.041	0.148	0.148	0.117	0.089
0.050	3000.000	0.057	0.057	0.057	0.059	0.070
0.130	3000.000	0.084	0.060	0.060	0.030	0.029
0.400	3000.000	0.247	0.122	0.122	0.051	0.093
0.130	5000.000	0.157	0.037	0.037	0.026	0.036
0.400	5000.000	0.056	0.075	0.075	0.032	0.064
0.180	8000.000	0.148	0.046	0.046	0.031	0.029
0.400	8000.000	0.061	0.057	0.057	0.034	0.020
0.180	12000.000	0.166	0.059	0.059	0.033	0.031
0.400	12000.000	0.047	0.048	0.048	0.017	0.011
0.400	20000.000	0.096	0.039	0.039	0.027	0.034

Table J.22: xF_3 values for the $(e^+p)^{820}$ and $(e^-p)^{920}$ samples

List of Figures

2.1 Schematic representation of a deep inelastic scattering event. 7

2.2 Scaling behavior of the structure function $F_2 = \nu W_2$. 8

2.3 Schematic representation of the quark parton model. 9

2.4 $F_2(x, Q^2)$ as a function of Q^2 for different x bins. 11

2.5 Schematic representation of processes that contribute in order α_s. 12

2.6 Illustration of the QCD factorization theorem for the $ep \to eX$ process. 12

2.7 Gluon splitting into two gluons and a quark-antiquark pair. Emission and absorption of a gluon by a quark. 14

2.8 Schematic representation of the hadronization and fragmentation that takes place after the scattering process. 15

2.9 Theoretical reduced cross section for NC e^+p DIS events. 18

2.10 Structure functions of the proton. 19

2.11 Partons distribution inside the proton for $Q^2 = 10$ GeV^2. 20

2.12 Electroweak couplings multiplied by the Z propagator $\chi_z(Q^2)$ ($-a_e\chi_z(Q^2)$, $-v_e\chi_z(Q^2)$, $(a_e^2 + v_e^2)\chi_z^2(Q^2)$ and $2a_e v_e \chi_z^2(Q^2)$) for e^+p data as a function of Q^2. 21

2.13 Contribution of $xG_3(x, Q^2)$ and $xH_3(x, Q^2)$ to the structure function of the proton $xF_3(x, Q^2)$. 22

2.14 Structure function of the proton $xG_3(x, Q^2)$. 23

2.15 Lowest order of QED corrections to the Born level cross section. 25

3.1 Top view of the HERA ring. 28

3.2 The HERA accelerator complex 29

4.1 Side view of the ZEUS detector along the beam axis 32

4.2 Front view of the ZEUS detector perpendicular to the beam axis 33

4.3 Layout of a CTD octant. 34

4.4 CTD Acceptance region. 35

4.5 ZEUS FCAL module. EMC and HAC sections are shown. 37

4.6 Luminosity monitor. 38

4.7 Schematic representation of the ZEUS three-level trigger. 39

6.1 Neutral current deep inelastic event. 47
6.2 η_{max} variable. 49
6.3 Reweighting of the Monte Carlo sample in the Q^2 variable. 52

7.1 Schematic representation of a neutral current DIS event. 53
7.2 Isolines of constant energy for the scattered lepton in the kinematic plane. . . . 55
7.3 Isolines of constant $p_{T,h}$ for the hadronic final state over the kinematic plane. . . 56
7.4 Isolines of constant $E - p_Z$ for the hadronic final state over the kinematic plane. 57
7.5 Double angle energy for the scattered lepton. 58
7.6 Isolines of constant scattered lepton angle Θ over the kinematic plane. 59
7.7 Isolines of constant γ_h for the hadronic final state over the kinematic plane. . . . 60
7.8 Comparison between different reconstruction methods before analysis cuts. . . . 61
7.9 Comparison between different reconstruction methods. 62

8.1 Neutral Current event in ZEUS detector. 63
8.2 Total $E - p_Z$ variable. 64
8.3 z-vertex measured with tracks from the CTD. 67
8.4 x- and y-vertices measured from tracks from the CTD. 68
8.5 Schematic representation of the cell islands algorithm. 68
8.6 SINISTRA95 probability for electromagnetic candidates. 70
8.7 Energy of the scattered lepton measured with the calorimeter before corrections. 71
8.8 Angle of the scattered lepton. 72
8.9 γ_{max} cut for CORANDCUT for two different proton energies $E_p = 820$ GeV and $E_p = 920$ GeV 74
8.10 $E - p_Z$ variable for the hadronic system measured with CORANDCUT. 75
8.11 p_T variable for the hadronic system measured with CORANDCUT. 76
8.12 γ_h variable for the hadronic system measured with CORANDCUT. 77
8.13 E_e/E_{DA} distribution along the z-position. 78
8.14 $x_{HES} - x_{track}$ plotted against the y_{HES} variable. 79
8.15 Data and Monte Carlo energies before and after dead material corrections. . . . 80
8.16 Comparison of the corrected energy in the BCAL with the momentum of the track. 81
8.17 Non-uniformity corrections for the BCAL. 82
8.18 Non-uniformity corrections along the $|x|$ (left) and $|y|$ (right) variables in the RCAL. 83

8.19 Scattered lepton energy after dead material and non-uniformity corrections. . . . 84
8.20 Sigma from Gaussian fit of the distribution E_e/E_{DA}. 85
8.21 Calculation of the smear constant for RCAL and BCAL. 86
8.22 Energy of the scattered lepton after dead material and non-uniformity corrections, and smearing. 87
8.23 $Pt/\sqrt{Et}$ distribution. 88
8.24 Bunch structure of run 22718 for paired bunches. 90

9.1 Efficiency of the ISOe trigger as a function of the scattered lepton energy E_e and its radius the RCAL face R_e. 92
9.2 Efficiency of the BMC trigger as a function of the scattered lepton energy E_e and its z-position along the BCAL. 93
9.3 Purity of the sample of well isolated tracks. 94
9.4 Efficiency of the electron-finder SIRA 5. 95
9.5 Comparison of the SIRA 5 probability in bins of the scattered lepton angle for data and Monte Carlo simulation. 96
9.6 Fit of mean and sigma for $\Delta\Theta$ and $\Delta\varphi$ for all calorimeter regions in 4 different energy bins. 98
9.7 ε^{found} and ε^{DIS} plotted versus the energy, angle and $\log_{10}(\mathrm{Q}^2)$ of the true scattered lepton for SIRA 5. 100
9.8 Distance of closest approach and momentum of the track distributions. 101
9.9 $P_{T,h}/E_{T,h}$ distribution. 102
9.10 Comparison of the efficiency rejecting data and Monte Carlo events with track cuts. 103
9.11 Mean value of the Gaussian fit of the $1-E_e/E_{DA}$ distribution for data and Monte Carlo sample. 104
9.12 Mean value of the $1 - E_e/E_{DA}$ distribution in data minus mean value of the Monte Carlo distribution. 105
9.13 Energy in an $\eta - \phi$ cone of radius $R = 1$ around the scattered lepton, that does not belong to it. 106
9.14 Photoproduction background in the Q^2 and y_e variables. 106
9.15 Distribution in the kinematic variables of the e-pilot bunches events. 107
9.16 Purity and efficiency of the double differential bins. 110

10.1 Single differential cross section $d\sigma/dQ^2$ for the 96/97 positron , 98/99 electron and 99/00 positron data samples. 112
10.2 Single differential cross section $d\sigma/dx$ for $Q^2 > 200$ GeV^2 for the 96/96 positron, 98/99 electron and 99/00 positron data sample. 113

10.3 Single differential cross section $d\sigma/dx$ for $Q^2 > 10000$ GeV^2 for the 96/97 positron, 98/99 electron and 99/00 positron data samples. 114

10.4 Single differential cross section $d\sigma/dy$ for $Q^2 > 200$ GeV^2 for the 96/97 positron, 98/99 electron and 99/00 positron data samples. 115

10.5 Reduced cross section $\tilde{\sigma}$ for $Q^2 > 200$ GeV^2 for the 96/97 positron, 98/99 electron and 99/00 positron data samples. 116

10.6 Reduced cross section $\tilde{\sigma}$ for $Q^2 > 200$ GeV^2 for the 96/97 positron, 98/99 electron and 99/00 positron data samples. 117

11.1 xF_3 bins in the $x\,Q^2$ kinematic plane. 120

11.2 Structure function $xF_3(x, Q^2)$ of the proton extracted for the $(e^+p)^{820}$ and $(e^-p)^{920}$ data samples. The result is shown in fixed bins of Q^2. 121

11.3 Structure function of the proton $xF_3(x, Q^2)$ extracted for the $(e^+p)^{820}$ and $(e^-p)^{920}$ data samples. The result is shown in fixed bins of x. 122

11.4 Extraction of the structure function $xG_3(x, Q^2)$. 123

11.5 Comparison of xG_3 and xF_3^{CC} values for different experiments. 123

11.6 Integral of G_3 for different values of Q^2. 124

12.1 Change of the statistical error of $xF_3(x, Q^2)$ with increasing luminosity. 126

12.2 Electroweak couplings multiplied by the Z propagator for different polarizations as a function of Q^2. 127

A.1 Change of the relative $xF_3(x, Q^2)$ errors with increasing luminosity. 133

A.2 Structure function of the proton $xF_3(x, Q^2)$ extracted for all data samples. The result is shown in fixed bins of Q^2. 134

B.1 E_e/E_{DA} in different bins of E_e for scattered leptons in the RCAL. 136

B.2 E_e/E_{DA} in different bins of E_e for scattered leptons in the BCAL. 137

C.1 ε^{DIS} plotted versus the energy, angle and $\log_{10}(\mathrm{Q}^2)$ of the true scattered lepton variables for SIRA 5, only for events in which $|V_z^{true} - V_z^{meas.}| \leq 5$ cm and only for non radiative events. 139

D.1 ε^{DIS} plotted versus the energy, angle and $\log_{10}(\mathrm{Q}^2)$ of the true scattered lepton variables for SIRA 5 (diamonds) and EM (crosses), for all events (left) and only for non radiative events and $|V_z^{true} - V_z^{meas.}| \leq 5$ cm (right). 142

E.1 $1 - E_e/E_{DA}$ in different bins of E_{DA} for scattered leptons in the RCAL. 144

E.2 $1 - E_e/E_{DA}$ in different bins of E_{DA} for scattered leptons in the BCAL. The events correspond to the sample used to perform the analysis. 145

E.3 $1-E_e/E_{DA}$ in different bins of E_{DA} for scattered leptons in the BCAL. The events correspond to the sample with tighter cuts on the $E-p_Z$ and the $E_{notinCone}$ variable. 146

E.4 $1 - E_e/E_{DA}$ in different bins of E_{DA} for scattered leptons in the BCAL. The events correspond to the high purity sample. 147

F.1 $E - p_z$ variable in bins of the scattered lepton angle Θ. This sample has no track cuts. 149

F.2 $E - p_Z$ variable in bins of the scattered lepton angle Θ. This sample has cuts on the track variables, i.e. $P_{trk} > 5\,GeV$ and $DCA < 10\,cm$. 150

F.3 Ratio from the $E-p_Z$ distributions with applied cuts divided by the distributions with no cuts in bins of the scattered lepton angle Θ. 151

F.4 Double ratio of the two distributions with and without cuts, data over Monte Carlo simulation, in bins of the scattered lepton angle Θ. 152

G.1 Resolution and bias for ZUFOSNT, CORANDCUT and ZUFOSNT with CORANDCUT γ_{max} cut implemented. 155

H.1 Reweighted z-Vertex for the 1996/97 data sample 157

H.2 Corrected scattered lepton energy E_e for the 1996/97 data sample 157

H.3 Scattered lepton angle Θ for the 1996/97 data sample 158

H.4 Hadronic γ_h angle for the 1996/97 data sample 158

H.5 Hadronic δ_h distribution for the 1996/97 data sample 159

H.6 Reweighted z-Vertex for the 1999/2000 data sample 159

H.7 Corrected scattered lepton energy E_e for the 1999/2000 data sample 160

H.8 Scattered lepton angle Θ for the 1999/2000 data sample 160

H.9 Hadronic γ_h angle for the 1999/2000 data sample 161

H.10 Hadronic δ_h distribution for the 1999/2000 data sample 161

I.1 Systematic uncertainties for the single differential cross section $d\sigma/dQ^2$ measured for $Q^2 > 200$ GeV^2 for the electron data sample 1998/99. 164

I.2 Systematic uncertainties for the single differential cross section $d\sigma/dx$ measured for $Q^2 > 200$ GeV^2 for the electron data sample 1998/99. 165

I.3 Systematic uncertainties for the single differential cross section $d\sigma/dx$ measured for $Q^2 > 10000$ GeV^2 for the electron data sample 1998/99. 166

I.4 Systematic uncertainties for the single differential cross section $d\sigma/dy$ measured for $Q^2 > 200$ GeV^2 for the electron data sample 1998/99. 167

I.5 Systematic uncertainty for the double differential cross section $d^2\sigma/dx\,dQ^2$ for $Q^2 > 200$ GeV^2 for the 98/99 electron data sample. 168

List of Tables

5.1 Summary of data samples for the years 1996-200. 44

J.1 $d\sigma/dx$ values for $Q^2 > 200$ GeV^2 for the $(e^+p)^{820}$ sample 169
J.2 $d\sigma/dx$ values for $Q^2 > 200$ GeV^2 for the $(e^-p)^{920}$ sample 169
J.3 $d\sigma/dx$ values for $Q^2 > 200$ GeV^2 for the $(e^+p)^{920}$ sample 170
J.4 $d\sigma/dx$ values for $Q^2 > 200$ GeV^2 for the $(e^+p)^{820}$ sample 170
J.5 $d\sigma/dx$ values for $Q^2 > 200$ GeV^2 for the $(e^-p)^{920}$ sample 170
J.6 $d\sigma/dx$ values for $Q^2 > 200$ GeV^2 for the $(e^+p)^{920}$ sample 171
J.7 $d\sigma/dx$ values for $Q^2 > 1000$ GeV^2 for the $(e^+p)^{820}$ sample 171
J.8 $d\sigma/dx$ values for $Q^2 > 1000$ GeV^2 for the $(e^-p)^{920}$ sample 171
J.9 $d\sigma/dx$ values for $Q^2 > 1000$ GeV^2 for the $(e^+p)^{920}$ sample 172
J.10 $d\sigma/dy$ values for $Q^2 > 200$ GeV^2 for the $(e^+p)^{820}$ sample 172
J.11 $d\sigma/dy$ values for $Q^2 > 200$ GeV^2 for the $(e^-p)^{920}$ sample 173
J.12 $d\sigma/dy$ values for $Q^2 > 200$ GeV^2 for the $(e^+p)^{920}$ sample 173
J.13 $d^2\sigma/dxdQ^2$ values for the $(e^+p)^{820}$ sample 174
J.14 $d^2\sigma/dxdQ^2$ values for the $(e^+p)^{820}$ sample 175
J.15 $d^2\sigma/dxdQ^2$ values for the $(e^+p)^{820}$ sample 176
J.16 $d^2\sigma/dxdQ^2$ values for the $(e^-p)^{920}$ sample 177
J.17 $d^2\sigma/dxdQ^2$ values for the $(e^-p)^{920}$ sample 178
J.18 $d^2\sigma/dxdQ^2$ values for the $(e^-p)^{920}$ sample 179
J.19 $d^2\sigma/dxdQ^2$ values for the $(e^+p)^{920}$ sample 180
J.20 $d^2\sigma/dxdQ^2$ values for the $(e^+p)^{920}$ sample 181
J.21 $d^2\sigma/dxdQ^2$ values for the $(e^+p)^{920}$ sample 182
J.22 xF_3 values for the $(e^+p)^{820}$ and $(e^-p)^{920}$ samples 183

Bibliography

[A+84] A. Argento et al. Measurement of the interference structure function $xG_3(x)$ in muon - nucleon scattering. *Phys. Lett.*, B140:142, 1984.

[A+91] A. Andresen et al. Construction and beam test of the ZEUS forward and rear calorimeter. *Nucl. Instrum. Meth.*, A309:101–142, 1991.

[A+92] J. Andruszkow et al. First measurement of HERA luminosity by ZEUS lumi monitor. 1992. DESY-92-066.

[A+93] I. Abt et al. Measurement of the proton structure function $F_2(x, Q^2)$ in the low x region at HERA. *Nucl. Phys.*, B407:515–538, 1993.

[A+01] C. Adloff et al. Measurement of neutral and charged current cross sections in electron proton collisions at high Q^2. *Eur. Phys. J.*, C19:269–288, 2001. hep-ex/0012052.

[ACS95] H. Abramowicz, A. Caldwell, and R. Sinkus. Neural network based electron identification in the zeus calorimeter. *Nucl. Instrum. Meth.*, A365:508–517, 1995. hep-ex/9505004.

[Alp92] H. Alphonsus. *The Global second level trigger for ZEUS*. PhD thesis, University of Amsterdam, 1992.

[Ame97] C. Amelung. Electron position reconstruction in ZEUS: Another update of the ELECPO package (based on 1995/96 data). ZEUS-Note 97-056, Juni 27 1997.

[Ame99] C. Amelung. *Measurement of the Proton Structure Function F_2 at Very Low Q^2 at HERA*. PhD thesis, Bonn University, 1999.

[AP77] G. Altarelli and G. Parisi. Asymptotic freedom in parton language. *Nucl. Phys.*, B126:298, 1977.

[B+] R. Brun et al. GEANT: Simulation program for particle physics experiments. user guide and reference manual. CERN-DD-78-2-REV.

[B+79] R. Brandelik et al. Evidence for planar events in e^+e^- annihilation at high- energies. *Phys. Lett.*, B86:243, 1979.

[B+89] S. Bhadra et al. The ZEUS third level trigger system. *Comput. Phys. Commun.*, 57:321, 1989.

[B+90] U. Behrens et al. Test of the ZEUS forward calorimeter prototype. *Nucl. Instrum. Meth.*, A289:115, 1990.

[B+96] A. Bamberger et al. The presampler for the forward and rear calorimeter in the ZEUS detector. *Nucl. Instrum. Meth.*, A382:419, 1996.

[B+98] J. Breitweg et al. Measurement of the diffractive structure function $F_2^{(D(4))}$ at HERA. *Eur. Phys. J.*, C1:81–96, 1998. hep-ex/9709021.

[B+99] J. Breitweg et al. Measurement of high-Q^2 neutral-current e^+p deep inelastic scattering cross-sections at HERA. *Eur. Phys. J.*, C11:427–445, 1999. hep-ex/9905032.

[B+00] J. Breitweg et al. Measurement of high-Q^2 charged-current e^+p deep inelastic scattering cross sections at HERA. *Eur. Phys. J.*, C12:411–428, 2000. hep-ex/9907010.

[Beh] T. Behnke. Electron polarization at HERA: Status and future prospects. Prepared for Workshop on Polarized Protons at High Energies - Accelerator Challenges and Physics Opportunities, Hamburg, Germany, 17-20 May 1999.

[BEK] S. Bentvelsen, J. Engelen, and P. Kooijman. Reconstruction of (x, Q^2) and extraction of structure functions in neutral current scattering at HERA. In *Hamburg 1991, Proceedings, Physics at HERA, vol. 1* 43- 55. (see HIGH ENERGY PHYSICS INDEX 30 (1992) No. 12988).

[Bot00] M. Botje. A QCD analysis of HERA and fixed target structure function data. *Eur. Phys. J.*, C14:285, 2000. hep-ph/9912439.

[Bri98] G. M. Briskin. *Diffractive Dissociation in ep Deep Inelastic Scattering.* PhD thesis, Tel Aviv University, 1998.

[BS87] M. Bohm and H. Spiesberger. Radiative corrections to neutral current deep inelastic lepton nucleon scattering at HERA energies. *Nucl. Phys.*, B294:1081, 1987.

[C+94] A. Caldwell et al. An electron energy correction method: A preliminary implementation and its effect on the F_2 measurement. ZEUS-Note 94-051, 10 May 1994.

[C+96] R. Carlin et al. The trigger of ZEUS, a flexible system for a high bunch crossing rate collider. *Nucl. Instrum. Meth.*, A379:542, 1996.

[C+98] A. Caldwell et al. BCAL electron studies. PART II:energy calibrations. ZEUS-Note 98-018, March 13 1998.

[CGCG69] Jr. C. G. Callan and D. J. Gross. High-energy electroproduction and the constitution of the electric current. *Phys. Rev. Lett.*, 22:156–159, 1969.

[CLS98] A. Caldwell, W. Liu, and B. Straub. BCAL electron studies. PART I: MC and test beam energy studies. ZEUS-Note 98-02, January 13 1998.

[Col93] ZEUS Collaboration. Status of the detector. Technical report, DESY, 1993.

[Cor] C. Cormack. http://www-zeus.desy.de/~cormack/nc98studies.htm.

[CP97] C. Catterall and F. Pelucchi. Comparison of CTD and calorimeter measurement of the DIS positron angle in high Q^2 events. ZEUS Note 97-056, July 1997.

[D+93] M. Derrick et al. Measurement of the proton structure function F_2 in ep scattering at HERA. *Phys. Lett.*, B316:412–426, 1993.

[D'A94] G. D'Agostini. On the use of the covariance matrix to fit correlated data. *Nucl. Instrum. Meth.*, A346:306–311, 1994.

[Def99] R. Defner. *Measurement of the Proton Structure Function F_2 at HERA using 1996 and 1997 ZEUS Data*. PhD thesis, Bonn University, 1999.

[dg00] Particle data group. Review of particle physics. *The European Physical Journal*, C15:1+, 2000.

[Dok77] Yu. L. Dokshitzer. Calculation of the structure functions for deep inelastic scattering and e^+e^- annihilation by perturbation theory in quantum chromodynamics. *Sov. Phys. JETP*, 46:641–653, 1977.

[E+73] T. Eichten et al. Measurement of the neutrino - nucleon anti-neutrino - nucleon total cross-sections. *Phys. Lett.*, B46:274–280, 1973.

[FK72] J. I. Friedman and H. W. Kendall. Deep inelastic electron scattering. *Ann. Rev. Nucl. Part. Sci.*, 22:203–254, 1972.

[G+91] R. Glaeser et al. ZEUS software update and supplement. ZEUS Note 91-070, July 16 1991.

[GK97] J. Grosse-Knetter. Energy correction for islands. ZEUS-Note 97-039, July 5 1997.

[GK98] J. Grosse-Knetter. Corrections for the hadronic final state. ZEUS-Note 98-031, April 30 1998.

[GL72] V. N. Gribov and L. N. Lipatov. Deep inelastic *ep* scattering in perturbation theory. *Yad. Fiz.*, 15:781–807, 1972.

[GL00] J.R Gonçalo and K. Long. A minimum bias vertex distribution for the 1998/99 e^-p data. ZEUS-Note 00-027, September 5 2000.

[Gla61] S. L. Glashow. Partial symmetries of weak interactions. *Nucl. Phys.*, 22:579–588, 1961.

[GRV95] M. Glück, E. Reya, and A. Vogt. Dynamical parton distributions of the proton and small x physics. *Z. Phys.*, C67:433–448, 1995.

[GS69] D. J. Gross and C. H. Llewellyn Smith. High-energy neutrino - nucleon scattering, current algebra and partons. *Nucl. Phys.*, B14:337–347, 1969.

[H+97] G.F. Hartner et al. VCTRACK(3.07/04):offline output information. ZEUS-Note 97-064, September 8 1997.

[Haa92] T. Haas. Generating Monte Carlos events with MOZART. ZEUS Note 92-021, February 10 1992.

[Har98] G.F. Hartner. Monte carlo shower terminators for ZEUS inside GEANT311. ZEUS-Note 88-049, June 1998.

[HES] Proposal for a hadron electron separator in the ZEUS forward and barrel calorimeters. Hamburg DESY - ZEUS-Note 91-044 (91/05,rec.Jun.) 46 p.

[HM84] F. Halzen and A. Martin. *Quarks and Leptons.* John Wiley and Sons, 1984.

[Hoe] K. C. Hoeger. Measurement of x, y, Q^2 in neutral current events. In *Hamburg 1991, Proceedings, Physics at HERA, vol. 1* 43- 55. (see HIGH ENERGY PHYSICS INDEX 30 (1992) No. 12988).

[IER97] G. Ingelman, A. Edin, and J. Rathsman. LEPTO 6.5 - a Monte Carlo generator for deep inelastic lepton-nucleon scattering. *Comput. Phys. Commun.*, 101:108–134, 1997. hep-ph/9605286.

[JB79] F. Jacquet and A. Blondel. Proceedings of the study of an *ep* facility for Europe. pages 391–394, 1979.

[Jun95] H. Jung. Hard diffractive scattering in high-energy *ep* collisions and the monte carlo generation RAPGAP. *Comp. Phys. Commun.*, 86:147–161, 1995.

[Kap] A. Kappes. http://www-zeus.physik.uni-bonn.de/~kappes/ZEUS_ONLY/alignment/alignment.html.

[Kap01] A. Kappes. *Thesis in preparation.* PhD thesis, Bonn Univerity, 2001.

[KR84] M. Klein and T. Riemann. Electroweak interactions probing the nucleon structure. *Z. Phys.*, C24:151, 1984.

[KSM92] A. Kwiatkowski, H. Spiesberger, and H. J. Mohring. HERACLES: An event generator for *ep* interactions at HERA energies including radiative processes: Version 1.0. *Comp. Phys. Commun.*, 69:155–172, 1992.

[L+95] H. L. Lai et al. Global QCD analysis and the CTEQ parton distributions. *Phys. Rev.*, D51:4763–4782, 1995. hep-ph/9410404.

[Liu] X. Liu. Energy scale studies. ZEUS Note (2001). In preparation.

[Lon99] K. R. Long. Future *ep* physics: The outlook for HERA. 1999. hep-ph/9909223.

[M+98] A. D. Martin et al. Parton distributions: A new global analysis. *Eur. Phys. J.*, C4:463, 1998. hep-ph/9803445.

[Mel01] B. Mellado. *Diffractive Heavy Vector Meson Photoproduction at HERA ep Colisions of* $\sqrt{s} = 318$ GeV *with the ZEUS Detector.* PhD thesis, Columbia University, New York, 2001. In preparation.

[Mor01] M. Moritz. *Thesis in preparation.* PhD thesis, Hamburg University, 2001.

[QR98] A. Quadt and O. Ruske. A new method to measure vertex distributions. ZEUS Note 98-036, Juny 08 1998.

[Qua96] A. Quadt. *Measurement and QCD Analysis of the Proton Structure Function* F_2 *from the 1994 HERA Data Using the ZEUS Detector.* PhD thesis, University of Oxford, 1996.

[RS00] E. Rizvi and T. Sloan. $xF_3^{\gamma Z}$ in charged lepton scattering. *Eur. Phys. J. C*, 2000. hep-ex/0101007.

[Rus00] O. C. Ruske. *Measurement and Phenomenology of the Proton Structure Function F_2 using the 1996 and 1997 ZEUS Data at HERA*. PhD thesis, University of Oxford, 2000.

[S+97] W. G. Seligman et al. Improved determination of α_s from neutrino nucleon scattering. *Phys. Rev. Lett.*, 79:1213–1216, 1997.

[Sal] A. Salam. Weak and electromagnetic interactions. Originally printed in *Svartholm: Elementary Particle Theory, Proceedings Of The Nobel Symposium Held 1968 At Lerum, Sweden*, Stockholm 1968, 367-377.

[Sch01] H. Schnurbusch. *Thesis in preparation.* PhD thesis, Bonn University, 2001.

[Sel97] W. G. Seligman. *A Next-to-Leading-Order QCD Analysis of Neutrino-Iron Structure Functions at the Tevatron.* PhD thesis, Columbia University, 1997.

[Sjo94] T. Sjostrand. High-energy physics event generation with PYTHIA 5.7 and JETSET 7.4. *Comput. Phys. Commun.*, 82:74–90, 1994.

[Smi] W. H. Smith. The ZEUS calorimeter first level trigger. Presented at Workshop on Triggering and Data Acquisition for Experiments at the Supercollider, Toronto, Canada, Jan 16- 19, 1989.

[SS] G. A. Schuler and H. Spiesberger. DJANGO: The interface for the event generators HERACLES and LEPTO. In *Hamburg 1991, Proceedings, Physics at HERA, vol. 3* 1419-1432. (see HIGH ENERGY PHYSICS INDEX 30 (1992) No. 12988).

[SSZ00] H. Spiesberger, M. Spira, and P. M. Zerwas. The Standard Model: Physical basis and scattering experiments. 2000. hep-ph/0011255.

[Str] B. Straub. http://www-zeus.desy.de/~straub/ZEUS_ONLY/doc/em.ps.

[SV97a] R. Sinkus and T. Voss. Particle identification with neural networks using a rotational invariant moment representation. *Nucl. Instrum. Meth.*, A389:160, 1997.

[SV97b] R. Sinkus and T. Voss. Particle identification with neural networks using a rotational invariant moment representation. *Nucl. Instrum. Meth.*, A391:360, 1997.

[Tun01a] N. Tuning. *Proton structure functions at HERA.* PhD thesis, Universiteit van Amsterdam, 2001.

[Tun01b] N. Tuning. ZUFOs: Hadronic final state reconstruction with calorimeter, tracking and backsplash correction. ZEUS-Note 01-021, June, 27 2001.

[VS00] A. López-Durán Viani and S. Schlenstedt. Electron finder efficiencies and impurities. a comparison between SINISTRA95, EM and EMNET. ZEUS Note 99-077, January 14 2000.

[Wei67] S. Weinberg. A model of leptons. *Phys. Rev. Lett.*, 19:1264–1266, 1967.

[Wod99] M.J. Wodarkzyc. *Measurement of the F_2 structure function of the proton at HERA from 1996 and 1997 ZEUS Data.* PhD thesis, University of Wisconsyn-Madison, 1999.

[Yos01] R. Yoshida. HERA small-x and / or diffraction. 2001. hep-ph/0102262.

[YS97] Y.Iga and S. Schlenstedt. Status and improvement of the ZEUS calorimeter simulation. ZEUS-Note 97-019, March 27 1997.

[Zer34] F. Zernike. *Physica*, 1:689, 1934.

[ZEU] *ZEUS Software*.